The Galaxy and Beyond with the Arcminute Microkelvin Imager

Yvette Perrott

Astrophysics Group, Cavendish Laboratory
and

Trinity College

University of Cambridge

A thesis submitted for the degree of

Doctor of Philosophy

17 September 2013

Declaration

This dissertation is the result of work carried out in the Astrophysics Group of the Cavendish Laboratory, Cambridge, between October 2010 and October 2013. The work contained in this thesis is my own except where stated otherwise. No part of this dissertation has been submitted for a degree, diploma or other qualification at this or any other university. The total length of this dissertation does not exceed sixty thousand words.

Yvette Perrott
September 2013

Summary

The Arcminute Microkelvin Imager (AMI) is a dual-array radio interferometer sited at Lord's Bridge, near Cambridge. Although it was designed specifically for studying galaxy clusters via observations of the Sunyaev-Zel'dovich (SZ) effect, it is also an ideal instrument for Galactic science. This thesis describes science programmes investigating both Galactic objects and galaxy clusters that I have carried out with AMI.

A new data analysis pipeline is described which has been developed to allow the automated processing of data taken by AMI in drift-scan mode, pointing the telescope at a fixed azimuth and elevation and observing the sky that drifts past. This is a very efficient mode for large-scale surveys, but the different character of the data has required innovative algorithms for effective processing.

The AMI Galactic Plane Survey uses drift-scanning to cover the northern Galactic plane between $|b| \lessapprox 5^{\circ}$. It is the first Galactic plane survey at cm-wave frequencies to achieve crucial mJy-sensitivity levels at arcminute-scale resolution over a wide area, and as such provides a unique opportunity to investigate hitherto unusual objects such as ultra- and hyper-compact HII regions. I describe my work on the survey strategy and its implementation and on some of the science I have extracted so far including the follow-up of candidate hyper-compact HII regions.

The recently-released *Planck* satellite results include the largest catalogue of SZ-selected clusters of galaxies to date. I describe the AMI follow-up programme to observe the clusters within the AMI observation limits, and present the first results from the programme including an interesting discrepancy between the cluster parameters according to AMI and *Planck*. Since the two instruments are observing the same physical process, this indicates a fundamental problem with the ‘universal’ pressure profile currently favoured for modelling clusters.

In an attempt to address the discrepancy, I use simulations to investigate the effect of allowing the shape of the pressure profile to vary. The derived parameter constraints are found to vary when clusters are not simulated and recovered with the same model; the effects are dependent on angular size, worsening for larger clusters. I also assess the potential for using AMI data to constrain the cluster shape parameters, and conclude that weak constraints on the shape parameters are possible with a careful choice of prior.

Acknowledgements

I acknowledge financial support from a Rutherford Foundation studentship supported by the Cambridge Commmonwealth Trust and the Cavendish Laboratory, administered by the Royal Society of New Zealand on behalf of the Rutherford Foundation Trust. Thank you so much for the opportunity to study in such a stimulating environment – it has been a truly amazing and unforgettable experience. Thanks also to Trinity College, for providing such a great environment to live and study in, and for the extra financial support that has enabled me to attend conferences.

To all of my supervisors, Keith Grainge, Richard Saunders and Dave Green, for all the encouragement, discussion and reading of innumerable drafts along the way – thank you! I couldn't have asked for more supportive and available supervisors.

I'd like to also thank Phil Yock, my supervisor at Auckland University, for introducing me to research and encouraging me to apply to Cambridge.

Thanks also to the rest of the AMI team, for help with everything from correlator boards to data reduction to McAdam: Farhan Feroz, Mike Hobson, Anthony Lasenby, Guy Pooley, Paul Scott, David Titterington and Elizabeth Waldram. In particular, thanks to David Titterington for all the help with computing and the SA. Massive thanks are also due to the AMI technical team, without whom nothing would happen: Bob Barker, Mike Crofts, Rob D'Alessandro, John Ely, Ian Northrop, and Clive Shaw.

Special thanks are also due to Anna Scaife for all the help, discussion and collaboration on AMI Galactic projects.

To the AMI students, past and present: it's been a privilege working with all of you. To Natasha Hurley-Walker, Matthew Davies and Tom Franzen, thank you for introducing me to the mysteries of AMI data when I first arrived. To Tim Shimwell, Carmen Rodríguez-Gonzálvez, Malak Olamaie, Michel Schammel and Clare Rumsey, thank you for all the help, discussion and advice over the years.

I've enjoyed being at the Cavendish so much, and that has been largely due to the warm and welcoming 'family' of students. Thanks to all of you for all the Castle pub-trips, movie nights, and random lunch-time conversations. In particular, thanks to the other students in my year: Lindley Lentati, Tamela Maciel, Peter Sims, Samatha Walker-Smith and Imogen Whittam – can you believe it's almost over??

To my Mum and Dad: words cannot express how much the support you've given me over the years have meant. Thank you for giving me so many opportunities and always encouraging me to follow my dreams and be the best I can be – I'm not the best street-sweeper in the world yet, but I'm still trying!

Last, but certainly not least, to Carl: thanks for picking up your life and moving to the opposite side of the world on your girlfriend's whim, for learning to sleep through my nocturnal teeth-grinding and generally putting up with me at my grumpiest. I couldn't have done it without your constant support.

Yvette Perrott
September 2013

Contents

Nomenclature

Conventions

α	Spectral index, where $S \propto \nu^{-\alpha}$
δ	J2000 declination
ν	Frequency
S	Flux density
RA	J2000 right ascension

Acronyms

AIPS	Astronomical Image Processing System
AME	Anomalous microwave emission
AMI	Arcminute Microkelvin Imager
CGPS	Canadian Galactic Plane Survey
CMB	Cosmic Microwave Background
LA	Large Array
NVSS	NRAO VLA Sky Survey
SA	Small Array
SED	Spectral energy distribution
SZ	Sunyaev-Zel’dovich (effect)

Chapter 1

Introduction

1.1 The Arcminute Microkelvin Imager

The Arcminute Microkelvin Imager (AMI) is a pair of radio synthesis telescopes, the Small Array (SA) and Large Array (LA), both operating over a frequency range of 13.5 – 18.0 GHz and sited at Lord's Bridge, Cambridgeshire. A full description of the telescope can be found in AMI Consortium: Zwart et al. (2008). Here I describe briefly the main features of the telescope, which are summarised in Table 1.1, and in Section 1.2.1 I summarise the choice of frequency.

The SA consists of ten 3.7-m dishes, arranged as shown in Fig. 1.1, on a steel floor to reduce ground-spill and surrounded by a steel screen to reduce terrestrial interference and further reduce ground-spill. It has baselines ranging between ≈ 5 and 20 m, corresponding to ≈ 250 to $1000\,\lambda$. The SA was optimised for observing objects on ≈ 3 arcmin scales, and has sensitivity to structures up to ≈ 10 arcmin in scale.

The LA comprises eight 12.8-m dishes, with baselines ranging between ≈ 17 and 107 m or ≈ 950 to $5600\,\lambda$. This gives it a much higher angular resolution than the SA, with a synthesised beam of ≈ 30 arcsec, and much less sensitivity to extended emission. The configuration of the telescope is shown in Fig. 1.1; five antennas are located on an (almost) east–west line, and the three remaining antennas are positioned to the north to improve the snapshot synthesised beam.

Each antenna on both arrays is polar mounted and has a single-polarisation receiver using InP high-electron-mobility transistors (HEMTs) and cooled to 12 K to reduce

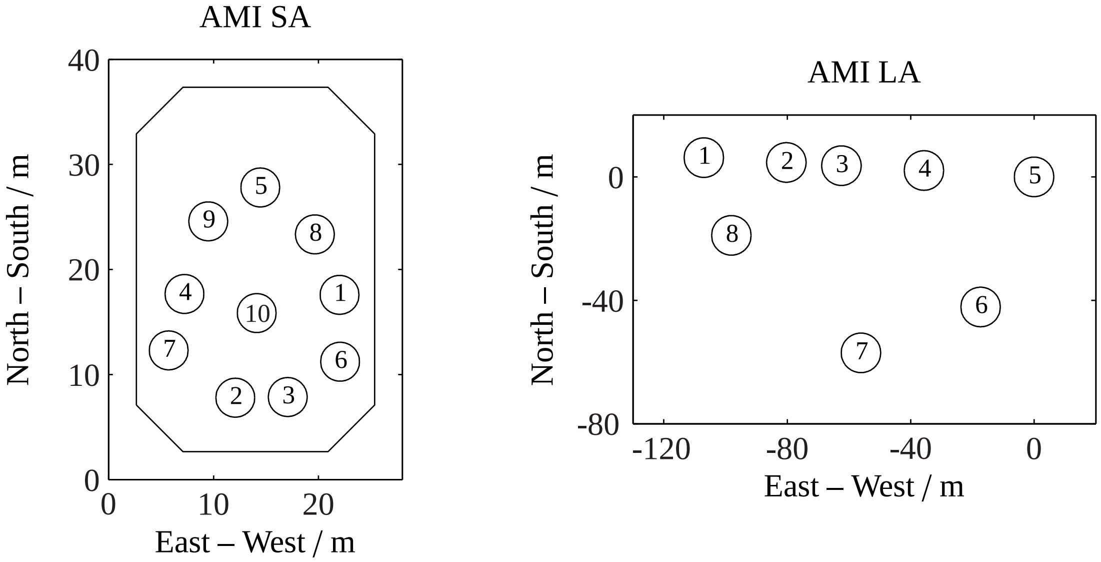

Figure 1.1: Configuration of the two AMI arrays.

Johnson noise. Each array has a local oscillator which allows downconversion at each antenna to an intermediate frequency (IF) covering 6 – 12 GHz. All these IF signals for each array are sent to a correlator, with amplification and cross-band slope equalisation en route. Before the correlator, analogue (cable and stripline) path compensation is performed with a smallest bit length of 25 mm (the IF signal has a coherence length of 50 mm), with each subsequent bit having a length of twice the previous one. Automatic gain control (AGC) at the end of each IF chain ensures that the power entering the correlator from each antenna is constant in time despite temperature, weather and airmass variations and variation between components. Also at the end of each IF chain is the synchronous detection of the 1 KHz square wave injected by a noise diode in each receiver horn; this ‘rain gauge’ signal provides a good measure for each telescope of the time-varying contributions to system temperature of atmospheric emission and rain.

The AMI correlators are ‘add and square’ Fourier Transform Spectrometers, which split the frequency band into eight channels each of 0.75 GHz by correlating the signals of each baseline simultaneously at 16 different discrete path (or equivalently, time) delays, with nominal delay length of 25mm; the data are then Fourier transformed to synthesise the frequency channels in software. To achieve full signal-to-noise performance, for each baseline the sum and difference of the two inputs are formed, resulting

Table 1.1: Main properties of the two AMI arrays. From AMI Consortium: Zwart et al. (2008).

	SA	LA
Antenna diameter	3.7 m	12.8 m
Antenna efficiency	0.75	0.67
Number of antennas	10	8
Number of baselines	45	28
Baseline lengths (current)	5–20 m	18–110 m
Primary beam (15.7 GHz)	20.1 arcmin	5.5 arcmin
Synthesized beam	≈ 3 arcmin	≈ 30 arcsec
Flux sensitivity	30 mJy $s^{-1/2}$	3 mJy $s^{-1/2}$
Observing frequency	13.9–18.2 GHz	
Bandwidth	4.3 GHz	
Number of channels	6	
Channel bandwidth	0.72 GHz	
System temperature	25 K	
Declination range	> -15°	> -20°
Elevation limit	+20°	+5°
Polarization measured	I+Q	

in two independent measurements for each lag. In practice, the bottom two channels are discarded due to a combination of poor correlator performance and satellite interference.

The presence of geostationary satellites also restricts the observing range of the telescopes. Although the SA and LA were designed to observe down to $\delta = -15°$ and $-20°$ respectively, satellite interference becomes problematic for the SA (LA) below $\delta \approx +20°$ ($+5°$). Below these limits, observation is possible but contamination from satellites becomes considerable and large amounts of the data must be discarded.

1.2 The Sunyaev-Zel’dovich Effect

AMI was designed to observe galaxy clusters via the Sunyaev-Zel’dovich (SZ) effect, which is the inverse-Compton scattering of cosmic microwave background (CMB) photons by high-energy electrons (Sunyaev and Zeldovich 1970, 1972; see also Birkinshaw 1999; Carlstrom et al. 2002 for reviews). This causes a distortion in the CMB spectrum, made up of three main components: the thermal SZ effect, caused by thermal motion of the electrons in the plasma in the huge gravitational potential wells of galaxy clusters; relativistic effects introduced by energetic non-thermal electrons in the plasma; and the kinematic SZ effect, caused by the peculiar velocity of the cluster with respect to the CMB rest frame. The dominant effect is the thermal SZ effect and the other two are neglected in the analysis of AMI data. The change in thermodynamic (not brightness) temperature due to the thermal SZ effect, ΔT_{SZ}, relative to the CMB temperature, T_{CMB}, is given by:

$$\begin{aligned}\frac{\Delta T_{SZ}}{T_{CMB}} &= f(x)y \qquad (1.1)\\ &= \left\{\left(x\frac{e^x+1}{e^x-1}-4\right)(1+\delta_{SZ}(x,T_e))\right\}\left\{\frac{\sigma_T}{m_e c^2}\int n_e k_B T_e \mathrm{d}\ell\right\}.\end{aligned}$$

The first factor $f(x)$ encodes the frequency dependence as a function of the dimensionless frequency $x \equiv (h\nu)/(k_B T_{CMB})$, where h is the Planck constant and k_B is the Boltzmann constant. δ_{SZ} is a relativistic correction (e.g. Challinor et al. 1997; Itoh et al. 1998) which is negligible for analysis of AMI data. In the Rayleigh-Jeans limit, $f(x) \approx$ -2. The second factor y is the Compton y-parameter, which encodes the number of scatterings a photon undergoes, $\sigma_T n_e$ where σ_T is the Thomson scattering cross-section and n_e is the electron number density, and the energy gain per scattering event, $(k_B T_e)/(m_e c^2)$ where m_e is the electron mass and c is the speed of light, integrated over the line of sight ℓ. This spectral distortion appears as a decrement in the CMB temperature at frequencies < 217 GHz and an increase at higher frequencies (see Fig. 1.2).

Equation 1.1 shows that the temperature decrement, and therefore the SZ surface brightness, are independent of redshift. Integrating the flux density over the solid angle of the cluster gives

$$\int \Delta T_{SZ} \mathrm{d}\Omega \propto \frac{N_e \langle T_e \rangle}{D_A^2} \propto \frac{M_{\mathrm{gas}} \langle T_e \rangle}{D_A^2} \qquad (1.2)$$

where $N_e, \langle T_e \rangle$ and M_{gas} are the total number of electrons in the cluster, mean electron temperature, and gas mass of the cluster, respectively and D_A is its angular diameter distance. For clusters at redshifts $z \gtrapprox 0.5$, D_A varies little with z, which is a strong

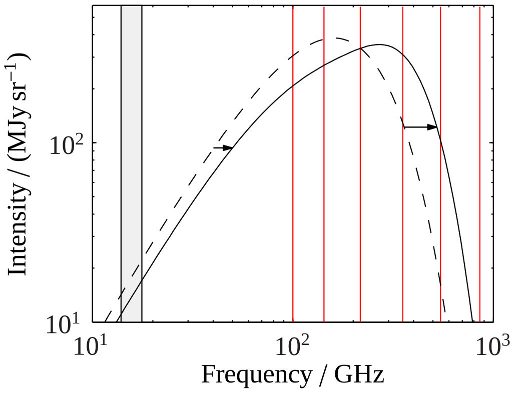

Figure 1.2: Spectrum resulting from the distortion caused by the SZ effect (solid line) to the black-body spectrum of the CMB (dashed line), for an exaggeratedly massive cluster with $y = 0.1$, according to equation 1.1. The AMI band is indicated by the grey rectangle, and the centres of the *Planck* bands used for SZ observations are also indicated as solid red lines (see Section 1.2.2).

advantage for observing distant clusters in SZ, as opposed to other observing methods such as X-ray for which the brightness of the cluster depends critically on the redshift. In addition, the y-parameter is proportional to the line-of-sight integral of electron number density (weighted by temperature), whereas X-ray luminosity is proportional to its square. This means that SZ data are less biased toward the concentrated, dense gas at the core of a cluster and can be used to detect and characterise the outer regions.

1.2.1 AMI design

The baseline range of the SA was designed to allow observation of extended objects of angular size up to ≈ 10 arcmin, which is necessary for observing the extended structure of the SZ effect for clusters at redshift $z \gtrapprox 0.2$, while excluding the biggest peaks in the primordial CMB power spectrum. The longer baselines of the LA were designed to exclude most of the cluster flux, and are primarily used to measure and subtract confusing foreground sources (Zwart, 2007); they can also be used to observe clusters at higher redshift with smaller angular sizes. Fig. 1.3(a) shows flux densities of a low- and higher- redshift cluster as a function of baseline length, compared to the primordial CMB anisotropies and confusing foreground sources, and illustrates the choice of baselines.

The AMI frequency band was chosen as a compromise between the SZ signal-

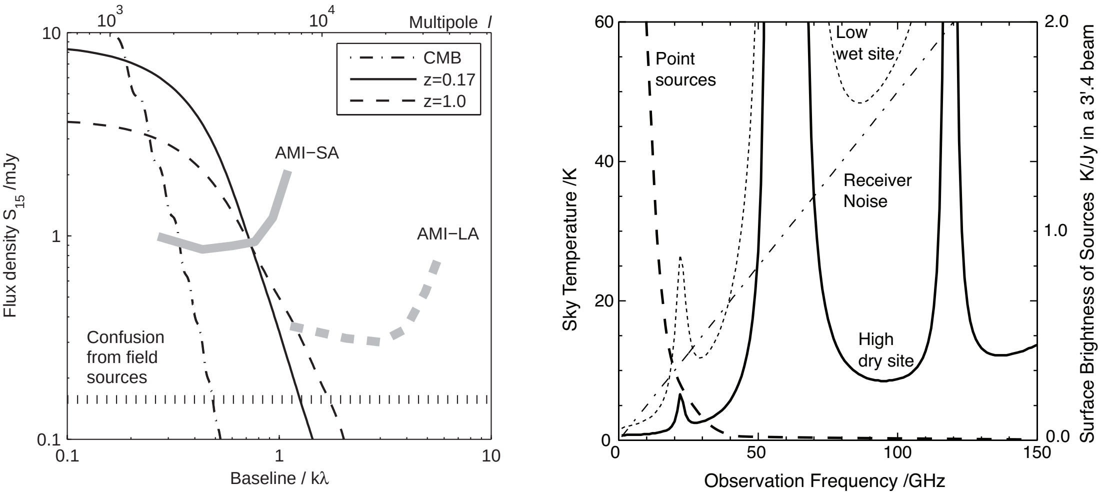

(a) (b)

Figure 1.3: An illustration of the conflicting effects which the AMI telescopes were designed around. (a) shows expected flux as a function of baseline for the primordial CMB anisotropies (dot-dash), the well-known cluster A2218 at redshift $z = 0.171$ (solid line), the same cluster shifted to $z = 1.0$ (dashed lines), and confusion from radio point sources (thick dotted line), assuming sources above 0.32 mJy have been detected by the LA and subtracted. The cluster flux density is plotted as positive for comparison with the other flux densities, but in reality is negative. The thick grey lines show the 4σ flux sensitivity of the two AMI arrays after a two-hour observation and illustrate the range of baseline lengths covered by both arrays. (b) shows the contribution of atmospheric emission to system temperature as a function of frequency, contrasting a high, dry site such as Mauna Kea to a low, wet site such as Cambridge. The thick dashed curve is the brightness temperature of an unresolved 1 Jy source at 15 GHz in a 3.4 arcmin beam, assuming $S \propto \nu^{-0.7}$. From Kaneko (2006).

to-noise ratio, the atmospheric conditions and cost. The maximum SZ decrement in intensity occurs at ≈ 130 GHz, but both the receiver noise and sky background rise with frequency while the effect of radio source confusion falls with frequency. These considerations, combined with the East Anglian climate and restrictions on commercially available equipment as well as the presence of the 22 GHz water line, set the bandwidth and frequency range (AMI Consortium: Zwart et al., 2008); these effects are illustrated in Fig. 1.3(b).

1.2.2 SZ surveys

Pointed observations toward previously-known clusters in SZ have become commonplace, and in recent years several blind surveys have been carried out in SZ, detecting many new clusters. The near-independence to redshift, as well as the strong correlation between the SZ signal and the mass of the cluster, makes SZ surveys very attractive for constructing cluster catalogues with well-understood, nearly cosmology-independent, selection functions. These catalogues can be used to construct number counts as a function of mass and redshift, which can be used to constrain some cosmological parameters and investigate the growth of large-scale structure from $z \approx 1$ to the present day. In addition, these catalogues can be used for studies of the (still poorly understood) physics of galaxy clusters.

Recently published results from large-scale SZ surveys include the South Pole Telescope (SPT) survey (Reichardt et al., 2013), with a total of 158 confirmed clusters from a 720 deg^2 survey; the Atacama Cosmology Telescope (ACT) survey (Hasselfield et al., 2013), with 91 confirmed clusters from 504 deg^2; and the *Planck* survey (Planck Collaboration et al., 2013a), with 861 confirmed clusters detected over the whole sky (excluding the Galaxy). Fig. 1.4 illustrates the range of redshifts over these three SZ surveys detect clusters, with comparison to X-ray surveys. The *Planck* survey will be described in more detail in Chapter 4, along with the AMI follow-up of the clusters detected. AMI is also conducting a deep survey over ≈ 10 deg^2, with 10 new detections (AMI Consortium: Shimwell et al., 2012).

1.3 Galactic science

Understanding the emission produced by the Milky Way is important both for foreground removal for cosmological studies, and for understanding the physics involved in processes occurring in other galaxies for accurate theoretical modelling and numerical simulations. Although AMI was designed to observe the SZ effect, it has also proved extremely useful for Galactic science. The short baselines of the SA allow observation of many extended Galactic objects, while the sensitivity and longer baselines of the LA make it useful for higher-resolution observations of point-like objects. The frequency lever-arm of AMI allows it to constrain the spectral index of an object, giv-

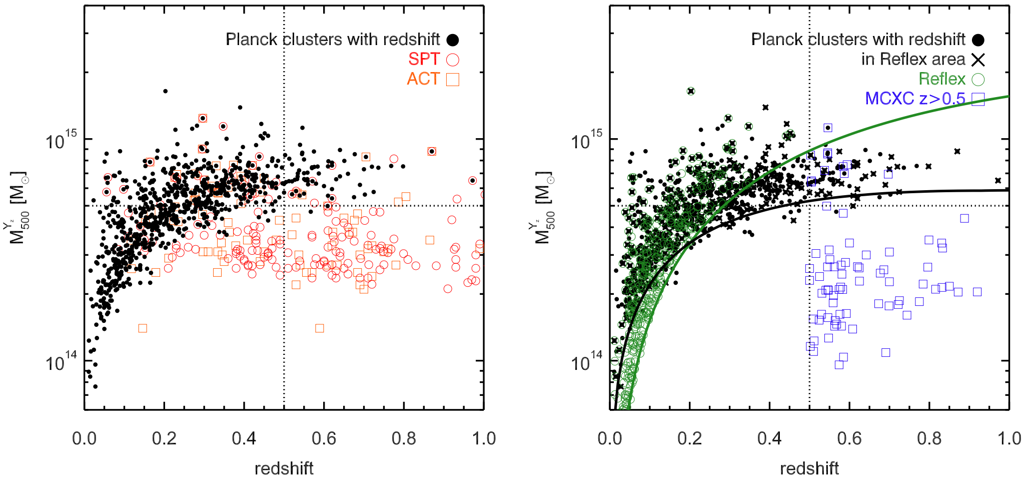

(a) (b)

Figure 1.4: From Planck Collaboration et al. (2013a): (a) shows the distribution in mass and redshift for clusters detected in the *Planck*, SPT and ACT SZ surveys. (b) compares the distribution to that of the ROSAT-ESO Flux-Limited X-ray Galaxy Cluster survey (REFLEX, Böhringer et al. 2004), and clusters from the Meta-Catalogue of X-ray detected Clusters (MCXC, Piffaretti et al. 2011) with $z > 0.5$. The green solid line shows the REFLEX detection limit, and the black solid line shows the *Planck* 20% completeness limit for the medium-deep survey area.

ing insight into the physical process producing the radiation. Some of the many fields of Galactic research AMI has made an important contribution to include the following.

1.3.1 Spinning dust

It was shown in Draine and Lazarian (1998a) and Draine and Lazarian (1998b) that rapidly rotating small dust grains would produce an emission spectrum detectable between 10 and 100 GHz and strongly peaked between 20 and 40 GHz. This was suggested to account for the ‘anomalous’ diffuse Galactic microwave emission (AME) discovered in the context of mapping the CMB (Leitch et al., 1997). Since the AMI frequency band lies very close to the peak of the emission spectrum, it has been possible to investigate the spinning-dust emission from several different types of object.

HII regions The behaviour of HII regions and their expected emission spectrum is believed to be well understood, so they provide a good testing ground for investigating possible excess emission from spinning dust. Below ~ 100 GHz HII regions are expected to emit dominantly via the free-free mechanism. Above ~ 1 GHz the emission is in the optically thin regime, with a canonical spectral index of $\alpha = 0.1$, where $S \propto \nu^{-\alpha}$. Sixteen compact Galactic HII regions were observed with the SA, finding no significant evidence for spinning dust towards these sources (AMI Consortium: Scaife et al., 2008). This non-detection is important for constraining physical models of AME, since any successful model must explain the lack of excess seen in these cases. Another two, more extended HII regions selected using *Planck* data as spinning dust candidates were also investigated with the SA (Perrott et al., 2013b); the emission from S235 was found to be consistent with free-free emission, while the spectrum of S140 was found to be rising across the AMI band, consistent with spinning dust emission. In both cases, the anomalous emission detected by *Planck* must arise on much larger angular scales than those measured by AMI.

Dark clouds Fourteen dark molecular clouds selected from the Lynds dark nebula catalogue on the basis of SCUBA measurements of angular size were observed with the SA in order to investigate possible spinning-dust emission. Five candidates had a clear excess at 16 GHz relative to the expected free-free spectrum, which is well-described by the spinning dust model; two of these (L1111 and L675) are considered definite detections and three (L944, L1103 and L1246) probable detections (AMI Consortium: Scaife et al. 2009b, AMI Consortium: Scaife et al. 2009a). These five candidates were followed up with the LA to provide 25 arcsec resolution images. L1103 and L1111 were resolved out by the LA, however it was able to provide useful observations of the other three. These suggested that L675 was associated with a stellar wind from a deeply embedded young protostar; emission towards L944 was consistent with either spinning dust or a collection of ultra-compact HII regions; and emission towards L1246 was consistent with rotation of polycyclic aromatic hydrocarbon molecules (AMI Consortium: Scaife et al., 2010a).

NGC6946 The nearby galaxy NGC6946 was observed with the LA to investigate reportedly anomalous emission from region E4. The spectrum derived from the AMI band was found to be $\alpha_{AMI} = 0.11 \pm 0.77$, consistent with optically thin free-free emission, but the spectrum rises between 8.5 (from Effelsberg 100m and VLA data) and 16 GHz ($\alpha_{8.5}^{16} = -0.67 \pm 0.08$). Two models for the spectrum were tested using Bayesian analysis, one with a spinning dust component, and the other with a high-opacity free-free component. Both also included a synchrotron and un-absorbed free-free component. The spinning dust model was found to be slightly favoured (AMI Consortium: Scaife et al., 2010b) – the first putative detection of extra-galactic spinning dust.

1.3.2 Supernova remnants

Twelve reported supernova remnants (SNRs) were observed with the SA to determine spectra in conjunction with data from the literature at lower radio frequencies. The spectra for well-studied objects were in good agreement with previous results, while for less well-studied objects the AMI data provide higher-frequency radio observations than were previously available, providing better constraints on their radio spectra (AMI Consortium: Hurley-Walker et al., 2009b).

In addition, a new shell-SNR, G64.5+0.9, was discovered by Natasha Hurley-Walker in NRAO VLA Sky Survey (NVSS) maps and confirmed with the SA and the Very Large Array (VLA) (AMI Consortium: Hurley-Walker et al., 2009a).

1.3.3 Young stellar objects

The LA has been used to follow up cores identified as young stellar objects by the *Spitzer* ‘From Cores to Disks’ programme (c2d). These observations are being used to improve constraints on correlations between radio luminosity, infra-red luminosity, bolometric luminosity and outflow force (AMI Consortium: Scaife et al. 2011a, AMI Consortium: Scaife et al. 2011b).

1.3.4 Source monitoring

The Ryle Telescope and subsequently the LA have participated in many long-term monitoring projects, including the following.

Cygnus X-3 The Galactic microquasar Cyg X-3 has been monitored as part of a multi-wavelength study. This is an unusual X-ray binary which produces radio jets and has also been shown to be a transient gamma-ray source. These observations have provided insight into the physical processes occurring in microquasars, showing that very efficient particle acceleration and gamma-ray propagation out of the inner disk of the microquasar usually occur a few days before relativistic jet ejections (Tavani et al., 2009).

Cygnus X-1 Long-term monitoring of the X-ray binary Cyg X-1 in X-rays and at 15 GHz with the Ryle Telescope and LA has shown a change in its super-orbital period from ≈ 150 days to ≈ 300 days. This is thought to be due to the changing viewing angle of a precessing accretion disc (Zdziarski et al., 2011).

1.4 Thesis outline

The remainder of this thesis is split into two sections, as follows:

Galactic studies

- Chapter 2 describes an improved and extended analysis pipeline for SA data taken in the ‘drift-scan’ observation mode.

- Chapter 3 presents the AMI Galactic Plane Survey (AMIGPS), a drift-scan survey of the Northern Galactic plane between $b \approx \pm 5^\circ$. The previous Galactic work on AMI has shown the benefit of AMI observations for constraining properties of unusual Galactic sources which are currently not well-understood – the AMIGPS provides a unique large-scale resource for furthering investigation into these sources.

Galaxy clusters

- Chapter 4 describes AMI follow-up observations of clusters detected in the *Planck* all-sky surveys, and presents some first results including a discrepancy between cluster fluxes measured by AMI and *Planck*.
- Chapter 5 presents one method for attempting to reconcile the discrepancy, by allowing the parameters describing the shape of the SZ effect to vary.

1.5 General acknowledgements

This work has made use of the distributed computation grid CAMGRID of Cambridge University, as well as several online resources including:

- NASA's Astrophysics Data System Bibliographic Services;
- NASA's SkyView facility (`http://skyview.gsfc.nasa.gov`) located at NASA Goddard Space Flight Center;
- the facilities of the Canadian Astronomy Data Centre operated by the National Research Council of Canada with the support of the Canadian Space Agency;
- the SIMBAD database and VizieR catalogue access tool, operated at CDS, Strasbourg;
- the ROSAT Data Archive of the Max-Planck-Institut für extraterrestrische Physik (MPE) at Garching, Germany.

Chapter 2

Drift scanning

The usual observation mode employed by AMI is a tracked observation, in which a particular source is followed as it moves across the sky. In drift scanning, on the other hand, the telescope is pointed at a fixed azimuth and elevation while the sky drifts past, resulting in an observation of a narrow strip at fixed elevation. In practice, the telescope is actually driven very slowly in elevation in order to maintain a constant declination (δ) as measured in J2000 coordinates. This enables strips to be easily reobserved at a later date if the data has been corrupted by weather or hardware failures.

An AMI drift scan pipeline was developed by Matthew Davies (Davies, 2010) as an extension of the usual pipeline for tracked observations. However, the data taken when drift scanning are quite different in character – one of the main differences is that the signal from a tracked observation of an astronomical source will maintain a constant amplitude in the absence of noise; for a drift scan, sources drift through the field of view of the telescope, so the amplitude of the signal changes as they pass through the primary beam. I have developed substantial changes and additions to the original pipeline in order to cope with this, which are described below.

2.1 Data calibration and automatic flagging

2.1.1 Original pipeline

Data are loaded into REDUCE, the AMI in-house data reduction system. Various flagging routines are applied to the data, in a similar manner to the pipeline which is used for

Table 2.1: Assumed I + Q flux densities of 3C286, 3C48 and 3C147.

Channel	$\overline{\nu}$/GHz	S^{3C286}/Jy	S^{3C48}/Jy	S^{3C147}/Jy
3	13.88	3.74	1.89	2.72
4	14.63	3.60	1.78	2.58
5	15.38	3.47	1.68	2.45
6	16.13	3.35	1.60	2.34
7	16.88	3.24	1.52	2.23
8	17.63	3.14	1.45	2.13

tracked observations, described in Hurley-Walker (2010). These include flagging for interference spikes, and data-points which differ from the bulk of the data by a multiple of the data standard deviation (usually three).

A mean is calculated and subtracted from the data for each spacing and each of the 16 lags before the gains are calibrated using a recent observation of either 3C48, 3C286 or 3C147. The assumed flux densities for 3C286 were converted from Very Large Array total-intensity measurements and are consistent with the Rudy et al. (1987) model of Mars transferred on to absolute scale, using results from the *Wilkinson Microwave Anisotropy Probe* (Perley and Butler, 2013). The assumed flux densities for 3C48 and 3C147 are based on long-term monitoring with the AMI-SA using 3C286 for flux calibration (see Table 2.1).

The data are then Fourier transformed to synthesise the frequency channels and further amplitude flagging is applied to excise remaining interference. Phase-calibration is performed using interleaved observations of secondary calibration sources; a correction for changing airmass is applied using the rain gauge (see Section 1.1); and noisy baselines are down-weighted. In order to process the continuous drift-scan data, the visibilities are assigned and phase-rotated to pointing centres separated by 10 arcmin, approximately the half-width at half-maximum of the AMI-SA primary beam, and output as multi-source *uv*-fits files.

2.1.2 Testing, problems and improvements

The procedures described above work very well for tracked observations when all the data are expected to be of the same amplitude, but the drift-scan maps produced using this pipeline were not entirely satisfactory. An example can be seen in Figure 2.9. The map is heavily striped, which indicates a problem with the zero levels of the lag data. This was found to be a result of two separate problems: the presence of geostationary satellites, and the presence of bright sources in the scan.

Geostationary satellites

Drift-scan data are taken in periods of 1800 seconds, interspersed with periods of 400 seconds observing bright calibrator sources (in a tracked manner) in order to perform interleaved calibration. On inspection of the raw lag data of several observations, it was noticed that the zero level of one or more sections of field data appeared to be different with respect to the majority of the data (see Figure 2.1). This translated into a signal in one channel after Fourier transforming, and was therefore deduced to be due to a monochromatic signal from a geostationary satellite.

In a tracked observation, this signal would appear as an interference spike as the telescope scanned past the satellite, and would be flagged by one of the automatic algorithms. When drift scanning, however, the telescope points at a fixed point in the sky with a constant displacement from the satellite, and so the signal is constant. When the telescope is moved to observe a calibrator, the sky continues drifting while the calibrator data are taken. When it is returned to drift scanning mode it must therefore point toward a slightly different azimuth and elevation to return to the RA and δ it left off from, i.e. at a different position relative to the satellite. Signal from a geostationary satellite may therefore be present in some sections of drift scan field data but not others.

In the original pipeline, as for tracked observations, the mean was calculated over all the unflagged field data, and this was subtracted to zero the lag data. However it is clear from Figure 2.1 that this results in incorrect mean calculation when satellites are present. Since the signal is constant over the field section and the amplitude of the signal is stable, the data are still usable provided the correct mean is subtracted. This could be achieved by simply calculating a mean separately for each field section, but a global mean from the field data is required for correct zeroing of the calibrator data. For bright sources which have a slow fringe rate, the mean can be biased away from the zero level, so that a zero-level cannot be calculated from the calibrator data, and since the calibrator observations are tracked they are not subject to the same satellite interference as adjacent field sections.

I therefore implemented the following algorithm, to correctly calculate a zero level for all spacings and all lags:

1. a global mean is calculated, including all field data;
2. individual field section means and standard deviations are calculated;
3. if all the lag means for a particular field section and a particular spacing are within one standard deviation of the corresponding global means, this field section is considered to be unaffected by satellite interference;
4. the global mean is recalculated, excluding those field sections which do not meet the above condition, and is subtracted from all data, including calibrator data;
5. individual means are subtracted from each field section, to account for any low-amplitude interference which survives the standard deviation test.

Additionally, if there are less than 50 unflagged samples in a field section (determined empirically to be the minimum number of samples that give a reasonably accurate mean), the global mean is used if the data pass the standard deviation test; if not, the data are flagged.

This algorithm appears to cope well with the demands of the data. Figure 2.1 shows the result of the mean-subtraction algorithm used on data affected by satellite interference. A map of the same data used in Figure 2.9 is shown in Figure 2.10. It can be seen that the striping is significantly reduced; however, there is still visible striping around the bright sources.

Bright sources

When the fringe rate is slow, the mean calculation is also biased by the presence of bright sources passing through the beam. Figure 2.2 shows drift scan data containing Cassiopeia (Cas) A, a very bright radio source with a very slow fringe rate on the selected baseline. The mean will clearly not represent the zero level when these data are included. This effect can also cause striping in the final map (see Figure 2.10).

In addition, I found that the automatic amplitude flagging procedures designed to flag interference spikes in tracked observations identify bright sources ($\gtrsim$ 100 mJy) as interference and flag out much of their amplitude. The effect of this is shown in

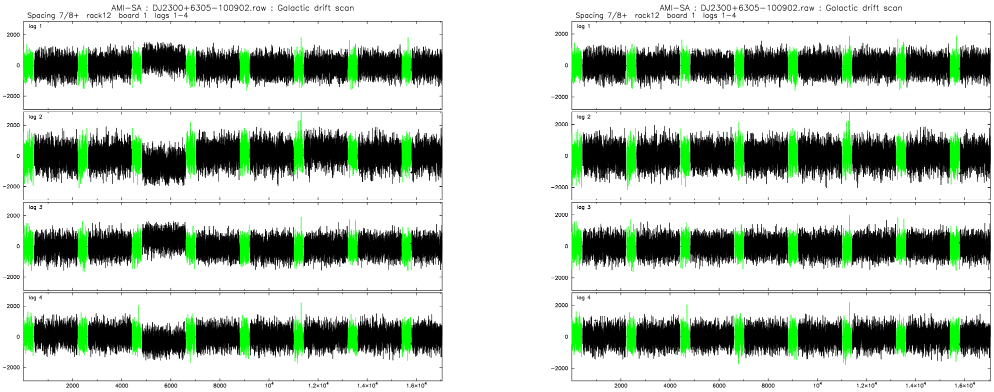

Figure 2.1: An example of drift scan data with interference from a geostationary satellite present in one field section (left), and after applying the mean subtraction algorithm (right). The data are still usable after the effect has been corrected for. Calibrator data are in green, field data in black.

Figures 2.2 and 2.3, where Cas A is flagged out by the automatic routines. This leads to an overall suppression of the amplitudes of bright sources.

Both of these problems can be resolved by identifying the data ranges containing the bright sources and excluding them from the mean calculation and flagging algorithms. As the mapping procedure – after outputting the data from REDUCE – is very time consuming compared to the calibration process, it was desirable to be able to identify the sources directly from the visibility data within REDUCE.

I found that an improved visibility dataset could be achieved using a bootstrapping procedure. The data are first analysed as if there were no sources, with all flagging algorithms used to detect and remove interference spikes. The bright sources are then identified using an algorithm called ‘find sources’ (see below), and the sample ranges over which they occur are written out into an ‘exclusion table’. The data are reloaded, and the pipeline is re-run, but this time means are calculated excluding the ranges containing sources, and amplitude-flagging procedures also exclude these ranges. This has resulted in another reduction in striping (see Figure 2.11), and correct source amplitudes being found for sources above $\sim$ 100 mJy (see Figure 2.5).

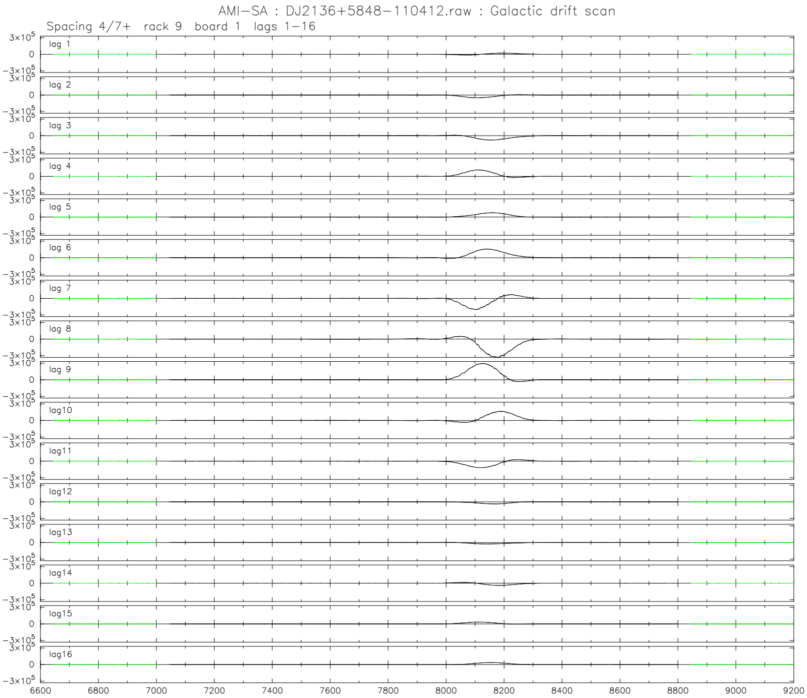

Figure 2.2: A section of drift scan data containing the bright (≈ 100 Jy) supernova remnant, Cas A, before the flagging routines are applied. Since the source has a slow fringe rate on this baseline, the mean calculation would clearly be biased by including these data. While this is an extreme example, sources above ≈ 100 mJy suffer from the same undesirable effect.

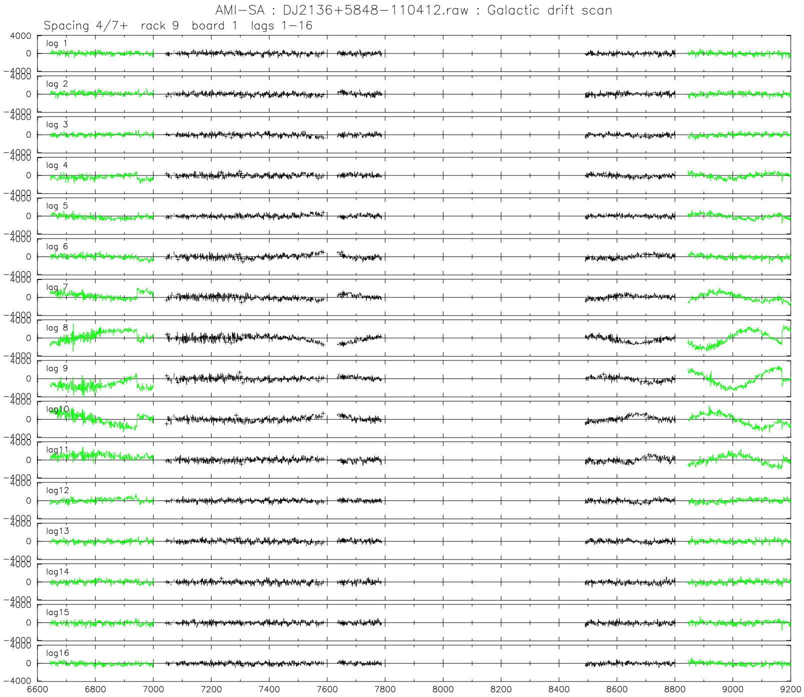

Figure 2.3: The same timestream data as shown in Fig. 2.2, after the automatic flagging routines are applied. Note the difference in scale between this plot and Figure 2.2. Sources above ≈ 100 mJy are found to be at least partially flagged out by the automatic routines. Calibrator data are in green, field data in black.

find sources The new ‘find sources’ algorithm is an adaptation of ‘flag interference’ (see Hurley-Walker 2010) which I have written. It works on the visibility data, which are averaged together in a weighted fashion over each spacing and each frequency channel to produce a single time-series. This reduces the effect of interference, which only occurs on some baselines and some channels, while increasing the signal-to-noise of peaks due to sources, which should appear on all baselines and all channels. The time-series is smoothed to increase the signal-to-noise ratio, and peaks are then identified as follows:

1. the highest peak is identified, and an initial range of 100/(smoothing factor) (giving an angular scale comparable with the full-width at half-maximum of the SA primary beam) samples to either side of the peak is set;
2. if the peak value is less than a tolerance value multiplied by the mean of the data, the algorithm stops;
3. otherwise, the range is extended asymmetrically on either side until the edge values are found to be less than the tolerance;
4. a new mean is calculated, excluding the range which has been identified as a source, and the process is repeated.

I tested ranges of smoothing and tolerance values to identify which would best detect the correct ranges corresponding to bright sources, and values of 20 samples and two were selected as defaults. An example plot is shown in Figure 2.4 of sources detected using this method.

2.2 FUSE

When multiple observations of the same declination strip are available, the *uv*-fits data output from REDUCE are concatenated using another piece of in-house software, FUSE, written by Jonathon Zwart and Tim Shimwell, and which I optimised to perform faster with large volumes of data. If pointing centres from two different observations are within a 10 arcsec tolerance of each other, the data belonging to those pointings are concatenated and a new pointing centre is assigned which is the average of the original pointing centres.

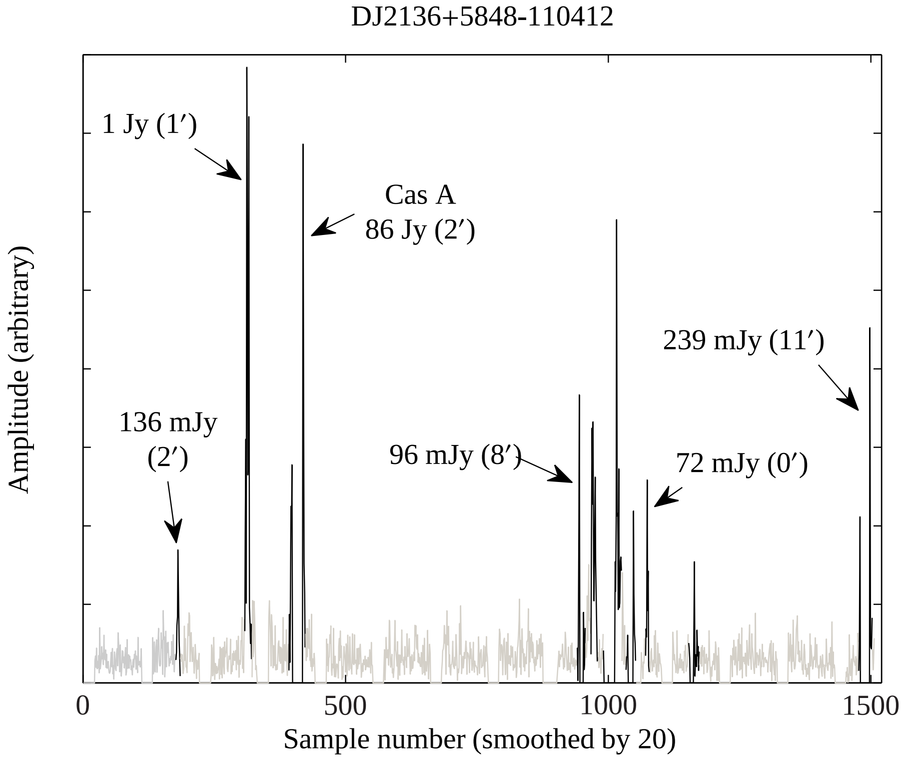

Figure 2.4: An example of sources detected using the ‘find sources’ algorithm (in black) in the declination strip containing Cas A. The amplitude is arbitrary since it depends on how much of the source has been cut out by the flagging routines. Not all sources are real, but the majority are and are labelled with their flux as measured from the final combined map, and distance in declination from the centre of the strip.

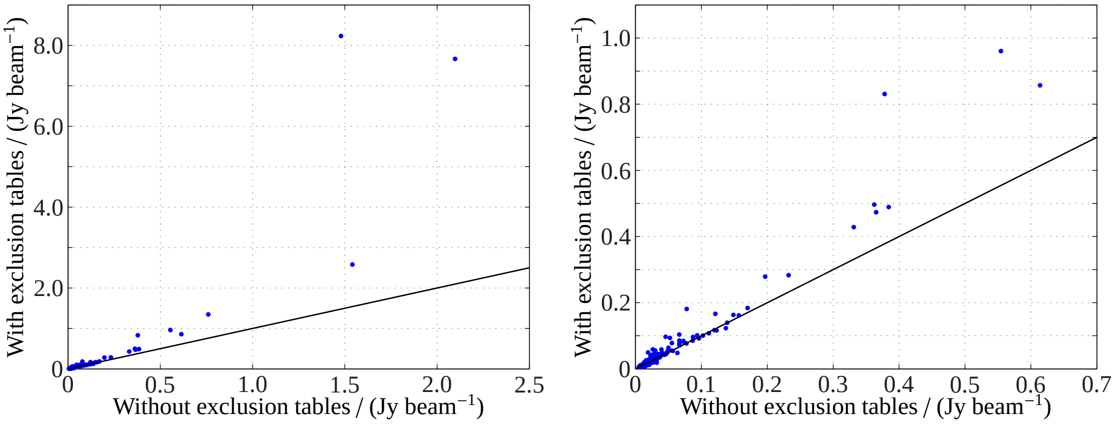

Figure 2.5: Peak flux density values measured for sources in a test area of the Galactic plane, with and without the exclusion tables applied during data reduction. The right hand plot is a zoomed-in version of the left hand plot. The black solid line indicates a one-to-one correspondence; sources with peak flux density above $\approx$ 100 mJy beam^{-1} show an amplitude suppression effect.

2.3 AIPS

Data that have been concatenated by FUSE are imaged using the Astronomical Image Processing System (AIPS[1]) as individual 128×128 pixel pointings with 20×20 arcsec^2 pixels. Natural weighting is used to maximise signal-to-noise, and all six frequency channels are imaged using a multi-frequency synthesis; as a consequence of different flagging of the channels, the effective frequency will vary slightly between pointings. Individual channel maps are not produced.

Matthew Davies wrote an automated algorithm which first produces a dirty map and then estimates its r.m.s. noise level σ using the IMEAN task over the whole map, which fits a Gaussian centred on zero to the distribution of pixel values, discarding outliers. The map is then CLEANed to 3σ, unless a bright source ($>$ 200 mJy on the map) is present, in which case the algorithm first CLEANS to 3σ using a 6×6 pixel CLEAN box around the brightest pixel, then removes the box and continues CLEANing to the same flux density level. Each component map is CLEANed using an elliptical Gaussian fitted to the central region of the dirty beam as the restoring beam. As a result, the restoring beam for each component map is slightly different.

---

[1] `http://aips.nrao.edu/`

I made various attempts to improve this step of the process, including experimenting with circular CLEAN boxes, adjusting the size of the boxes, and attempting self-calibration; however, these made little difference to the resulting maps.

2.4 Beam correction

The individual pointings mapped in AIPS need to be corrected for the effect of the primary beam before being combined into a single map, however this is not straightforward. The SA primary beam is usually approximated as a Gaussian fitted to the central lobe of the actual beam. This has a best-fit FWHM of 19.6 arcmin at the central frequency, 15.75 GHz. Since each drift scan pointing actually consists of data taken at different sub-pointings along the RA axis of the pointing, the primary beam at each data point must be taken into account. Matthew Davies devised a beam correction method for drift-scan data which takes a weighted average over primary beams centred at each contributing data point, ie for any pixel in the map

$$\begin{aligned}\text{primary beam} &= \frac{\sum_{i=1}^{N} w_i \, \exp\left(-\frac{\Delta_i^2}{2\sigma^2}\right)}{\sum_{i=1}^{N} w_i} \\ &= \frac{\sum_{i=1}^{N} w_i \, \exp\left(-\frac{(x-x_i)^2+y^2}{2\sigma^2}\right)}{\sum_{i=1}^{N} w_i}, \end{aligned} \tag{2.1}$$

where N is the number of samples constituting the pointing, $w_i = 1/\sigma_{\mathrm{rms,i}}^2$ is the weight of the i'th sample (i.e. the sum of weights for all baselines and all channels contributing to a one-second sample) where $\sigma_{\mathrm{rms,i}}$ is the r.m.s. noise on the sample, $2\sigma\sqrt{2\ln(2)}$ is the FWHM of the SA primary beam (19.6 arcmin), and $\Delta_i = \sqrt{(x-x_i)^2+y^2}$ is the separation of the pixel from the pointing centre of the sample, where (x, y) is the pixel location and $(x_i, 0)$ is the pointing centre of the sample along the RA axis. The pixel value is then divided by the weighted-average beam for that pixel; pixels with a weighted-average beam of ≤ 0.1 are blanked. This has the effect of elongating the beam along the RA axis to ≈ 37 arcmin between the 10%-power points, compared to the normal SA primary beam RA width (to 10%) of ≈ 35 arcmin; this is illustrated in Figure 2.6.

The beam correction algorithm also produces a noise map, which is the inverse of the beam correction, scaled by the r.m.s. noise value of the map calculated by IMEAN.

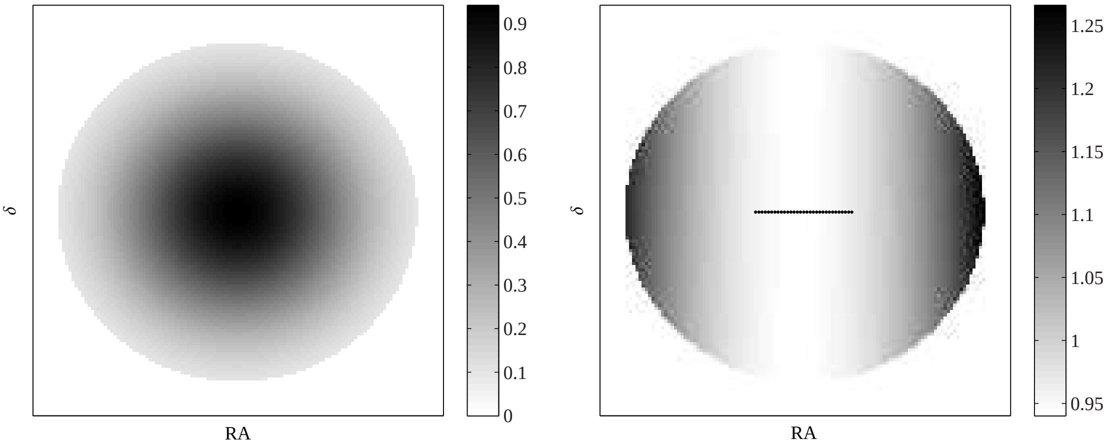

Figure 2.6: An example of the drift-scan primary beam. This is the weighted average of the SA primary beam centred at each of the samples taken along the RA axis. The left-hand figure shows the weighted-average primary beam for a typical pointing; the right-hand figure shows this primary beam divided by the usual SA primary beam for a typical, non-drift-scan pointing. The coordinates of the samples constituting the pointing are overplotted in black. The width in RA of the pointing is ≈ 37 arcmin, whereas the width of a typical, non-drift-scan pointing cut off at the 10%-power point is ≈ 35 arcmin.

To test the beam correction algorithm, I found peak fluxes for two well-characterised non-variable sources, 3C48 and NGC 7027, in all the individual beam-corrected pointing maps which contained them inside the 10% beam point which is used as a cutoff. A plot of the (beam-corrected) peak flux values versus distance from the pointing centre is shown in Figure 2.7 along with their expected values, derived from long-term monitoring with tracked observations on the SA. It is clear that when the source is detected far from the pointing centre, the flux density is less accurate. This is to be expected since, as well as the thermal noise level being higher, phase errors are expected to have a greater effect toward the edge of a pointing. When the individual maps are combined, the pixels nearer the centre of a pointing are given higher weight, so that the more reliable central values contribute more to the final flux density and the scatter in the more-distant points averages out. The pointing centres are spaced by 10 arcmin in RA and 12 arcmin in δ, so any pixel at a distance $\gtrapprox 6$ arcmin from the centre will contribute less to the final map than the corresponding pixel from the adjacent pointing centre.

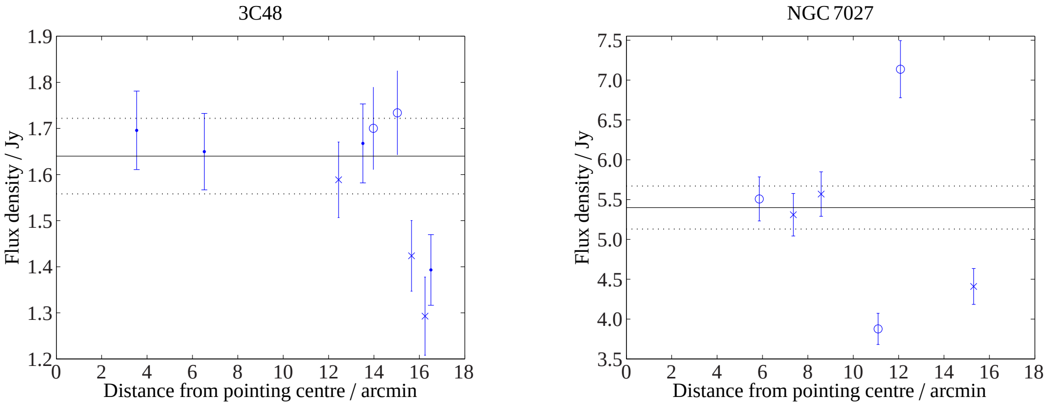

Figure 2.7: Peak flux densities measured from beam-corrected, component pointing maps and plotted as a function of distance from the pointing centre, for 3C48 (left) and NGC 7027 (right). The dots represent pointings where the source lies nearly on the RA axis; the crosses are pointings in which it lies above the axis; and the open circles are pointings in which it lies below the axis. The solid and dotted black lines represent the expected value and ±5% uncertainty levels respectively. The error bars are the value of the constituent noise maps at the point of measurement added in quadrature with a 5% calibration uncertainty.

2.5 Combining the maps

Finally, the individual beam-corrected pointing maps are added together, weighting each pixel by the inverse of its variance calculated from the noise map, into larger continuous maps using the in-house software PROFILE (Grainge et al., 2002), which I also adapted to produce maps in Galactic coordinates. Corresponding continuous noise maps for use in source-finding are also produced in the same way from the noise maps for the individual pointing centres; these are found to provide an accurate representation of the noise, except around bright sources as discussed in Section 2.7.2. Fig. 2.8 shows an example noise map section illustrating the variation in noise level across a typical map.

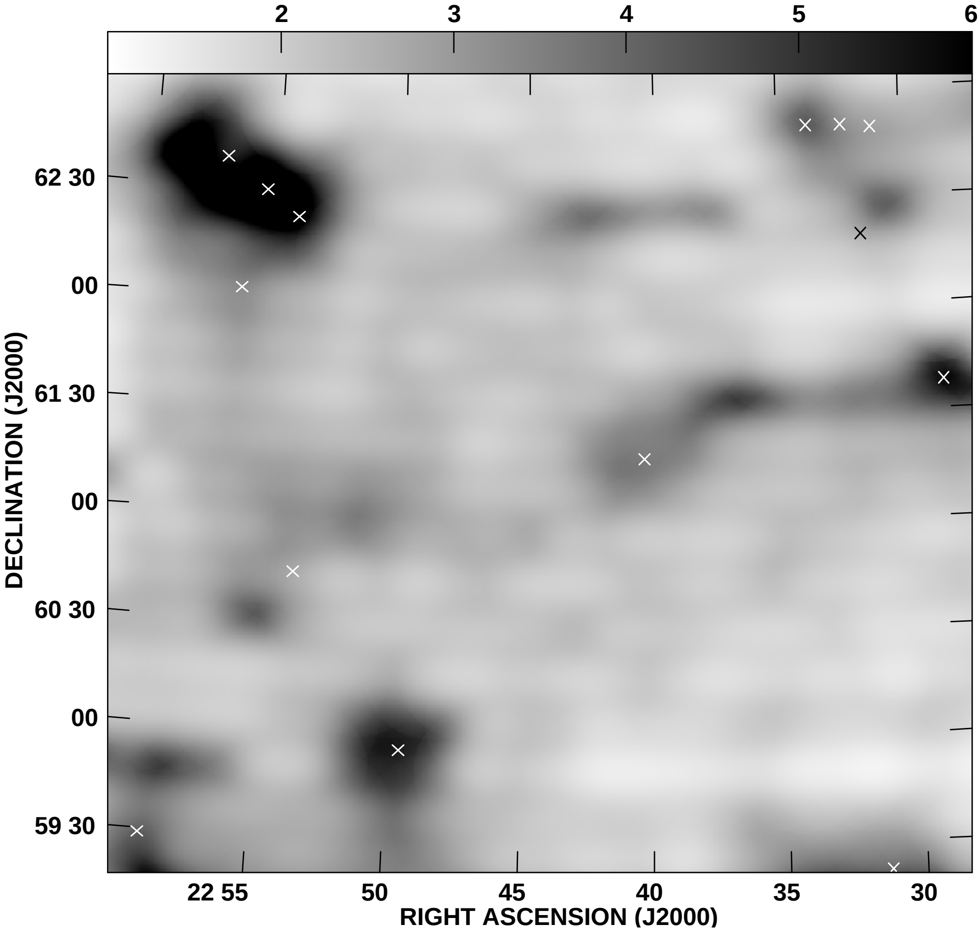

Figure 2.8: A typical noise map illustrating the variation in noise level across the map. The grey-scale is in mJy beam^{-1} and is truncated at 6 mJy beam^{-1} to show the low-level variation; the highest noise level in the area shown is ≈ 10 mJy beam^{-1} in the north-eastern corner. Crosses mark the positions of sources with peak flux densities > 50 mJy beam^{-1}, around which it can be seen that the noise level increases. Away from the bright sources, the noise level is $\lessapprox 3$ mJy beam^{-1}.

2.6 Example maps

Figures 2.9, 2.10 and 2.11 show maps produced at various stages of improving the pipeline. The reduction in striping can be seen as the effects of geostationary satellites and bright sources are allowed for.

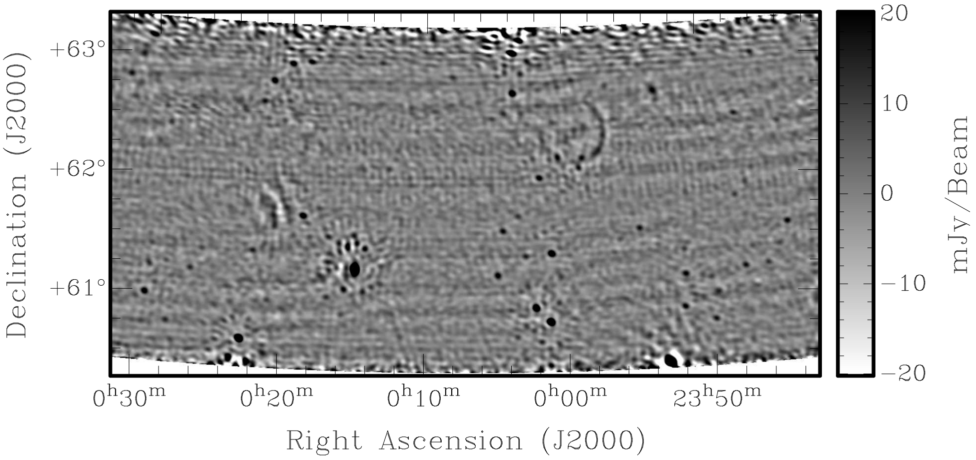

Figure 2.9: A drift scan map of the Galactic plane, made using the original pipeline. Objects visible in the map include the supernova remnant CTB 1 at RA ≈ 00h 00m, $\delta \approx$ 62d 30m; a resolved HII region, Sh 2-173, at RA ≈ 00h 20m, $\delta \approx$ 61d 30m, and the bright radio source 4C 60.01 at RA ≈ 00h 15m, $\delta \approx$ 61d 18m. The striping is caused by problems with the zero-levels in the lag data due to geostationary satellites and bright sources.

2.7 Source extraction

Sources are found using another piece of in-house software, SOURCEFIND, developed by Elizabeth Waldram and Thomas Franzen. This searches for maxima in the map which are greater than a specified multiple of the corresponding noise-map pixel (usually 5). A peak position and flux density value is measured by interpolating between the grid points. An initial estimate of the integrated flux density and source size is also calculated by integrating contiguous pixels down to 2.5× the local thermal noise level,

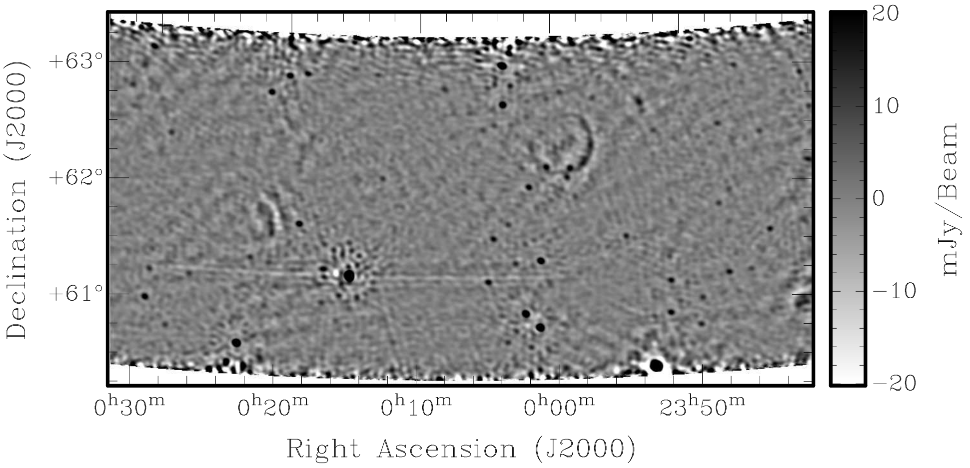

Figure 2.10: An improved drift scan map of the Galactic plane. The zero-levels are now calculated individually to remove the effect of geostationary satellites. The striping is now caused only by the bright sources.

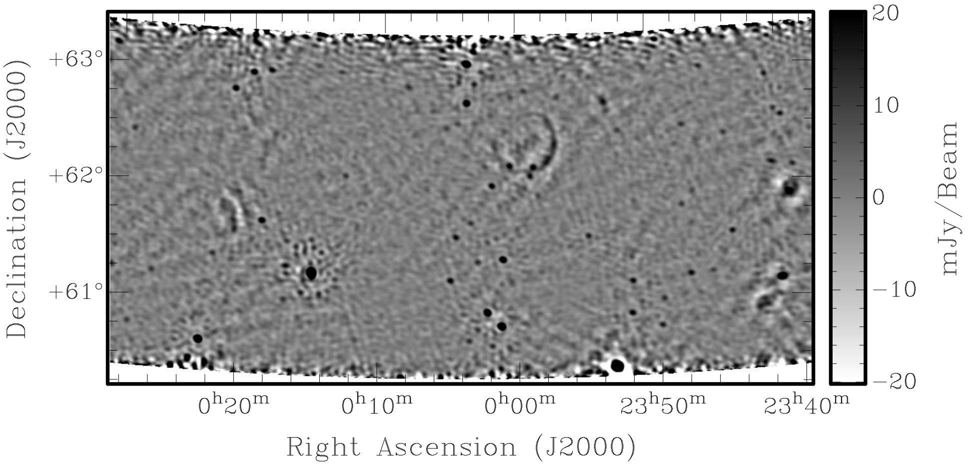

Figure 2.11: A further improvement on the pipeline. The zero-levels are calculated individually, and exclusion tables are employed to remove the effect of bright sources. The striping is now removed. Spurious sources can be seen around 4C 60.01; these will be excluded from the final catalogue.

and sources are identified as overlapping if the integration area contains more than one peak $> 5\sigma$. This information is used to fit an elliptical Gaussian to each source in an automated fashion, using the AIPS task JMFIT. Overlapping sources are fitted simultaneously.

2.7.1 Source size and classification

The deconvolved source size is calculated by JMFIT using the synthesised beam size at the pointing with the highest weight at the position of the source. This size is used to classify the source as point-like or extended to the SA beam, following the method described in AMI Consortium: Franzen et al. (2011), scaled to the SA beam size. A source is classified as extended if the fitted major axis size $e_{\mathrm{maj}} \geq e_{\mathrm{crit}}$, where

$$e_{\mathrm{crit}} = \begin{cases} 3.0 b_{\mathrm{maj}}\, \rho^{-1/2} & \text{if } 3.0 b_{\mathrm{maj}}\, \rho^{-1/2} > 100.0 \text{ arcsec,} \\ 100.0 \text{ arcsec} & \text{otherwise,} \end{cases} \tag{2.2}$$

where ρ is the signal-to-noise ratio and b_{maj} is the synthesised-beam major-axis size.

If a source is classified as extended, its integrated flux density fitted by JMFIT is considered to represent best its total flux density; otherwise the peak flux density is considered to provide a more accurate measurement.

When adjacent pointing centre maps are added together by PROFILE, a source lying near the midway point between the two pointing centres will have a final shape that is a combination of both beams. If the restoring beam shapes for the two pointing centres happen to be quite different, it is possible that the resulting appearance of the source on the combined map will not be approximated well by either of the beam shapes, which could lead to errors in flux density estimation when the incorrect beam is deconvolved from the source. I investigated the error inherent in using the beam from the pointing with the highest weight at the position of the source for source extraction by remapping a section of the Galactic survey with identical restoring beams for all pointing centres. The flux densities derived from this map were compared with the catalogue values for sources which lie between pointing centres with different beam shapes and sizes. For point-like sources, the difference in the flux density is $\lessapprox 1\%$ and is considered to be negligible. For extended sources it is $\lessapprox 5\%$, so a conservative extra 5% error on the flux density is added in quadrature (see Section 3.3.2).

2.7.2 Spurious source exclusion

An implausibly large number of sources are frequently detected in the vicinity of bright sources – these are likely spurious and are caused by residual amplitude and phase errors in the data and unCLEANed sidelobes. In order to prevent these from contaminating catalogues derived from drift scan maps, 'exclusion zones' are applied to sources with peak flux density $> 50\,\mathrm{mJy\ beam^{-1}}$. The radii r_E of the exclusion zones are determined by the peak flux density $S_{\mathrm{peak,bright}}$ of the source as $r_E = 18\left(S_{\mathrm{peak,bright}}/300\,\mathrm{mJy}\right)^{1/3}$ arcmin. This was chosen empirically to describe the fall-off in the elevated, non-Gaussian noise around bright sources, illustrated in Fig. 2.12. Within the exclusion zones, only 'sources' with peak flux density $S_{\mathrm{peak}} \geq S_{\mathrm{peak,bright}}/10$ are retained. The factor of ten was conservatively chosen by eye to retain most of the sources which appear to be real, while excluding as many spurious sources as possible. There may be some real sources which are excluded by this procedure. Fig. 2.13 illustrates the exclusion zones around two bright sources.

2.8 Conclusions

In this chapter, I have described the testing and implementation of a new pipeline for analysing data taken in drift-scan mode with AMI. In particular:

1. I have adapted the pipeline to account for the presence of geostationary satellites, allowing recovery of the affected data. This reduces stripiness due to incorrect zero-level calculation in the final map.

2. I have implemented a new algorithm to search for the presence of bright sources drifting through the beam during an observation, and account for their presence when reducing data. This allows their amplitudes to be measured correctly from the final map, and also reduces stripiness.

3. The primary beam correction has been tested for two well-characterised radio sources, and accurate flux densities have been shown to be recovered from individual pointing centre maps within ≈ 10 arcmin.

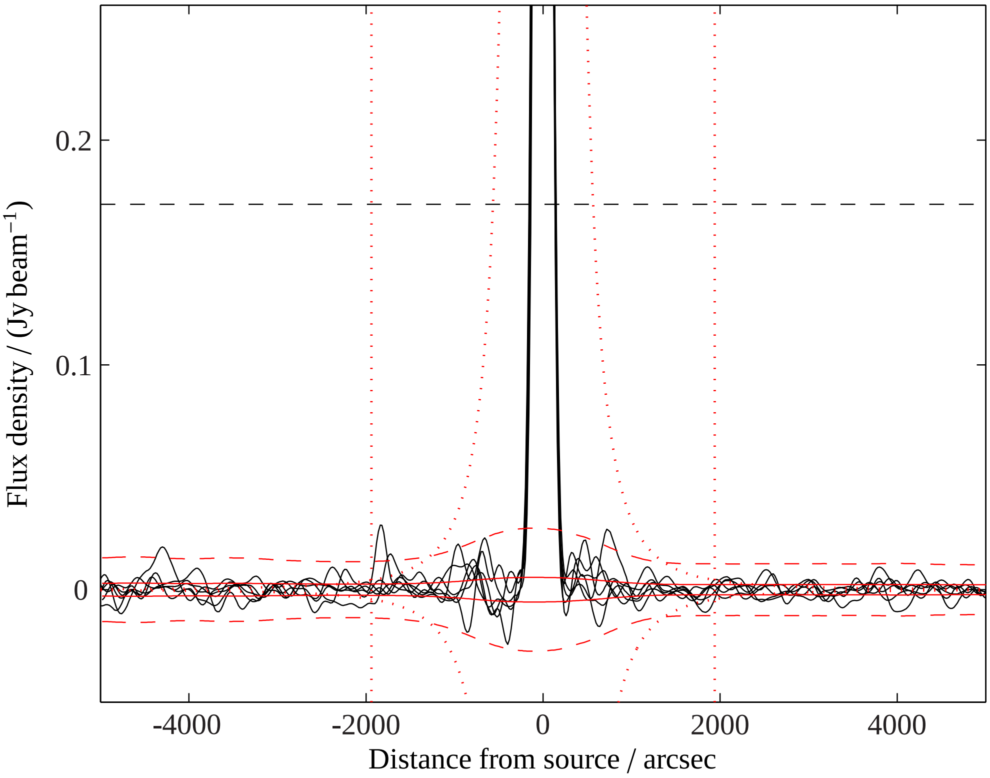

Figure 2.12: Pixel values (solid black lines) interpolated through map points in lines intersecting the bright, central source in Fig. 2.13, and the spurious sources around it; the mean noise- and 5σ-detection-levels (solid and dashed red lines) from the noise map; the fall-off law and exclusion zone radius for this source (red curved and vertical dotted lines); and the $S_{\text{peak,bright}}/10$ cutoff line (dashed black line). It can be seen that the noise outside the exclusion zones is well represented by the map noise, but closer to the central source the noise is elevated and the 5σ cutoff is not high enough. The conservative $S_{\text{peak,bright}}/10$ cutoff excludes the spurious detections.

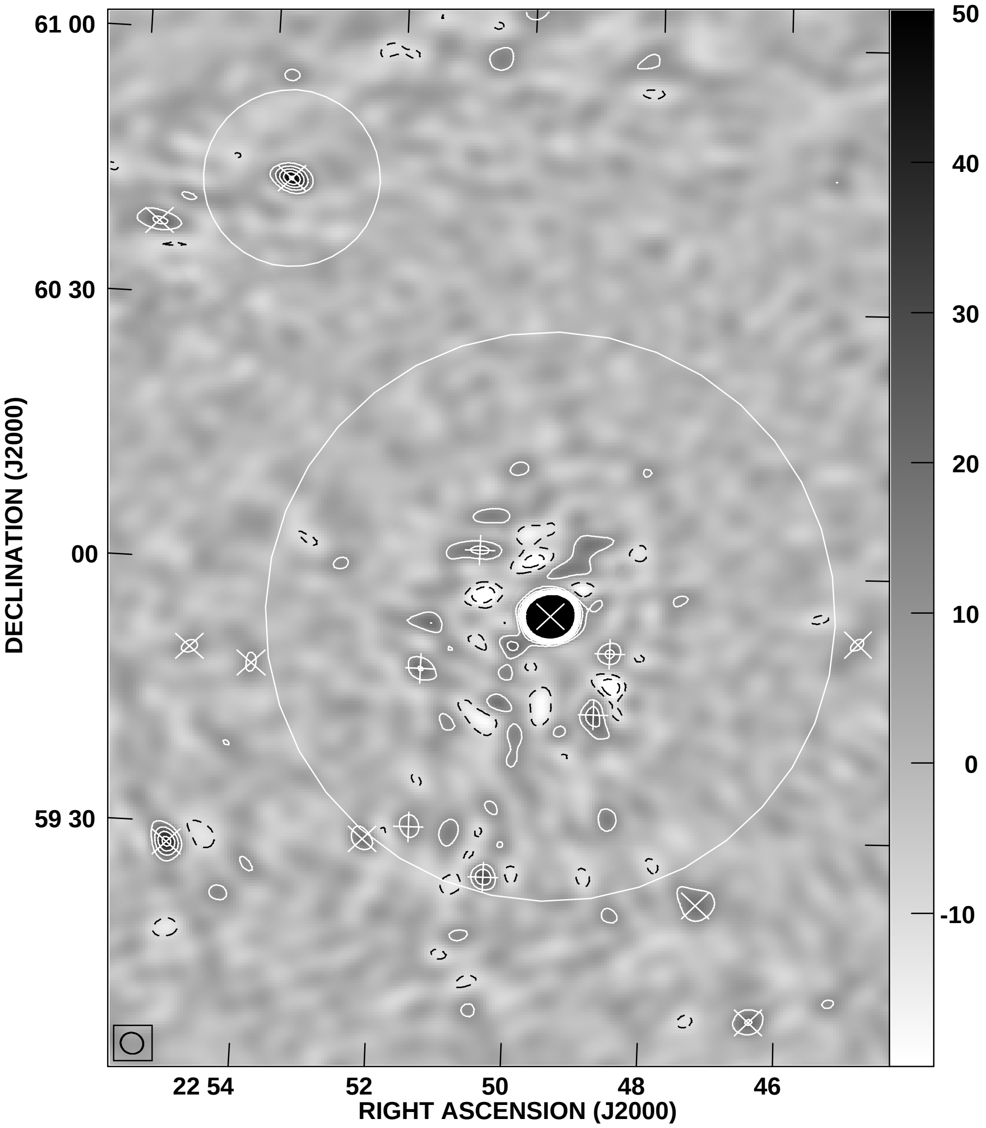

Figure 2.13: A section of the map illustrating the spurious source exclusion method. The grey-scale is in mJy beam^{-1} and is truncated to show the fainter sources; the flux densities of the brightest and second brightest sources are ≈ 1700 mJy and 50 mJy respectively. The contour levels are between ± 100 mJy beam^{-1} in steps of 10 mJy beam^{-1} (it is not possible to use σ contours since the noise level varies across the map); solid contours are positive and dashed contours are negative. Exclusion zones are shown as circles around the bright sources. Source detections are marked by $\times$, and 'sources' detected but excluded by $+$. The synthesised beam at the position of the brightest source is shown in the bottom left hand corner.

4. The source extraction techniques developed for the 10C survey have been successfully applied to maps at different resolution and regions of the sky with many extended sources present.

Chapter 3

The AMI-SA Galactic Plane Survey

In this chapter, I describe my application of the drift-scanning data reduction methods described in Chapter 2 to produce a survey of the Northern Galactic Plane. Parts of the survey were observed by Natasha Hurley-Walker; the remainder, as well as all of the data reduction and subsequent analysis, is my own work.

3.1 Motivation

Large-area radio surveys contribute to our understanding of the Universe in numerous and diverse ways. Discoveries from these surveys have become key ingredients of modern astrophysics: pulsars, radio galaxies and quasars, and more (see e.g. Longair 1998). For studies of our Galaxy, radio surveys are particularly beneficial as the radio emission does not suffer from the same extinction and opacity effects as optical and infra-red surveys and the dense regions of dust and gas which dominate the low-latitude Galactic plane become largely transparent, allowing us to study sources in these regions. However, the bulk of Galactic radio surveys are at frequencies at or below 1.4 GHz and as such are necessarily biased against objects whose spectra rise with frequency. Two examples of the need for higher-frequency, centimetre-wave Galactic surveying are as follows.

The first is the hypercompact Hɪɪ (HCHɪɪ) region. Thought to indicate the earliest visible stage of massive star formation, these objects are two orders of magnitude more dense than the better known ultracompact (UCHɪɪ) region (see Table 3.4) and have steeply rising spectra. HCHII regions were discovered serendipitously in observations of UCHII, having been missed previously in their entirety by Galactic plane surveys concentrated at $\nu < 5$ GHz. The turnover frequency between the optically thick and thin regimes for thermal bremsstrahlung is a linear function of emission measure (e.g. Mezger and Henderson 1967) causing such low frequency surveys (e.g. $\nu \leq 5$ GHz) to preferentially select against dense plasmas ($n_{\rm e} \leq 10^{11}$ m^{-3}). Such plasmas are not limited to HCHII regions but also include a variety of other Galactic objects such as massive stellar winds, ionised jets from young stellar objects (e.g. Anglada 1995) and young planetary nebulae (e.g. Bains et al. 2009).

The second is the anomalous microwave emission (AME), now being identified in an increasing number of Galactic objects, that was missed in low frequency Galactic surveys. First identified by CMB experiments (Leitch et al., 1997) as a large scale foreground contaminant, this form of emission has since been demonstrated to exist in more compact objects such as dark clouds (e.g. Casassus et al. 2006; AMI Consortium: Scaife et al. 2009b; AMI Consortium: Scaife et al. 2010a) and molecular clouds (Watson et al. 2005; Tibbs et al. 2011). Although multiple mechanisms have been proposed to explain AME, dipole emission from rapidly rotating very small dust grains (Draine and Lazarian 1998a, Draine and Lazarian 1998b) is generally considered to be most likely. Such spinning dust emission has a peaked spectral energy distribution (SED) with a maximum in the frequency range 10 – 50 GHz depending on grain size distributions.

A current lack of surveys in this frequency range means that our knowledge of the overall properties of objects which exhibit emission from spinning dust, objects which are characterized by dense plasmas, and indeed the global distribution of rising-spectrum emission in the Galaxy, is extremely poor. Those surveys which are available, such as the 9C Ryle Telescope survey (15 GHz; Waldram et al. 2003), the GPA survey (14.35 GHz; Langston et al. 2000) and the AT20G survey (20 GHz; Murphy et al. 2010b) have provided us with tantalising insights into the high frequency Galactic plane, but there is a continuing need for higher sensitivity, resolution and sky area coverage at these frequencies.

The interferometric Arcminute Microkelvin Imager Galactic Plane Survey (AMIGPS) provides the most sensitive centimetre-wave Galactic plane survey of large extent at $\nu > 1.4$ GHz. AMIGPS is a drift-scan survey of the northern Galactic plane at $\approx 16\,\mathrm{GHz}$, covering (in the first data release) the region $76^\circ \lesssim \ell \lesssim 170^\circ$ and $|b| \lesssim 5^\circ$. The AMI-SA has been used for the survey since its relatively large field of view ($\approx 400\,\mathrm{arcmin}^2$) makes covering large areas feasible, and its short baselines mean that extended objects, very common in the Galaxy, are at least partially observable. The resolution of the survey is ≈ 3 arcmin and the noise level is $\approx 3\,\mathrm{mJy\,beam}^{-1}$ away from bright sources.

3.2 Observation strategy

The AMIGPS is observed in drift-scan mode, as described in Chapter 2. In order to perform phase calibration, bright nearby point sources selected from the Very Long Baseline Array Calibrator Survey (VCS, Beasley et al. 2002) were observed for 400 seconds at 30-minute intervals during each scan. Strips were observed at a separation of 12 arcmin in δ, corresponding to the 35% point of the power primary beam, i.e. at distance x from the centre where $\exp(-x^2/(2\sigma^2)) = 0.35$, assuming the beam is Gaussian with width σ. This produces a very even noise level across the combined map, with a variation of $\approx 3\%$ between the centre of a declination strip and the point halfway between declination strips. The noise level in the survey is typically $\approx 3\,\mathrm{mJy\,beam}^{-1}$ away from bright sources and is as low as $\approx 1\,\mathrm{mJy\,beam}^{-1}$ at some points.

The first data release consists of observations above $\delta = 40^\circ$ and between $b \approx \pm 5^\circ$ and is now publicly available at `http://www.mrao.cam.ac.uk/surveys/AMIGPS/` (AMI Consortium: Perrott et al., 2013a). A later data release will extend the coverage to $\delta \geq 20^\circ$, corresponding to $53^\circ \lesssim \ell \lesssim 76^\circ$ and $170^\circ \lesssim \ell \lesssim 193^\circ$. The coverages of some other, currently available Galactic plane surveys along with their resolutions and noise levels are shown in Table 3.1, and some of these are illustrated in comparison to the (full) AMIGPS in Fig. 3.1. The AMIGPS is the first survey at cm-wave frequency to achieve similar coverage area, resolution and noise level to lower frequency surveys such as the Canadian Galactic Plane Survey (CGPS; Taylor et al. 2003); earlier surveys have either been wide and shallow with lower resolution (e.g. the GPA), or narrower, with comparable resolution but still more shallow than the AMIGPS (e.g. Nobeyama at 10 GHz; Handa et al. 1987).

The observations for the first data release were performed between 22 Jun 2010 and 4 Nov 2011. Approximately two thirds of the strips were observed multiple times

Table 3.1: Coverage, resolution and noise levels of selected Galactic plane surveys. The noise level marked with (*) is actually a detection limit. The coverages listed for the AMIGPS are for the first (full) data releases.

Telescope/ Survey name	Frequency (GHz)	Coverage (deg^2)	Resolution (arcmin)	Noise level ($\mathrm{mJy\,beam}^{-1}$)
7C(G)[a]	0.151	1700	$1.17\,\mathrm{cosec}(\delta)$	40
AMIGPS	15.75	868 (1346)	≈ 3	≈ 3
AT20G[b]	20	20086	1.7	10
CGPS[c]	1.42	1500	$1\,\mathrm{cosec}(\delta)$	0.23
	0.408		$3.4\,\mathrm{cosec}(\delta)$	3
CORNISH[d]	5	110	0.017	0.4
Effelsberg	4.875[e]	125	2.6	120(*)
	1.4[f,g]	2400	9.3	80
	2.7[h,i]		4.3	50
GPA[j]	8.35	2700	10	230
	14.35		7	800
MAGPIS[k]	1.42	43.2	0.083	0.2
Nobeyama[l]	10	183	3	33
RATAN[m]	0.96	400	4×75	60
	3.9		1×39	10
	11.2		0.35×14	100
Stockert[n]	2.72	10200	18	140
VGPS[o]	1.42	< 200	1	2
VLA	5[p]	40	0.07	2.5–10
	1.42[q]	224	0.07	10
VSA[r]	30	152	13	90

[a] Vessey and Green (1998); [b] Murphy et al. (2010b); [c] Taylor et al. (2003);
[d] Purcell et al. (2008); [e] Altenhoff et al. (1979);
[f] Reich et al. (1990b); [g] Reich et al. (1997);
[h] Reich et al. (1984); [i] Reich et al. (1990a); [j] Langston et al. (2000);
[k] Helfand et al. (2006); [l] Handa et al. (1987); [m] Trushkin (1998);
[n] Reif et al. (1987); [o] Stil et al. (2006); [p] Becker et al. (1994);
[q] Zoonematkermani et al. (1990); [r] Todorović et al. (2010)

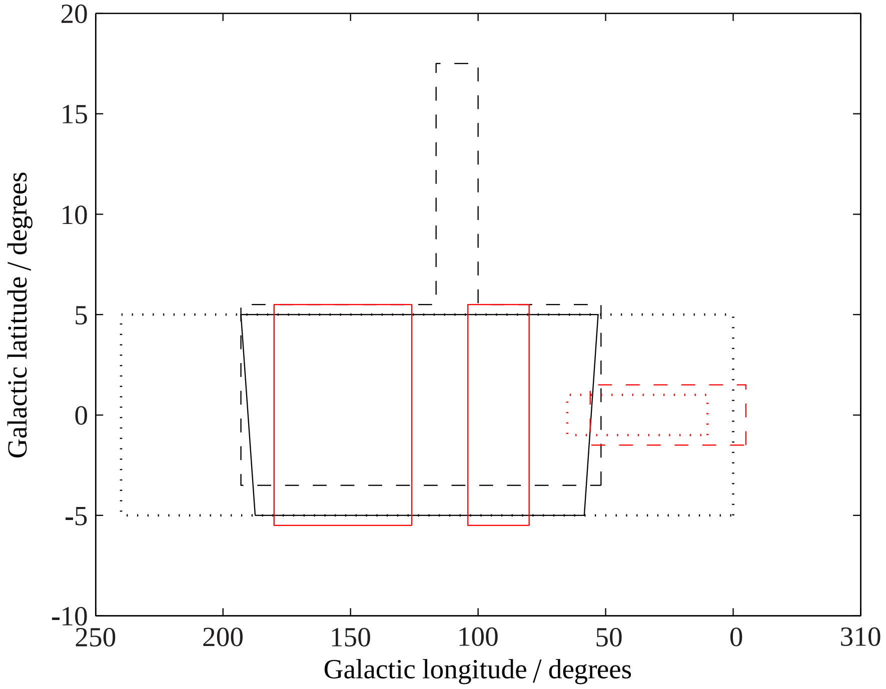

Figure 3.1: Coverage of the full AMIGPS compared to other northern Galactic plane surveys of similar area and/or resolution and noise level. The AMIGPS boundaries are shown as a solid black line, CGPS (408, 1420 MHz) as a dashed black line, Effelsberg (1.4, 2.7 GHz) as a dotted black line, 7C(G) (151 MHz) as a solid red line, Nobeyama (10 GHz) as a dashed red line, and CORNISH (5 GHz) as a dotted red line.

in order to improve the noise level, resulting in a total observing time of ≈ 1200 hours.

3.3 Calibration accuracy checks

3.3.1 Positional accuracy

3.3.1.1 Point-like sources

The catalogue of source positions (for point-like sources only) derived from the survey maps was matched to the milliarcsecond-accurate positions from the VCS catalogue (Beasley et al., 2002), resulting in 125 matches with signal-to-noise ratio (SNR) in the drift-scan maps ranging from ≈ 8 to 600. In addition, the positions derived from follow-up observations of objects that were also point-like to the LA were compared to the drift-scan catalogue positions, resulting in 270 additional matches (not matched to a VCS source) with SNR in the drift-scan maps ranging from ≈ 5 to 400.

The errors σ_{RA} and σ_{δ} in RA and δ for a point source are assumed to be given by

$$\sigma_{\mathrm{RA}}^2 = \epsilon_{\mathrm{RA}}^2 + \sigma_{\mathrm{M}}^2 \sin^2(\phi) + \sigma_{\mathrm{m}}^2 \cos^2(\phi) \tag{3.1a}$$

$$\sigma_{\delta}^2 = \epsilon_{\delta}^2 + \sigma_{\mathrm{M}}^2 \cos^2(\phi) + \sigma_{\mathrm{m}}^2 \sin^2(\phi), \tag{3.1b}$$

where $\epsilon_{\mathrm{RA\,or\,}\delta}$ are the r.m.s. calibration errors in RA and δ, $\sigma_{\mathrm{M\,or\,m}}$ are the noiselike uncertainties parallel to the synthesised beam major (M) and minor (m) axes, and ϕ is the position angle of the beam (e.g. Condon et al. 1998). We assume the noiselike uncertainties are given by

$$\sigma_{\mathrm{M\,or\,m}} = \frac{\theta_{\mathrm{M\,or\,m}}}{\sqrt{2\ln(2)}\,\mathrm{SNR}}, \tag{3.2}$$

where $\theta_{\mathrm{M\,or\,m}}$ are the major and minor FWHM of the synthesised beam.

To test for systematic RA and δ offsets, the mean offsets between both the AMIGPS and VCS catalogue and AMIGPS and LA positions were calculated separately and as a single group, and by selecting sources with SNR >50 and SNR >100 in the drift-scan maps. These are listed in Table 3.2, and are all consistent with zero within $< 2.5\sigma$, so we assume no systematic offset in RA or δ.

To determine the r.m.s. calibration errors, ϵ_{RA} and ϵ_{δ} were varied until 99.7% of

Table 3.2: Mean RA and δ position offsets for high SNR sources in the drift-scan catalogue. Consistency is checked by using the offsets from VCS catalogue and LA positions separately, and combined, and by changing the minimum SNR. All offsets are given in arcsec.

SNR limit	Offset from	Number of sources	Mean RA offset	Mean δ offset
50	VCS	56	0.9 ± 0.5	-0.4 ± 0.3
	LA	18	-1.1 ± 0.7	-0.9 ± 0.7
	Combined	74	0.5 ± 0.4	-0.5 ± 0.3
100	VCS	30	0.6 ± 0.7	-0.6 ± 0.4
	LA	5	-0.5 ± 1.5	-1.0 ± 1.0
	Combined	35	0.5 ± 0.4	-0.65 ± 0.3

the sources with VCS positions had offsets within 3σ calculated from Equation 3.1. This gave $\epsilon_{\mathrm{RA}} = 2.6$ arcsec and $\epsilon_{\delta} = 1.7$ arcsec. Fig. 3.2 shows the positional offsets for all sources in both datasets, normalised by the calculated error. They agree well, with 99% of all offsets lying within the 3σ circle. (Note that the statistics are expected to be only approximately Gaussian since the extremely different resolutions of the surveys can result in positional shifts where extra, extended flux detected by lower-resolution surveys can shift the centroids of the sources – a Kolmogorov-Smirnov test shows that the offsets from the VCS sources are consistent with a normal distribution, with p-values (indicating the probabilities of obtaining these offsets if drawn from normal distributions) of 0.15 for offsets in RA and 0.40 for offsets in δ; including the LA sources decreases the p-values to 0.02 and 0.17 respectively, but plotting the histograms shows that the low p-values are due to over-estimation of the errors, i.e. since the resolution mismatch is less extreme, the added r.m.s. calibrations errors would be smaller if considering LA matches alone).

3.3.1.2 Extended sources

For sources that are extended relative to the SA beam, the positional uncertainty is calculated slightly differently. The errors in RA and δ are given by

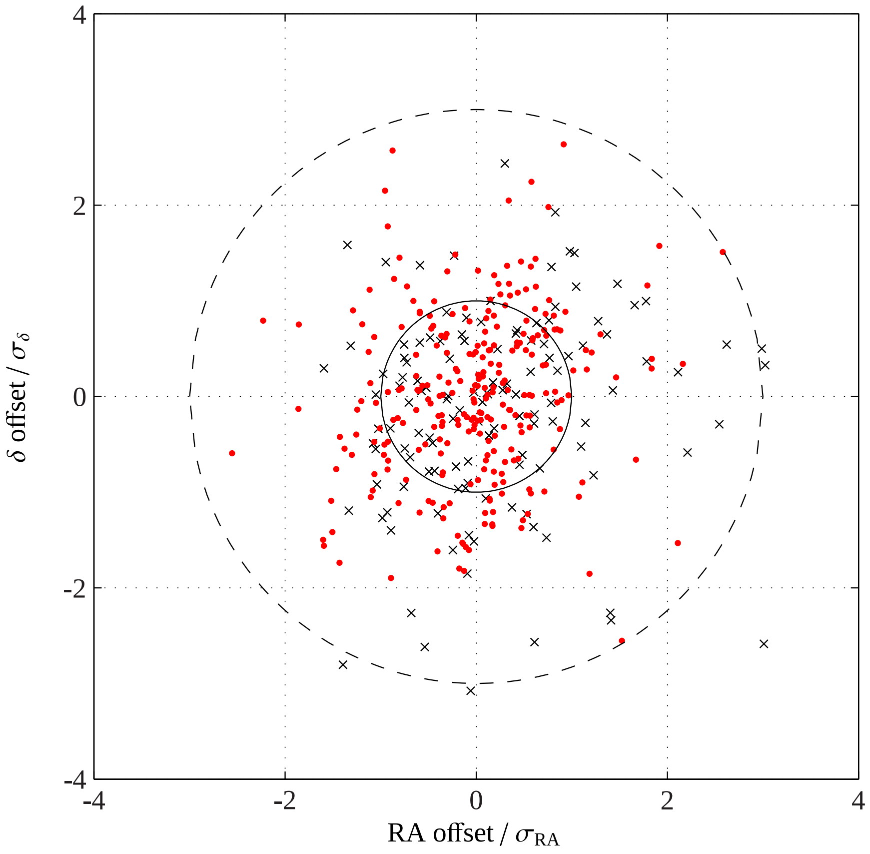

Figure 3.2: RA and δ offsets normalised by their calculated errors for all sources which are matched to a VCS source with well-known position (black crosses) or have been followed up with the LA (red dots). The estimated 1 and 3σ error circles are also shown.

$$\sigma^2_{\mathrm{RA}} = \epsilon^2_{\mathrm{RA}} + \sigma^2_{\mathrm{J,RA}} \tag{3.3a}$$
$$\sigma^2_{\delta} = \epsilon^2_{\delta} + \sigma^2_{\mathrm{J},\,\delta}, \tag{3.3b}$$

where the $\sigma_{\mathrm{J,RA\ or\ J},\,\delta}$ terms are the errors estimated by the AIPS fitting task JMFIT, which folds in an estimate of the noiselike error as well as the error associated with the fit.

3.3.2 Flux-calibration accuracy

We assume flux calibration errors are given by

$$\sigma^2_{S_{\mathrm{peak}}} = (0.05\,S_{\mathrm{peak}})^2 + \sigma^2 \qquad \text{for a point-like source} \tag{3.4a}$$
$$\sigma^2_{S_{\mathrm{int}}} = 2\,(0.05\,S_{\mathrm{int}})^2 + \sigma^2 \qquad \text{for an extended source,} \tag{3.4b}$$

where S_{peak} is peak flux density and S_{int} is integrated flux density. This error estimation comprises a 5% calibration uncertainty (including rain-gauge correction) and a noise-like error σ which for a point-like source is the r.m.s. map noise measured from the CLEANed map, and for an extended source is the error estimated by JMFIT which accounts for the number of independent pixels present in the fit and also folds in an estimation of the fitting error. The error for an extended source also contains an extra 5% error due to the uncertainty in the beam shape (see Section 2.7).

Although a Gaussian is a reasonable approximation to the shape of many sources, clearly in the Galactic plane there are many sources which are not Gaussian in shape. Integrated flux densities should therefore be used with caution. The 'χ^2' statistic is included in the catalogue as an indication of the goodness of fit, calculated as

$$\chi^2 = \frac{\sum_{i=1}^{N}(S_i - \overline{S}_i)^2}{\sigma^2(N - 6 \times N_{\mathrm{src}})} \tag{3.5}$$

where N is the number of pixels in the fitting area, S_i and $\overline{S}_i$ are the actual and modelled flux densities of pixel i respectively, σ is the estimated thermal noise at the position of the source, and N_{src} is the number of sources fitted simultaneously, for each of which

6 parameters (central RA, δ, $S_{\rm pk}$, major and minor axis size and position angle) are fitted. This should be treated as an indicator, rather than a formal reduced χ^2 since it does not take into account the number of independent pixels in the fitting area, and the value of the noise is uncertain and likely underestimated around bright sources, as described in Section 2.7. The values of 'χ^2' in the catalogue for the first data release range from ≈ 0.2 to 160; note that this indicates how well the source can be represented by a Gaussian, rather than the believability of the detection. It should also be noted that integrated flux densities will also be affected by flux loss when the source is extended on scales that are larger than the SA synthesised beam.

At 16 GHz, intrinsic source variability is important. AMI Consortium: Franzen et al. (2009) find that of 93 extra-galactic sources monitored with the AMI-SA for periods between one and 18 months, $\approx 50\%$ are variable above the flux density calibration uncertainties and 15% are variable at a level of more than 20%. Variability must therefore be considered when attempting to test the flux calibration accuracy.

The flux density accuracy of the pipeline was first tested on two well-characterised non-variable radio sources, 3C48 and NGC 7027.

3C48 This is one of the primary calibration sources used by AMI and is known to be variable on the level of $\lessapprox 1\%$ on the time-scale of the survey (Perley and Butler, 2013). It is assumed to have a 16 GHz flux of 1.64 Jy, consistent with the updated VLA calibration scale (see Table 2.1). Drift-scan observations were made of an area around it between Mar and Dec 2010 as an initial test of the drift-scan observation mode. These observations were reduced both in the standard Galactic pipeline, which uses the closest primary calibrator observations in time including 3C48, as well as using only 3C286 as a primary calibrator. The drift-scan flux density derived from the final, combined map is 1.60 ± 0.08 Jy, using 3C48 and 3C286 as primary calibrators, and 1.63 ± 0.08 Jy using only 3C286. Both values are consistent with each other and are within 0.5σ of the nominal value, 1.64 Jy. They are also well within the standard 5% calibration accuracy quoted for SA pointed observations.

NGC 7027 This is a planetary nebula lying within the Galactic drift-scan survey area and for present purposes is essentially non-variable (see, e.g. Zijlstra et al. 2008). It is also frequently monitored by AMI with tracked observations so an accurate flux density at 16 GHz can be calculated for comparison. Using data taken between 2007 and July 2012 with the SA, the 16-GHz flux density of NGC 7027 is 5.4 Jy. The drift-scan flux for NGC 7027 from the combined map is 5.1±0.3 Jy, agreeing with the tracked value to within 1.0σ or $\approx 5.5\%$.

3.3.2.1 Concurrent observations

Since AMI is continually observing phase calibrators for many of its observations, there is a high probability that there exist quasi-simultaneous tracked observations of bright compact sources – mostly extra-galactic – which are also prominent in the drift-scan survey. Extrapolating from Fig. 3 of AMI Consortium: Franzen et al. (2009) which shows the variability index for extra-galactic sources at 15 GHz as a function of time, an interval of ten days, within which source variability should be small, was chosen for comparing flux density measurements. Since the drift-scan survey also consists of multiple observations on different dates, each observation which contained a potential match within ±10 days was re-imaged separately and source-finding was done on the individual declination strips. Any archival SA tracked observations within ±10 days of drift observations of matching sources were averaged and compared with the individual drift-scan values. Fig. 3.3 illustrates the comparison between the peak flux densities of these sources; 93% of the drift-scan flux densities are within 3σ (where $\sigma = \sqrt{\sigma^2_{\rm drift} + \sigma^2_{\rm tracked}}$) of the mean archival flux.

The three outliers had lower drift-scan flux densities than the mean archival flux density and were found to lie near the edge of the declination strip, where phase errors are expected to have the greatest effect. In each case, the source appears near the centre of the adjacent strip, which was observed a day later. When creating the final combined map, the pixels nearer the centre of individual pointings are given greater weight, so the discrepant flux densities will be down-weighted. The flux densities for these sources derived from raster maps produced from observations close in time agree with the mean archival flux to within 1σ.

It is common for survey flux densities to be slightly suppressed due to small phase errors shifting the positions of sources which lie away from the pointing centres in the constituent maps (see, e.g. AMI Consortium: Davies et al. 2011). The concurrent observations were tested for this effect, but the median percentage difference

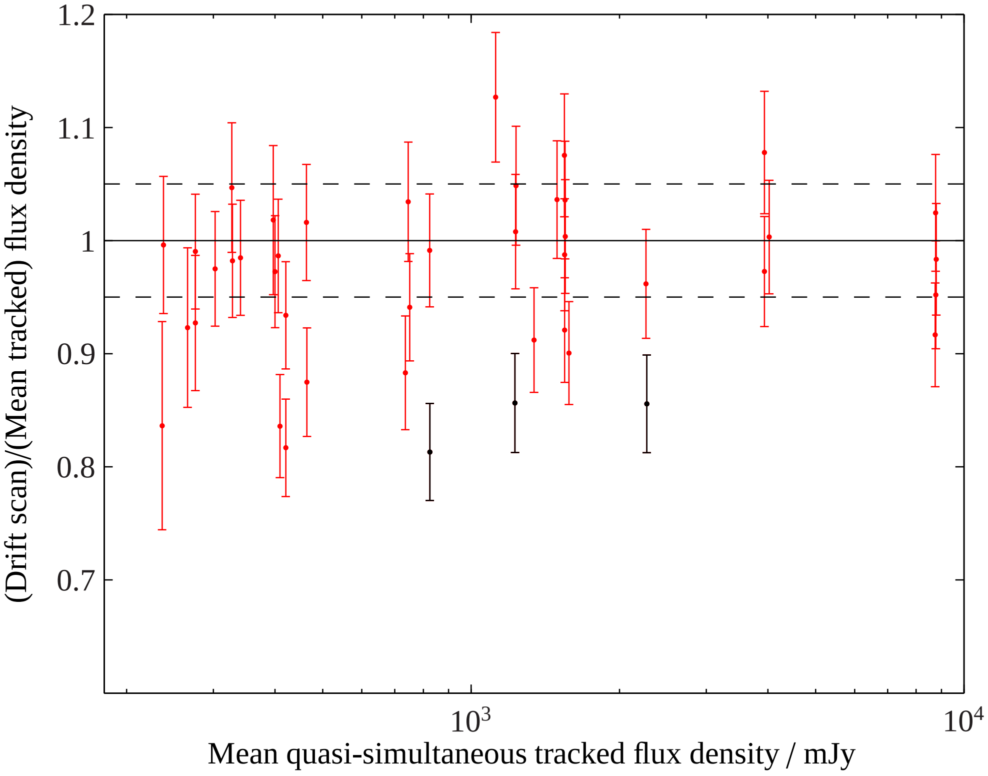

Figure 3.3: Drift-scan flux densities compared to the mean flux density from tracked SA archival observations within 10 days. 3σ outliers are plotted in black. The black solid and dotted lines show a one-to-one correspondence and ±5% flux-calibration uncertainty.

$((S_{\rm mean,tracked} - S_{\rm drift})/S_{\rm mean,tracked})$ was found to be only $\approx 2\%$; the AMIGPS flux densities have not been adjusted for this effect.

3.3.2.2 Non-concurrent observations

A final check of the flux calibration accuracy can be made by comparing the LA follow-up flux densities to the drift-scan flux densities for sources that are found to be point-like to the LA, although these observations are widely spaced in time (by up to ≈ 1.5 years). Very little is known about variability statistics in the Galactic plane at cm-wavelength. However, some idea of the expected number of variable sources can be obtained using results from the 5-GHz Galactic plane variability study by Becker et al. (2010), where $\approx 8\%$ of sources detected in the flux density range from $1 - 100$ mJy between $b \approx \pm 1.0^\circ$ were found to be variable at levels between 20 and 1800%, on a time scale of years or shorter (when no correction for the inclusion of the extra-galactic source population was applied).

Fig. 3.4 shows the comparison between the pointed LA and drift-scan SA survey peak flux densities: 87% are within 3σ, taking into account the LA errors which are generally smaller than the drift-scan errors and are not plotted for clarity. The remaining 13% seems consistent with the 8% of sources predicted to be variable, given that no correction for differences in frequency, flux density range, Galactic latitude, or bias due to selecting for rising-spectrum sources, has been attempted. The apparent bias towards higher drift-scan flux densities at the lower end of the flux density scale is likely to be an Eddington bias caused by low-SNR sources selected from the AMIGPS map being more likely to occur on positive noise peaks.

3.4 Data products

3.4.1 Raster maps

The field is divided into 38 square maps of side 6°, which are given names constructed from the Galactic coordinates of their centres, e.g. G78.0−2.2. These are shown in Fig. 3.5. The centres are spaced by 5° in longitude, and 4.4° in latitude, and start at $\ell = 78.0^\circ$, $b = -2.2^\circ$.

These raster maps are available from `http://www.mrao.cam.ac.uk/surveys/AMIGPS/`, along with:

- noise maps containing the estimated thermal noise level at each pixel;
- noise maps adjusted for the exclusion zones around the bright sources. For a given pixel, the value is max(thermal noise, $S_{\mathrm{peak,bright}}/50$), i.e. the (flux-detection limit)/5 for the catalogue;
- a FITS data-cube giving the synthesised beam major and minor axis FWHM and position angle appropriate to each pixel (i.e. the synthesised beam belonging to the pointing with the highest weight at that pixel).

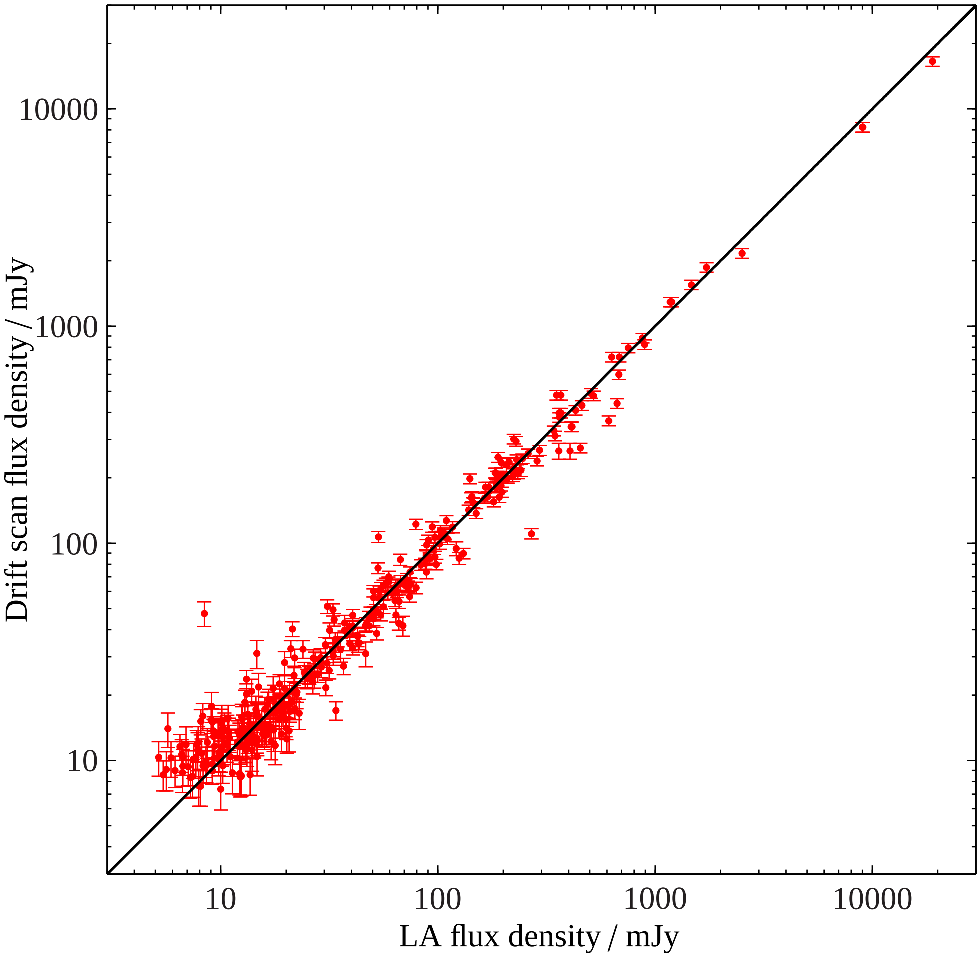

Figure 3.4: Drift-scan flux densities compared to the LA follow-up flux. The black solid line shows a one-to-one correspondence.

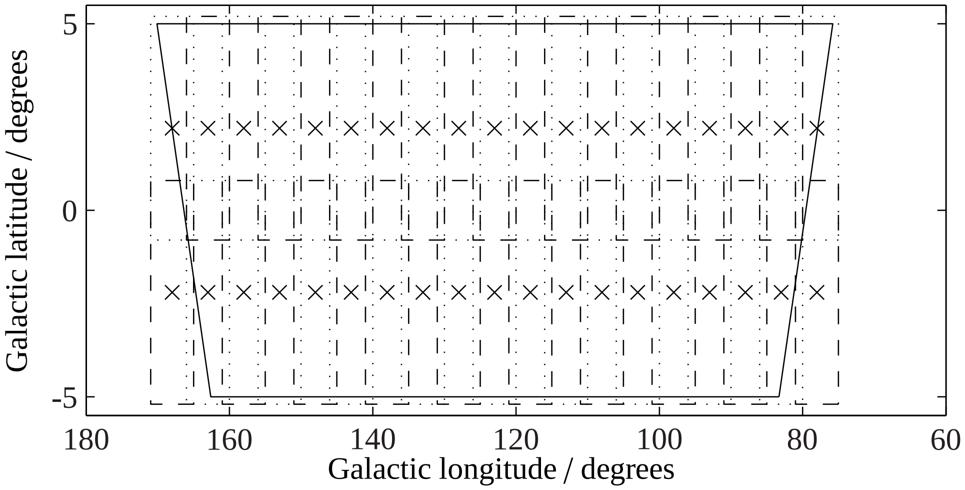

Figure 3.5: The positions of the raster maps in Galactic coordinates. The solid black line marks the extent of the data, the dotted and dashed lines show the boundaries of the raster maps and the crosses mark the centres of the maps.

Fig. 3.6 shows an example 6 deg^2 map, with annotations marking the sources detected within it. Also shown for comparison is a CGPS total intensity 1.4 GHz map showing the same region. It can be seen that many sources detected by CGPS are also detected by the AMIGPS; however some larger-scale features such as the supernova remnant G116.5+1.1 are resolved out.

3.4.2 Source catalogue

A sample of the catalogue containing the first ten sources detected in Fig. 3.6 is shown in Table 3.3. The complete source list, which contains 3503 entries, is available from `http://www.mrao.cam.ac.uk/surveys/AMIGPS/`. For each source, the catalogue contains:

- A source name, constructed from the J2000 RA and δ coordinates of the source.
- The peak RA, δ, flux density and associated errors (these are the appropriate quantities to use for point-like sources).
- The fitted centroid RA and δ, integrated flux density and associated errors (these are the appropriate quantities to use for extended sources).

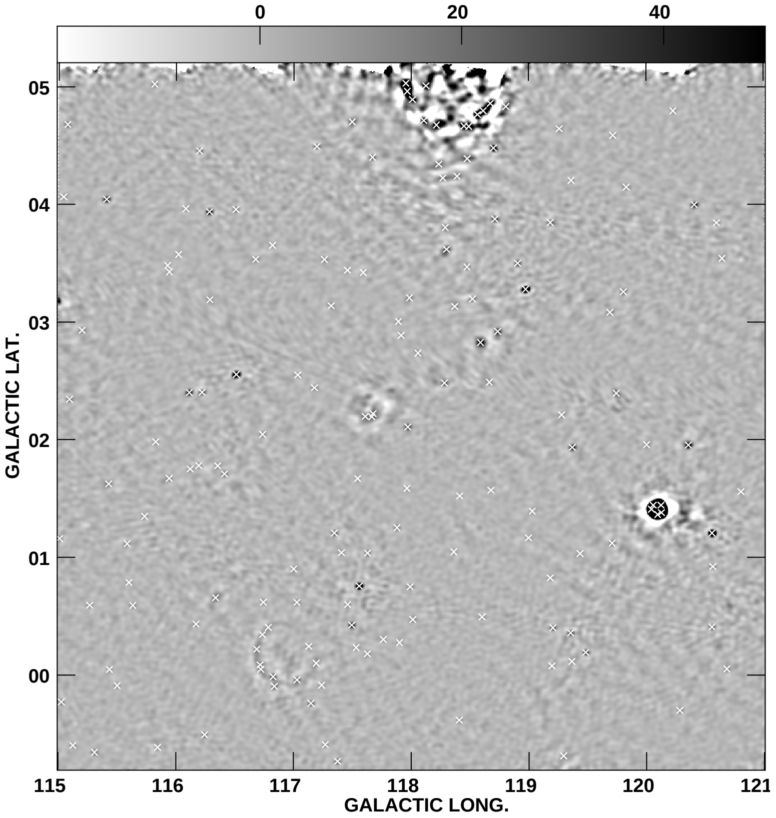

(a)

Figure 3.6: An example AMIGPS raster map (a) centred at $\ell = 118.0°$, $b = 2.2°$. Source detections are marked with ×. (b) shows a CGPS 1.4-GHz total-intensity map of the same region. The grey-scales of the maps are in mJy beam^{-1} and K respectively and are truncated to show the fainter features. Some well-known supernova remnants (SNR) and HII regions visible in the map are labelled on the CGPS map (Green 2009, Sharpless 1959). It can be seen that the AMIGPS sees many features common to the CGPS, however the larger-scale features such as the SNR G116.5+1.1 are resolved out.

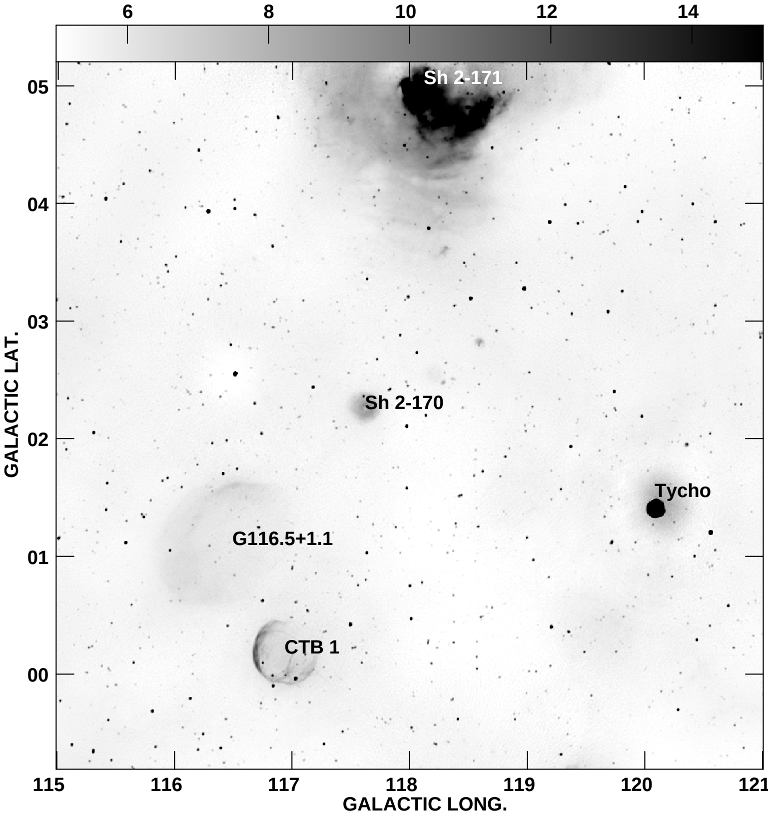

(b)

Figure 3.6: Continued.

- The critical source size as defined in Eqn. 2.2 and the deconvolved source major and minor axis sizes and position angle. A deconvolved size of 0.0 indicates that the source was not found to be wider than the synthesised beam in the major or minor axis direction.
- The χ^2 value for the fit.
- The source classification (point-like or extended).

3.5 Completeness

Estimation of the completeness of the survey, or the fraction of sources expected to be detected over the survey region at a given flux density level, is made difficult due to the 'exclusion zones' which were employed around bright sources. As described in Section 2.7.2, it was found that the noise map values do not adequately represent the elevated, non-Gaussian noise present around sources with peak flux density $\gtrapprox 50\,\mathrm{mJy}$. To account for this, 'exclusion radii' r_E were defined based on the peak flux density of the bright source, $S_{\mathrm{peak,bright}}$ as $r_E = 18\left(S_{\mathrm{peak,bright}}/300\,\mathrm{mJy}\right)^{1/3}$ arcmin and sources within this distance from the bright source were required to have peak flux density $S_{\mathrm{peak}} \geq S_{\mathrm{peak,bright}}/10$ to be included in the catalogue. Since source-finding is carried out at 5σ, this effectively redefines the noise level within the exclusion zone to be $\max(\sigma_{\mathrm{orig.}}, S_{\mathrm{peak,bright}}/50)$ where $\sigma_{\mathrm{orig.}}$ is the existing thermal noise estimate from the map.

The probability of a source with true flux density $\hat{S}$ being detected when lying on a pixel with thermal noise σ_{n} is given by

$$P(\hat{S} \geq 5\sigma_{\mathrm{n}}) = \int_{5\sigma_{\mathrm{n}}}^{\infty} \frac{1}{\sqrt{2\pi\sigma_{\mathrm{n}}^2}} \exp -\frac{\left(x - \hat{S}\right)^2}{2\sigma_{\mathrm{n}}^2}\,\mathrm{d}x, \tag{3.6}$$

assuming Gaussian statistics. The theoretical probability of the source being detected can therefore be calculated by averaging the probabilities given by Eqn. 3.6 for each pixel in the map. This is illustrated in Fig. 3.7 and was calculated in three different ways:

Table 3.3: An example section of the AMIGPS catalogue, containing the brightest ten sources detected in the map shown in Fig. 3.6. See text for details of the quantities in the columns.

Source	RA$_{\rm peak}$ (J2000)	$\delta_{\rm peak}$ (J2000)	ΔRA$_{\rm peak}$ (arcsec)	$\Delta\delta_{\rm peak}$ (arcsec)	$S_{\rm peak}$ (mJy)	$\Delta S_{\rm peak}$ (mJy)	RA$_{\rm cent}$ (J2000)	$\delta_{\rm cent}$ (J2000)	ΔRA$_{\rm cent}$ (arcsec)	$\Delta\delta_{\rm cent}$ (arcsec)	$S_{\rm int}$ (mJy)	$\Delta S_{\rm int}$ (mJy)	$e_{\rm crit}$ (arcsec)	$e_{\rm maj}$ (arcsec)	$e_{\rm min}$ (arcsec)	e_{θ} (°)	χ^2	Type
J001449+611744	00:14:49.92	+61:17:44.1	2.7	1.8	844.2	42.4	00:14:49	+61:17:42.4	2.6	1.7	842.5	60.0	100.0	18.2	0.0	20.7	2.31	P
J235300+602850	23:53:00.43	+60:28:50.1	3.0	2.1	426.8	21.8	23:53:01	+60:28:53.1	2.8	1.9	1032.2	74.3	100.0	178.5	169.6	130.3	3.80	E
J002704+595854	00:27:04.28	+59:58:54.1	2.8	2.0	379.6	19.2	00:27:04	+59:58:56.4	2.7	1.8	366.8	26.5	100.0	13.8	0.0	92.6	3.30	P
J003608+585548	00:36:08.21	+58:55:48.4	3.8	3.5	168.6	9.1	00:36:08	+58:55:49.4	2.9	2.1	157.4	12.5	100.0	95.0	0.0	119.4	2.10	P
J002240+604014	00:22:40.73	+60:40:14.1	3.3	2.5	162.6	8.5	00:22:41	+60:40:15.3	2.8	1.9	154.1	11.6	100.0	0.0	0.0	0.0	2.29	P
J000336+630750	00:03:36.22	+63:07:50.9	4.0	3.1	127.7	7.0	00:03:36	+63:07:52.0	2.9	2.1	121.3	9.7	100.0	0.0	0.0	0.0	1.30	P
J000107+605120	00:01:07.75	+60:51:20.3	3.9	3.1	121.4	6.6	00:01:07	+60:51:21.4	2.9	2.1	117.8	9.4	100.0	0.0	0.0	0.0	2.65	P
J000206+605832	00:02:06.98	+60:58:32.5	4.8	3.9	79.7	4.6	00:02:07	+60:58:31.1	3.1	2.4	74.1	6.5	100.0	32.3	0.0	176.2	2.54	P
J003043+590415	00:30:43.99	+59:04:15.6	9.2	5.8	73.7	5.1	00:30:44	+59:04:16.8	4.6	3.0	67.2	7.3	145.8	0.0	0.0	0.0	1.12	P
J003552+595008	00:35:52.98	+59:50:08.6	4.6	3.7	60.9	3.4	00:35:54	+59:50:08.4	3.1	2.3	57.6	4.8	100.0	0.0	0.0	0.0	2.41	P

- Using pixels outside the exclusion zones only (solid line).
- Using all pixels in the map, and assuming that the effective noise level defined above for the pixels inside exclusion zones can be treated as an approximation to the Gaussian noise level σ_{n} in Eqn. 3.6 (dashed line). This should be a slight overestimation of the completeness since $S_{\mathrm{peak,bright}}/10$ was chosen to be a conservative cutoff to exclude as many spurious sources as possible.
- Using all pixels in the map, and assuming that the original thermal noise level $\sigma_{\mathrm{orig.}}$ from the map represents the true thermal noise level, but the 5σ cutoff is taken as $S_{\mathrm{peak,bright}}/10$, i.e.

  $$P(\hat{S} \geq S_{\mathrm{peak,bright}}/10) = \int_{S_{\mathrm{peak,bright}}/10}^{\infty} \frac{1}{\sqrt{2\pi\sigma_{\mathrm{orig.}}^2}} \exp -\frac{\left(x - \hat{S}\right)^2}{2\sigma_{\mathrm{orig.}}^2}\, \mathrm{d}x. \tag{3.7}$$

  This was calculated as a consistency check and made little difference to the completeness curve; it is not plotted.

The accuracy of these completeness curves was also tested via simulation. Some 5300 simulated sources were inserted in the maps using the AIPS task IMMOD at random positions drawn from a uniform distribution in ℓ and b. Ten realisations were performed in which the peak flux density was altered but the positions remained constant. The standard source-finding pipeline was run on the maps and the fraction of sources detected was recorded for each peak flux density. Sources which fell within 1.5 arcmin ($\approx 0.5\times$ the average synthesised beam width) of the edge of the map were excluded; otherwise, if a source was detected within 1.5 arcmin of its input position and closer to its input position than to the nearest real source position it was considered to be detected. The results of the simulations are plotted with the theoretical curves in Fig. 3.7 and can be seen to agree well.

Outside the exclusion zones, the survey is 99% complete above ≈ 75 mJy, but when including the exclusion zones it does not reach 99% completeness until ≈ 7.5 Jy. The corresponding 90% completeness limits are ≈ 17 and ≈ 35 mJy respectively. It should be noted however that any effect due to correlation between source positions is not included in the completeness estimation. The completeness curve is expected to be slightly overestimated due to this effect.

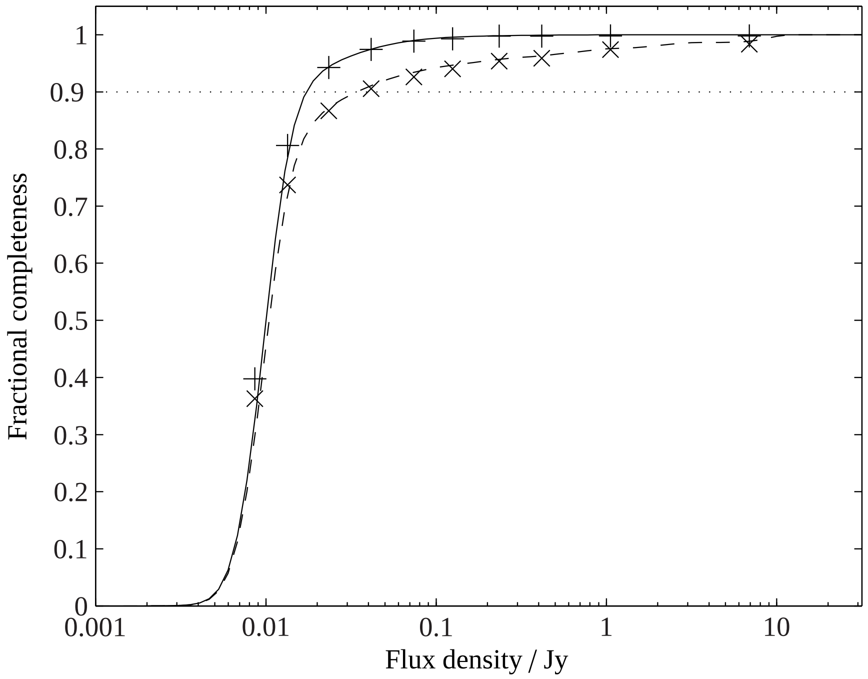

Figure 3.7: An estimation of the completeness of the AMIGPS, calculated from the noise maps (continuous lines) and from simulations (discrete points). The completeness was calculated over the whole survey area (dashed line, ×) and outside the exclusion zones around bright sources only (solid line, +). The dotted line shows the 90% completeness limit.

3.6 Source counts

Source counts are calculated for sources classified as compact to the AMI-SA beam, in order to estimate the source density as a function of flux density and galactic latitude in comparison with extra-galactic counts derived at the same frequency from the 9C and 10C surveys. These are plotted in Fig. 3.8 for the entire survey area and for $0.0 \leq |b| < 2.5$ and $2.5 \leq |b| < 5.2$, corrected by the appropriate completeness curve calculated from Eqn. 3.6. No attempt has been made to fit a power law to these counts since the completeness estimation is unlikely to be accurate enough for this purpose. Included for comparison is the fit to the combined 9C and 10C (extra-galactic) source counts (AMI Consortium: Davies et al., 2011); note that beyond 1 Jy this is an extrapolation, since the fields were chosen to exclude very bright sources; both theoretical models and observations show a drop-off in the source counts past 1 Jy (see, e.g. Fig. 7 of de Zotti et al. 2010). It is clear that the Galactic source count is generally higher than the extra-galactic count, showing the presence of Galactic sources; the source count is also higher in the bin closer to the centre of the Galactic plane, in particular for the higher flux density bins.

3.7 Matching with 1.4-GHz surveys

In order to search for rising spectrum objects which may be ultra/hyper-compact HII or spinning dust regions, the AMIGPS catalogue was matched with the NRAO VLA Sky Survey (NVSS) at 1.4 GHz. AMIGPS positional errors, $\sigma_{\rm AMI}$, were calculated as described in Section 3.3.1, and the NVSS catalogue was searched for matches to the AMIGPS sources within 4σ, where $\sigma = \sqrt{\sigma^2_{\rm AMI} + \sigma^2_{\rm NVSS}}$ and $\sigma_{\rm NVSS}$ is the positional error given in the NVSS catalogue. For extended sources, an extra 10% of the source fitted major-axis size was added (up to a maximum of 30 arcsec) to account for possible morphological shifts between frequencies. Although initially a 3σ limit was used, it was found in practice to exclude a significant fraction of sources which on inspection were clearly associated, and was revised to 4σ; this is probably due to the different angular scales covered by the two instruments, i.e. NVSS sources will often correspond to knots of emission embedded within more extended emission which is visible to AMI but resolved out by NVSS. Since the resolutions of the sur-

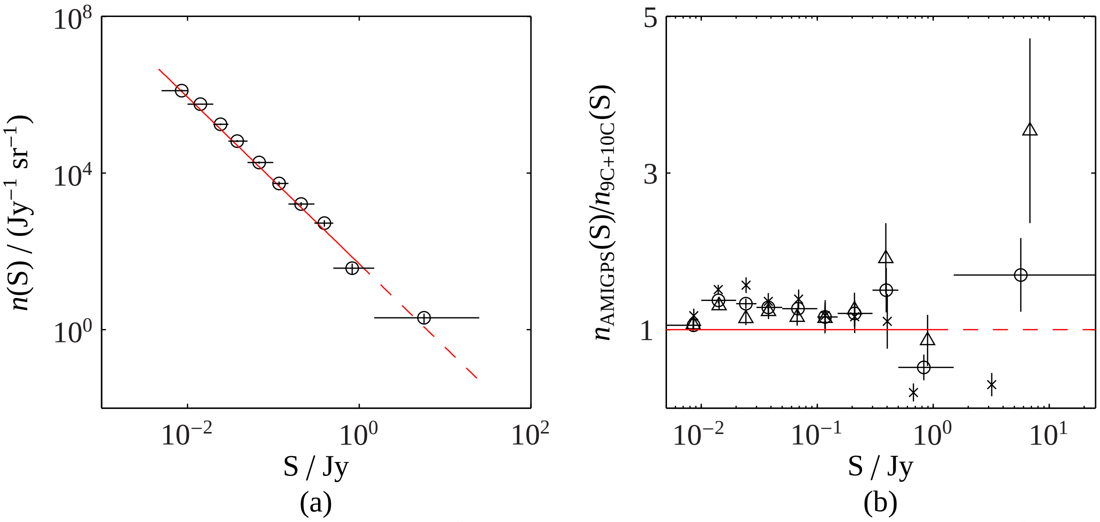

Figure 3.8: Source counts, $n(S)$, for sources compact to the AMI-SA beam for the entire survey area (circles), between $0.0 \leq |b| < 2.5$ (triangles) and $2.5 \leq |b| < 5.2$ (crosses), compared to the fit to the combined 9C and 10C count (solid red line), extrapolated past the 9C limit of 1 Jy (dashed red line). (a) shows the absolute counts, while (b) shows the counts relative to the extragalactic 9C and 10C counts. Flux density bin widths are shown as horizontal error bars, and are the same for all b bins. The vertical error bars are Poisson errors.

veys are different (≈ 45 arcsec for NVSS and ≈ 3 arcmin for the AMIGPS), in some cases multiple matches were returned. A minimum error cutoff of 20 arcsec was also imposed to account for effects such as multiple matches unresolved by the SA beam shifting the peak position. 4177 matches were made in total, or 3086 unique AMIGPS sources were matched to (possibly multiple) NVSS sources. This leaves a total of 417 AMIGPS sources unmatched; most of these are extended sources which are resolved out by the NVSS (90% have fitted major axis sizes $e_{\rm maj} > 50$ arcsec).

For each of the matched AMIGPS sources which are compact to the SA beam, spectral indices α are calculated. If there are multiple NVSS matches, the sum of the NVSS flux densities is used to calculate the spectral index. The error, $\Delta\alpha$ is calculated by error propagation to be

$$\Delta\alpha = \frac{1}{\ln(16/1.4)} \sqrt{\left(\frac{\Delta S_{16}}{S_{16}}\right)^2 + \left(\frac{\Delta S_{1.4}}{S_{1.4}}\right)^2}, \tag{3.8}$$

where $(\Delta)S_{16}$ is the 16 GHz flux density (error) and $(\Delta)S_{1.4}$ is the 1.4 GHz flux density (error).

In Waldram et al. (2010) it is shown that the 1.4 to 15 GHz spectral index distribution is different depending on the 15 GHz flux density range used for sample selection. Figure 3.9 shows spectral index distributions for three flux density ranges drawn from the AMIGPS matched catalogue in comparison to the 9C spectral index distributions for extragalactic sources in the same flux density range, without correction for the small shift in frequency. In the two higher ($25 \leq S < 100$ and $S \geq 100$ mJy) flux density bins, a two-sample Kolmogorov–Smirnov test shows that the two samples are not drawn from the same distribution at a confidence level of > 90%, with p-values (probability of obtaining a test statistic at least as extreme as the one actually observed) of 0.07 and 0.04 respectively. In the lowest flux density bin, the hypothesis that the samples are drawn from the same distribution cannot be rejected as the p-value is 0.48. To test the effect of differing resolution on these statistics, the same test was performed restricting the sample to AMIGPS sources matched to a single NVSS source only. The conclusions are unchanged, with the two higher flux density bins both having p-values of 0.06, and the lower flux density bin having a p-value of 0.64. In all cases, it is clear from the distributions that there are an excess of sources with $\alpha < 0$ with respect to the extra-galactic sample.

3.8 Ultra- and hyper-compact HII region candidates

UCHII and HCHII regions are thought to be stages in the development of massive stars. As a dense molecular cloud core collapses to eventually form a massive star, the young star produces ultraviolet photons which photoionise nearby molecular cloud material.

UCHII regions were first defined observationally in Wood and Churchwell (1989), as small (diameter $\leq$ 0.1pc), dense (electron density $\geq 10^{10}$ m^{-3}) ionised regions of gas surrounding young, massive O and B stars, with emission measures (EM $= \int N_\mathrm{e} N_\mathrm{i} \, \mathrm{d}\ell$, where $N_\mathrm{e} \approx N_\mathrm{i}$ are the number densities of electrons and ions and $\mathrm{d}\ell$ is the line of sight) $\geq 10^{19}$ pc m^{-6}. Dust in the molecular gas surrounding the stars and UCHII regions absorbs nearly all the stellar radiation and reradiates in the far-infrared (FIR), so the stars are invisible at optical wavelengths but visible as very bright point sources in, for example, the Infrared Astronomical Satellite (IRAS) survey. They are distinct from more evolved HII regions, which are optically thin at radio wavelengths.

Examples of an even more compact phase of the gas with diameters less than a few thousand AU were found by Gaume et al. (1995), and denoted as HCHII regions. It is unclear at this stage whether HCHII regions are earlier phases which evolve into UCHII regions, and then eventually to a more evolved HII region, or whether they constitute a distinct class of objects to UCHII regions (Murphy et al., 2010a).

Murphy et al. (2010a) have defined a set of criteria for UCHII and HCHII regions based on a survey of the literature. These are given in Table 3.4. Both classes of object are expected to be optically thick at radio wavelengths and so to have rising spectra, for example from 1420 MHz (NVSS) to 15 GHz (AMI). The AMIGPS and NVSS correlations will therefore be useful in detecting these objects and characterising their global distributions in the northern Galactic plane. For each class, the angular size expected is also calculated assuming it is in the closest known massive star-forming region, Orion, at a distance of $\approx$ 400 pc (see, e.g. Hirota et al. 2007), and assuming it is in the Perseus spiral arm at a distance of 1.95 kpc (Xu et al., 2006).

A simple model for the radio spectrum of an unresolved HII region with constant electron density is given by assuming an optical path length τ_ν for the free–free emission

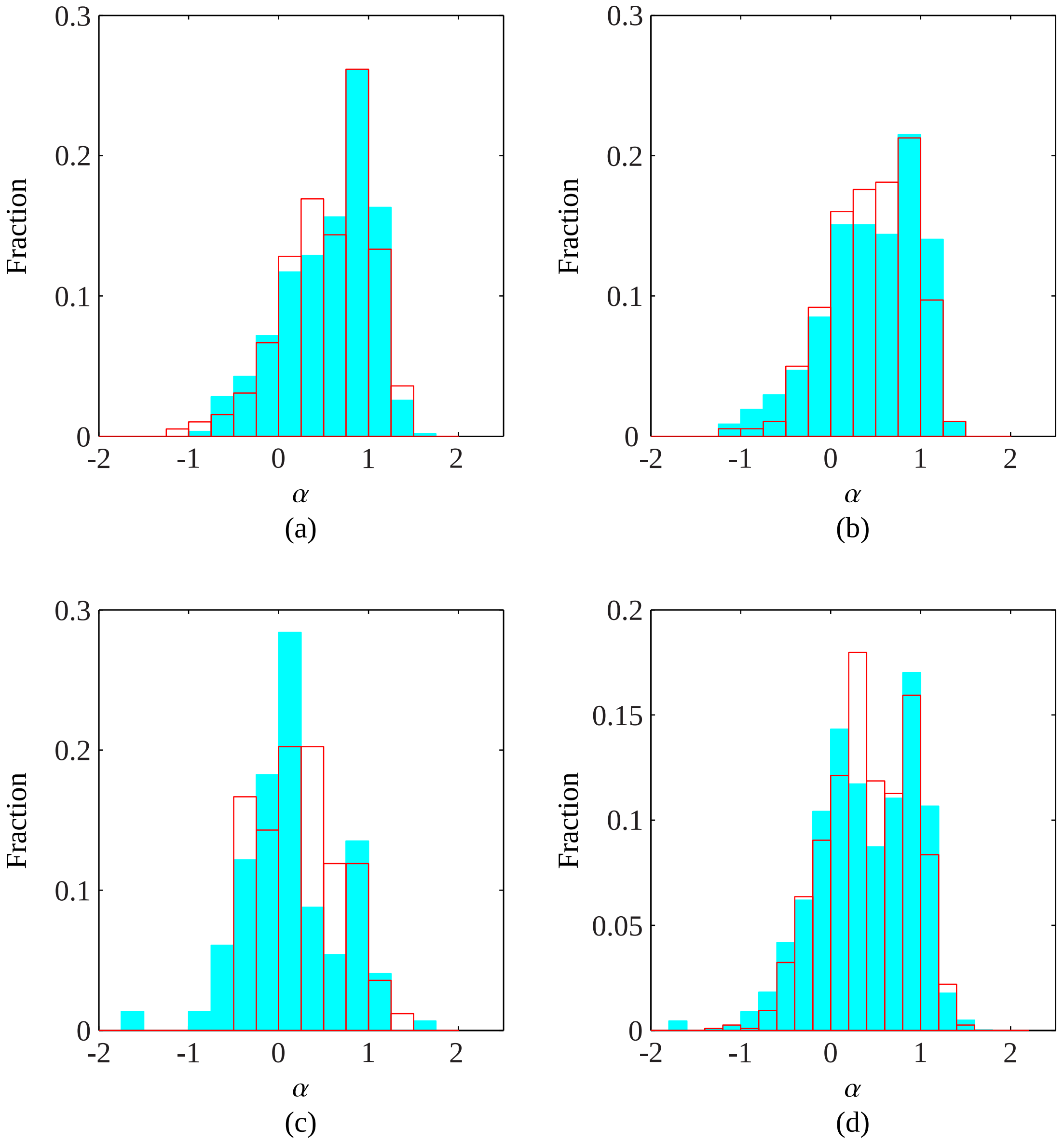

Figure 3.9: 1.4 to 15 GHz spectral index distributions from the AMIGPS (blue) and 9C (red outline) matched catalogues, for flux density ranges (a) $10 \leq S < 25$, (b) $25 \leq S < 100$, (c) $S \geq 100$ mJy and (d) all flux density ranges combined.

Table 3.4: Quantitative criteria for UCHII and HCHII regions from Murphy et al. (2010a).

Class	Size (pc)	Density (cm^{-3})	EM (cm^{-6} pc)	Angular size (Orion)	Angular size (Perseus)
Hyper-compact	≤ 0.03	$\geq 10^6$	$\geq 10^{10}$	$\leq$ 15 arcsec	$\leq$ 3.2 arcsec
Ultra-compact	≤ 0.1	$\geq 10^4$	$\geq 10^7$	$\leq$ 52 arcsec	$\leq$ 11 arcsec
Compact	≤ 0.5	$\geq 5 \times 10^3$	$\geq 10^7$	$\leq$ 4.3 arcmin	$\leq$ 0.88 arcmin
Classical	~ 10	~ 100	$\sim 10^2$	$\sim 1.4^\circ$	$\sim 0.3^\circ$

$$\begin{aligned}\tau_\nu &= 3.014 \times 10^{-2} T_\mathrm{e}^{3/2} \left(\frac{\nu}{\mathrm{GHz}}\right)^{-2} \left\{\ln\left[4.955 \times 10^{-2} \left(\frac{\nu}{\mathrm{GHz}}\right)^{-1}\right] + 1.5 \ln(T_\mathrm{e})\right\} \times \mathrm{EM} \\ &\approx 8.235 \times 10^{-2}\, T_\mathrm{e}^{-1.35} \left(\frac{\nu}{\mathrm{GHz}}\right)^{-2.1} \left(\frac{\mathrm{EM}}{\mathrm{cm}^{-6}\,\mathrm{pc}}\right) \qquad (3.9)\end{aligned}$$

where T_e is the electron temperature in K. The brightness temperature of the source, T_b and corresponding flux density S_ν are then given by

$$\begin{aligned}T_\mathrm{b} &= T_\mathrm{e}\,(1 - \mathrm{e}^{-\tau_\nu}) \\ \left(\frac{S_\nu}{\mathrm{Jy}}\right) &= \frac{2k_B T_\mathrm{b} \nu^2 \Omega \times 10^{26}}{c^2} \qquad (3.10)\end{aligned}$$

where Ω is the source size in steradians. This model has a characteristic spectral shape, with an optically thick region where $\alpha \approx -2$ at lower frequencies, and an optically thin part with $\alpha \approx 0.1$ at higher frequencies. The 'turnover frequency', where $\tau_\nu = 1$, divides the two parts.

Fig. 3.10(a) shows the spectral energy distribution for the different types of HII region given the nominal parameters listed in Table 3.4, a common electron temperature of 10^4 K and scaled to a distance of 10 kpc. It can be seen from Equation 3.9 that the position of the turnover frequency scales approximately as the square root of the emission measure (with a weaker electron temperature dependence); the HCHII regions are expected to still be optically thick at AMI frequencies and may therefore

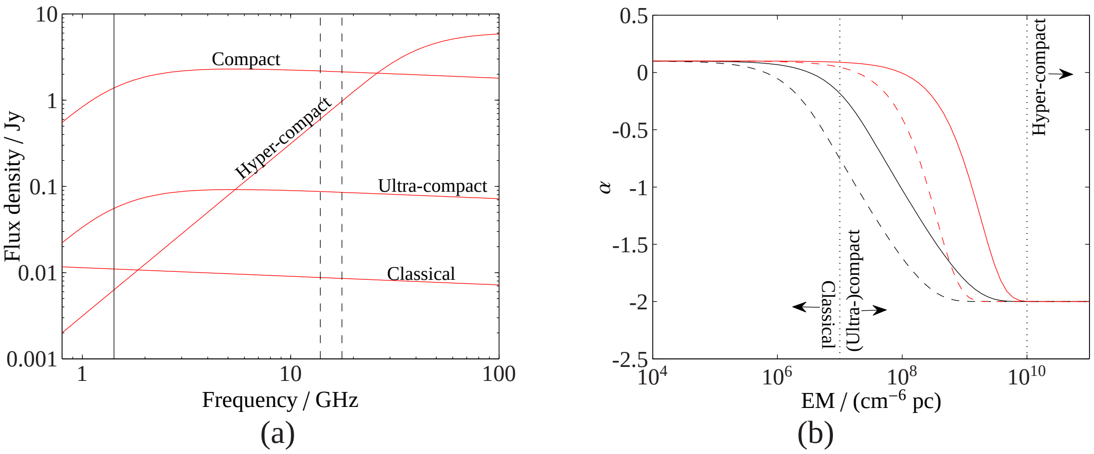

Figure 3.10: (a) SEDs for the types of Hɪɪ region listed in Table 3.4, with a fixed electron temperature of 10^4 K. The vertical solid and dotted lines show the NVSS and AMI frequencies. (b) Expected spectral index between 1.4 and 15.75 GHz (black lines) and between the AMI channel 3 and 8 frequencies (red lines), for an electron temperature of 10^4 K (solid) and 3000 K (dashed), as a function of EM. The vertical solid lines show the division into hyper-, (ultra-)compact and classical regions.

have been missed by surveys at lower frequency, where they will be relatively faint. Fig. 3.10(b) shows the expected 1.4 to 15.75 GHz and AMI channel 3 to 8 spectral indices as a function of EM for two different temperatures. Equation 3.9 assumes a uniform density distribution; in practice, observed SEDs of Hɪɪ regions differ, often showing spectral indices intermediate between the optically thick and thin limits. This can be explained by models with density gradients (Franco et al., 1990) and/or clumpiness along the line of sight (Ignace and Churchwell, 2004).

3.9 Blind candidate selection from the AMIGPS

HCHɪɪ regions will be unresolved to the AMI-LA, and even the maximum angular-size UCHɪɪ regions in the closest star-forming region are expected to be only barely resolved to the LA. The AMIGPS and NVSS correlated catalogues were therefore searched for point-like (to the SA) sources which could have rising spectra, and followup observations were performed with the LA to obtain a more accurate flux density measurement and spectral index over the AMI band. The LA observations, with a resolution of $\simeq 30$ arcsec, were also a better match in resolution to the NVSS catalogue which allowed spatial correlations to be more thoroughly tested and ruled out any biases due to flux loss in the NVSS observations.

It can be seen from Fig. 3.10(b) that the limiting 1.4 to 15.75 GHz spectral index for (H/U)CHII regions is ≈ -0.2. In order to be conservative and account for the 'clumpiness' effect tending to flatten the observed spectrum, objects with $\alpha_{1.4}^{15.75} \leq -0.1$ were selected for. Following up an initial test sample indicated that the 15.75 GHz fluxes could vary by up to $\approx 30\%$ from the AMIGPS catalogue values, whether due to thermal noise, calibration error, or variability, and so to take this into account the spectral index cutoff was extended to $\alpha_{1.4}^{15.75} \leq 0.05$. Multiple matches were dealt with as follows:

- If the spectral index between the summed NVSS flux densities and AMIGPS flux density met the criteria, the object was selected.
- Otherwise, if one match was much closer to the AMIGPS position than the others, this was taken as the 'true' match, and the selection criterion was applied.
- Otherwise, if any of the matches could meet the selection criterion, the spectral index the rest would be required to have was calculated. These were inspected manually, and if plausible (i.e. the potential rising spectrum source was closer than or at roughly the same distance as any other matches, the spectral index for the remainder was physical), selected.

In addition, objects which were resolved to NVSS were inspected manually and excluded if they were obviously part of an extended structure which would be resolved out by the LA. The well-known quasar QSO B2005+40 (Adgie et al., 1975) was also excluded. This resulted in a total of 497 objects to be followed up on the LA.

A further 221 sources classified as point-like in the AMIGPS catalogue were unmatched to any NVSS source and are therefore also potential compact HII region candidates. However, at low SNR the critical angular size required for classification as an extended source increases (see equation 2.2) and a source classified as point-like is more likely to prove to be extended on further observation, in which case the source will be resolved out in NVSS rather than rising-spectrum. Only the nine high significance (SNR $\geq$ 10) unmatched sources were therefore followed up on the LA.

3.9.1 Observations and data reduction

Observations were carried out on the LA between March 2011 and Oct 2012, in 'list observation' mode, in which a set of sources is observed in sequence, passing through the list multiple times and including an interleaved phase calibrator at set intervals. Nearby sources were organised into lists, including a phase calibrator selected from either the VCS catalogue, or from the AMIGPS catalogue itself if a nearer and/or brighter source was available that was not resolved to NVSS. The length of time spent on each source was calculated based on the AMIGPS flux density and the LA sensitivity, to aim for a signal-to-noise level of at least 10 on each channel, and all the sources on the list were passed through at least twice to improve the *uv*-coverage. A small number of sources were subsequently reobserved individually to increase the signal-to-noise ratio.

Reduction is performed as described in previous chapters for pointed observations. Since the amplitude of the LA is not as stable as that of the SA, a secondary amplitude calibration is applied based on the flux density and spectral index of the interleaved phase calibrator source, observed separately on the SA within ten days of the LA observation to avoid variability issues.

The sources are imaged in AIPS, individually from channels 3 to 8 inclusive as well as at an averaged, central frequency. Since the LA is primarily an east–west array, the *uv*-plane is relatively poorly filled for a snapshot observation resulting in a dirty beam with significant sidelobes in the north–south direction; this is illustrated in Fig. 3.11, which shows the *uv*-coverage and a dirty beam for a typical observation. It was found on inspection of the initial CLEANed maps that flux was being transferred from the source to the positions of the sidelobes, resulting in an overall suppression of the flux densities of the sources. An automated algorithm was therefore developed to CLEAN the maps which was found in practice to be successful in deconvolving the dirty beam from the map, as follows:

- the continuum map is CLEANed with no CLEAN box down to the first negative component;

- the AIPS task IMEAN is used to estimate a noise level σ_{rms} over the entire map, by fitting a histogram to the pixel values, discarding outliers;
- the brightest pixel on the map is located and a circular CLEAN box with radius 5 pixels ($\approx$ 0.8× the CLEAN beam FWHM) centred on this pixel is defined;
- the continuum map is re-CLEANed from scratch, with the CLEAN box, to a flux density level of σ_{rms};
- the box is removed and the map is CLEANed further, to a flux density level of $3\sigma_{\mathrm{rms}}$;
- the process is repeated for each of the individual channels, using the CLEAN box defined from the continuum map.

As a final check, the dirty map is also produced for all channels, and all flux densities measured from CLEAN maps are tested for consistency with the corresponding dirty map.

All the maps are primary beam corrected, and corresponding noise maps are produced which are the inverse of the primary beam correction scaled by the noise level measured by IMEAN over the whole CLEAN map. Source-finding is carried out individually over all channel and continuum maps, in a similar manner as described in Section 2.7, at 5σ. To be included in the final result, sources detected on the map are required to be classified as point-like to the LA on the continuum map. Those sources which are resolved to the LA will require more analysis to investigate the effect of flux loss on both the LA and NVSS measured flux densities; this will be addressed in future work (and are not expected to be compact HII regions based on the size criteria anyway). It is known that at lower flux densities a population of extra-galactic sources with rising spectra starts to appear (Whittam et al., 2013); therefore when point-like sources with flux densities much lower than (and clearly not associated with) the original AMIGPS detection are found without NVSS matches, they are also excluded.

For each source, the positional errors along the major and minor axes are estimated as

$$\sigma_{\mathrm{M\ or\ m}} = \frac{\theta_{\mathrm{M\ or\ m}}}{\sqrt{2\ln(2)}\mathrm{SNR}} \tag{3.11}$$

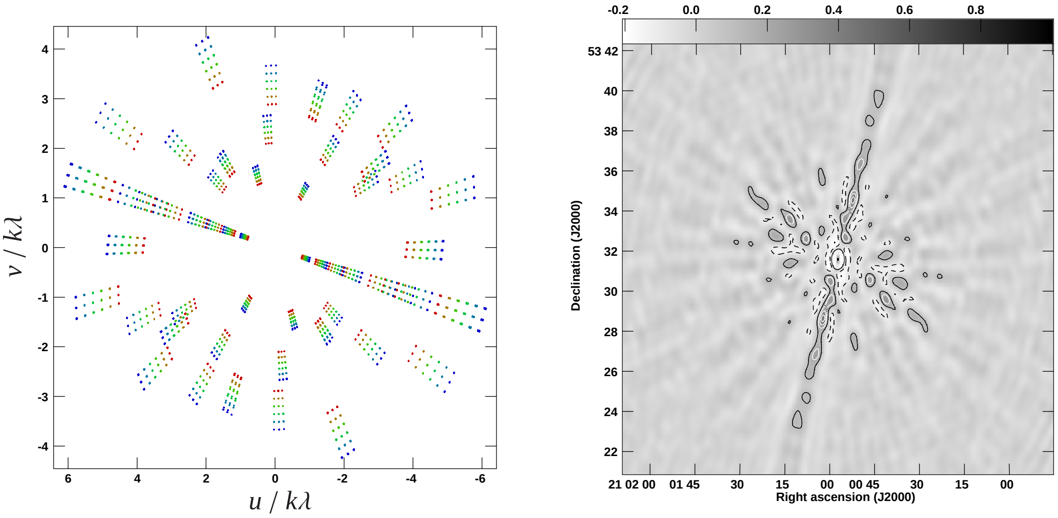

(a) (b)

Figure 3.11: (a) *uv*-coverage, coloured by channel and (b) the dirty beam for a source in a typical LA source list observation. The contours are between ±1 in steps of 0.1; dashed contours are negative. The source has been passed through three times, as evidenced by the three discrete groups of *uv*-points, but since the majority of the points are still roughly in the east-west direction the resulting dirty beam has significant sidelobes (≈ 45% at the most) in the north-south direction.

where $\theta_{\mathrm{M\,or\,m}}$ is the FWHM of the synthesised beam in the major or minor axis direction, and rotated into RA and δ positional errors. The error in the position of the phase calibrator is added in quadrature; this is only significant when the calibrator position has been taken from NVSS.

All sources detected on the map are matched to the closest source within 40 arcsec in the NVSS catalogue, and a 1.4 to 16 GHz spectral index calculated. If a source is detected at $\geq 5\sigma$ on at least three of the channel maps, a spectral index is fitted to the AMI channel flux densities by METROMOD, a Markov-chain Monte Carlo sampling algorithm (Hobson and Baldwin, 2004). Sources without detections on all channels that showed signs of a rising spectrum either from NVSS or over the AMI band were reobserved to improve the signal-to-noise until they were detected on all channels.

3.9.1.1 Unmatched sources

All of the nine high-significance unmatched sources are detected and remain unmatched to any NVSS source. In addition, six of the sources originally matched to an NVSS source were found with the higher resolution of the LA to not have an NVSS match. The NVSS postage stamps for each of the unmatched sources were inspected manually to gauge if flux was present at the position of the AMI detection; in four cases, there was clearly a faint ($1.4 < S < 2.0$ mJy) source present at the position and the peak flux density was entered in the catalogue. In the case of J0210+5954a, the NVSS postage stamp showed flux at the position of the AMI detection which was barely resolved from a nearby, brighter source (see Fig. 3.12). The AIPS task JMFIT was used to fit two Gaussian sources to the map, fixing the positions of both, and obtain an integrated flux estimate at 1.4 GHz for the rising spectrum source.

For the ten remaining unmatched sources, a limiting spectral index is calculated based on the $\approx 90\%$ completeness limit of the NVSS survey, 3 mJy.

3.9.2 Results

Of the 506 sources selected based on their spectrum with respect to NVSS, at least one source meeting the above criteria was detected in the field of the LA observation in 434 cases. In some cases this/these source(s) are not associated with the original AMIGPS detection.

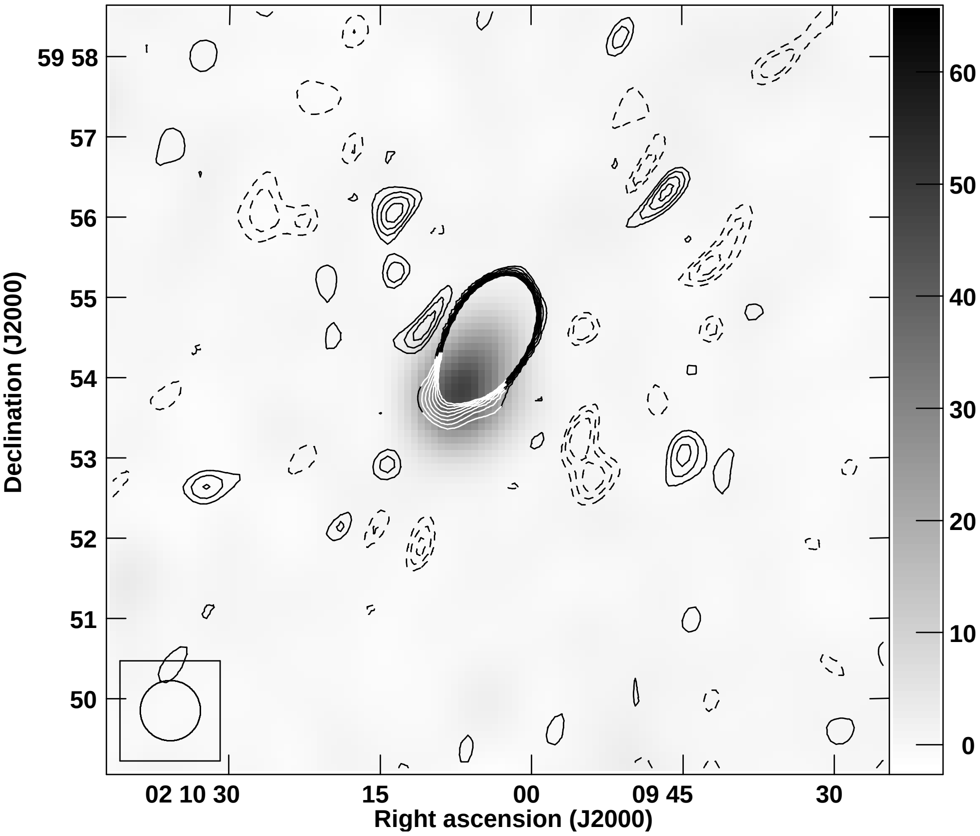

Figure 3.12: AMI-LA contours (not primary-beam-corrected) at ±3 to 10× the r.m.s. noise on the map of 323 μJy, overlaid on NVSS grey-scale, in mJy beam^{-1}. Solid contours are positive; dashed contours are negative. The NVSS beam is shown in the bottom right-hand corner. Flux is clearly present at the position of the AMI source, although barely resolved from the brighter, neighbouring source.

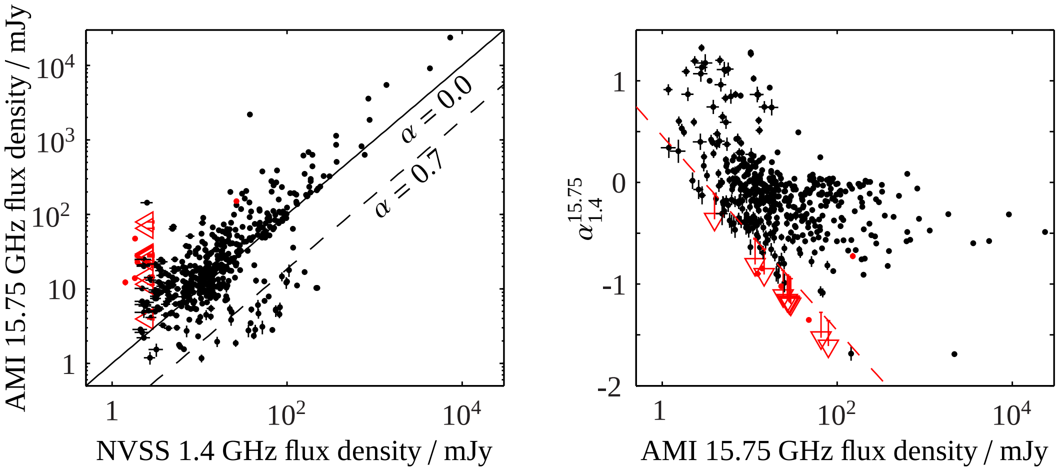

Figure 3.13: AMI continuum vs NVSS flux densities (a) and AMI flux density vs $\alpha_{1.4}^{16}$ (b) for all point-like sources detected in the follow-up fields. The dotted and dashed lines in (a) indicate spectral indices of 0.0 and 0.7 respectively; those sources with $\alpha \sim 0.7$ are likely extra-galactic synchrotron sources appearing in the fields by chance. The dashed red line in (b) shows the NVSS 90% completeness limit. In both plots, red points (upper limits) show values estimated from the NVSS maps (upper limits derived from the $\approx$90% completeness limit of the catalogue) for the sources without matches in the NVSS catalogue.

Fig. 3.13 shows the AMI flux densities for the detected sources vs NVSS flux densities. It is clear that most of the sources have spectral indices $\alpha \leq 0.0$, while a small population of sources with $\alpha \sim 0.7$ is also detected which are likely extra-galactic synchrotron sources appearing in the fields by chance.

3.9.2.1 Spectral indices over the AMI band

Fig. 3.14 shows spectral indices calculated between 1.4 and 15.75 GHz against those calculated over the AMI band. Upper limits are shown for sources without NVSS matches. Based on Fig. 3.10, a comparison between the two spectral indices should be extremely useful for discriminating between types of HII regions – HCHII regions should have both $\alpha_{1.4}^{15.75}$ and $\alpha_{\mathrm{AMI}} = -2$, and a cut of $\alpha_{1.4}^{15.75} < -0.1$ and $\alpha_{\mathrm{AMI}} < +0.1$ should select for (ultra-)compact HII regions. In practice however, there are various issues with the spectral index over the AMI band. Since the frequency lever arm is so short, the errors in α_{AMI} are large, and since the flux density measurements are correlated both between baselines sharing a common antenna and between channels, a small systematic error can completely skew the measured spectral index resulting in ‘catastrophic outliers’. In addition, on the LA since the baselines are longer, more path compensation is required, and attenuation along longer cables must be adjusted for. Since this process is not perfect, larger, frequency-dependent errors in flux density result compared with a similar observation on the SA.

These uncertainties manifest themselves in the lack of correlation shown in Fig. 3.14. It is highly unlikely, for example, that a physical spectrum would be steeply rising between 1.4 and 15.75 GHz with $\alpha \approx -1$, then completely turn over to have $\alpha \approx +1$ between 13 and 18 GHz. I therefore apply only the $\alpha_{1.4}^{15.75}$ criterion, which selects 255 candidate sources as candidate (ultra-)compact H II regions; $\alpha_{\rm AMI}$ is plotted for illustration only in the following plots.

3.9.2.2 Extreme sample

To select a manageable number for initial further analysis, a cut of $\alpha_{1.4}^{15.75} < -0.6$ is applied to select $\approx$ 10% of the most extreme objects. These sources and their NVSS matches are listed in Table 3.5. A SIMBAD, VIZIER and literature search was performed to collate as much ancillary data as possible and attempt to identify these – sources with identifications are discussed individually in the following sections. The VLA Archive Imaging Pilot[1] was also searched for observations of fields containing the sources, and JMFIT was used to fit parameters to the automatically-produced maps. Table 3.6 lists these sources and their fitted parameters.

---

[1] `http://www.aoc.nrao.edu/~vlbacald/avla.shtml`

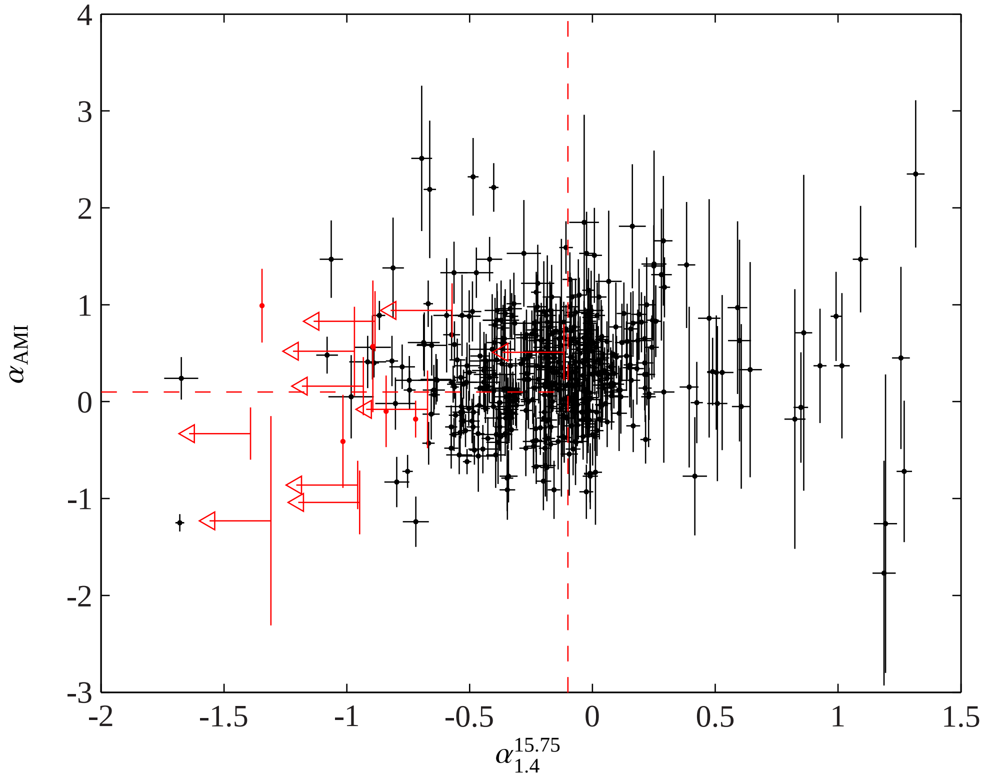

Figure 3.14: Spectral indices calculated between 1.4 and 15.75 GHz vs those calculated over the AMI band. Red points and upper limits are as in Fig. 3.13. The dashed red vertical and horizontal lines show the selection criteria for sources to be compact HII regions.

Table 3.5: AMIGPS sources with $\alpha_{1.4}^{16} < -0.6$. Sources are named for the field they are in detected in, in order of peak flux density (i.e. J0450+5125b is the second-brightest source in the field centred at RA ≈ 04h 50m, δ ≈ 51d 25m; sources without an ‘a’ or ‘b’ were used as calibrators, and their positions taken from NVSS. e_{maj} and e_{min} are the fitted (deconvolved) major and minor axis FWHM. ‘Reference’ refers to the following catalogues for ancillary radio data: (1) NVSS 1.4 GHz (Condon et al., 1998), (2) GB6 5 GHz (Gregory et al., 1996), (3) Effelsberg 2.7 GHz (Fürst et al., 1990), (4) VLBA 8 GHz (Immer et al., 2011), (5) Radio continuum emission from stars (multiple frequencies, Wendker 1995), (6) Radio patrol of the Northern Milky Way (5 GHz, Gregory and Taylor 1986). (*) There is a GB6 source at 49.4 arcsec from J0450+5125b with peak flux density 22 ± 4 mJy which appears, from looking at the maps, to match the AMI-LA source, but it is extended, with size ≈ 8 × 3 arcmin given in the GB6 catalogue. This very large angular size does not seem consistent with the AMIGPS source. Performing a fit on the map myself gives a source size consistent with the beam size; I therefore consider this a point-like source and take its peak flux density.

Name	RA	δ	ΔRA arcsec	$\Delta\delta$ arcsec	S_{16} mJy	ΔS_{16} mJy	α_{AMI}	$\Delta\alpha_{\mathrm{AMI}}$	e_{maj} arcsec	e_{min} arcsec	$\alpha_{1.4}^{16}$	Reference
J0017+5855a	00:17:51.5	+58:55:20	1.1	1.9	47.4	2.6	0.99	0.38	8.5	< 13.8	−1.35	1
J0132+5818a	01:32:08.0	+58:19:02	1.1	1.9	143.7	7.2	0.24	0.22	6.5	1.0	−1.68	1
J0134+6722a	01:34:05.4	+67:22:33	1.2	1.7	13.89	0.77	−0.10	0.37	6.4	< 8.0	−0.84	1
J0155+6525a	01:55:23.3	+65:25:53	1.2	1.6	26.9	1.4	0.16	0.30	7.8	-	< −0.91	
J0158+5900a	01:58:09.3	+59:00:06	1.1	1.6	79.1	4.0	−0.33	0.27	9.6	4.0	< −1.36	
HCHII133.9+1.0a	02:27:03.9	+61:52:25	1.2	1.7	2188	29	−1.25	0.09	8.1	-	−1.69	1
J0210+5954a	02:10:04.3	+59:54:30	1.4	1.8	150.2	7.5	−0.18	0.19	-	-	−0.72	1, 2, 6
J0235+5839a	02:35:11.5	+58:39:49	1.2	2.9	36.7	1.9	−0.13	0.26	7.0	4.1	−0.66	1, 2
J0249+6101a	02:49:54.4	+61:02:08	1.2	1.9	24.7	1.3	−0.83	0.26	8.1	< 7.8	−0.80	1
J0301+5730a	03:01:47.4	+57:30:42	1.5	2.2	14.54	0.94	−0.08	0.40	12.1	< 10.2	< −0.66	
J0314+6024a	03:14:22.1	+60:24:42	1.2	1.9	11.50	0.61	0.94	0.28	7.1	< 4.1	< −0.56	
J0359+5418a	03:59:56.7	+54:18:53	1.6	1.7	14.24	0.76	0.61	0.29	< 6.6	< 2.1	−0.69	1, 2, 6
J0405+5554a	04:05:22.5	+55:54:30	1.6	1.6	24.8	1.3	0.12	0.26	7.5	< 7.5	−0.65	1

Continued on next page

Table 3.5 – continued from previous page

Name	RA	δ	ΔRA	$\Delta\delta$	S_{16}	ΔS_{16}	α_{AMI}	$\Delta\alpha_{\mathrm{AMI}}$	e_{maj}	e_{min}	$\alpha^{16}_{1.4}$	Reference
J0418+4626a	04:18:28.3	+46:26:10	1.4	2.2	55.1	2.9	0.59	0.33	15.5	5.0	–0.69	1, 2
J0430+4937a	04:30:56.0	+49:37:33	1.3	1.7	13.07	0.67	0.23	0.26	2.1	< 5.1	–0.64	1
J0434+5459a	04:34:34.9	+54:59:19	2.5	1.4	20.1	1.1	0.56	0.33	18.9	< 8.8	–0.90	1
J0439+5231a	04:39:40.3	+52:31:18	1.1	1.8	67.0	2.4	0.07	0.15	3.0	< 2.7	–0.65	1, 2
J0442+4407a	04:42:15.8	+44:07:36	1.3	2.3	50.8	2.6	0.36	0.23	13.0	2.9	–0.78	1, 6
J0450+5125b	04:50:04.6	+51:25:21	1.2	1.9	24.0	1.1	0.83	0.31	7.2	3.1	< –0.86	2(*)
J0457+4435a	04:57:44.1	+44:35:52	1.1	1.9	89.8	3.2	0.89	0.15	7.3	3.4	–0.87	1, 2
J0458+4833a	04:58:37.1	+48:33:21	1.2	2.0	17.54	0.93	0.58	0.31	7.6	< 6.2	–0.66	1
J2020+4058	20:20:36.0	+40:57:55	0.6	0.6	390	14	1.01	0.24	11.5	0.9	–0.68	1, 4
J2020+4356a	20:20:07.9	+43:56:45	1.6	2.6	64.2	3.3	1.47	0.40	< 6.8	-	–1.07	1
J2020+4505a	20:20:52.6	+45:06:01	1.2	1.6	65.1	3.3	–1.2	1.1	-	< 7.3	< –1.28	
J2031+4505a	20:31:35.5	+45:05:45	1.1	1.8	163.0	8.3	2.19	0.71	7.3	2.7	–0.67	1, 2, 3
J2032+4039	20:32:45.4	+40:39:38	0.6	0.7	377	19	0.42	0.26	9.9	< 1.7	–0.82	1, 5
J2033+4508a	20:33:46.6	+45:08:41	1.2	1.9	37.7	2.1	2.51	0.75	10.9	6.5	–0.70	1, 2
J2105+4807a	21:05:38.4	+48:07:18	1.4	1.4	77.0	3.9	1.38	0.52	8.2	5.0	–0.82	1, 2
J2108+5405a	21:08:27.5	+54:05:28	1.1	1.8	28.4	1.5	–0.86	0.25	2.5	< 4.2	< –0.93	
J2121+4646a	21:21:51.2	+46:46:58	1.2	1.9	68.3	2.5	0.48	0.19	5.9	-	–1.09	1, 2
J2132+4435	21:32:30.9	+44:35:47	0.6	0.7	207	10	0.12	0.20	6.5	1.4	–0.75	1, 2
J2132+5316a	21:32:55.9	+53:16:26	1.2	2.3	24.8	1.3	0.05	0.43	18.0	6.2	–0.99	1
J2203+5824a	22:03:36.8	+58:24:15	1.5	1.9	21.1	1.1	0.41	0.27	8.8	< 5.3	–0.92	1
J2226+5336	22:26:21.2	+53:36:17	0.8	0.9	199.7	7.1	0.40	0.15	5.0	2.6	–0.91	1, 2
J2239+5334a	22:39:44.9	+53:34:37	1.5	2.1	10.17	0.41	0.22	0.22	7.9	-	–0.64	1
J2300+5656a	23:00:04.8	+56:56:43	1.1	1.7	27.8	1.5	–1.04	0.33	10.4	< 9.3	< –0.93	5
J2308+5611a	23:08:09.3	+56:11:31	1.3	2.2	22.8	1.4	–0.41	0.48	9.9	9.1	–1.02	1

Continued on next page

Table 3.5 – continued from previous page

Name	RA	δ	ΔRA	$\Delta\delta$	S_{16}	ΔS_{16}	α_{AMI}	$\Delta\alpha_{\mathrm{AMI}}$	e_{maj}	e_{min}	$\alpha_{1.4}^{16}$	Reference
J2308+5748a	23:08:55.9	+57:48:45	1.3	2.2	29.3	1.8	0.52	0.46	6.0	< 14.9	< -0.95	2
J2314+5610a	23:14:00.4	+56:10:23	1.3	2.1	132.7	6.7	-0.43	0.22	7.6	0.3	-0.67	1, 2
J2322+6153a	23:22:42.6	+61:53:11	1.1	2.0	189.1	6.8	-0.72	0.17	21.7	< 20.9	-0.76	1, 2, 6
J2346+5701a	23:46:26.2	+57:00:54	1.3	2.0	19.4	1.0	-1.24	0.26	6.5	-	-0.72	1
J2354+5824a	23:54:42.9	+58:24:18	1.3	2.1	21.6	1.1	-0.02	0.27	7.9	< 8.3	-0.81	1
J2354+5929b	23:53:58.6	+59:29:01	2.2	3.2	12.3	1.2	0.57	0.68	12.2	8.6	-0.90	1
J2357+6643a	23:57:55.9	+66:43:29	1.3	2.2	23.08	0.93	0.22	0.25	12.3	< 10.3	-0.75	1

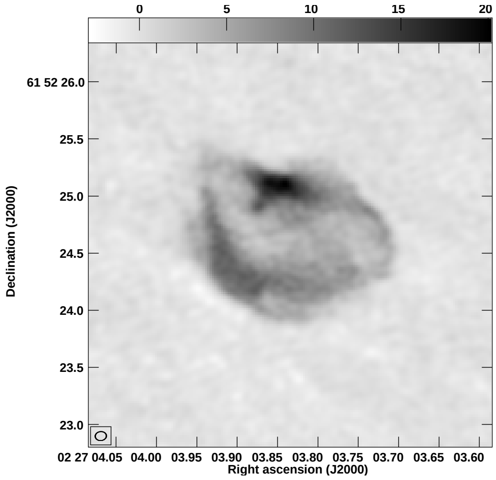

Figure 3.15: A VLA 22 GHz image ($\approx$ 3.5 $\times$ 3.5 arcsec) of W3(OH) at 0.1 arcsec resolution. The grey-scale is in mJy beam^{-1} and the synthesised beam is shown in the bottom left-hand corner.

3.9.2.3 Sources with identifications in the literature

Compact HII regions

HCHII133.9+1.0a at RA $\approx$ 02h 27m, δ $\approx$ 61d 52m is a well-known UCHII region, (W3(OH), Mezger et al. 1967, Harris and Scott 1976), which has been observed over a long period of time on the LA as part of a different project (it is the source with the smallest error on $\alpha_{\rm AMI}$ in Fig. 3.14). It has been studied at many frequencies and at very high angular resolution with many instruments (e.g. Hirsch et al. 2012, Dzib et al. 2013); there is little that the LA observation can add to the information available in the literature. Fig. 3.15 shows a high-resolution VLA image of the source, showing its shell-like structure.

J2031+4505a is at $\approx$ 1.5 arcsec distance from a compact HII region identified in the Red MSX Source (RMS) survey, which aims to identify massive young stellar objects (MYSOs) by observing sources selected from the Midcourse Space Experiment (MSX) survey both in the radio continuum, using both archival data and new follow-up observations with the VLA at 6 cm with $\approx$ 1 to 2 arcsec resolution (Urquhart et al., 2009), and in ^{13}CO (Urquhart et al., 2008). This particular source, [UHP2009] VLA G083.0934+03.2720, is detected both at 6 cm and in CO, and is classified as an HII

Table 3.6: Sources with data available from the VLA Archive Imaging Pilot website. S and T stand for serendipitous and targeted observation. When more than one observation is available at a given frequency, an average is taken of the flux densities and the position and source size parameters are given from the highest resolution observation. The 'resolution' is the CLEAN beam major axis FWHM. There are also observations available of J2032+4039, J2132+4435, J2300+5656a and HCHII133.9+1.0a; I do not list these here since the sources are significantly resolved in many of the observations (and there are many flux density estimates available in the literature; see Section 3.9.2.3 for more detail).

AMI-LA source	Number	S/T	Freq. (GHz)	Resolution (arcsec)	Year	RA	δ	ΔRA (arcsec)	$\Delta\delta$ (arcsec)
J0155+6525a	1	S	4.86	5.94	1984	01:55:23.74	65:25:52.2	0.4	0.2
J0359+5418a	2	S	1.39, 1.47	15.9, 51.2	1992, 1999	03:59:56.42	54:18:52.3	0.2	0.2
J2020+4058	1	T	8.44	0.73	1991	20:20:36.1389	40:57:53.6352	0.0000	0.0003
J2020+4356a	1	T	1.67	4.8	1991	20:20:07.89	43:56:47.5	0.4	0.4
	1	T	4.99	0.50	1991	20:20:07.9967	43:56:46.4858	0.00000	0.00005
	22	S	1.43 – 1.66	12.8 – 53.9	1986 – 2004	20:20:08.03	43:56:45.0	0.2	0.2
J2020+4505a	1	S	1.51	49.1	1995	20:20:53	45:05:47	17	16

AMI-LA source	S_{pk} (mJy)	ΔS_{pk} (mJy)	S_{int} (mJy)	ΔS_{int} (arcsec)	e_{maj} (arcsec)	e_{min} (°)	e_{θ}	Notes
J0155+6525a	2.0	0.2	2.4	0.5	5.4	-	61.4	Source undetected in NVSS; $\alpha^{16}_{4.86} = -2.20 \pm 0.09$
J0359+5418a	3.30	0.09	4.3	0.2	9.7	5.7	66.4	
J2020+4058	85.5	0.1	88.8	0.2	0.16	0.083	37.7	
	8.1	1.3	16.1	3.7	4.1	1.4	163.6	Snapshot observation with highly elliptical synthesised beam; source properties poorly constrained
J2020+4356a	87.69	0.02	87.95	0.04	0.025	0.019	38.1	
	8.85	0.04	11.08	0.08	7.5	< 3.1	122.4	
J2020+4505a	3.3	1.4	13.5	7.1	83.2	76.4	72.8	Source located between two brighter sources; poorly detected. Undetected in NVSS, $\alpha^{16}_{1.5} = -1.3 \pm 0.2$

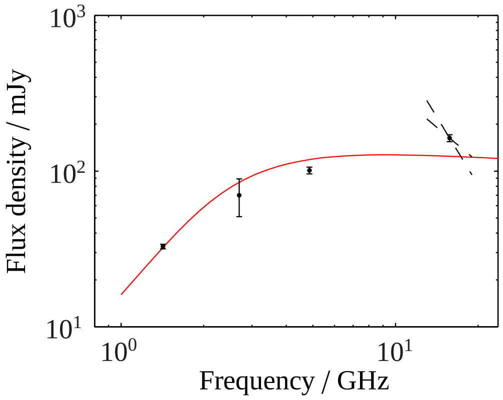

Figure 3.16: A fit to the radio spectrum of J2031+4505a, with EM $\approx 3.6 \times 10^7$ cm^{-6} pc and electron temperature $\approx 1.1 \times 10^4$ K. Note that the error on the 5 GHz point has been increased to 5%. The $\pm 1\sigma$ boundaries on the spectral index over the AMI band are also shown with black, dotted lines.

region. Its distance is calculated as 3.4 kpc from the CO data, and its size as 1.8×1.0 arcsec from the radio continuum data, giving it a physical size of ≈ 0.02 pc and putting it in the hyper-compact category. A fit to the radio data points (NVSS, VLA 6 cm, and AMI-LA plus an 11 cm data point from Fürst et al. 1990) with fixed size gives EM $= (3.6 \pm 0.1) \times 10^7$ cm^{-6} pc and electron temperature $= (1.09 \pm 0.04) \times 10^4$ K, also placing it in the hyper-compact category, although as Fig. 3.16 shows the simple model does not provide a particularly good fit to the spectrum.

Radio stars

J2032+4039 is associated with the well-studied emission-line star, MWC 349A (see, e.g. Gvaramadze and Menten 2012), which has a subarcsecond-scale bipolar radio nebula which has been imaged at very high angular resolution with the VLA (Fig. 3.17 shows a 44 GHz image at 0.04 arcsec resolution from the VLA Imaging Archive), as well as a more recently discovered arcminute-scale infrared nebula. Fig. 3.17 also shows the radio SED for MWC 349A, with points taken from Wendker (1995) plus the AMI-LA point and $\alpha_{\rm AMI}$ in red; the AMI point is consistent with the other data but can add little to the overall picture. This source appears to have been misclassified as a compact HII region by Giveon et al. (2005).

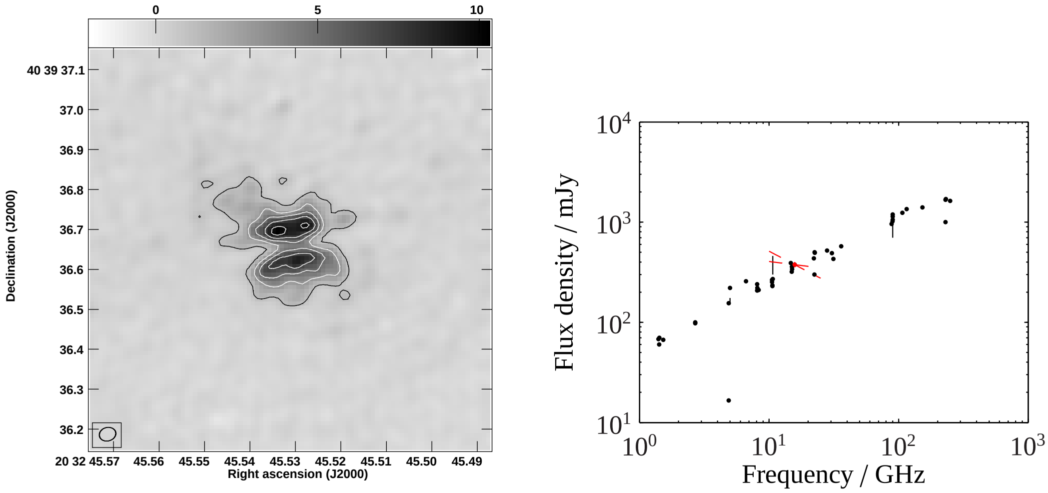

(a) (b)

Figure 3.17: A VLA 44 GHz image (≈ 0.5×0.5 arcsec) of the radio nebula surrounding MWC 349A at 0.04 arcsec resolution (a). Contour levels are at ±10, 30, 50, 70, 90% of the peak flux density of the image, and the grey-scale is in mJy beam^{-1}. The synthesised beam is shown in the bottom left-hand corner. (b) shows the radio spectrum of MWC 349A, black points taken from Wendker (1995) and the AMI-LA point with $\pm 1\sigma$ boundaries on the spectral index over the AMI band shown in red.

J2300+5656a is 2.6 arcsec from the radio star V* V509 Cas (also known as HR 8752). This yellow hypergiant has a stellar wind which is ionised by a hot companion, resulting in partially optically thick free-free radio emission (Piters et al., 1988). The spectrum of J2300+5656a is shown in Fig. 3.18 (points from Wendker 1995); the AMI-LA point is in good agreement with the other data.

Planetary nebulae

J2033+4508a is at 1.5 arcsec distance from MSX6C G083.3609+02.9902, a source which was also followed up at 6 cm and in ^{13}CO as part of the RMS survey. Its null-detection in ^{13}CO caused it to be classified as a planetary nebula. The source has also been observed in H_α (Viironen et al., 2009) and given a preliminary classification as a likely planetary nebula. It is not resolved enough either by the RMS VLA observation or in H_α to detect any structure. Siódmiak and Tylenda (2001) give a simple model for the radio continuum flux densities of planetary nebulae, assuming the nebula is made

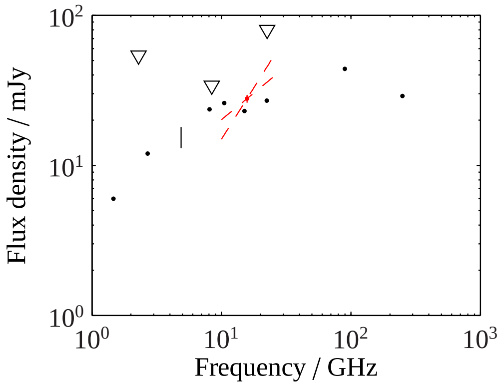

Figure 3.18: The radio spectrum of J2300+5656a from Wendker (1995) (black points). Upper limits are shown as downward-pointing triangles. The AMI-LA flux density and $\pm1\sigma$ bounds on the spectrum over the AMI band are shown in red.

up of some dense and opaque regions characterised by optical thickness τ_ν plus some thinner regions having optical thickness $\epsilon\tau_\nu$, taking up solid angles $\xi\Omega$ and $(1-\xi)\Omega$ respectively, where Ω is the solid angle of the nebula as a whole:

$$\begin{aligned} S_\nu(\mathrm{Jy}) &= \frac{2\times10^{26}\,\nu^2 k_B T_e}{c^2}\left[(1-\mathrm{e}^{-\tau_\nu})\,\xi\Omega + (1-\mathrm{e}^{\epsilon\tau_\nu})\,(1-\xi)\,\Omega\right] \\ \tau_\nu &\approx \tau_0\,(\nu/\nu_0)^{-2.1} \end{aligned} \tag{3.12}$$

where k_B is the Boltzmann constant, T_e is the (common) electron temperature and τ_0 is the optical thickness at a reference frequency, ν_0. Adopting their overall best-fit $\xi = 0.27$ and $\epsilon = 0.19$, taking the size from the RMS survey, and fitting for T_e and τ_0 gives best-fit values of $T_\mathrm{e} = (1.1 \pm 0.1) \times 10^4\,\mathrm{K}$, $\tau_0 = 0.61 \pm 0.08$; the fit is plotted in Fig. 3.19. There is some indication of disagreement between the spectrum fitted over the AMI band and the model, but higher-frequency data points would be required to confirm this due to the unreliability of the spectral index measurement.

J2132+4435 is the well-studied young planetary nebula IC 5117 (see, e.g. Sahai et al. 2011). It has also been observed at 30 GHz with OCRA-p (Pazderska et al., 2009) to test for spinning dust emission; the AMI-LA data point supports the OCRA-p conclusion that there is no evidence for spinning dust emission. Fitting the model given in Equation 3.12 to the data points gives $T_e = (1.01\pm0.03)\times10^4\,\mathrm{K}$, $\tau_0 = 0.025\pm0.001$; the spectrum fitted over the AMI band agrees well with the model. Fig. 3.20 shows an

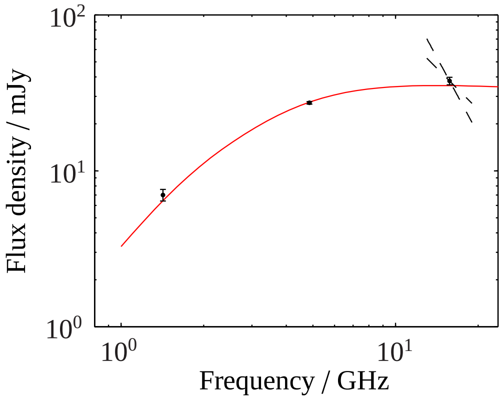

Figure 3.19: A fit to the radio spectrum of J2033+4508 using the model given in Equation 3.12. Also shown are the $\alpha_{\rm AMI} \pm 1\sigma$ bounds; there is some indication that the spectrum is falling off faster than expected from the model, but higher frequency data-points would be required to confirm this due to the unreliability of the spectral index measurement.

HST image of the nebula and the model fit with the data points.

3.9.2.4 Unidentified sources with other associations

In the following, a source lying $< 3\sqrt{\sigma^2_{\rm AMI} + \sigma^2_{\rm Other}}$ from the AMI-LA position (where $\sigma_{\rm AMI/Other}$ are the appropriate positional errors), is considered to be a match.

X-ray associations

Seven sources have X-ray sources nearby or have been included in catalogues of radio/X-ray associations; these are listed in Table. 3.7. Where an AMI-LA source has a match in more than one X-ray catalogue, the closest match is given as the associated X-ray source.

J0359+5418a is also detected in Gregory and Taylor (1986), a 6 cm survey of the Galactic plane searching for variability, as GT 0356+541 and is classified as non-variable both in the short- and long-term. This decreases the likelihood of the source being a quasar.

J2020+4058 was also detected at 8 GHz with the VLBA (Immer et al., 2011) and given a compactness grade of D (where A is most compact, and F is least compact). It has also been observed at 8 GHz with the VLA at 0.7 arcsec resolution (see Table 3.6).

Table 3.7: Sources with X-ray associations. References refer to: (1) Watson et al. (2009), (2) D'Elia et al. (2013), (3) Flesch (2010), (4) Combi et al. (2011), (5) Combi et al. (2008), (6) ROSAT Consortium (2000), (7) Angelini et al. (2000), (8) Brinkmann et al. (1997), (9) Laurent-Muehleisen et al. (1997).

AMI-LA source	X-ray source	Sep (arcsec)	Sep (σ)	Instrument	Ref.	Other information
J0132+5818a	2XMMi J013207.5+581857	5.3	2.4	XMM-Newton	1	
J0134+6722a	1SWXRT J013404.5+672231	5.3	1.0	Swift-XRT	2	
J0359+5418a	2XMM J035956.3+541854	3.9	1.5	XMM-Newton	1	Pr(Gal) = 18%, Pr(star) = 30%, Pr(err) = 52% (3); microquasar candidate (5); also in 2, 4, 6, 7
J2020+4058	2XMM J202036.3+405753	4.3	1.3	XMM-Newton	1	Microquasar candidate (5); also in 4
J2020+4356a	1SWXRT J202008.1+435647	4.0	0.6	Swift-XRT	2	ROSAT-detected quasar (8, 9)
J2020+4505a	1WGA J2020.9+4506	36.5	1.2	ROSAT	7	Source within bright background
J2354+5824a	2RXP J235443.4+582420	4.6	0.3	ROSAT	6	Pr(QSO) = 1%, Pr(Gal) = 46%, Pr(star) = 1%, Pr(err) = 52% (3); also in 7

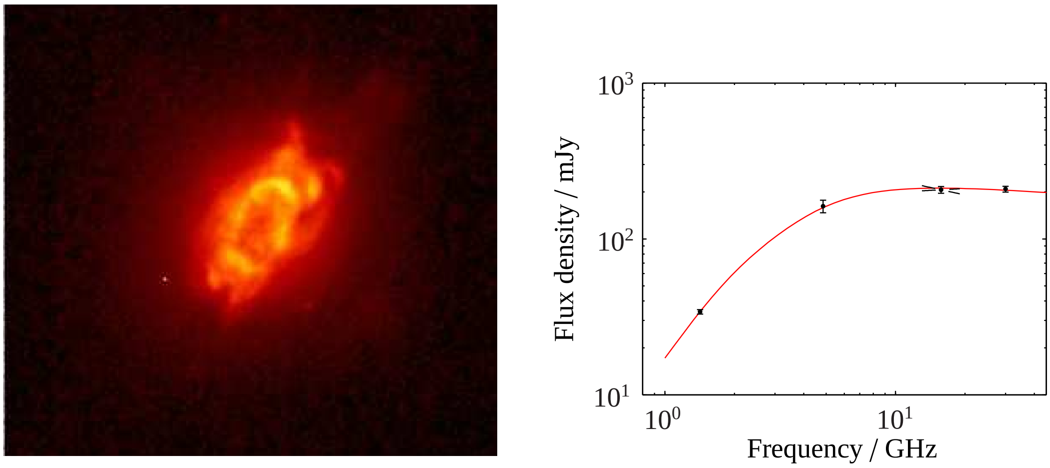

(a) (b)

Figure 3.20: (a) HST H_α image of IC 5117 (≈ 9 arcsec along the horizontal axis), processed to enhance sharp structures, in false-colour (from Sahai et al. 2011). (b) shows a fit to the radio spectrum of IC 5117 using the model given in Equation 3.12. Also shown are the $\alpha_{\text{AMI}} \pm 1\sigma$ bounds, which show good agreement with the model.

Its radio spectrum (Fig. 3.22) does not appear to be consistent with that of an HII region. It is likely that this source is extra-galactic.

J2020+4356a has targeted VLA observations in the imaging archive at 1.4 and 5 GHz, and is in the field of view of 22 observations of another source at 1.43 – 1.66 GHz. The serendipitous observations occur over a long period of time and it is therefore possible to assess possible variability of the source; there is some evidence for variability at 1.4 GHz (see Fig. 3.21), which might be expected if the source is a quasar.

The nature of the other X-ray sources is unclear without further data. Higher angular resolution radio observations will help to distinguish between Galactic and extra-galactic objects. Some Galactic objects are expected to have associated X-ray emission, including YSOs (see, e.g. Forbrich and Wolk 2013), so associated X-ray emission does not exclude these sources from being Galactic.

IRAS matches

Compact HII regions are expected to emit strongly in the far-mid infrared range due to thermal dust emission; these sources might therefore be expected to have matches

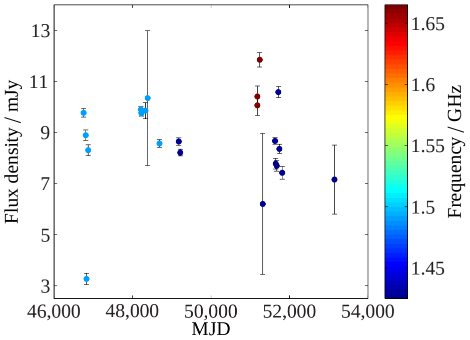

Figure 3.21: Flux densities of J2020+4356a, measured from serendipitous VLA observations in the imaging archive at ≈ 1.4 GHz between 1986 and 2004. No correction has been attempted for the slightly different frequencies, and the errors shown are thermal errors measured from the maps (no calibration error has been added). There is some evidence for variability, but the uncertainties in the errors make it difficult to be sure.

in the IRAS Point Source Catalogue (Helou and Walker, 1988). In fact, only seven of the sources do. Four of these are identified sources (W3(OH), MWC 349A, IC 5117 and V* V509 Cas); the other three are J0249+6101a, J2239+5334a and J2354+5929b. This may be due to the resolution mismatch between IRAS (≈ 4 arcmin at 100 μm), and the AMI-LA.

J0249+6101a and J2354+5929b are 4 and 27 arcsec from ^{12}CO emission associated with IRAS 02459+6049 and IRAS 23514+5912, respectively (Kerton and Brunt, 2003). In both cases, the CO emission is located closer to the AMI-LA source than the original IRAS source. The resolution of the CO survey is 45 arcsec. J2239+5334a is located outside of the CO survey area.

MSX matches

The Midcourse Space eXperiment (MSX) surveyed the Galactic plane between $|b| < 5^\circ$ at ≈ 18 arcsec resolution, in 5 spectral bands between 4 and 25 μm (Price et al., 2001). The higher resolution and sensitivity of the survey compared to IRAS mean that it should be ideal for matching with the AMI-LA sources. However, again only five sources have matches – the two that are part of the RMS survey (J2031+4505a, J2033+4508a); W3(OH) and V* V509 Cas; and only one (J0249+6101a) that is unidentified. From visual inspection of the maps, it is clear that MWC 349A is also detected, with a positional offset of 3.4σ, slightly outside the matching radius. IC 5117 is just outside the survey area at $b = -5.1°$.

There is an MSX source at 28 arcsec ($\approx 7\sigma$) from J2354+5929b, which appeared to have an IRAS and CO association, making it a good compact Hɪɪ region candidate. The IRAS and CO sources are closer to the MSX position than the AMI-LA position, and sources are detected in WISE and 2MASS at 1.5 arcsec separation from the MSX position. The source has a match in the CGPS point source catalogue (Russ Taylor, private communication; it was undetected in NVSS) at 7 arcsec from the LA position, confirming the position of the radio source; this may therefore be a spurious association.

The lack of detection of the other sources does not appear to be due to confusion or the presence of foreground diffuse sources. Fig. 3.23 shows spectra from radio to FIR for all the sources, with the MSX 90% completeness limits shown as upper limits (Egan et al., 2003). From the overlap between the WISE and MSX bands, it seems that the MSX sensitivity may be insufficient to detect these sources (see next section).

High-resolution NIR-MIR and optical matches

Several newer, higher resolution and sensitivity NIR and MIR surveys are now available – WISE (Wright et al., 2010) with resolution 6.1, 6.4, 6.5, and 12.0 arcsec at 3.4, 4.6, 12, and 22 μm; 2MASS (Skrutskie et al., 2006) with resolution ≈ 2 arcsec at J (1.25 μm), H (1.65μm) and K_s (2.16μm); and UKIDSS (Lucas et al., 2008) (at $\delta < +60°$ and $|b| < 5.0°$) at $\lessapprox 0.8$ arcsec resolution in J, H and K bands. In addition, since two of the identified sources are radio stars, it is important to investigate whether any more could be associated with stars. The Naval Observatory Merged Astrometric Dataset (NOMAD, Zacharias et al. 2004) was therefore searched for positional coincidences.

All of these catalogues are at higher resolution than the AMI-LA data, and also have a high density of sources; it is therefore important to take into consideration the probability of random spatial coincidences. For each AMI-LA source, the local density of IR/optical sources within a 1° radius is therefore calculated, and the number of chance associations expected within a circular area with radius given by the AMI-IR/optical source separation is estimated and multiplied by $\sqrt{N}$, where N is the number of sources, to account for the 'look elsewhere' effect. These matches are summarised in Table 3.8; it is clear that in most cases higher positional accuracy is required to be confident of the matches.

3.9.2.5 Radio SEDs for unidentified sources

Most of the unidentified sources have some matches at lower frequency; if more than two data points are available, their spectra with a model fit when appropriate are plotted in Fig. 3.22. The model fits are fairly unconstrained in most cases since there are few data points and the source size is not known; the model parameters are not reported.

The spectra all (with the exception of J2020+4058, as mentioned previously) look consistent with free-free emission, with a turnover frequency either just before or after 16 GHz. It is notable that the sources with turnover frequency $>$ 16 GHz do not appear to be well-fitted by the model; as mentioned in Section 3.8, this is consistent with other results for HCHII regions where a model with a density gradient is required to fit the data points (e.g. Lizano 2008). For these sources, a simple power-law fit is plotted for comparison.

3.9.2.6 Radio to FIR spectra for all sources

Fig. 3.23 shows spectra between the radio and FIR for all sources, assuming the matches with the high-resolution IR surveys are correct. Upper limits are shown as downward-pointing triangles where a source was not detected in all bands in an IR survey. 90% completeness estimates are also shown for the sources with no MSX matches.

Table 3.8: Summary of matches with high-resolution IR and optical catalogues. ‘Sep’ is the separation between the AMI-LA and IR/optical position in arcsec; $N_{\rm exp}$ is the number of sources expected to fall in a circular area with radius = Sep by chance, given the density of sources within a 1° radius of the position. In the case of UKIDSS $N_{\rm exp}$ is adjusted for the uneven coverage of the survey; N/A indicates a position not covered by the UKIDSS GPS.

Source	WISE			2MASS			UKIDSS GPS			NOMAD		
	ID	Sep	$N_{\rm exp}$	ID	Sep	$N_{\rm exp}$	ID	Sep	$N_{\rm exp}$	ID	Sep	$N_{\rm exp}$
J0017+5855a							N/A					
J0132+5818a	J013207.66+581857.3	5.1	0.9				N/A			1483-0066784	6.3	3.1
J0134+6722a	J013405.86+672236.4	4.3	0.7				N/A			1573-0040680	3.7	1.0
J0155+6525a	J015523.32+652552.7	0.30	0.003	01552308+6525536	1.6	0.1	N/A			1554-0048137	1.7	0.2
J0158+5900a							N/A					
J0210+5954a	J021004.32+595430.3	0.60	0.01	02100488+5954341	6.1	1.5	N/A			1499-0078715	6.2	2.5
HCHII133.9+1.0a	J022704.19+615226.4	2.7	0.2	02270391+6152255	0.85	0.03	N/A			1518-0078059	0.85	0.04
J0235+5839a							N/A					
J0249+6101a	J024954.64+610208.1	2.0	0.1	02495443+6102089	1.1	0.05	N/A			1510-0092918	0.4	0.01
J0301+5730a	J030146.98+573039.2	4.2	0.6	03014697+5730388	4.5	0.9	N/A			1475-0128376	4.4	1.3
J0314+6024a							N/A					
J0359+5418a	J035956.63+541852.7	0.94	0.03	03595651+5418586	5.7	1.1	N/A			1443-0121280	4.3	0.9
J0405+5554a	J040522.41+555429.8	0.60	0.01				N/A					
J0418+4626a							N/A					
J0430+4937a	J043056.05+493733.9	0.71	0.02				N/A					
J0434+5459a	J043434.97+545914.8	4.4	0.7				N/A					
J0439+5231a							N/A					
J0442+4407a	J044215.69+440736.5	0.68	0.02				J044215.70+440736.5	0.62	0.02			
J0450+5125b	J045004.35+512519.4	2.8	0.3				N/A					
J0457+4435a	J045744.09+443553.1	0.88	0.03				J045744.06+443553.6	1.4	0.1			
J0458+4833a	J045837.20+483323.3	2.5	0.2				N/A			1385-0134701	1.6	0.2
J2020+4356a							N/A					
J2020+4058	J202036.18+405753.9	2.1	0.1				J202036.13+405753.7	1.7	0.8			
J2020+4505a	J202052.58+450558.9	1.7	0.1				N/A					
J2031+4505a	J203135.45+450545.8	0.98	0.03	20313550+4505465	1.6	0.2	N/A			1350-0387830	1.6	0.2
J2032+4039				20324553+4039366	2.7	0.5	J203245.49+403939.0	2.0	0.8	1306-0410333	2.2	0.4
J2033+4508a	J203346.48+450840.0	1.6	0.1	20334647+4508401	1.6	0.2	N/A			1351-0390145	1.1	0.1
J2105+4807a	J210538.31+480717.6	0.86	0.03				J210538.31+480717.5	0.8	0.2			
J2108+5405a	J210827.44+540531.3	3.9	0.5	21082716+5405261	3.2	0.5	N/A			1440-0355777	3.2	0.7
J2121+4646a							N/A					
J2132+4435	J213230.95+443547.6	0.30	0.003	21323096+4435475	0.3	0.006	N/A			1345-0460852	1.7	0.3
J2132+5316a				21325581+5316236	2.3	0.4	J213255.79+531623.7	2.3	1.2	1432-0428281	2.3	0.5
J2203+5824a	J220336.39+582414.7	3.5	0.4	22033634+5824135	4.1	1.0	N/A			1484-0358840	3.7	1.2
J2226+5336	J222621.15+533617.7	0.78	0.03				N/A			1436-0421880	0.90	0.09
J2239+5334a	J223944.61+533440.5	4.6	0.8				N/A					
J2300+5656a	J230005.12+565643.1	2.7	0.3	23000509+5656433	2.6	0.3	N/A			1469-0485179	2.6	0.6
J2308+5611a	J230810.11+561128.1	7.0	1.7	23080905+5611260	5.2	1.2	N/A			1461-0463944	4.4	1.5
J2308+5748a				23085599+5748461	1.6	0.1	N/A			1478-0531298	1.7	0.3
J2314+5610a	J231400.14+561021.3	2.6	0.2	23135983+5610219	4.9	1.0	N/A			1461-0467833	4.8	1.9
J2322+6153a							N/A					
J2346+5701a	J234625.93+570053.5	2.2	0.2	23462592+5700538	2.2	0.2	N/A			1470-0526444	2.4	0.5
J2354+5929b				23535878+5928501	10.8	4.8	N/A			1494-0406590	10.7	8.5
J2354+5824a	J235442.84+582416.7	1.0	0.04	23544285+5824162	1.4	0.08	N/A			1484-0435107	0.96	0.08
J2357+6643a	J235755.67+664334.2	5.4	0.8	23575547+6643354	6.9	1.6	N/A			1567-0275883	6.9	2.7

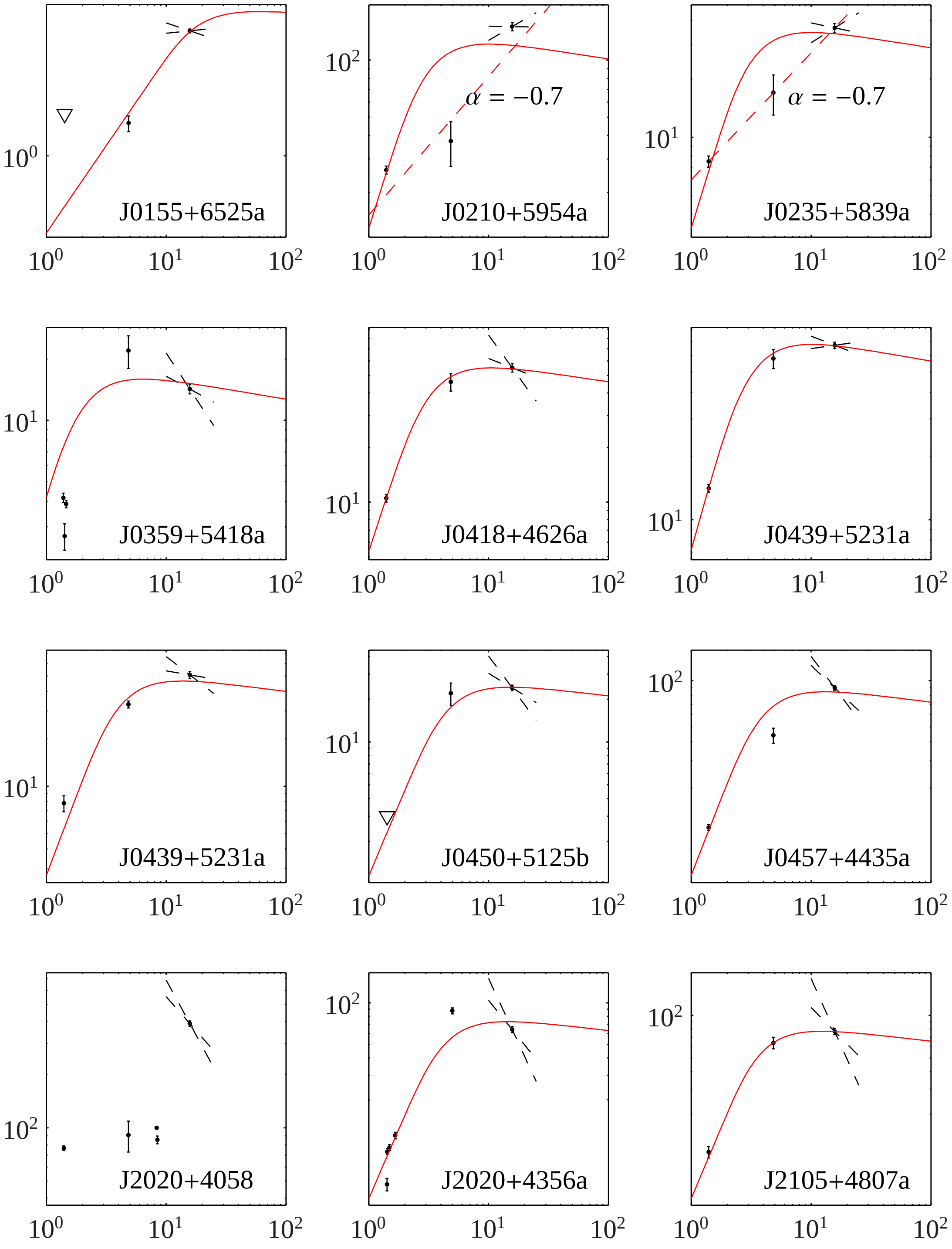

Figure 3.22: Data and model fits (where appropriate) for unidentified sources with more than two available radio flux densities. The *x*-axes are frequency in GHz, and the *y*-axes are flux density, in mJy.

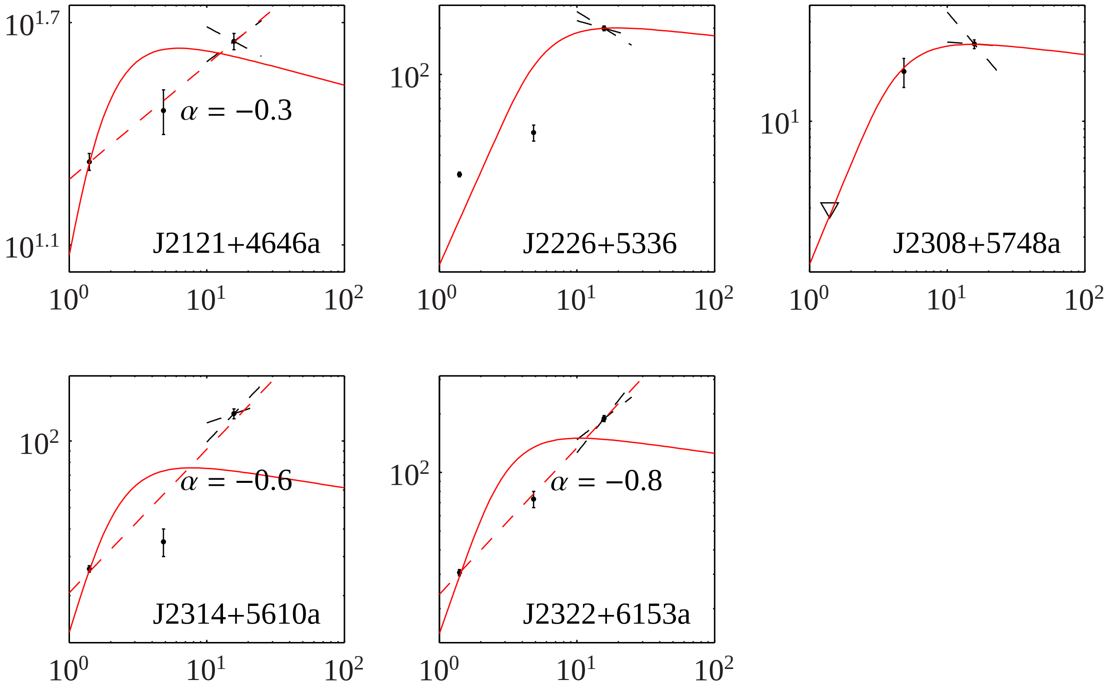

Figure 3.22: Data and model fits (where appropriate) for unidentified sources with more than two available radio flux densities. The x-axes are frequency in GHz, and the y-axes are flux density, in mJy.

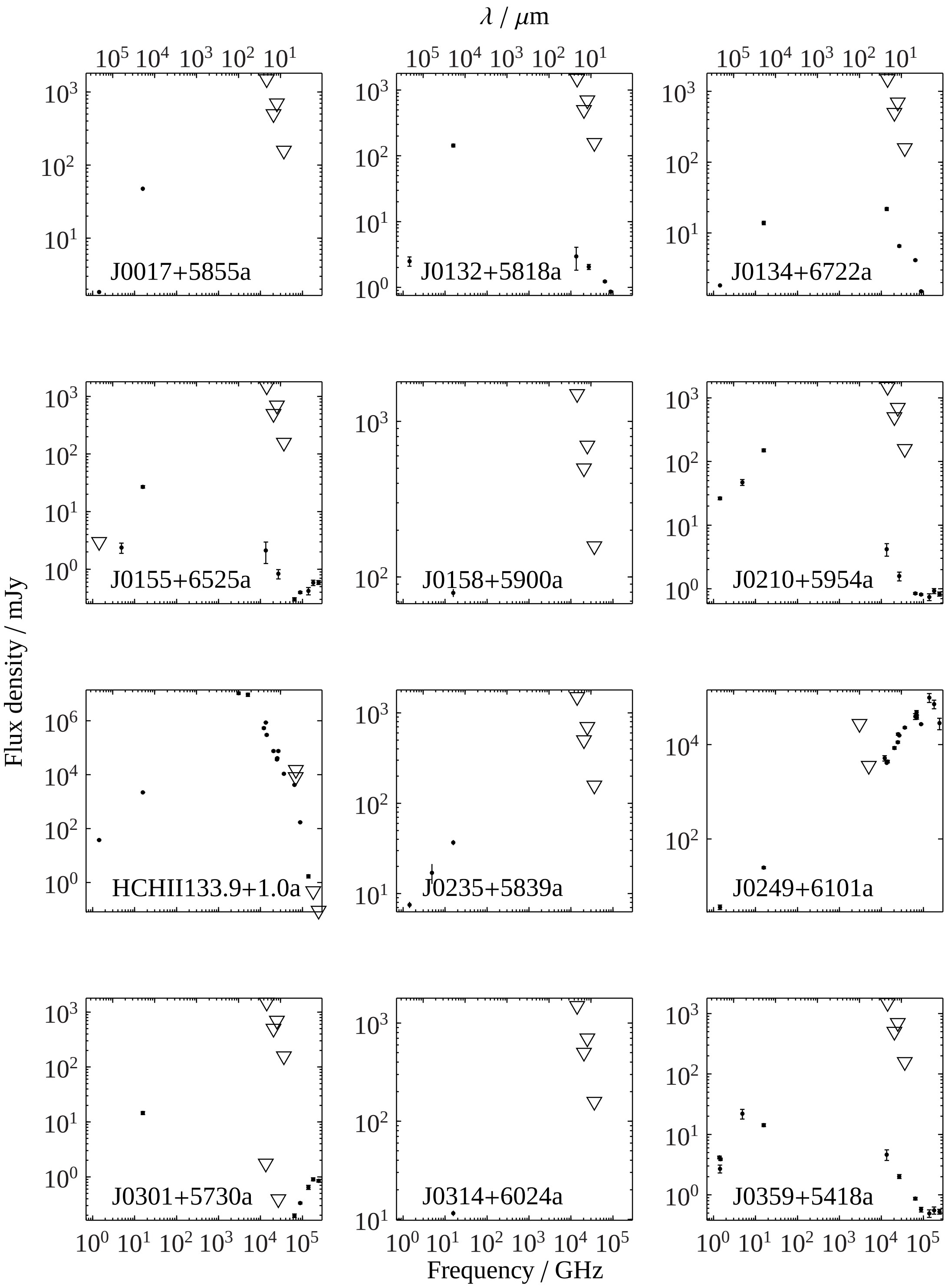

Figure 3.23: Radio to FIR spectra for all sources, with upper limits where appropriate.

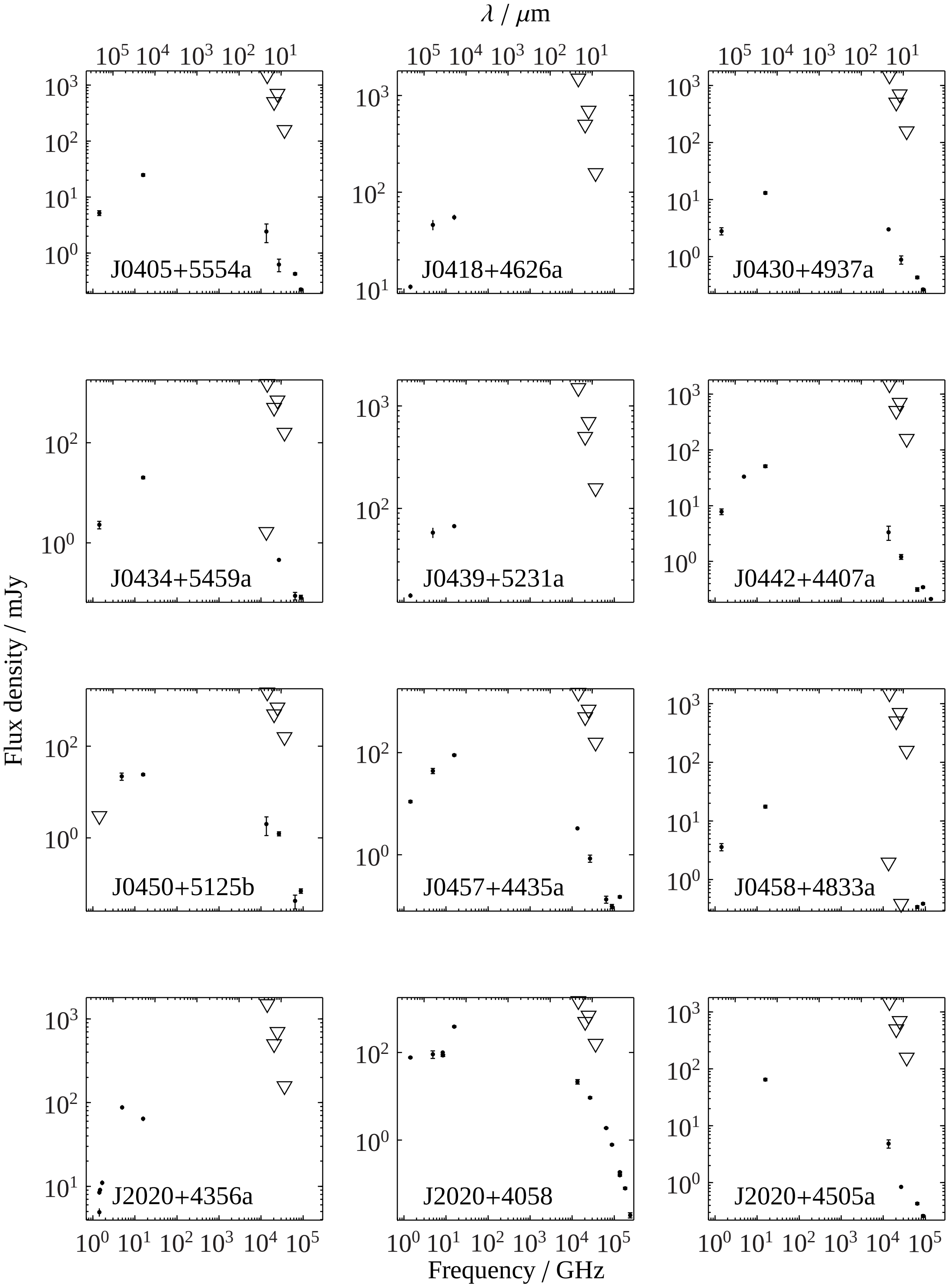

Figure 3.23: Radio to FIR spectra for all sources, with upper limits where appropriate.

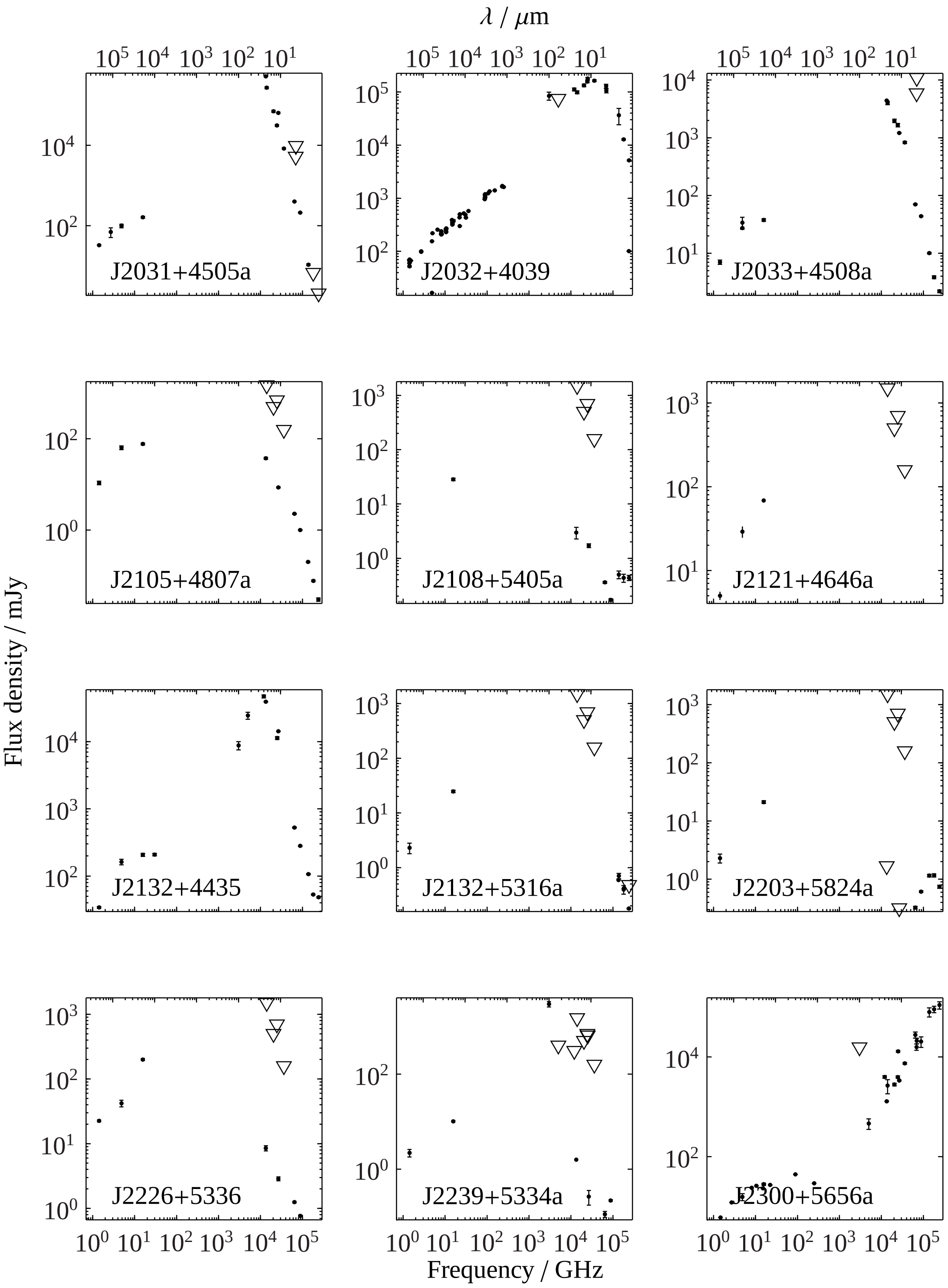

Figure 3.23: Radio to FIR spectra for all sources, with upper limits where appropriate.

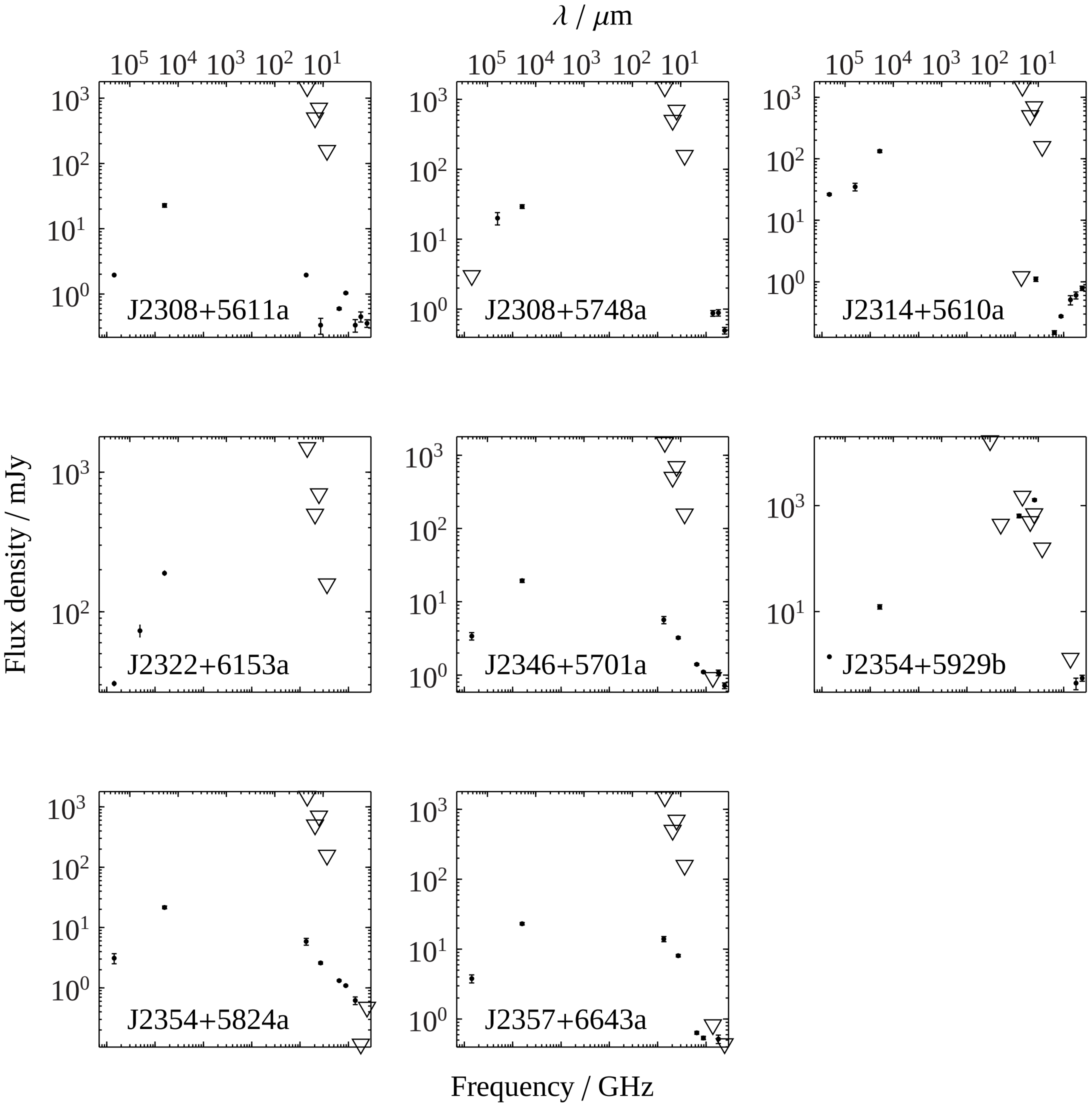

Figure 3.23: Radio to FIR spectra for all sources, with upper limits where appropriate.

Table 3.9: Properties of the JVLA configurations that will be available in Semester 2014A. Note that the ‘largest angular scale’ applies for a full synthesis observation, and will be somewhat smaller for the proposed short observations.

Configuration	A	D
Bmax (km)	36.4	1.03
Bmin (km)	0.68	0.035
Band	Synthesized Beamwidth θ_{HPBW} (arcsec)	
1.5 GHz (L)	1.3	46
3.0 GHz (S)	0.65	23
6.0 GHz (C)	0.33	12
10 GHz (X)	0.20	7.2
15 GHz (Ku)	0.13	4.6
22 GHz (K)	0.089	3.1
33 GHz (Ka)	0.059	2.1
45 GHz (Q)	0.043	1.5
	Largest Angular Scale θ_{LAS} (arcsec)	
1.5 GHz (L)	36	970
3.0 GHz (S)	18	490
6.0 GHz (C)	8.9	240
10 GHz (X)	5.3	145
15 GHz (Ku)	3.6	97
22 GHz (K)	2.4	66
33 GHz (Ka)	1.6	44
45 GHz (Q)	1.2	32

3.9.3 Future work

More data at different frequency and higher angular resolution is clearly required to understand the nature of these sources.

3.9.3.1 VLA proposal

The 2014A observing semester for the Karl G. Jansky Very Large Array will be in configurations A and D, which have the properties summarised in Table 3.9[1].

---

[1] `https://science.nrao.edu/facilities/vla/docs/manuals/oss2014a/performance/resolution`

Which frequency and configuration to observe in is a trade-off between angular resolution, largest angular scale visible, and expected flux density as a function of frequency. Nearly all of the sources have angular size $\lessapprox 10$ arcsec according to the LA (see Fig. 3.24), so the largest angular scale should be ≈ 10 arcsec (note that the given 'largest angular scale' applies to full synthesis observations, and will be slightly smaller for the proposed short observations). This rules out A-configuration at frequency > 6 GHz. The resolution should be a significant improvement on the AMI-LA beam size of ≈ 40 arcsec, ruling out D-configuration at frequency < 10 GHz. At frequency > 15 GHz atmospheric effects become extremely important, meaning that calibrators must be observed more frequently, which will not be efficient for this kind of observing programme which calls for relatively short observations of sources which are scattered spatially. These sources are known to have rising spectral indices between 1.4 and 16 GHz, therefore a higher observing frequency is preferable for SNR purposes. Taking all of these considerations together, the optimal choices are 6 GHz in A-configuration, or 15 GHz in D-configuration. The A-configuration is at higher resolution and will provide more information about the structure of the sources which will be important in determining their type; I therefore have decided to apply for observing time in this configuration.

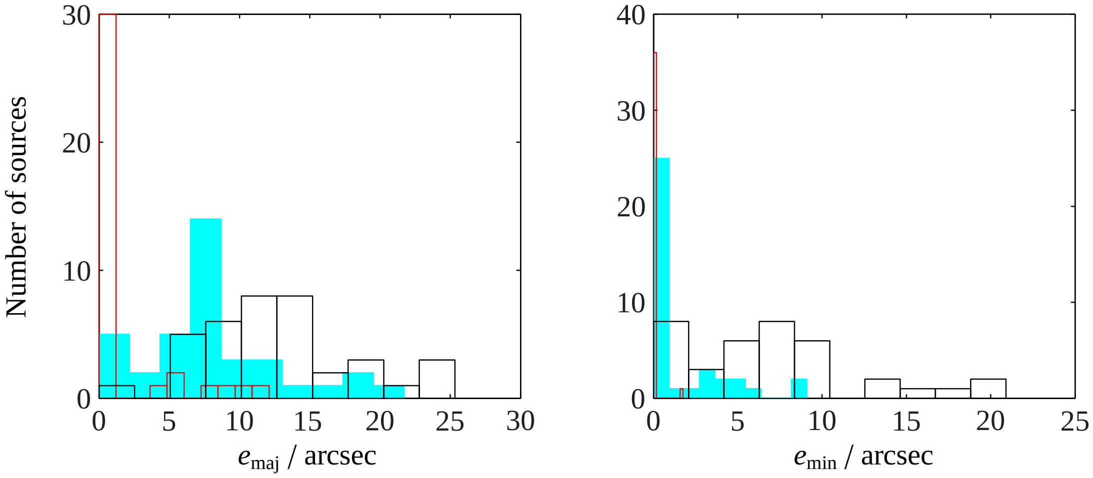

Figure 3.24: Distribution of major and minor axis FWHM of the sources. Solid distributions are the nominal sizes and red and black outlines show the minimum and maximum sizes respectively. A value of 0 means no constraint is obtained from the fit.

Source sizes

To predict the amount of observing time necessary for a good detection at high resolution, it is important to have an estimate of the source size. However, these objects are all (by selection) unresolved in the AMI-LA observations so this is difficult to determine. The JMFIT estimates of the source size appear to give some indication, but require closer inspection. The AMI-LA synthesised beam is highly elliptical due to the East-West nature of the array, with a $b_{\mathrm{maj}}/b_{\mathrm{min}}$ ratio ranging between 1.4 – 2.7. Most of the JMFIT deconvolved source size estimates are constrained only in the source major axis direction, and on visual inspection it can be seen that the reported deconvolved source position angles are approximately the same as the position angle of the synthesised beam. It seems highly unlikely that AMI has detected a population of elliptical sources which happen to be larger in the same direction as the LA synthesised beam. In fact, it would be much more likely for sources that are truly partially resolved in one direction to have a position angle approximately orthogonal to the beam position angle, since the resolution is $\approx 2\times$ better in this direction. Fits which have source position angles consistent with the beam position angle are therefore discarded; these are probably measuring residual phase errors in the data caused by atmospheric changes which will tend to ‘blur out’ the source, rather than the actual source size.

Only four sources have reported deconvolved source position angles which are not aligned with their respective synthesised beam position angles – J2031+4505a, J2308+5611a, J2322+6153a and J2354+5824a. However, the ‘minimum’ values for the sizes of these sources are mostly unconstrained, so these fits only give upper limits on the source size.

A further test of the accuracy of the AMI derived source sizes can be made by comparison to those sources for which there exists higher-resolution VLA archive data. These comparisons are listed in Table 3.10 and confirm that the AMI-LA source sizes can be regarded as upper limits at best, even when an apparently well-constrained size is returned by JMFIT, and even when $b_\theta \neq e_\theta$.

All of the sources with VLA observations at higher resolution have angular sizes $\lessapprox 1.5$ arcsec (with the exception of J0155+6525a and J0359+5418a, which however are less reliable since they are only marginally resolved, are toward the edge of the field of view and have low SNR). There is no reason to assume that these sources

Table 3.10: Comparison of source sizes derived from AMI-LA data and higher-resolution VLA archive data (except for J2031+4505a and J2033+4508a, where the VLA maps are taken from the RMS survey). $b_{\rm maj}$ and $b_{\rm min}$ are the major and minor axis CLEAN beam FWHM sizes (in arcsec) and $e_{\rm maj}$ and $e_{\rm min}$ are the deconvolved source FWHM sizes (in arcsec). b_θ and e_θ are the respective position angles.

Source	VLA archive					AMI-LA				
	Freq	$b_{\rm maj}$	$b_{\rm min}$	$e_{\rm maj}$	$e_{\rm min}$	$b_{\rm maj}$	$b_{\rm min}$	$e_{\rm maj}$	$e_{\rm min}$	$b_\theta = e_\theta$
J0155+6525a	4.86	5.93	3.90	5.4 ± 1.5	-	37.1	26.0	1.6 ± 0.6	-	T
HCHII133.9+1.0a	8.46	0.91	0.64	1.461 ± 0.001	0.942 ± 0.001	40.2	26.9	8^{+3}_{-5}	-	T
J0359+5418a	1.39	15.9	12.3	9.7 ± 1	5.7^{+1}_{-3}	44.8	27.3	< 6.6	< 2.1	T
J2020+4058a	8.44	0.73	0.62	0.157 ± 0.003	0.083 ± 0.008	48.3	26.3	11.5 ± 3	$0.9^{+3}_{-0.9}$	T
J2020+4356a	4.99	0.50	0.38	0.025 ± 0.003	0.019 ± 0.006	62.8	25.7	< 6.8	-	T
J2031+4505a	4.86	1.3	1.1	1.26 ± 0.01	1.00 ± 0.01	41.4	25.6	7^{+3}_{-7}	$2.7^{+7}_{-0.8}$	F
J2032+4039	4.86	0.40	0.32	0.769 ± 0.002	0.750 ± 0.002	47.4	26.0	9.9 ± 5	< 1.7	T
J2033+4508a	4.86	1.3	1.1	0.74 ± 0.06	0.54 ± 0.07	40.3	26.4	11^{+4}_{-11}	$6.5^{+4}_{-6.5}$	T
J2132+4435	4.86	0.40	0.34	1.041 ± 0.005	0.815 ± 0.004	47.6	27.0	$6.5^{+3}_{-6.5}$	$1.4^{+3}_{-1.4}$	T
J2300+5656a	4.86	0.47	0.33	0.408 ± 0.005	0.270 ± 0.004	38.5	23.5	$2.1^{+1}_{-2.1}$	< 9.3	T

are not representative of the sample as a whole. I therefore conservatively assume a somewhat larger nominal angular size of 3×3 arcsec (FWHM, for a Gaussian source) when calculating required VLA observation times; this corresponds to $N_{\rm beams} = 83$.

Observing time estimates

For each source, a 6 GHz flux density estimate is calculated by interpolating between 15.75 GHz and the next-highest-frequency measurement available. In the case that only the 16 GHz flux density is available, this is extrapolated to 6 GHz assuming the minimum physical spectral index of -2; this should be an underestimate.

The time required for a 5σ detection of a source with this integrated flux density is then calculated using the VLA Exposure Calculator, a source size of $3{\times}3$ arcsec and the maximum bandwidth (4 GHz) with the recommended effective bandwidth of 3.4 GHz to account for RFI. For all except the three faintest sources, this gives an unfeasibly short integration time which I increase to 10 min, which will be split into two blocks of 5 min to ensure good *uv*-coverage. In most cases, this should give much better than 5σ detections (especially for over-estimated source sizes and/or under-estimated flux densities), enabling the estimation of the spectral index across the band as well as the central flux density.

3.9.3.2 JCMT proposal

A proposal to observe the sources with SCUBA-2 on the JCMT at 850 μm has also been submitted in collaboration with Samantha Walker-Smith to investigate the morphology and properties of the associated dust. A previous SCUBA survey of UCHII regions found that the sub-mm emission associated with the regions followed a range of morphologies, from single centrally-peaked cores to multiply peaked regions to ridge-like structures with multiple condensations embedded along the ridges (Thompson et al., 2006). It was also found that the 850 μm peak was shifted away from the radio source position, indicating clearing of the surrounding material by the HII region. Studying the sub-mm emission associated with the AMIGPS sources will shed light on the star formation processes and environments associated with the sources, and confirm their status as HCHII regions. SEDs constructed in combination with other, shorter wavelength data will also enable the calculation of the temperatures and column densities around the sources.

3.9.3.3 Remaining rising spectrum sources

Once more information on the most extreme sources has been obtained, the remaining ≈ 200 rising spectrum sources should be investigated. A similar attempt should be made to correlate these sources with catalogues of known HII regions, planetary nebulae and radio stars to investigate further the distribution and nature of rising spectrum compact sources in the Northern Galactic plane.

3.9.3.4 Resolved sources

The interpretation of data on resolved sources is more challenging because missing flux must be accounted for, but these sources are also potentially interesting. The CGPS (total-power) compact source catalogue is now available, which will simplify the interpretation of spectral indices for the follow-up candidates which are resolved to the LA (and therefore also to NVSS). The data on these sources should also be investigated further and correlated with catalogues of known objects. Nearby (U)CHII regions will be resolved to the LA (see Table 3.4), so these sources are also potential (U)CHII region candidates; they could also be anomalous microwave emitters – AME so far has been more likely to be detected from extended objects, rather than compact.

3.9.3.5 AME

Very little is known about the overall distribution of AME in the Galaxy; large-scale searches for AME have so far only been made using *Planck* data (Planck Collaboration et al., 2011b), which is much lower resolution than AMI-SA data and therefore hampered by confusion. The AMIGPS would be an excellent testing ground for detecting AME but this does depend on being able to extract spectral index information for extended objects. Since the (full-power) CGPS data covers approximately the same areas as the AMIGPS, one way to do this would be to ‘observe’ the CGPS maps using a simulated drift-scan procedure, and look for emission that is brighter in the AMIGPS maps than in the ‘observation’ of the CGPS maps.

3.9.3.6 DR2

The observations for the second data release of the AMIGPS, to extend the survey down to $\delta \geq 20^\circ$, are mostly complete; in addition, some of the LA follow-up observations of compact rising-spectrum source candidates have been made. The data need to be processed and released to complete the survey.

3.10 Conclusions

The Galactic plane between $b \approx \pm 5^\circ$ has been surveyed using the interferometric AMI-SA at ≈ 16 GHz, to a noise level of ≈ 3 mJy beam^{-1} at ≈ 3 arcmin resolution. This is the most sensitive and highest resolution Galactic plane survey at cm-wave frequencies above 1.4 GHz.

1. 868 deg^2 of the Galactic plane have been surveyed and a catalogue of 3503 sources produced. This is the first data release of the AMIGPS, now available publicly at `http://www.mrao.cam.ac.uk/surveys/AMIGPS/` (AMI Consortium: Perrott et al., 2013a).

2. In testing the flux calibration of the survey by comparing source flux densities derived from the AMIGPS to tracked observations of both extra-galactic and Galactic sources taken with the AMI-SA and AMI-LA, I find that the AMIGPS flux calibration is accurate to within 5%.

3. The r.m.s. positional accuracy of the survey, assessed by comparing positions derived from the AMIGPS with well-known source positions from the VLBA calibrator survey and with AMI-LA follow-up positions, is 2.6 arcsec in RA and 1.7 arcsec in δ.

4. The source count for the unresolved sources in the AMIGPS and spectral index distribution when correlated with the NVSS have been compared to the extra-galactic 15 GHz source count and spectral index distribution from the 9C survey, and found to be significantly different. This shows the expected increase in source counts corresponding to the population of Galactic objects.

5. The AMIGPS has been searched for candidate hyper- and ultra-compact HII regions by selecting sources which have a rising spectrum from 1.4 GHz. 506 of these objects were followed up with the AMI-LA to provide higher resolution information, better constraints on the 16 GHz flux density and a spectral index over the AMI band. Of these, 255 have spectral indices between 1.4 and 16 GHz which are consistent with those expected from a simple model of (ultra-)compact HII regions.

6. To select a manageable sample for further analysis, a cut of $\alpha_{1.4}^{16} < -0.6$ was applied to select the $\approx 10\%$ most extreme objects. An extensive SIMBAD, VIZIER and literature search identified 6 of these 44 as being compact HII regions, planetary nebulae and radio stars; a further one is probably extra-galactic. The remaining 37 are unidentified; ancillary radio data available are consistent with free–free emission.

7. A VLA proposal has been submitted to observe the unidentified 37 at 0.33 arcsecond resolution between 4 and 8 GHz. These observations will provide further information on the source sizes and radio spectra and aid in identifying the sources.

8. A JCMT proposal has also been submitted to investigate the sub-mm emission around the sources. The morphology of the associated dust will provide insight into the star formation processes occurring around the regions, and the sub-mm data point will be used in conjunction with shorter-wavelength data to calculate temperatures and column densities of the dust.

Chapter 4

AMI follow-up of *Planck* clusters

This chapter describes the follow-up programme of *Planck* clusters which I have conducted. Observations of new clusters were performed in collaboration with Tim Shimwell and Clare Rumsey; historical data was used when existing for previously-known clusters. The analysis builds on previous work on a smaller sample performed by Malak Olamaie.

4.1 The *Planck* satellite

Planck (Planck Collaboration et al., 2011a) is a European Space Agency (ESA) satellite, launched in May 2009 and orbiting at the second Lagrangian point of the Earth-Sun system (L2), ≈ 1.5 million km from the Earth. It carries two instruments – the High Frequency Instrument (HFI), and the Low Frequency Instrument (LFI), covering a range of frequencies between ≈ 30 and ≈ 900 GHz with beam sizes between ≈ 30 and ≈ 5 arcmin (see Table 4.1).

One of *Planck*'s main science objectives was the detection and characterisation of clusters of galaxies via the SZ effect. The 2013 release of data included the *Planck* SZ catalogue (PSZ, Planck Collaboration et al. 2013a). Containing 1227 entries, the catalogue is the largest SZ-selected cluster catalogue to date. The catalogue is produced from the union of the output of three cluster detection methods, MMF1, MMF3 and PowellSnakes (PwS), using a blind multi-frequency search on the six HFI channel maps. MMF1 and MMF3 are matched multi-frequency filter algorithms, while PwS is

Table 4.1: Effective full width at half maximum (FWHM) of the *Planck* beams for the LFI (Planck Collaboration et al., 2013e) and HFI (Planck Collaboration et al., 2013b) instruments.

	Frequency (GHz)	FWHM (arcmin)
LFI	30	32.34
	44	27.12
	70	13.31
HFI	100	9.66
	143	7.27
	217	5.01
	353	4.86
	545	4.84
	857	4.63

a Bayesian detection algorithm (Carvalho et al. 2009, Carvalho et al. 2012); since PwS matches AMI analysis more closely than the MMF algorithms, I prefer where possible the parameters produced by PwS for comparison purposes.

4.2 AMI-*Planck* follow-up programme

AMI and *Planck* are highly complementary instruments since, while observing the same physical process, AMI has much higher angular resolution than *Planck* and can therefore provide information on cluster profiles at smaller radii. Conversely, since AMI is an interferometer, information on the large-scale flux density of resolved clusters is lost; this can be provided by *Planck*.

In Planck Collaboration et al. 2013f – from now on ‘the 11-cluster paper’ – a sample of 11 clusters from the *Planck* Early Release SZ catalogue was studied with AMI and there was found to be some disagreement between the results from the two instruments, with AMI finding the SZ signal to be, overall, smaller in angular size and fainter, and with significant discrepancies for some clusters. This was interpreted as an indication that the GNFW model used to describe the cluster profiles may not be flexible enough to describe clusters universally. To further investigate this possibility, as well as for validation purposes, the full catalogue of clusters observable by AMI has here been followed up.

4.2.1 Cluster selection

An initial cut of $20^\circ \leq \delta \leq 87^\circ$ was applied to the catalogue to satisfy AMI's reasonable observing limits. In addition, clusters with known redshifts of $z \leq 0.100$ were excluded since these are known to have large angular sizes and will be mostly resolved out by AMI; although the brightest of these will still be detectable, it will be difficult to constrain the overall properties using AMI data. These initial cuts resulted in a sample size of 337 with *Planck* SNR values ranging from 4.5 – 20.

A benign radio point source environment is important for AMI, but is difficult to quantify. For each cluster remaining in the sample that had not been previously observed with AMI, a short pre-screening observation was carried out with the AMI-LA to investigate this. In practice, the effect of the source environment on the detection potential of a cluster depends on many factors including the number and location of the sources with respect to each other and to the sidelobes of the primary and synthesised beams, and is almost impossible to quantify in a systematic way. In order to apply consistent criteria across the whole sample, clusters with radio sources of peak flux density $S_{\rm peak} > 5\,$mJy within 3 arcmin of the phase centre, with $S_{\rm peak} > 20\,$mJy within 10 arcmin of the phase centre, or with extended emission with fitted (deconvolved) major axis size $> 2\,$arcmin and integrated flux density $S_{\rm int} > 2\,$mJy, were discarded as experience suggests that observation of the SZ signal in such clusters with AMI is hampered. It should be noted however that some clusters which have been previously observed and detected with AMI are excluded by these cuts; some of the new clusters discarded by this process may also be observable.

In addition, clusters were manually inspected at various stages of the follow-up and analysis process, and some were rejected due to source environment at later stages. At the time of writing, the sample had been observed completely down to SNR ≥ 6, and this sub-sample will be considered in the following sections. This final sub-sample, which I will refer to as the SZ sample, consists of 59 clusters, including 19 observed with AMI and published previously as part of other samples. A breakdown of the fraction of clusters rejected for various reasons is shown in Table 4.2.

Table 4.2: Numbers of clusters in the $20^\circ \leq \delta \leq 87^\circ$, SNR ≥ 6 sub-sample in various categories. The 59 clusters in the sample include the 19 previously observed with AMI.

Category	Number of clusters
Total	122
$z \leq 0.1$	16
Automatic radio-source environment rejection	39
Manual radio-source environment rejection	8
Included in sample	59
Included in sample and previously observed with AMI	19

4.2.2 Observation

Clusters are observed as a single pointing centre on the AMI-SA, and as a 61-point hexagonal raster on the AMI-LA, to typical noise levels of $\lessapprox 120\,\mu$Jy beam^{-1} and $\lessapprox 100\,\mu$Jy beam^{-1} in the centre, respectively. The LA raster is observed to a lower noise level in the central 19-point raster than in the outer regions. Typical noise maps and *uv*-coverages are displayed for both arrays in Figs. 4.1 and 4.2.

Data on both arrays are flagged for interference and calibrated using REDUCE, then CLEANed using AIPS in an automated manner. Source-finding is carried out at 4σ on the LA continuum map, as described in AMI Consortium: Davies et al. (2011), and sources that are detected at $\geq 3\sigma$ on at least three channel maps and are not extended have a spectral index α fitted across the AMI band. SA data are binned according to *uv*-distance in order to reduce the memory required for subsequent analysis.

4.2.3 Analysis

The McAdam package (Feroz et al., 2009) is used to fit for the parameters of a model containing radio point sources and a cluster, simultaneously, in a fully Bayesian manner. The primordial CMB anisotropies and confusion noise from the point source population below the LA detection threshold are accounted for as extra noise sources, taking into account the correlations between visibilities. The software package GETDIST is used to extract the marginalised one- and two-dimensional posterior distributions from the Monte Carlo chains.

The fitted parameters for the radio sources are used to produce source-subtracted maps, which should contain only the cluster and noise (from primordial CMB fluctua-

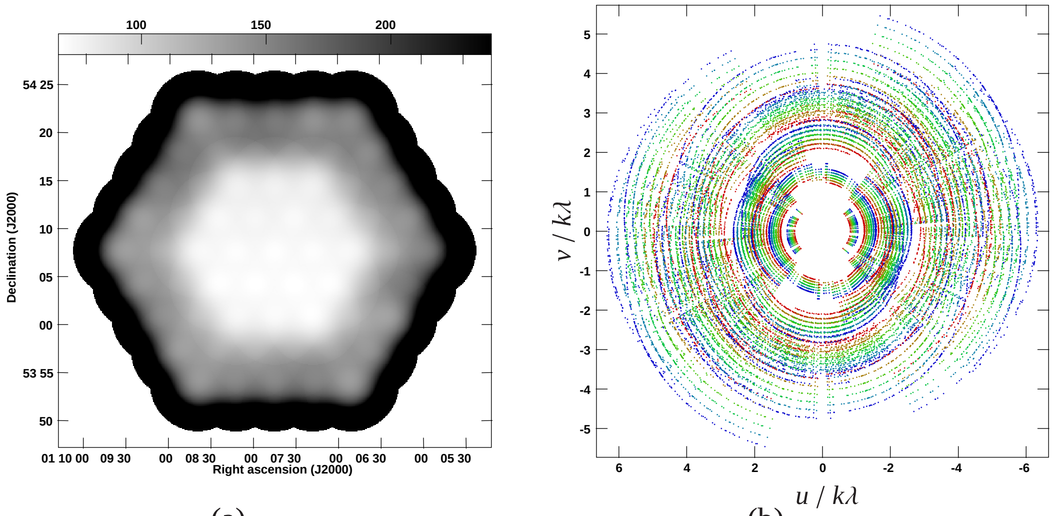

(a) (b)

Figure 4.1: AMI-LA noise map (a) and *uv*-coverage (b) for a typical cluster. The grey-scale on (a) is in μJy beam^{-1} and is truncated to show the range of noise levels. The colours in (b) indicate different channels.

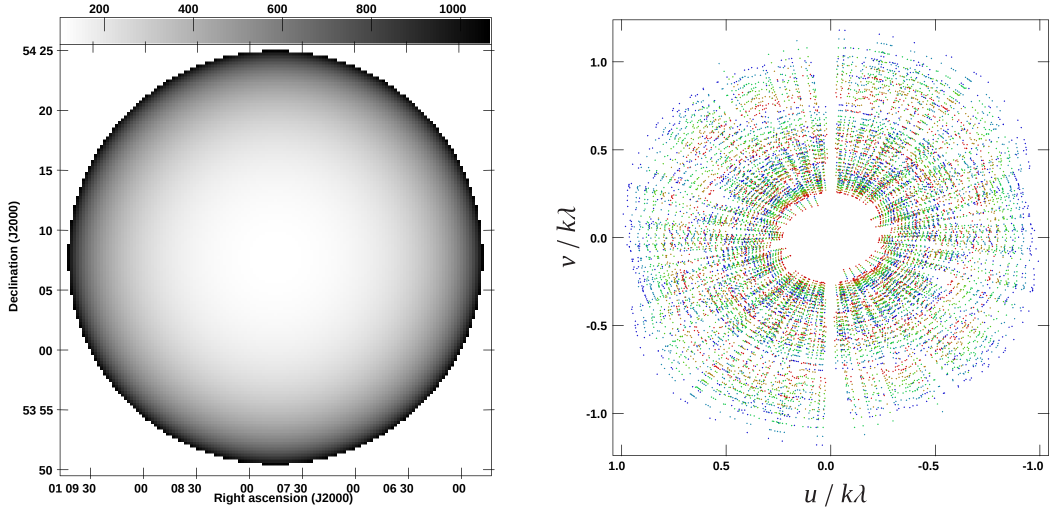

(a) (b)

Figure 4.2: AMI-SA noise map (a) and *uv*-coverage (b) for a typical cluster. The grey-scale on (a) is in μJy beam^{-1} and the map is cut off at the 10% power point of the primary beam. The colours in (b) indicate different channels.

tions, unsubtracted sources and system temperature). Since most clusters are extended with respect to the SA synthesised beam, I have produced source-subtracted maps both with natural weighting (for optimised signal-to-noise for non-resolved structures), and with a Gaussian weighting function of width 600λ at the 30%-power point applied to the visibilities (decreasing the weighting of the longer baselines, to increase the signal-to-noise of resolved structures). These maps are useful mainly for visual inspection of the cluster, to check the residual radio source environment, and to compare the structure of the cluster with maps produced by other instruments.

For each cluster, two McAdam runs are performed – one with the full cluster + radio source environment model, and one with only the radio source environment model (the ‘null’ run). The difference in Bayesian evidence, which takes into account the various sources of noise as well as the goodness of fit of the radio source and cluster models, between these runs provides a natural quantity for categorising the clusters into clear detections and non-detections. I have defined an additional category, moderate detections, to account for cases where the data are more consistent with the presence of a cluster than not, but there is not enough information in the data to constrain the model parameters well. The boundaries for these categories are listed in Table 4.3. The boundary between clear and moderate detections was determined empirically, from inspecting final maps and posterior distributions.

Table 4.3: The evidence difference ($\Delta\log_{10}(Z)$) boundaries used for categorising clusters as clear detections, clear non-detections, and moderate detections.

Category	$\Delta\log_{10}(Z)$ boundaries
Clear detection (Y)	$\Delta\log_{10}(Z) \geq 3$
Moderate detection (M)	$0 \leq \Delta\log_{10}(Z) < 3$
Clear non-detection (N)	$\Delta\log_{10}(Z) < 0$

4.2.3.1 Radio-source modelling

The results from the LA source-finding are used as input priors for source subtraction from the SA map, as summarised in Table 4.4. If a source appears at $\geq 4\sigma$ on the SA map, its flux density and spectral index are fitted for in McAdam; otherwise, the source is subtracted directly based on the LA values. Wide (σ = 40% Gaussian) priors are put on source flux densities to allow for variability and for SA-LA measurement discrepancies. When a spectral index cannot be fitted to the LA data for a source, a prior based on the 10C distribution of spectral indices between 1.4 and 16 GHz is used if the source flux is to be fitted in the SA data; if not, α is fixed to the median value of the 10C prior, 0.5. The positions of the sources are fixed to the positions derived from the LA continuum map in all cases.

4.2.3.2 Cluster modelling

The cluster model used for AMI-*Planck* analysis is the 'universal' generalised Navarro-Frenk-White pressure profile defined in Arnaud et al. (2010). Further details of the model will be given in Chapter 5. The model can be parameterised by the 'flux' parameter Y_{tot}, which is the Comptonisation parameter integrated over its detected area on the sky, and the 'shape' parameter θ_s, which indicates the characteristic angular scale of the cluster on the sky. In addition, the position of the cluster centre is described by offsets from the phase centre (which is either the *Planck* catalogue position, or the previously known X-ray or optical position for clusters with existing AMI observations) in RA and δ, x_0 and y_0. The priors on these are Gaussian, centred on the *Planck* catalogue position, with width given by the *Planck* positional uncertainty up to a maximum of 5 arcmin; this cut-off applies only to one cluster which is only detected by MMF3, and as will be shown, the MMF3 positional errors are over-estimated.

The priors assigned to Y_{tot} and θ_s in the 11-cluster paper and used for the *Planck* PwS analysis are based on marginalised distributions of Y_{tot} and θ_s in a simulated population of clusters generated according to the Jenkins mass function, as described in Carvalho et al. (2012). The parameterisation functions for these priors are listed in Table 4.5 and plotted in Fig. 4.3. In practice, these priors are incorrect since they ignore the correlation between Y_{tot} and θ_s. In addition, they take into account the *Planck* selection function only in assuming minimum and maximum cutoffs in each parameter. Fig. 4.4 illustrates the difference between the two-dimensional prior produced by multiplying the one-dimensional priors, and a better approximation to the true distribution of clusters expected to be detected by *Planck* (data from Pedro Carvalho). This was produced by injecting a cluster population based on the Tinker mass function (Tinker et al., 2008) into the *Planck* maps and running the *Planck* detection algorithms as described in Planck Collaboration et al. (2013a).

Table 4.4: Priors for source subtraction from SA map based on LA source-finding results. $S_{\rm peak}$ and $S_{\rm int}$ are the peak and integrated flux densities from the continuum map; $S_{\rm fit}$ is the central flux density estimate from the fit to the channel flux densities. ‘P’ and ‘E’ refer to point-like and extended sources, respectively.

LA source type	P				E	
LA significance	$> 3\sigma$ on ≥ 3 channel maps		$> 3\sigma$ on < 3 channel maps		$S_{\rm peak} > 4\sigma$ on continuum map	
Central flux density estimate	$S_{\rm fit}$		$S_{\rm peak}$		$S_{\rm int}$	
α estimate	$\alpha_{\rm fit}$		0.5		0.5	
SA significance	$> 4\sigma$	$\leq 4\sigma$	$> 4\sigma$	$\leq 4\sigma$	$> 4\sigma$	$\leq 4\sigma$
SA central flux density prior	$\mathcal{N}(S_{\rm fit}, 0.4 \times S_{\rm fit})$	$\delta(S_{\rm fit})$	$\mathcal{N}(S_{\rm peak}, 0.4 \times S_{\rm peak})$	$\delta(S_{\rm peak})$	$\mathcal{N}(S_{\rm int}, 0.4 \times S_{\rm int})$	$\delta(S_{\rm int})$
SA α prior	$\mathcal{N}(\alpha_{\rm fit}, \Delta\alpha_{\rm fit})$	$\delta(\alpha_{\rm fit})$	10C	$\delta(0.5)$	10C	$\delta(0.5)$
Symbol used for plotting	×	+	×	+	×	+

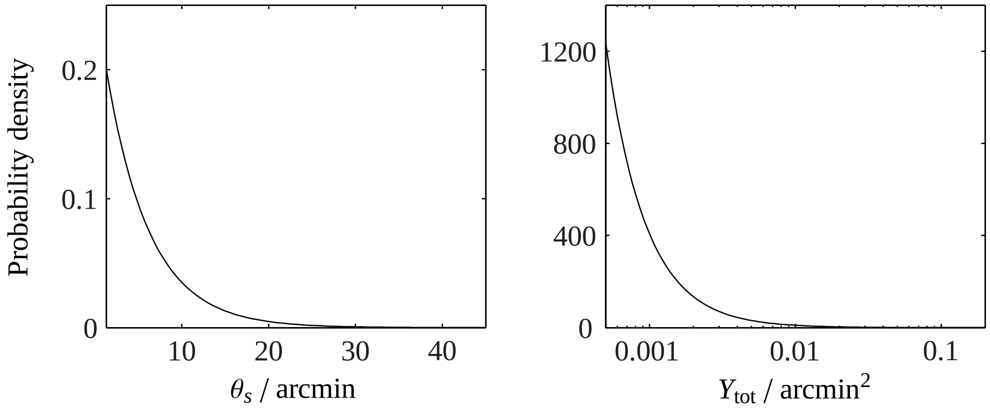

(a) (b)

Figure 4.3: Prior on θ_s (a) and $Y_{\rm tot}$ (b) in previous analysis.

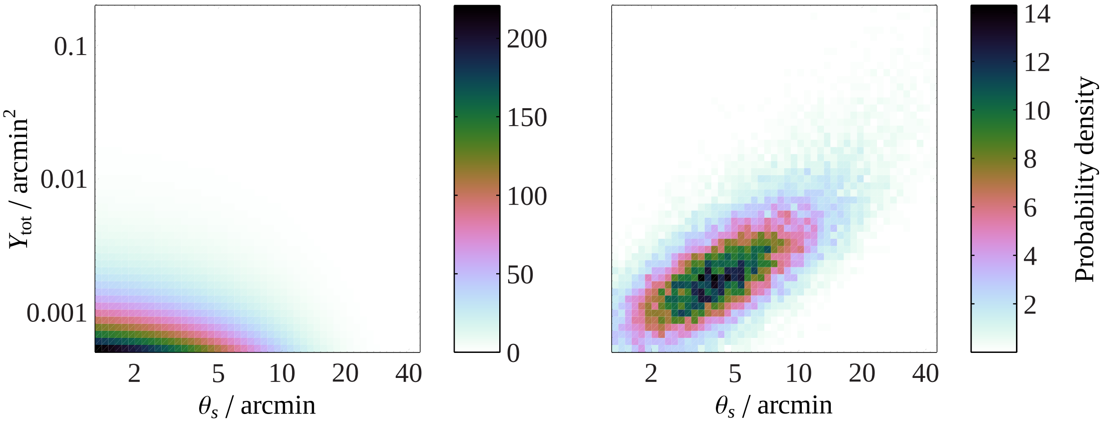

(a) (b)

Figure 4.4: Two-dimensional $Y_{\rm tot}$ vs θ_s prior, assuming separability and using the priors shown in Fig. 4.3 (a), and a closer approximation to the real (correlated) $Y_{\rm tot}$ vs θ_s distribution (b) – see text for more detail.

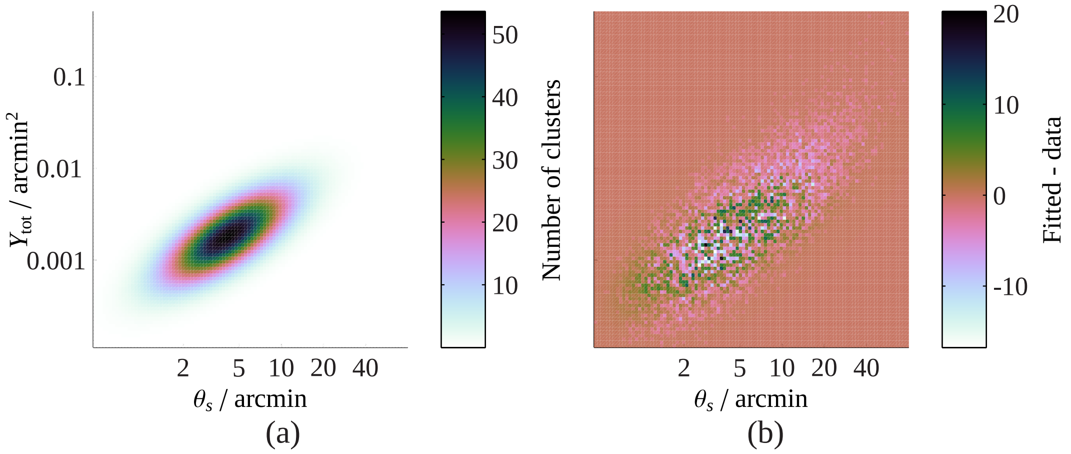

Figure 4.5: Two-dimensional elliptical Gaussian fit to the $Y_{\rm tot}$ vs θ_s distribution in log-space (a) and residuals with respect to the simulated distribution (b).

Non-separable prior

Since the distribution of points looked similar to a two-dimensional, elliptical Gaussian in log-space, I decided to attempt to represent the prior in that way. A least-squares fit was performed to find the optimal fit to the two-dimensional histogram, resulting in the fit shown in Fig. 4.5. The fit agrees well, although the residuals do show a 'tail' of increased probability in the distribution with respect to the analytical fit towards high values of $Y_{\rm tot}$ and θ_s.

The fit is parameterised by offset and width in both $x = \log_{10}(\theta_s)$ and $y = \log_{10}(Y_{\rm tot})$, and by the angle ϕ measured clockwise from the y-axis, i.e.

$$\frac{\mathrm{dP}(x,y)}{\mathrm{d}x\,\mathrm{d}y} \propto \exp\left[-\frac{1}{2}\left(A(x-x_0)^2 + B(y-y_0)^2 + 2C(x-x_0)(y-y_0)\right)\right],$$

where

$$\begin{aligned} A &= \frac{\cos^2(\phi)}{2\sigma_x^2} + \frac{\sin^2(\phi)}{2\sigma_y^2} \\ B &= \frac{\sin^2(\phi)}{2\sigma_x^2} + \frac{\cos^2(\phi)}{2\sigma_y^2} \\ C &= \frac{\sin(2\phi)}{4\sigma_x^2} - \frac{\sin(2\phi)}{4\sigma_y^2}. \end{aligned} \tag{4.1}$$

The best-fit parameters are listed in Table 4.5. The advantage of this parameterisation is that there are simple, analytical solutions for the marginalised and conditional distributions. The marginal distribution of $\log_{10}(\theta_s)$ is given by

$$\begin{aligned} \frac{\mathrm{dP(x)}}{\mathrm{d}x} &= \int_{-\infty}^{\infty} \frac{\mathrm{dP}(x,y)}{\mathrm{d}x\,\mathrm{d}y}\mathrm{d}y \\ &\propto \exp\left[-\frac{1}{4}\frac{(x-x_0)^2}{\sigma_y^2\sin^2\phi + \sigma_x^2\cos^2\phi}\right], \end{aligned} \tag{4.2}$$

i.e. Gaussian with $\mu = x_0$ and $\sigma = \sqrt{2(\sigma_y^2\sin^2\phi + \sigma_x^2\cos^2\phi)}$. The conditional distribution of $\log_{10}(Y_{\mathrm{tot}})$ is given by

$$\begin{aligned} \frac{\mathrm{dP}(y|X)}{\mathrm{d}y} &= \frac{\mathrm{dP}(X,y)}{\mathrm{d}x\,\mathrm{d}y} \\ &\propto \exp\left[-\frac{1}{2}B\left((y-y_0) + \frac{C(X-x_0)}{B}\right)^2\right], \end{aligned} \tag{4.3}$$

i.e. also Gaussian with $\mu = y_0 - C(X-x_0)/B$ and $\sigma = 1/\sqrt{B}$.

The new prior is clearly very different to the old prior. The prior is important, especially for clusters with larger angular sizes where AMI data cannot simultaneously constrain θ_s and Y_{tot} because the zero-spacing flux is not measured (see Chapter 5 for more details). The effects of changing the prior will be investigated in Section 4.2.4.4.

Table 4.5: Priors used on profile fit parameters

Parameter	Prior type	Parameters	Limits
x_0/y_0	Gaussian, $e^{-x^2/2\sigma^2}$	$\sigma = \max(5\,\mathrm{arcmin}, \sigma_{\mathrm{Planck}})$	-
Y_{tot} (old)	Power-law, x^{-a}	$a = 1.6$	$0.0005 < x < 0.2$
θ_s (old)	Exponential, $\lambda e^{-\lambda x}$	$\lambda = 0.2$	$1.3 < x < 45$
Y_{tot} (new)	2D elliptical Gaussian in $\log_{10}(Y_{\mathrm{tot}})$	$y_0 = -2.743, \sigma_y = 0.2856,$ $\phi = 40.17°$	-
θ_s (new)	2D elliptical Gaussian in $\log_{10}(\theta_s)$	$x_0 = 0.6171, \sigma_x = 0.1153,$ $\phi = 40.17°$	$1.3 < x$

4.2.4 Results

In the final subsample, 48 are clear detections, seven are moderate detections, and only four are clear non-detections. A summary of the results for each cluster is presented in Table 4.6.

Some representative examples from each category are discussed in the following. In each case, source-subtracted maps are shown both with and without the *uv*-tapering (see Section 4.2.3 for details); the symbols × and + show the positions of subtracted sources (as described in Table 4.4), □ shows the AMI, McAdam-determined position of the cluster, and the $1 \times \sigma_{Planck}$ positional error radius is shown as a circle. Contours are plotted at ±3 to 10× the r.m.s. noise level, and dashed contours are negative. The synthesised beam is shown in the bottom left-hand corner.

Posterior distributions for position offset, cluster model parameters and the closest radio sources to the cluster centre are also shown; in these plots the units are arcsec on the sky for offset in RA (x_0) and δ (y_0), arcmin^2 for Y_{tot}, arcmin for θ_s and mJy for radio source flux densities. The Y_{tot}-θ_s posterior distribution is shown in black overlaid with that obtained by PwS using *Planck* data for the cluster in red, as well as the prior (black dotted line). Appendix A contains similar maps and posterior distribution plots for the entire sample.

Table 4.6: Summary of results for the final subsample of 59 clusters. Reference numbers refer to (1) AMI Consortium: Barker et al. (2006), (2) AMI Consortium: Hurley-Walker et al. (2011), (3) AMI Consortium: Zwart et al. (2011), (4) AMI Consortium: Hurley-Walker et al. (2012), (5) AMI Consortium: Rodríguez-Gonzálvez et al. (2012), (6) Planck Collaboration et al. (2013f), (7) AMI Consortium: Shimwell et al. (2013b). $\Delta \log_{10}(Z)$ is the Bayesian evidence difference, and 'category' is as defined in Table 4.3. 'EE' refers to a class of clusters with significant extended radio emission present.

AMI ID	*Planck* SNR	$\Delta \log_{10}(Z)$	Category	Aliases	Previous AMI analysis	Redshift	Notes
CAJ1635+6612	17.207	33.75	Y	A2218, RXC J1635.8+6612	3, 5, 6	0.171	
CAJ1938+5409	14.971	16.01	Y	CL1938+54, RXC J1938.3+5409		0.260	
CAJ2122+2311	13.092	1.61	M	ZW8503		0.143	
CAJ0830+6551	12.974	47.39	Y	A665, RXC J0830.9+6551		0.182	
CAJ1425+3750	11.764	27.71	Y	A1914, RXC J1426.0+3749	1, 3, 4, 6	0.171	
CAJ1510+3329	10.459	26.59	Y	A2034, RXC J1510.1+3330	6	0.113	
CAJ0107+5407	10.225	18.24	Y	RXC J0107.7+5408		0.107	
CAJ1720+2637	9.904	1.59	M	RXC J1720.1+2637	5	0.164	
CAJ1155+2324	9.791	25.06	Y	A1413, RXC J1155.3+2324	5, 6	0.143	
CAJ1948+5114	9.544	6.62	Y	RXC J1948.3+5113		0.185	
CAJ0917+5143	9.527	34.23	Y	A773, RXC J0917.8+5143	3, 5, 6	0.217	
CAJ0638+4748	9.425	6.51	Y	ZW1133, RXC J0638.1+4747		0.174	
CAJ1414+7116	8.975	4.53	Y	A1895, RXC J1414.2+7115		0.225	
CAJ1524+2954	8.964	0.91	M	A2069, RXC J1524.1+2955		0.115	
CAJ2200+2058	8.740	35.09	Y	A2409, RXC J2200.8+2058	5, 6	0.147	
CAJ0622+7442	8.658	20.45	Y	PLCKESZ G139.59+24.18	6	0.267	
CAJ1724+8553	8.566	11.06	Y	A2294, RXC J1723.7+8553		0.178	
CAJ1752+4440	8.457	13.38	Y	MAJ1752+4440,		0.366	

Continued on next page

Table 4.6 – continued from previous page

AMI ID	*Planck* SNR	$\Delta \log_{10}(Z)$	Category	Aliases	Previous AMI analysis	Redshift	Notes
				RXC J1752.0+4440			
CAJ1023+4907	8.444	17.43	Y	A990, RXC J1023.6+4907	5, 6	0.144	
CAJ1157+3336	8.429	8.04	Y	A1423, RXC J1157.3+3336	5	0.214	
CAJ0308+2645	8.354	25.79	Y	MAJ0308+2645, RXC J0308.9+2645	3	0.356	
CAJ1022+5006	8.261	4.76	Y	A980, RXC J1022.5+5006		0.158	
CAJ0748+5941	8.191	36.81	Y	RXC J0748.7+5941, [ATZ98] B100	6		
CAJ1159+4946	8.186	6.25	Y	RXC J1159.2+4947		0.211	
CAJ0142+4438	8.087	25.15	Y	RXC J0142.9+4438		0.341	
CAJ1115+5320	7.609	11.91	Y	XMJ1115+5319, RXC J1115.2+5320	7	0.470	
CAJ2228+2037	7.261	28.47	Y	RXC J2228.6+2036		0.412	
CAJ1858+2916	7.217	16.99	Y				
CAJ1212+2732	7.186	13.96	Y	RXC J1212.3+2733		0.353	
CAJ1819+5711	7.129	3.34	Y	RXC J1819.9+5710		0.179	Positional error increased to encompass visible decrement in map
CAJ1149+2223	7.117	120.00	Y	MAJ1149+2223, RXC J1149.5+2245	6	0.545	
CAJ1428+5651	7.056	-0.29	N	A1925, RXC J1428.4+5652		0.105	
CAJ1747+4512	7.008	2.54	M	ZW8284, RXC J1747.2+4512		0.156	
CAJ2226+7818	6.997	3.87	Y	PLCKESZ G115.71+17.52	2		

Continued on next page

Table 4.6 – continued from previous page

AMI ID	*Planck* SNR	$\Delta \log_{10}(Z)$	Category	Aliases	Previous AMI analysis	Redshift	Notes
CAJ1229+4737	6.969	5.25	Y	RXC J1229.0+4737		0.254	
CAJ0742+7414	6.942	6.30	Y	ZW1370, RXC J0741.7+7414		0.215	
CAJ1856+6622	6.891	3.27	Y	ZwCl 1856.8+6616		0.300	
CAJ0227+4904	6.857	11.09	Y				
CAJ0842+6234	6.848	-1.88	N				
CAJ0637+6654	6.766	3.76	Y				EE
CAJ1259+6004	6.721	12.76	Y	PLCKESZ G121.11+57.01	2, 6	0.344	
CAJ1354+7714	6.669	6.63	Y	RXC J1354.6+7715		0.397	
CAJ1832+6449	6.656	-1.27	N	RXC J1832.5+6449		0.162	
CAJ2137+3531	6.585	25.76	Y				EE
CAJ2234+5243	6.562	6.77	Y				EE
CAJ1905+3233	6.526	2.07	M				
CAJ2322+4845	6.493	18.47	Y				EE
CAJ1756+4007	6.476	16.00	Y	WHL J269.219+40.1353		0.570	
CAJ0909+5133	6.376	4.24	Y	RXC J0909.3+5133		0.232	
CAJ1414+5447	6.351	34.62	Y	WHL J213.697+54.7844		0.631	
CAJ1539+3426	6.314	17.02	Y	A2111, RXC J1539.7+3424	4, 5	0.229	
CAJ1314+6433	6.249	26.98	Y	A1704, RXC J1314.4+6434	5	0.220	EE
CAJ0850+3604	6.225	4.65	Y	ZW1953, RXC J0850.2+3603		0.378	
CAJ1016+3339	6.142	0.04	M	A961, RXC J1016.3+3338		0.124	
CAJ0947+7622	6.123	7.86	Y	MAJ0947+7623, RXC J0947.2+7623		0.345	
CAJ2146+2029	6.096	-1.03	N	ZwCl 2143.5+2014		0.250	

Continued on next page

Table 4.6 – continued from previous page

AMI ID	*Planck* SNR	$\Delta \log_{10}(Z)$	Category	Aliases	Previous AMI analysis	Redshift	Notes
CAJ1123+2128	6.085	0.29	M	A1246, RXC J1123.9+2129		0.190	
CAJ0801+3605	6.065	21.91	Y	A611, RXC J0800.9+3602	3, 4, 5	0.288	
CAJ0851+4829	6.009	23.26	Y			0.513	

4.2.4.1 Clear detections

Abell 2218

Abell 2218 (Abell, 1958) is an extremely well-known cluster and one of the earliest SZ detections (e.g. Gull and Northover 1976, Jones et al. 1993). It lies at redshift $z = 0.171$ (Böhringer et al., 2000). It has been observed by AMI previously as part of the LoCuSs sample (AMI Consortium: Rodríguez-Gonzálvez et al., 2012) and was part of the previous AMI-*Planck* follow-up paper. It has the highest *Planck* SNR in the final subsample and is also well-detected by AMI with $\Delta\log_{10}(Z) = 33$. Fig. 4.6 shows that the cluster is resolved by AMI as the depth of the decrement increases in the *uv*-tapered map, and structure can be clearly seen in the naturally-weighted map. The posterior distributions (Fig. 4.7) show a good constraint in both position and the cluster model parameters. The two-dimensional posterior distributions for the flux densities of the three closest sources are included in the plot; it can be seen that there is some correlation between the flux densities of the sources and Y_{tot}, i.e. lower values of the flux densities allow lower values of Y_{tot}, but this does not affect the parameter constraints significantly. The PwS Y_{tot}-θ_s posterior overlaps with the AMI posterior, but AMI finds the cluster to be smaller and fainter than *Planck*.

CAJ1858+2916

This is a new cluster discovered by *Planck* at high SNR (7.2) and clearly detected by AMI with $\Delta\log_{10}(Z) = 17.0$. The source-subtracted maps for the cluster are shown in Fig. 4.8, and the posterior distributions in Fig. 4.9. Again, it is clear that AMI resolves the cluster. The source flux densities of the two nearest sources are shown in the posterior distributions; there is no apparent degeneracy between the source flux densities and any of the parameters. In this case, the posterior distributions for θ_s and Y_{tot} are very consistent with the PwS posteriors. The AMI and PwS degeneracies are in different directions, meaning that the joint constraints produced by combining the two will be considerably tighter.

4.2.4.2 Moderate detections

ZW8503

ZW8503 is a well-known cluster at $z = 0.143$ (Allen et al., 1992) with a large an-

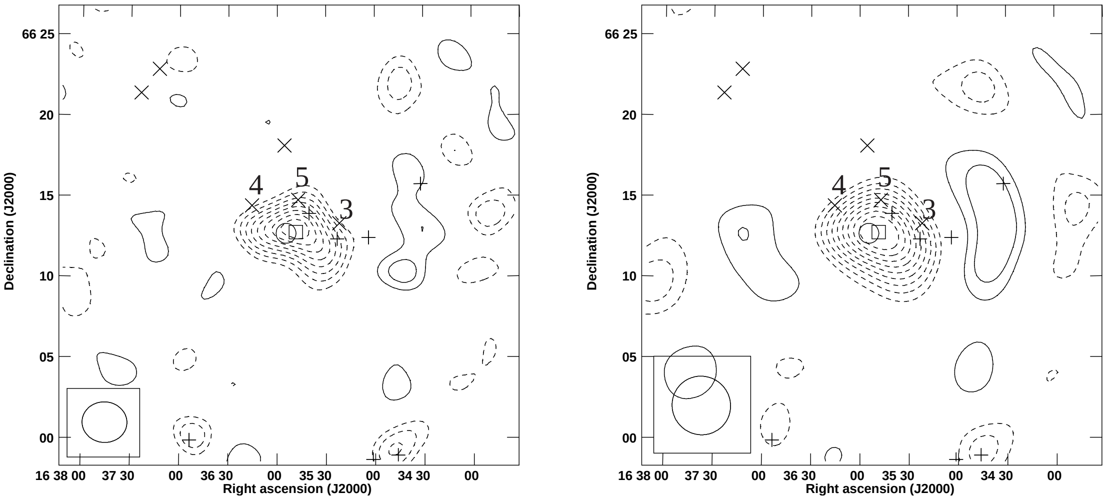

(a)

(b)

Figure 4.6: SA source-subtracted map of A2218 with natural weighting (a) and with a *uv*-taper (b) (see Section 4.2.3 for details). The r.m.s. noise levels are 131 and 163 μJy beam^{-1} respectively. The numbered sources have posterior distributions for their flux densities plotted in Fig. 4.7.

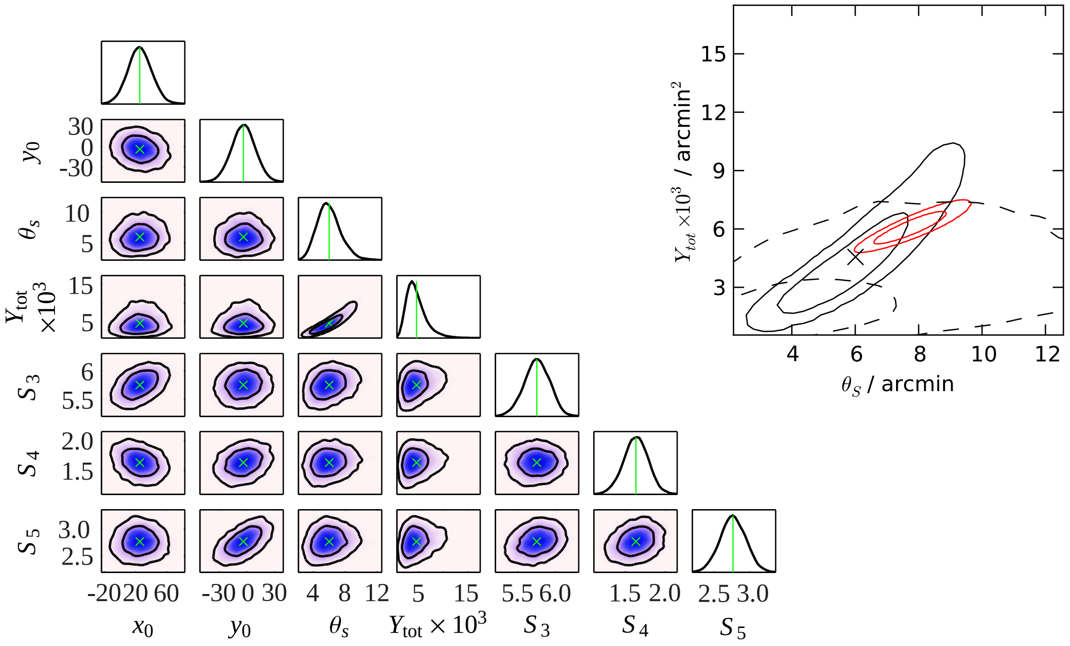

Figure 4.7: AMI posterior distributions for A2218 and the $Y_{\rm tot}$-θ_s posterior overlaid with that obtained by *Planck* in red, and the prior as a black dotted line (upper right-hand corner).

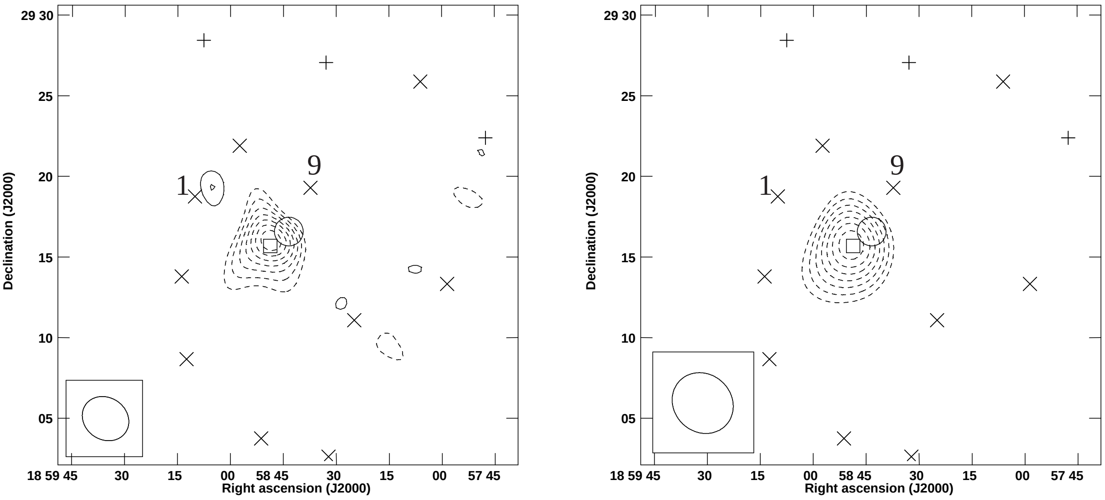

(a) (b)

Figure 4.8: SA source-subtracted map of CAJ1858+2916 with natural weighting (a) and with a *uv*-taper (b) (see Section 4.2.3 for details). The r.m.s. noise levels are 98 and 134 μJy beam^{-1} respectively. The numbered sources have posterior distributions for their flux densities plotted in Fig. 4.9.

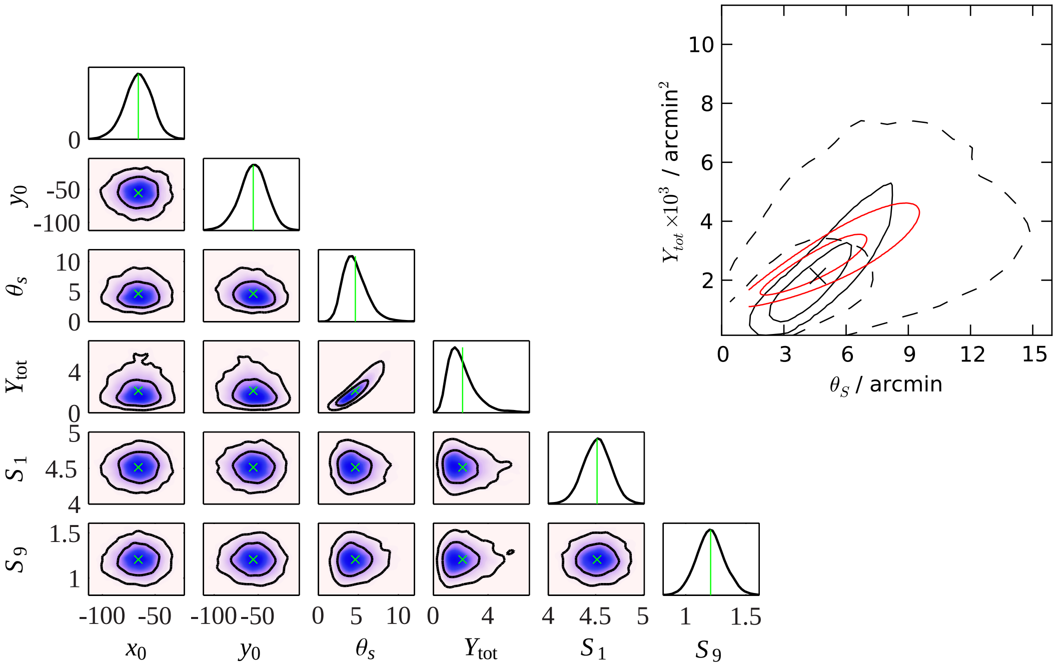

Figure 4.9: AMI posterior distributions for CAJ1858+2916 and the Y_{tot}-θ_s posterior overlaid with that obtained by *Planck* (upper right-hand corner).

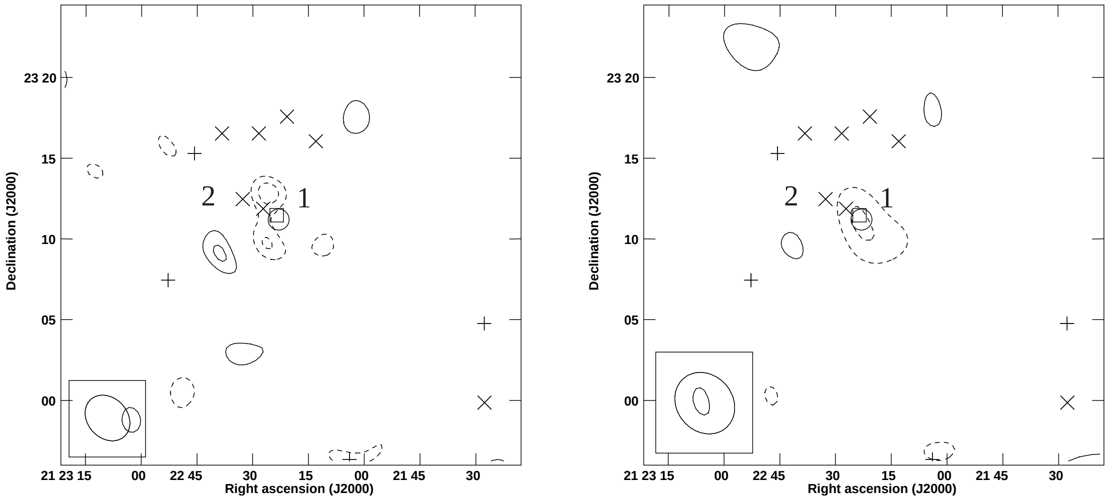

(a)

(b)

Figure 4.10: SA source-subtracted map of ZW8503 with natural weighting (a) and with a *uv*-taper (b) (see Section 4.2.3 for details). The r.m.s. noise levels are 89 and $122\,\mu$Jy beam^{-1} respectively. The numbered sources have posterior distributions for their flux densities plotted in Fig. 4.11.

gular size (≈ 8 arcmin as measured by *Planck*); it is therefore not too surprising that AMI does not detect it well. A decrement at the phase centre is visible in the source-subtracted maps, and a model with a cluster is favoured over one without by $\Delta \log_{10}(Z) = 1.6$, but there is not enough information in the AMI data to constrain the cluster parameters well, and the $Y_{\rm tot}$-θ_s posterior distribution is strongly influenced by the prior (plotted as a black dotted line for comparison). There is also significant degeneracy between the cluster parameters and the flux density of the closest source. The parameter space indicated by the *Planck* posterior is completely ruled out by the AMI posterior distribution. The AMI maps also show some substructure within the cluster, so the spherical, isothermal cluster model does not provide a good fit.

4.2.4.3 Non-detections

CAJ2146+2029

CAJ2146+2029 is associated with ZwCl 2143.5+2014. Despite having an SNR of 6.1 and being detected by all three of the *Planck* detection algorithms, it is not detected by AMI. There is no hint of a decrement at the phase centre, and the posterior distributions

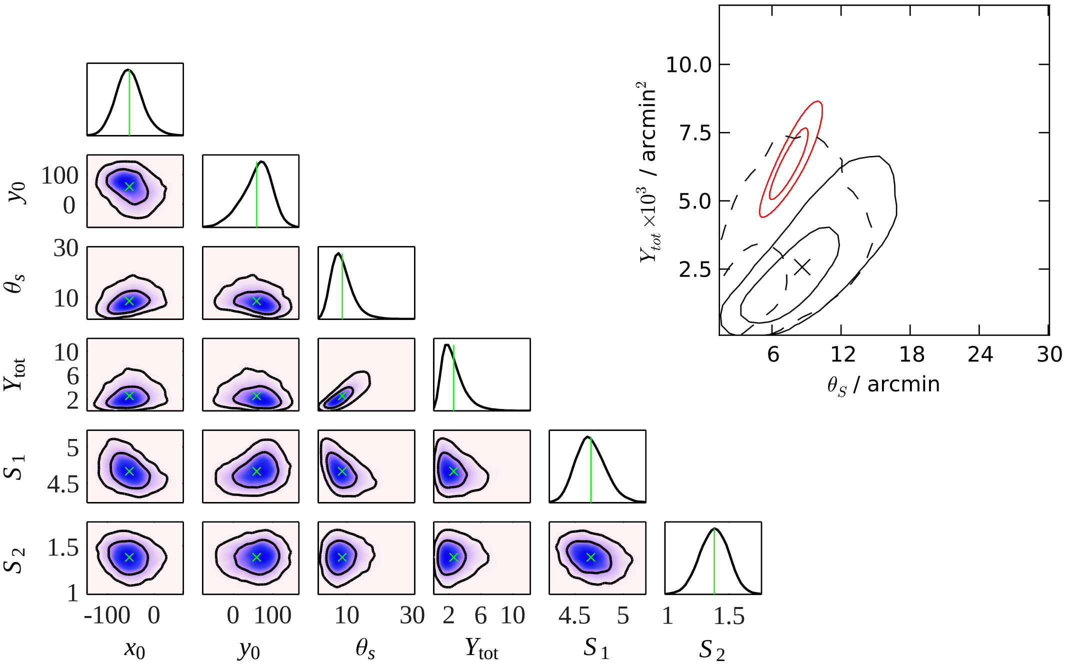

Figure 4.11: AMI posterior distributions for ZW8503 and the $Y_{\rm tot}$-θ_s posterior overlaid with that obtained by *Planck* (upper right hand corner).

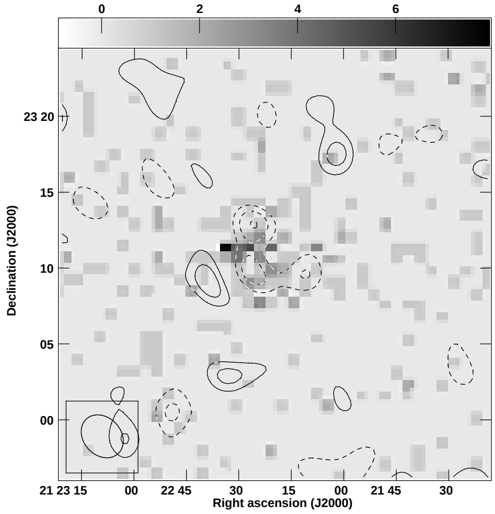

Figure 4.12: A ROSAT broad-band X-ray map of ZW8503 with the AMI-SA contours overlaid (at ±2 to $4 \times 100\,\mu$Jy) to show the substructure. The grey-scale is in units of counts and is not truncated.

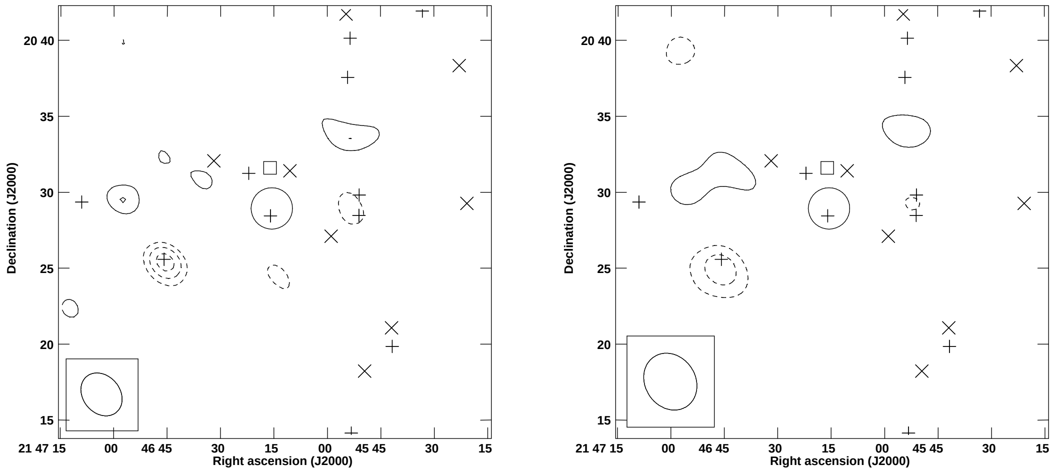

(a)

(b)

Figure 4.13: SA source-subtracted map of CAJ2146+2029 with natural weighting (a) and with a *uv*-taper (b) (see Section 4.2.3 for details). The r.m.s. noise levels are 124 and 180 μJy beam^{-1} respectively.

mostly recover the priors, ruling out the larger $Y_{\rm tot}$ values. A simulated cluster using the PwS maximum a-posteriori values for θ_s and $Y_{\rm tot}$, ‘observed’ using the same visibilities and noise levels as those in the real AMI observation, shows that this cluster should be detected at a SNR of ≈ 7 in the naturally-weighted map, and ≈ 9 in the *uv*-tapered map. If the cluster is not a spurious detection, it must therefore be much more extended than the *Planck* estimate shows (however, the redshift is given as 0.250 so this is not likely) and/or be significantly offset from the phase centre.

4.2.4.4 Effect of changing the θ_s vs $Y_{\rm tot}$ prior

Fig. 4.15 shows the effect of changing to the two-dimensional θ_s vs $Y_{\rm tot}$ prior on the mean parameter estimates. There is little overall change in θ_s, indicating that the data constrain this parameter well without being greatly influenced by the prior. For clusters with low values of $Y_{\rm tot}$, the two-dimensional prior slightly increases the $Y_{\rm tot}$ estimate; this is especially noticeable for the moderate detections. Conversely, for clusters with high values of $Y_{\rm tot}$ the two-dimensional prior systematically decreases the estimate by as much as 1σ. However, overall the changes are not very significant when the error-bars are taken into account (some representative 1σ error bars are plotted for context).

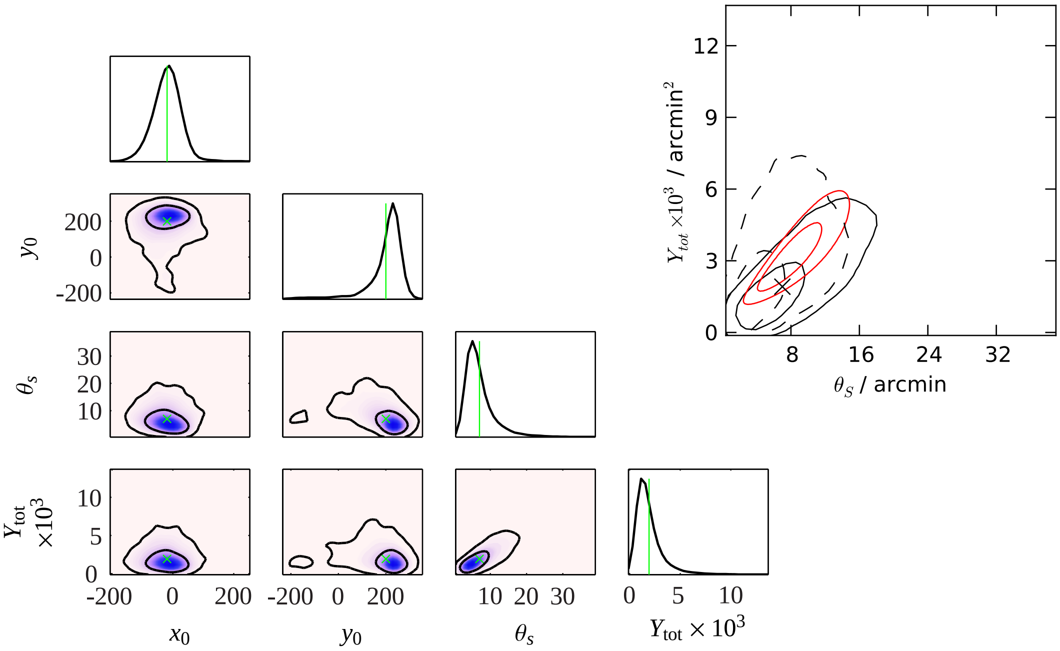

Figure 4.14: AMI posterior distributions for CAJ2146+2029 and the Y_{tot}-θ_s posterior overlaid with that obtained by *Planck* (upper right hand corner).

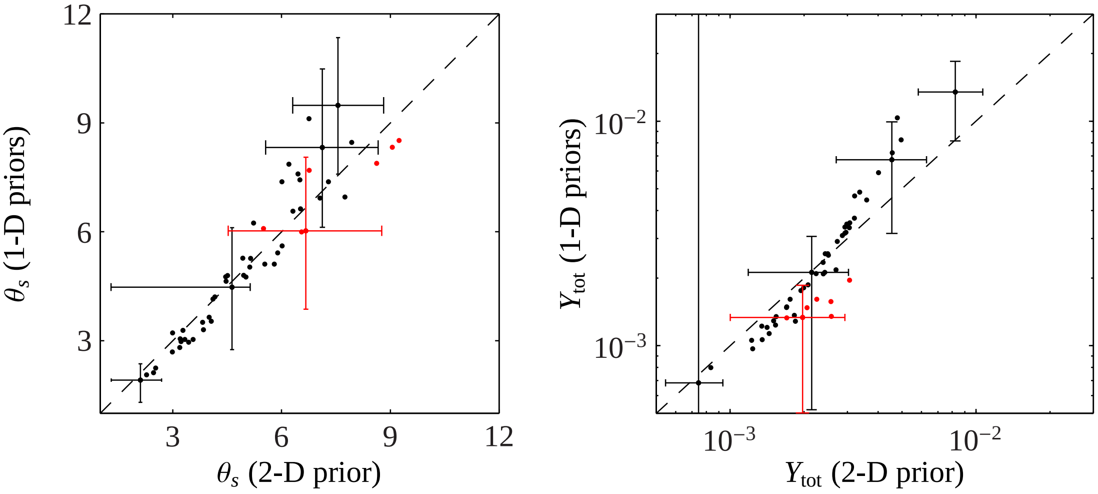

(a)

(b)

Figure 4.15: Mean parameter estimates of θ_s (a) and Y_{tot} (b) obtained using the new two-dimensional priors compared to the old one-dimensional priors, for clear (black) and moderate (red) detections. The one-to-one relationship is shown as a dashed line, and some 1σ error bars are plotted for as illustration.

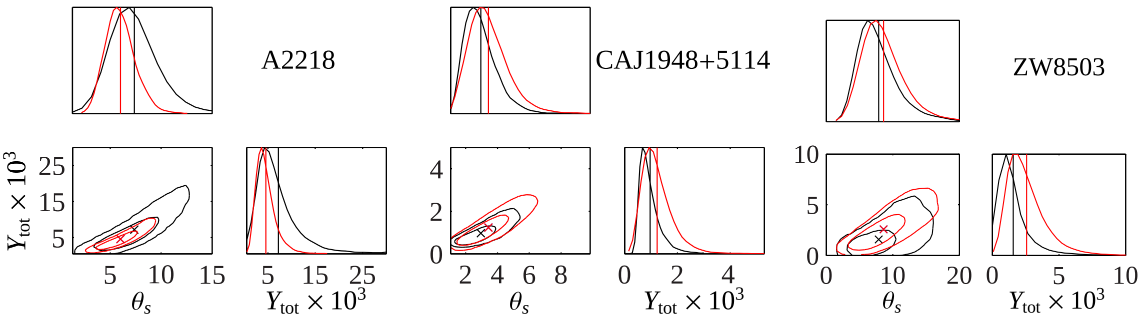

(a) (b) (c)

Figure 4.16: θ_s-Y_{tot} constraints for large (a) and small (b) angular size clusters in the 'clear detection' category, and a moderate detection (c), using the old, one-dimensional priors (black) and the new, two-dimensional prior (red). Posterior means are indicated with vertical lines and crosses.

Fig. 4.16 shows the marginalised one- and two-dimensional posteriors for A2218 and CAJ1948+5114 (a smaller angular size clear detection) and ZW8503 (the moderate detection from Section 4.2.4.2). In all three cases, the maximum a-posteriori (MAP) estimate is approximately the same, and the shift in the mean value is caused by the shrinking or widening of the posterior. Generally, for large angular-size clusters the posteriors shrink because the sampling points are restricted to the narrow area in $\theta_s - Y_{\mathrm{tot}}$ space allowed by the prior, which causes the apparent *decrease* in the mean values of Y_{tot} seen in Fig. 4.15. For small angular-size clusters, the opposite is true. The two-dimensional prior does not pull the sampling points so sharply towards the (0,0) point in $\theta_s - Y_{\mathrm{tot}}$ space, so the posteriors widen slightly, causing the apparent *increase* in the mean value of Y_{tot}.

4.3 AMI-*Planck* comparison

4.3.1 Positional comparison

The higher angular resolution of AMI enables a more accurate positional estimate to be produced for the clusters (although in practice this depends on a variety of factors such as signal-to-noise over the angular scales observed by both telescopes, and how successful the decoupling of the signal from the foregrounds is), and the accuracy of

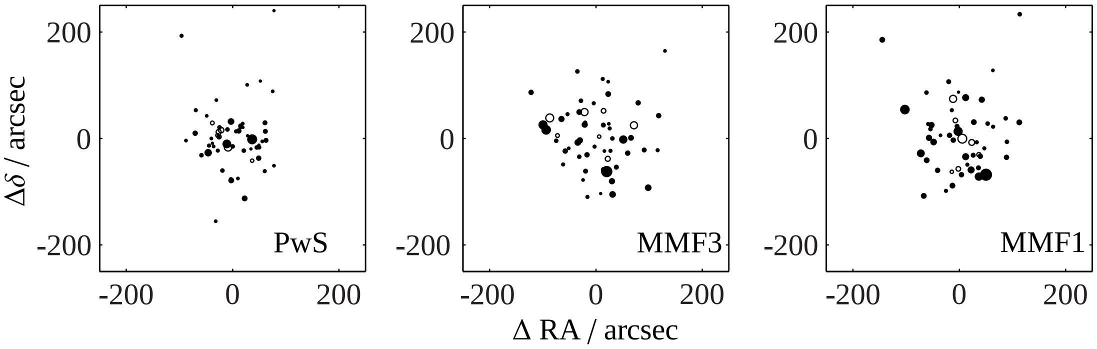

Figure 4.17: Positional offset from AMI for the three *Planck* detection algorithms. The size of the points plotted increases with increasing *Planck* SNR; clear detections are plotted as filled circles, and moderate detections as empty circles.

the *Planck* positions and error estimates can be checked. Fig. 4.17 compares positional offsets between AMI and the three *Planck* detection algorithms. The offsets for MMF1 and MMF3 are very similar. The PwS offsets are slightly more clustered toward zero, and also show a greater correlation with the SNR (i.e. the highest SNR points are closer to zero than the low-SNR points).

The MMF1 algorithm does not currently output positional errors, so Fig. 4.18 shows the distribution of positional offsets normalised by the total error $\left(\sqrt{\sigma^2_{\mathrm{AMI}} + \sigma^2_{Planck}}\right)$ for PwS and MMF3 only; a Rayleigh distribution, $(x/\sigma^2)\exp(-x^2/2\sigma^2)$ with $\sigma = 1$, is plotted for comparison – this is the expected distribution assuming the errors in RA and δ are uncorrelated and normally distributed. The PwS distribution is a good match, showing that the error estimates are a good representation of the true uncertainty in the positions. In contrast, the MMF3 errors are generally over-estimated.

4.3.2 Y_{tot}-θ_s comparison

A major conclusion of the 11-cluster paper was that the clusters were found overall to be smaller in angular size and fainter (lower Y_{tot}) by AMI than by *Planck*. The comparison for the larger sample shows a similar trend. Fig. 4.19 shows the comparison between the AMI and PwS MAP values for the entire sample of clear and moderate detections. Aside from some outliers, the θ_s values do not show a bias, but are only weakly correlated with a Pearson correlation coefficient of 0.31 (0.25) for all clusters

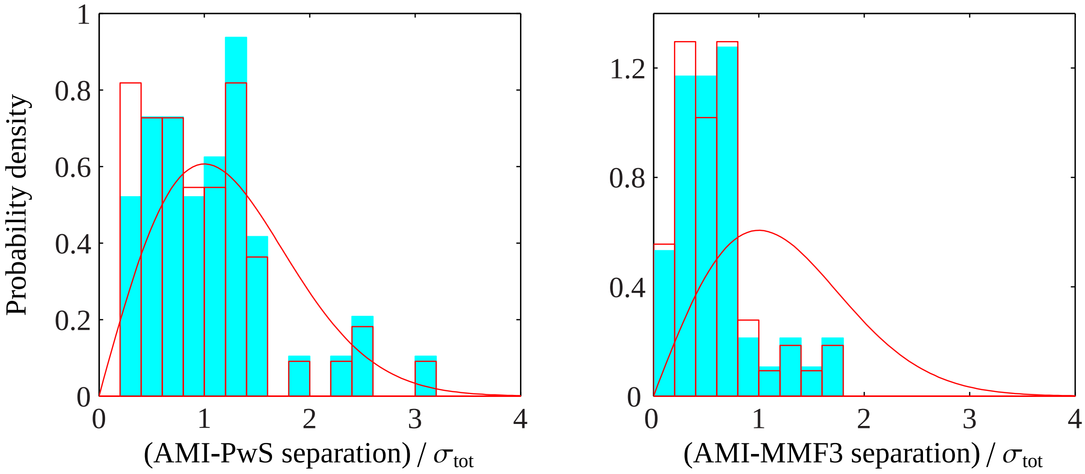

Figure 4.18: Positional offset from AMI, normalised by total error $\sigma_{\rm tot} = \sqrt{\sigma^2_{\rm AMI} + \sigma^2_{Planck}}$, for PwS and MMF3. The solid histogram shows the clear detections only, and the red outline shows clear and moderate detections together. A Rayleigh distribution is plotted in red for comparison.

detected (clear detections only). However, the $Y_{\rm tot}$ values as measured by AMI are still lower overall than the *Planck* values. The comparison between AMI and the MMF algorithms is very similar.

This inconsistency could be due to the fact that AMI does not measure $Y_{\rm tot}$ directly, since it is an interferometer and therefore resolves out the larger scales; as long as the cluster is resolved, the zero-spacing flux, and therefore $Y_{\rm tot}$, is never measured directly. However, in this case the discrepancy should be worse for larger angular-size clusters since more of an extrapolation is required to infer the zero-spacing flux. Fig. 4.20(a), in which the ratio of the $Y_{\rm tot}$ values is plotted as a function of θ_s, shows that this is not the case; the discrepancy is clearly present for both small and large angular-size clusters. In Fig. 4.20(b) the correlation betweeen θ_s and $Y_{\rm tot}$ is plotted as measured by AMI and *Planck*, and it is clear that the discrepancy occurs over the entire sample.

4.3.3 Potential origins of the discrepancy

Several potential origins of the discrepancy were investigated in the 11-cluster paper, as follows.

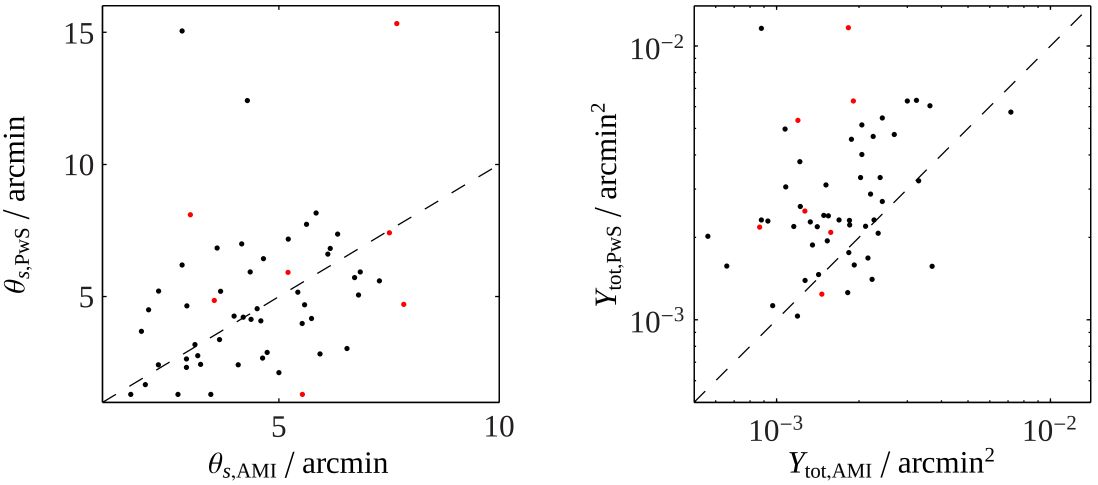

Figure 4.19: Comparison between PwS and AMI MAP Y_{tot} and θ_s values. Clear detections are plotted in black, and moderate detections in red. The one-to-one relationship is plotted as a black dashed line.

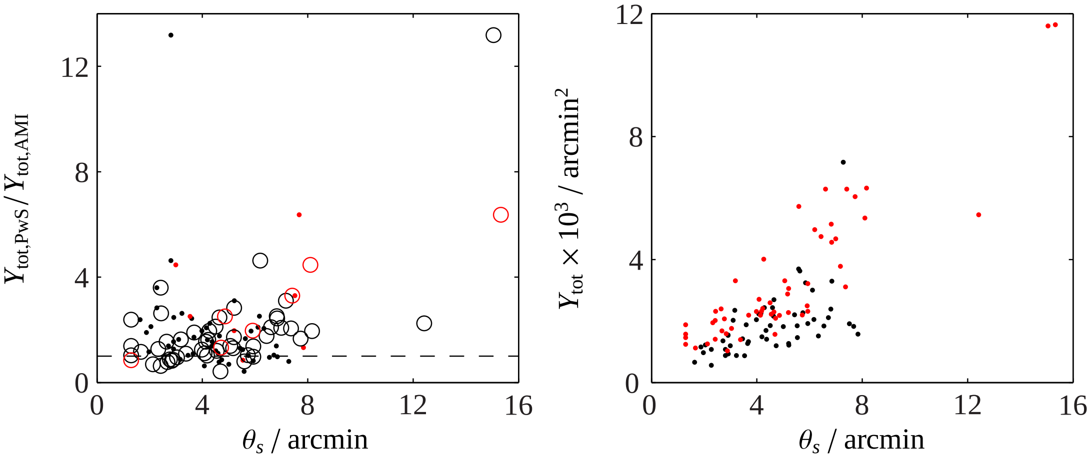

(a) (b)

Figure 4.20: (a) shows a comparison between PwS and AMI MAP Y_{tot} values as a function of θ_s, with solid dots (open circles) indicating AMI (PwS) θ_s values. Clear detections are plotted in black, and moderate detections in red, and the one-to-one relationship is plotted as a black dashed line. (b) shows Y_{tot} as a function of θ_s as measured by AMI (black) and PwS (red) for all of the moderate and clear detections.

1. The possibility that a population of faint sources existed below the LA detection threshold and acted to 'fill in' the decrement was investigated by obtaining very deep LA observations toward the central pointing of the raster, obtaining r.m.s. noise levels $\lessapprox 30\,\mu$Jy beam^{-1}, and the cluster parameters were re-extracted, subtracting any extra sources detected. In one case this shifted the $Y_{\rm tot}$ estimate upward by $\approx 1\sigma$, but the parameters for the remaining 10 cases were not significantly changed. This is clearly not the source of the discrepancy.

2. In the 11-cluster paper, to eliminate any effects from differing centroid positions, the AMI and *Planck* data were both analysed with the position of the cluster fixed to the best-fit position obtained from an initial AMI analysis where the central position was allowed to vary. Fixing the position also had a negligible effect on the derived θ_s and $Y_{\rm tot}$ posterior distributions.

3. For five clusters with measured X-ray profiles, the cluster parameters were re-extracted using the appropriate fitted γ and α parameters rather than the 'universal' parameters. This did not significantly improve the agreement. Note that the parameter affecting the cluster outskirts, β, was not varied since the X-ray data does not extend to this region. See the 11-cluster paper for more detail.

When a point source very near the cluster centre is fitted simultaneously with the cluster model, there is often a correlation between the point source flux and the $Y_{\rm tot}$ value, i.e. the data can constrain the sum of the point source flux and the cluster flux well, but not separate the two components. This effect can lead to biases in the fitted $Y_{\rm tot}$ values and worsens for smaller angular-size clusters since it becomes more difficult to differentiate between the profiles in *uv*-space of a marginally-resolved cluster and an unresolved point source. To test whether this could cause the discrepancy, I replotted Fig. 4.20 using only clusters with no fitted sources within 3 arcmin of the cluster position. This is shown in Fig. 4.21; the discrepancy is clearly not resolved.

Another potential problem is the mismatch between the spherical model and the real data; the higher resolution AMI data will be much more sensitive to this issue than the *Planck* data (in some cases, also dependent on other factors as discussed in Section 4.3.1). Some of the clusters have clearly non-spherical shapes in the AMI maps, but modelling with an ellipsoidal GNFW profile does not change the constraints on $Y_{\rm tot}$ and θ_s significantly.

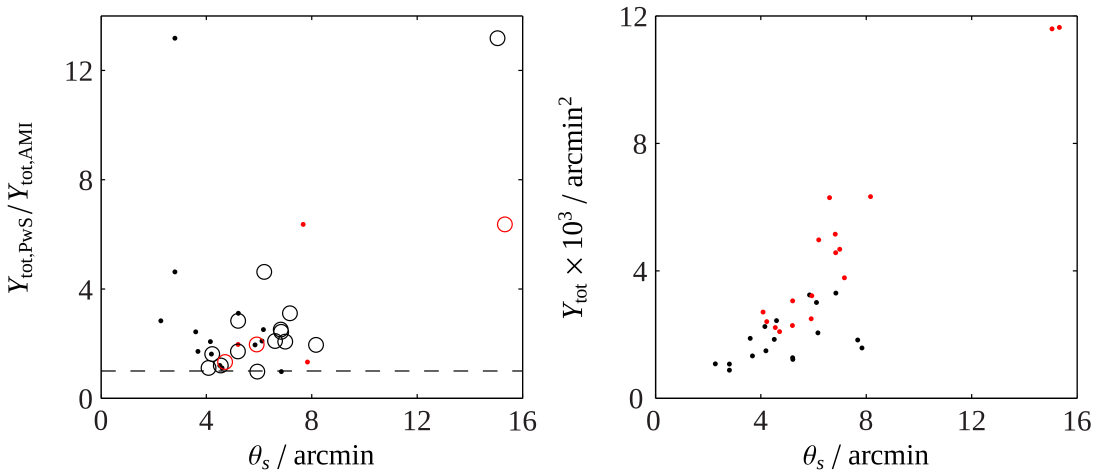

(a) (b)

Figure 4.21: (a) shows a comparison between PwS and AMI MAP $Y_{\rm tot}$ values as a function of θ_s for clusters selected to have no radio point sources within 3 arcmin of the cluster position, with solid dots (open circles) indicating AMI (PwS) θ_s values. Black points show clear detections and red points show moderate detections. In (b), the black (red) points show the AMI (PwS) values for the same clusters.

An outstanding issue is the effect of using a universal profile shape to model all clusters. In the following chapter, the potential for AMI data to constrain the GNFW profile parameters and the possible effect of variations of the shape on the derived parameters will be investigated.

4.4 Future work

Observations and analysis of the remainder of the sample with SNR $<$ 6 are ongoing; the whole catalogue, which continues to SNR of 4.5, will eventually be observed (within AMI's observing limits). At the time of writing, the total number of detections was 85 (69 clear), with 132 clusters remaining to be classified (see Fig. 4.22).

Many of the clusters in the catalogue have been or will be observed both with other SZ telescopes, and in other wavebands. Combining AMI data with these other datasets will allow testing of the current understanding of cluster physics, in particular enabling the investigation of cluster gas pressure profiles (discussed in more detail in Chapter 5).

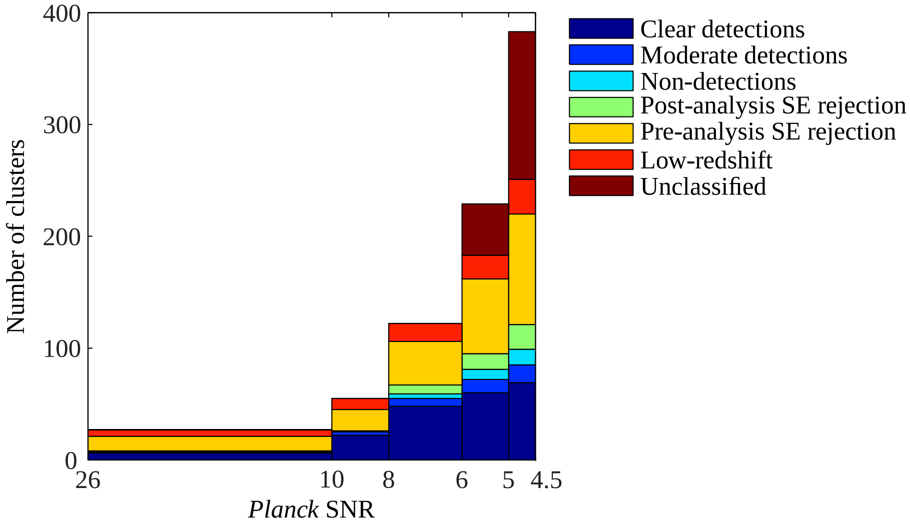

Figure 4.22: Cumulative count of clusters within AMI's observing limits in the entire *Planck* catalogue in various categories, as a function of SNR.

4.5 Conclusions

A sample of 59 clusters detected by *Planck* with SNR > 6 between $20^\circ \leq \delta \leq 87^\circ$ and with benign radio source environments have been followed up with AMI, and the clusters have been analysed assuming the 'universal' GNFW pressure profile. 55 are detected.

1. The effects of changing the prior on θ_s and $Y_{\rm tot}$ to a closer approximation to the real, correlated distribution have been tested and found to be minimal.

2. Comparison between the *Planck* and higher-resolution AMI positions have shown that the PwS positions and error estimates are more accurate than the corresponding MMF1 and 3 values.

3. Although the AMI and *Planck* θ_s values correlate weakly with no apparent bias, with the exception of some outliers, the *Planck* $Y_{\rm tot}$ values are systematically higher than those measured by AMI, irrespective of angular size. The potential to resolve the discrepancy by varying the profile shape parameters will be investigated in the following chapter.

Chapter 5

Cluster modelling

This chapter presents new analysis using simulations to investigate the effect of differing cluster gas pressure profile shapes on the parameter constraints that AMI produces, and to assess the potential for constraining the shape of the profile using the GNFW parameterisation using AMI data.

5.1 Generalised Navarro-Frenk-White profile

Numerical simulations have shown that the equilibrium density profiles of dark matter halos of galaxy clusters in CDM universes can be described by a universal parameterisation, known as the Navarro-Frenk-White (NFW) profile (Navarro et al., 1996, 1997):

$$\frac{\rho(r)}{\rho_{\mathrm{crit},z}} = \frac{\delta_c}{(r/r_s)\,(1 + r/r_s)^2} \tag{5.1}$$

where ρ is the density of the cluster as a function of the physical radius r, $\rho_{\mathrm{crit},z} = 3H^2/(8\pi G)$ is the critical density of the Universe at the redshift of the cluster, r_s is a characteristic scale radius, and δ_c is a characteristic (dimensionless) density.

Since the gas pressure distribution is largely determined by the distribution of the (gravitationally dominant) dark matter component, the pressure profile should be well represented by a similar shape. Nagai et al. (2007) proposed a ‘generalised Navarro-

Frenk-White' (GNFW) pressure profile, given by

$$P_e(r) = P_0 \left(\frac{r}{r_s}\right)^{-\gamma} \left[1 + \left(\frac{r}{r_s}\right)^{\alpha}\right]^{(\gamma-\beta)/\alpha}, \tag{5.2}$$

and showed that the parameterisation was consistent with both numerical simulations and observational (X-ray) evidence. P_e is the electron pressure, P_0 is a normalising constant, r is the radius of interest and r_s is a characteristic scaling radius which determines the point at which the profile starts to fall off (cf. θ_c in the isothermal β model). The parameters α, β and γ describe the slope of the profile at radii $\approx r_s$, $\gg r_s$ and $\ll r_s$ respectively.

Given this model, the total integrated Comptonisation parameter, $Y_{\rm tot}$, is given by

$$Y_{\rm tot} = \frac{\sigma_T}{m_e c^2} \int_0^\infty P_e(r') 4\pi r'^2 {\rm d}r', \tag{5.3}$$

where σ_T is the Thomson scattering cross-section, m_e is electron mass and c is the speed of light and spherical symmetry is assumed. When physical parameters are being considered, it is useful to define a 'concentration parameter' $c_X \equiv r_X/r_s$ so that quantities at a given overdensity radius X (radius internal to which the mean density is $X \times \rho_{{\rm crit},z}$) can be easily calculated, i.e.

$$P_e(r) = P_0 \left(c_X \frac{r}{r_X}\right)^{-\gamma} \left[1 + \left(c_X \frac{r}{r_X}\right)^{\alpha}\right]^{(\gamma-\beta)/\alpha}. \tag{5.4}$$

However, in this chapter I will consider a version of the GNFW profile in which clusters are parameterised only in terms of their appearance on the sky, i.e.

$$\begin{aligned}
P_e(\theta) &= P_0 \left(\frac{D_A\theta}{D_A\theta_s}\right)^{-\gamma} \left[1 + \left(\frac{D_A\theta}{D_A\theta_s}\right)^{\alpha}\right]^{(\gamma-\beta)/\alpha} \\
Y_\theta &= \frac{4\pi\sigma_T}{m_e c^2} P_0 D_A \int_0^\infty \left(\frac{\theta'}{\theta_s}\right)^{-\gamma} \left[1 + \left(\frac{\theta'}{\theta_s}\right)^{\alpha}\right]^{(\gamma-\beta)/\alpha} \left(\frac{\theta'}{\theta_s}\right)^2 \theta_s^3 d\left(\frac{\theta'}{\theta_s}\right),
\end{aligned} \tag{5.5}$$

where $Y_\theta \equiv Y_{\rm tot}/D_A^2$, θ is the angular scale on the sky of interest, $\theta_s \equiv r_s/D_A$ is the characteristic scale in angular coordinates, and D_A is the angular diameter distance to the cluster. This equation has an analytic solution (e.g. Gradshteyn et al. 2007),

$$Y_\theta = \frac{4\pi\sigma_T}{m_e c^2} P_0 D_A \theta_s^3 \frac{\Gamma\left(\frac{3-\gamma}{\alpha}\right)\Gamma\left(\frac{\beta-3}{\alpha}\right)}{\alpha\Gamma\left(\frac{-\gamma+\beta}{\alpha}\right)}, \tag{5.6}$$

which for a given Y_θ and θ_s defines the normalisation constants. Note that $\lim_{x\to 0}\Gamma(x) = \infty$, so there are non-differentiable points in equation 5.6 at $\beta = 3$, $\gamma = 3$ and $\gamma = \beta$. Y_θ is also not differentiable at $\alpha = 0$. From this point onwards, I use Y_{tot} to refer to Y_θ.

To describe the observed profile of a cluster on the sky, the three-dimensional pressure profile is integrated along the line of sight to produce a two-dimensional projected profile, and is converted to the Comptonisation parameter via

$$y(\theta) = \frac{\sigma_T}{m_e c^2}\int_{-\infty}^{\infty} P_e(\sqrt{\theta^2 + z^2})dz. \tag{5.7}$$

This has an analytical solution at $\theta = 0$; for other radii the integral is performed numerically, with cut-offs at $\theta_{\mathrm{min}} = 0.2$ and $\theta_{\mathrm{max}} = 20$ arcmin. Past θ_{max}, the profile has fallen off sufficiently to be ≈ 0; if θ_{min} is made smaller, the integral is slow to converge. The effect of changing these limits was tested for the 11-cluster paper, and found to be negligible. This two-dimensional 'y-map' is then converted to an intensity decrement map, Fourier-transformed to the uv-plane, and compared with the data.

5.2 Universal GNFW profile

Arnaud et al. (2010) used the REXCESS sample to find an average profile for clusters at low redshift by fitting GNFW pressure profiles to X-ray data to constrain α, γ and c_{500}, and to numerical simulations to constrain β. They define a 'universal' profile with parameter values $[\alpha, \beta, \gamma, c_{500}] = [1.0510, 5.4905, 0.3081, 1.177]$. Within the sample, the best-fit parameter values range between 0.33 – 2.54, 0.000 – 0.860, and 0.17 – 2.16 for α, γ and c_{500} respectively. Fig. 5.1 shows the 'universal' profile along with profiles calculated by varying each parameter to its extreme values from the REXCESS sample, to show the effect that each parameter has on the profile.

When not relating the observed quantities to an over-density radius, the concentration parameter is irrelevant and the cluster profile can be completely described by the parameters Y_{tot}, θ_s, α, β and γ.

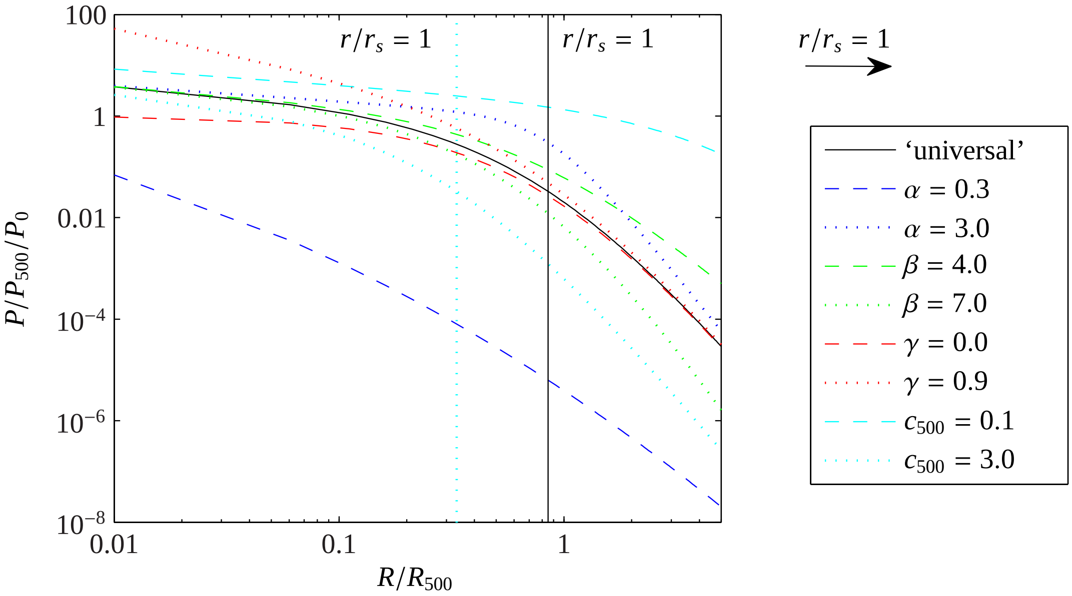

Figure 5.1: Variation in pressure profile produced by varying single parameters in the GNFW model, compared to the 'universal' profile. Vertical lines show the relationships $r/r_s = 1$ (depending only on c_{500}); when $c_{500} = 0.1$, $r/r_s = 1$ corresponds to $R/R_{500} = 10$, off the scale of the plot.

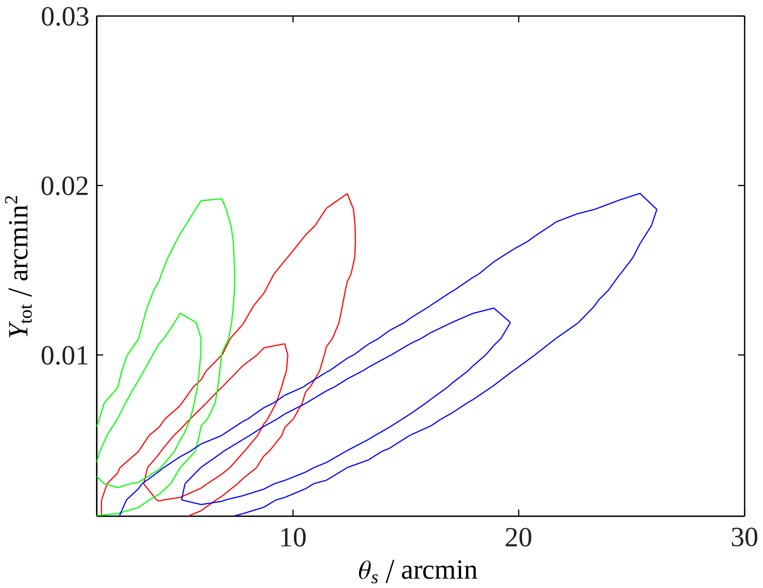

Figure 5.2: Constraints on $Y_{\rm tot}$ and θ_s for A2218 (real data), using three different sets of α,β and γ: the 'universal' parameter values (red), an extreme individual profile from the REXCESS sample (green), and the average profile parameter values from an analysis of *Planck* data (blue). The contours are at the 68% and 95% confidence limits.

5.3 Effects on AMI constraints

Is a change in parameter values significant for the constraints produced from AMI data? Fig. 5.2 shows the $Y_{\rm tot}$-θ_s constraints assuming three different sets of (γ, α, β): the 'universal' values, an extreme individual example from the REXCESS data set with values (0.065, 0.33, 5.49), and the average parameter values produced from *Planck* data in Planck Collaboration et al. (2013d) with values (0.31, 1.33, 4.13). It is clear that there are large differences both in the shape of the constraints produced and the posterior mean and MAP values of $Y_{\rm tot}$ and θ_s; this is a problem that must be addressed.

The effects of changing the shape parameter values of the GNFW profile on AMI data are heavily dependent on the angular size of the cluster. The effect of varying the values on a cluster's profile in *uv*-space is demonstrated in Fig. 5.3 for the smallest and largest angular size clusters in the *Planck* sample that are well-detected by AMI. These have angular sizes $\theta_s = 1.8$ and 9.5 arcmin respectively (as determined by AMI, but consistent with *Planck*). As in Fig. 5.1, the shape parameter values are varied to the

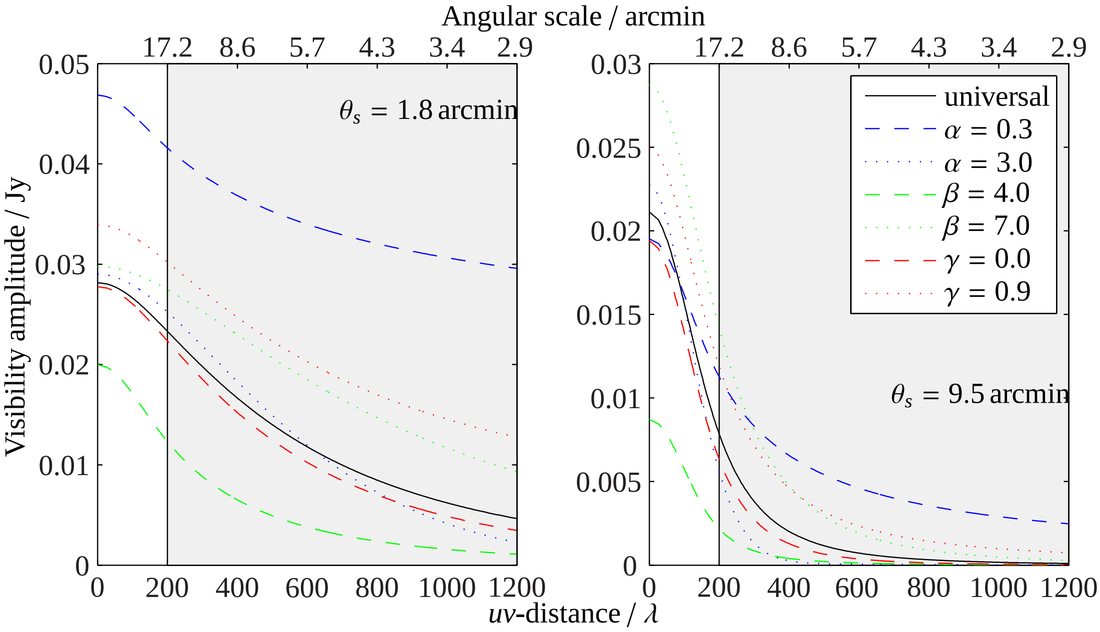

(a) (b)

Figure 5.3: Visibility amplitude profiles in *uv*-space for a small (a) and large (b) angular size cluster; note that the ordinate scales are very different. The grey shaded area shows the AMI-SA range of baselines.

extremes of the REXCESS sample to illustrate the variation produced.

For the small angular size cluster, the range of baselines probed by AMI corresponds to $1.6 < \theta/\theta_s < 9.6$, so the shape of the profile is most affected by the β parameter. For the large angular size cluster, the range of baselines corresponds to $0.3 < \theta/\theta_s < 1.8$, so α is the most important parameter. In this case, Y_{tot} will also be very poorly constrained since most of the flux of the cluster is resolved out. The majority of clusters will fall somewhere between these two extremes in angular size, and the AMI data will be affected by the real values of both α and β. In all cases, however, AMI data are not of high enough resolution to provide information on γ and so a change in γ will correspond to a change in the overall amplitude of the data rather than the shape of the part of the profile observed by AMI.

5.3.1 Simulations

In order to investigate more thoroughly the effect of changing the GNFW shape parameter values on the constraints on $Y_{\rm tot}$ and θ_s produced by AMI data, I created a bank of simulations loosely based on the REXCESS sample. Since the angular size of the cluster has a large effect on the constraints, I chose three representative values of θ_s and chose $Y_{\rm tot}$ values for each based on clusters in the *Planck* follow-up sample that are well-detected by AMI and have similar θ_s values. The parameter values are $(\theta_s, Y_{\rm tot}) = (1.8, 0.0009), (4.5, 0.001)$ and $(7.4, 0.007)$, based on CAJ0441+6813, CAJ0303+7755, and A2218 – these represent clusters that are only partially resolved; resolved but still well covered by the AMI-SA range of baselines; and mostly resolved out by the AMI-SA. For each of the three angular sizes, I simulated clusters with the 31 pairs of (γ, α) values fitted to the individual clusters in the REXCESS sample. Little is known about the distribution of β since X-ray data do not extend far enough into the cluster outskirts to provide information on it. A first attempt was made at measuring this parameter using the SZ signal measured by *Planck* for a sample of 62 clusters in Planck Collaboration et al. (2013d), but this sample was selected on the basis of *Planck* SNR, and is neither representative nor complete. In addition, the analysis does not take into account the non-differentiable points in the equations describing the SZ signal and so non-physical models are not excluded from the set of solutions; there are also large degeneracies between the parameters, and so although a best-fit value of $\beta = 4.13$ to the stacked profile was reported, their Fig. 5 shows a range of approximately 3 to 7 at 68% confidence level, with only a slight peak at 4.13. I therefore drew values of β for each cluster from a uniform distribution $U[4.5, 6.5]$ centred about the 'universal' value.

The *uv*-coverage of an observation depends on declination, so for a fair comparison all clusters were simulated at $\delta = 50^\circ$ (roughly the midpoint of the SA observing range). A simulated observation was performed over the usual HA range of -4 to 4 hours, and thermal noise of 0.697 Jy was added to each 1-s visibility. This gives a total noise close to the nominal level for the entire array, i.e. $0.697/\sqrt{N_{\rm base} \times N_{\rm chan}} = 30\,{\rm mJy\,s^{-1/2}}$ where $N_{\rm base} = 90$ is the number of baselines and $N_{\rm chan} = 6$ is the number of channels. Two 'days' (2×8 hrs) of observation were simulated giving a total thermal noise level of $125\,\mu{\rm Jy\,beam^{-1}}$, close to the nominal observing noise level on the SA for

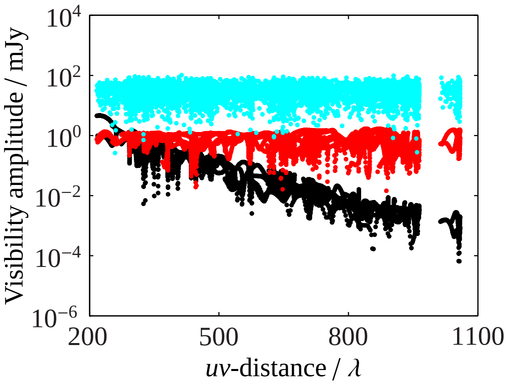

Figure 5.4: Noise added to the simulated visibilities as a function of *uv*-distance. The black, red and cyan points are CMB anisotropy noise, source confusion noise and thermal noise respectively.

the *Planck* sample (in practice, this is usually an upper limit).

Noise due to source confusion was also added to the simulations by creating and adding (in map-space) a random population of sources with flux densities between 10 and 400 μJy, with the distribution drawn from the 10C source count. The 400 μJy upper limit assumes that the LA noise level is 100 μJy beam^{-1} in the centre of the map, and source detection is performed at 4σ so that all sources above 400 μJy beam^{-1} have been detected and removed. Finally, CMB noise was added assuming the spectrum derived from the 7-year *Wilkinson Microwave Anisotropy Probe* (WMAP) results (Komatsu et al., 2011). For each visibility, the power at the corresponding ℓ value was randomised slightly to simulate sky variance, and a real and imaginary part with randomised phase was simulated. The added noise is shown as a function of *uv*-distance in Fig. 5.4. For the shortest baselines, the CMB noise is more important than the source confusion noise, and the opposite is true on longer ($\gtrsim 300\,\lambda$ baselines. The thermal noise is the dominant noise source overall.

The simulations were then analysed using the standard pipeline described in Chapter 4 (with no source subtraction). The resulting constraints on θ_s and $Y_{\rm tot}$ are plotted in Fig. 5.5, along with the constraints resulting when the cluster is simulated and recovered with the 'universal' profile for comparison. For the two smaller clusters, the true value is within the 68% confidence limit 29 times out of 31, but it is clear that the size and degeneracy direction of the contours varies wildly as the shape parameter values are changed; on the whole, the mean and MAP values of θ_s and $Y_{\rm tot}$ are biased upward.

For the larger cluster, the true value is within the 68% confidence limit only 2 times out of 31, and within the 95% confidence limit only 14 out of 31 times; on the whole, the mean and MAP values of θ_s and $Y_{\rm tot}$ are biased downward.

5.4 AMI constraints on cluster shape

Given that there is clearly information in AMI data on the shape parameters, it is interesting to consider whether there is enough information present to simultaneously constrain θ_s, $Y_{\rm tot}$ and any of the shape parameters. In order to investigate the intrinsic limitations and biases produced by the limited *uv*-coverage and the parameter degeneracies, I simulated clusters with the same three pairs of θ_s and $Y_{\rm tot}$, and using the 'universal' GNFW α, β and γ values, and added an unrealistically small amount of thermal noise to the visibilities ($100\,\mu$Jy s$^{-1/2}$) so that the cluster profile in *uv*-space was clearly visible. I then ran this through McAdam, first only varying θ_s and $Y_{\rm tot}$, using uniform priors to recover the likelihood distribution. The position offset parameters were given Gaussian priors centred on zero, with $\sigma = 1$ arcmin.

Even for this very low-noise case, since $Y_{\rm tot}$ is not directly measured by the telescope there is some degeneracy between θ_s and $Y_{\rm tot}$, especially for the two larger angular-size clusters. Larger-angular-scale clusters can be made to fit the data nearly as well as a cluster with the true parameter values by increasing $Y_{\rm tot}$. Fig. 5.6 shows the degeneracy and an example of a degenerate model for the cluster with $\theta_s = 7.4$.

I then allowed the three parameters α, β and γ to vary one at a time, giving them uniform priors. The widths of the priors on α and γ were based on the extreme values from the REXCESS sample. I set a wide prior on β with the lower limit at $\beta = 3$ because of the non-differentiable point in equation 5.6, and with an arbitrarily high upper limit of 9. In all cases, the positional offset priors were kept as Gaussian and were found to be uncorrelated with any other parameter. The priors are listed in Table 5.1.

Varying γ

Firstly, γ was varied while holding α and β fixed at the true values. Increasing γ makes the radial pressure profile of the cluster more peaked toward the centre (see Fig. 5.1). AMI data are not of high enough angular resolution to resolve this part of the

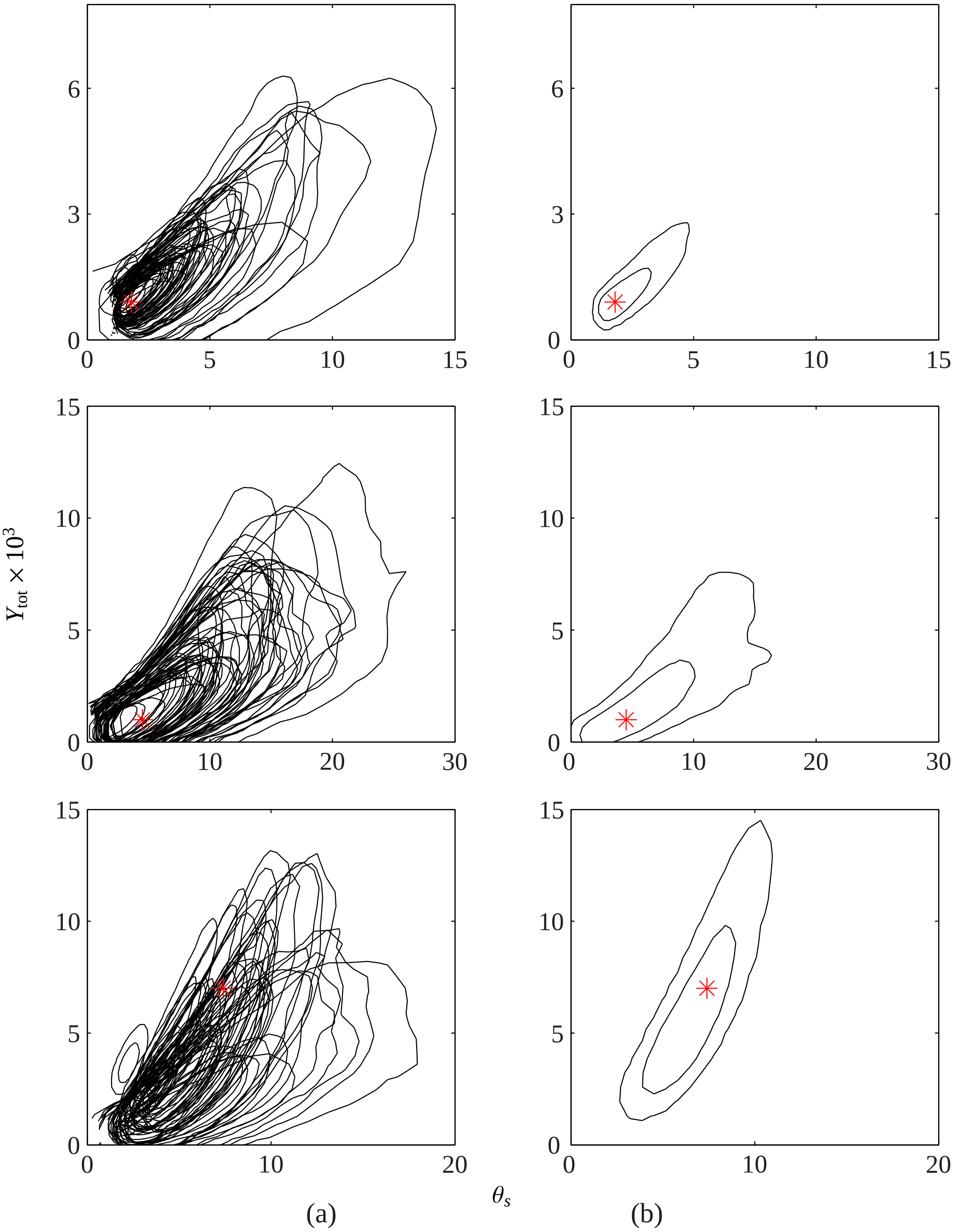

Figure 5.5: The posterior distribution for $Y_{\rm tot}$ and θ_s for simulated clusters with realistic noise levels (see text for details), and differing GNFW shape parameter values based on the REXCESS sample (a), and simulated with the 'universal' values (b). In all cases the model used for recovering the parameters has the shape parameter values fixed to the 'universal' values, and the joint two-dimensional posterior on $Y_{\rm tot}$ and θ_s is used. Results for three different angular sizes are shown (from top to bottom, $\theta_s = 1.8, 4.5$ and 7.4); the input parameter values are marked with red stars. The contours are at the 68% and 95% confidence boundaries.

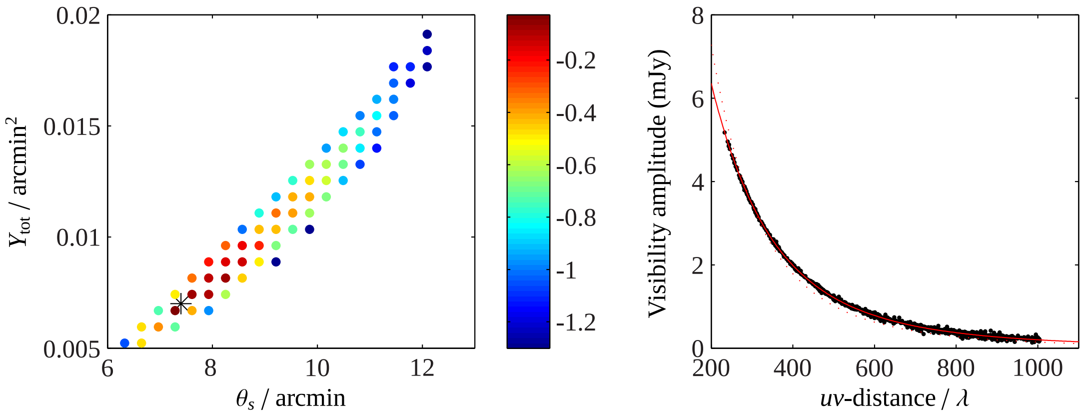

(a) (b)

Figure 5.6: (a) The degeneracy between $Y_{\rm tot}$ and θ_s, with uniform priors on both, for simulated low-noise data for a cluster with $\theta_s = 7.4$, with the input parameter values marked by the black star. The colour axis is in units of $\Delta \log(L) = \log(L) - \log(L_{\rm true})$, where $L_{\rm true}$ is the likelihood value for the input model. (b) shows the binned visibility data for channel 5 input to McAdam, and true cluster model (red line), and a model with $\theta_s = 10$ and $Y_{\rm tot} = 0.012$ (red dotted line), which provides a fit with $\Delta \log(L) \approx -0.6$ with respect to the true input model.

Table 5.1: Priors used on profile fit parameters

Parameter	Prior type	Lower limit	Upper limit
α	Uniform	0.1	3.0
β	Uniform	3	9
γ	Uniform	0.0	0.9
Y_{tot}	Uniform	0.0005	0.2
θ_s	Uniform	1.3	15
x_0	$\mathcal{N}(0, 1\,\mathrm{arcmin})$	-	-
y_0	$\mathcal{N}(0, 1\,\mathrm{arcmin})$	-	-

cluster, so as shown in Fig. 5.3, changing γ produces a shift in the overall amplitude of the *uv*-profile, rather than in the shape. The likelihoods for the three simulated clusters are shown in Fig. 5.7, showing the degeneracies between Y_{tot}, θ_s and γ. In all three cases the $Y_{\mathrm{tot}} - \theta_s$ degeneracy has been broadened and stretched to include much higher values of θ_s. For the largest cluster, this can be seen by comparison to Fig. 5.6. This shows that models of clusters which are mostly resolved out by AMI can appear to fit the data by increasing γ and hence increasing the flux of the cluster over the AMI-SA range of baselines. In the one-dimensional marginal posterior distributions (Fig. 5.8), this effect translates into a spurious constraint on γ, simply because more θ_s-Y_{tot} parameter space is available for a higher value of γ. For the two resolved clusters, θ_s and Y_{tot} are also pushed higher than their true values for the same reason. Because of this spurious constraint, I choose to fix γ at the 'universal' value of 0.3081 for future analyses. The effect of choosing an incorrect γ value will be investigated in following sections. Note also that for previously known clusters, a value for γ based on higher-resolution X-ray data is often known.

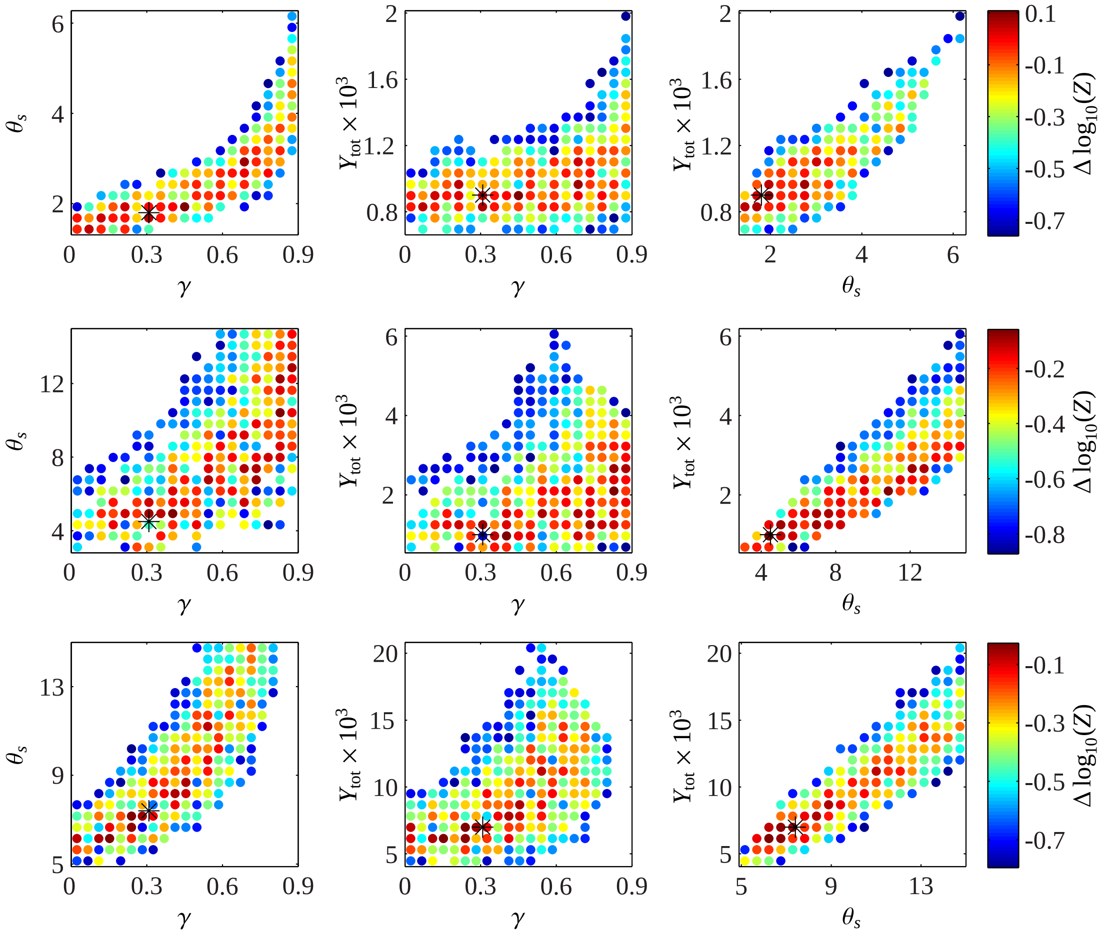

Figure 5.7: The degeneracies between $Y_{\rm tot}$, θ_s and γ for simulated low-noise data, for clusters with $\theta_s = 1.8$ (top), 4.5 (centre) and 7.4 (bottom), using uniform priors on all three parameters. The input values are indicated by a black star.

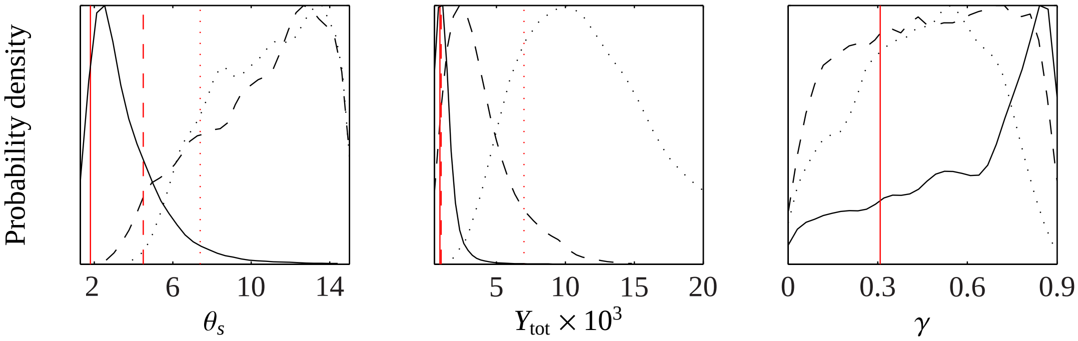

Figure 5.8: The one-dimensional marginal constraints on $Y_{\rm tot}$, θ_s and γ for simulated low-noise data, for clusters with $\theta_s = 1.8$ (solid lines), 4.5 (dashed lines) and 7.4 (dotted lines), using uniform priors on all three parameters. Input values are shown as red lines.

Varying α

α is the natural parameter to vary for the two larger clusters, where the AMI-SA baselines cover $\approx (0.6 \text{ to } 4) \times \theta_s$ and $\approx (0.4 \text{ to } 2) \times \theta_s$ respectively. The data for the smallest cluster should not contain much information on α since the AMI-SA baselines cover $\approx (1.6 \text{ to } 10) \times \theta_s$.

Fig. 5.9 shows that a low value of α tends to allow higher values of θ_s and therefore also of $Y_{\rm tot}$. Inspection of Fig. 5.1 confirms that a low value of α tends to flatten the *uv*-profile of a small angular-size cluster, making it resemble that of a larger angular-size cluster, and giving it a larger amplitude overall.

In the one-dimensional marginal posterior distributions (Fig. 5.10), as expected the two larger angular-size clusters produce a constraint on α. However, as when γ was varied, θ_s is pushed higher because more parameter space is allowed by a low α value. Similarly, a spurious constraint on α is produced for the small angular-size cluster.

Varying β

The best constraints on β should be produced by the smallest angular size cluster, since the AMI-SA baselines cover $\theta \gg \theta_s$, and there should not be much information on β at all in the data for the largest angular size cluster, since the part of the *uv*-profile

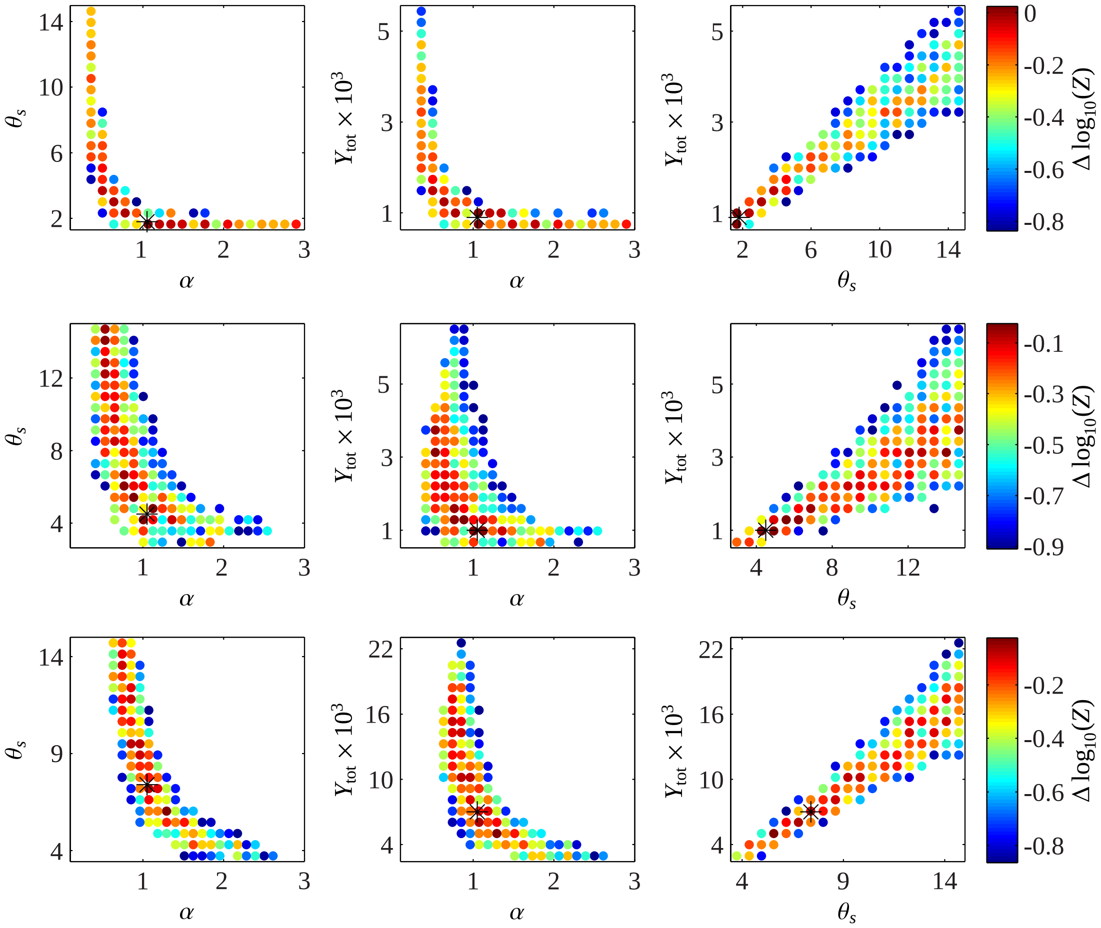

Figure 5.9: The degeneracies between $Y_{\rm tot}$, θ_s and α for simulated low-noise data, for clusters with $\theta_s = 1.8$ (top), 4.5 (centre) and 7.4 (bottom), with uniform priors on all three parameters. The input values are indicated by a black star.

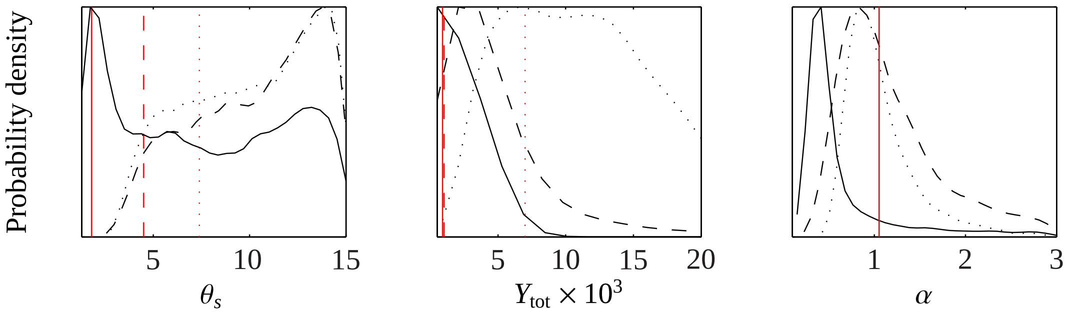

Figure 5.10: The one-dimensional marginal constraints on $Y_{\rm tot}$, θ_s and α for simulated low-noise data, for clusters with $\theta_s = 1.8$ (solid lines), 4.5 (dashed lines) and 7.4 (dotted lines), with uniform priors on all three parameters. Input values are shown as red lines.

which β governs is resolved out.

Initial runs with the planned prior range of $\beta = [3.0, 9.0]$ produced the 3-D degeneracy shown in Fig. 5.11 for the largest cluster (and similarly for the medium cluster). As β approaches 3, small (unresolved) cluster sizes become preferred, but $Y_{\rm tot}$ becomes essentially unconstrained. This is probably because of the discontinuity in equation 5.6. I therefore changed the range of the prior to $\beta = [3.5, 9.0]$.

Fig. 5.12 shows the likelihoods using the new prior range. There is a strong, nearly linear, correlation between β and θ_s for all of the clusters. This can be understood since at $\theta \gg \theta_s$, $P_{\rm e}(r) \approx P_0(\theta/\theta_s)^{-\beta}$. Increasing β causes the profile to fall off more steeply and resemble a profile generated with a larger value of θ_s, for a given range of θ; this effect is illustrated in Fig. 5.13.

Fig. 5.12 also shows that small values of β produce extremely large values of $Y_{\rm tot}$, especially for the larger clusters, which produces spurious constraints on β in the one-dimensional marginals (Fig. 5.14)

5.4.1 Priors derived from scaling relationships

Many of the problems caused by allowing the parameter values to vary stem from the fact that doing so opens up a new area of $\theta_s - Y_{\rm tot}$ parameter space with implausibly large values of θ_s. The two-dimensional joint prior on θ_s and $Y_{\rm tot}$ used in Chapter 4

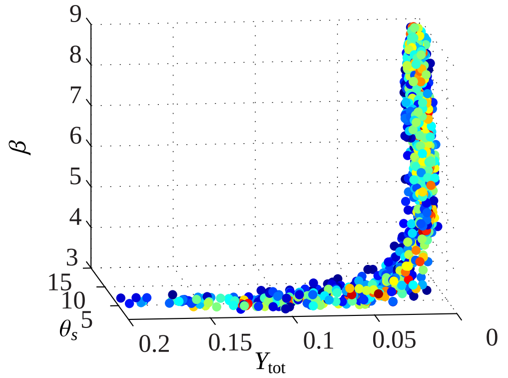

Figure 5.11: The degeneracy between $Y_{\rm tot}$, θ_s and β in 3-D for simulated low-noise data, for a cluster with angular size $\theta_s = 7.4$. The colour axis indicates the likelihood and is the same as in Fig. 5.12.

acts to suppress these regions of parameter space. As described in Planck Collaboration et al. (2013c), this prior was derived from an X-ray versus SZ scaling relation calibrated using *Planck* data for the highest SNR clusters, assuming the 'universal' pressure profile; it may therefore itself be affected by biases due to variation of the GNFW profile parameters. This should be considered in future analysis, but for the purpose of assessing the potential of AMI data to constrain the parameters, the current prior is a useful first step.

The two- and one-dimensional posterior distributions when α is varied, with the physically motivated prior on θ_s and $Y_{\rm tot}$, are shown in Fig. 5.15 and 5.16. For the smallest cluster, the results are similar to the previous results with uniform priors: the input values of θ_s and $Y_{\rm tot}$ are recovered well since these are well constrained by the data, but a spurious constraint of $\alpha \approx 0.7$ is produced because of the shape of the α-θ_s degeneracy. For the medium-size cluster, the results are more promising: the input values of θ_s and $Y_{\rm tot}$ are recovered well and α is constrained (weakly) to approximately the correct value. For the largest cluster, the constraints on θ_s and $Y_{\rm tot}$ are now heavily influenced by the prior and the input values are not recovered; to compensate, α is pushed to higher values.

The corresponding posteriors when β is varied are shown in Figs. 5.17 and 5.18. For the smallest cluster, the results are better than the previous results with uniform priors: θ_s and $Y_{\rm tot}$ are recovered reasonably well, and there is some constraint on β, but the constraint on β is weak and favours higher values than the input because of the

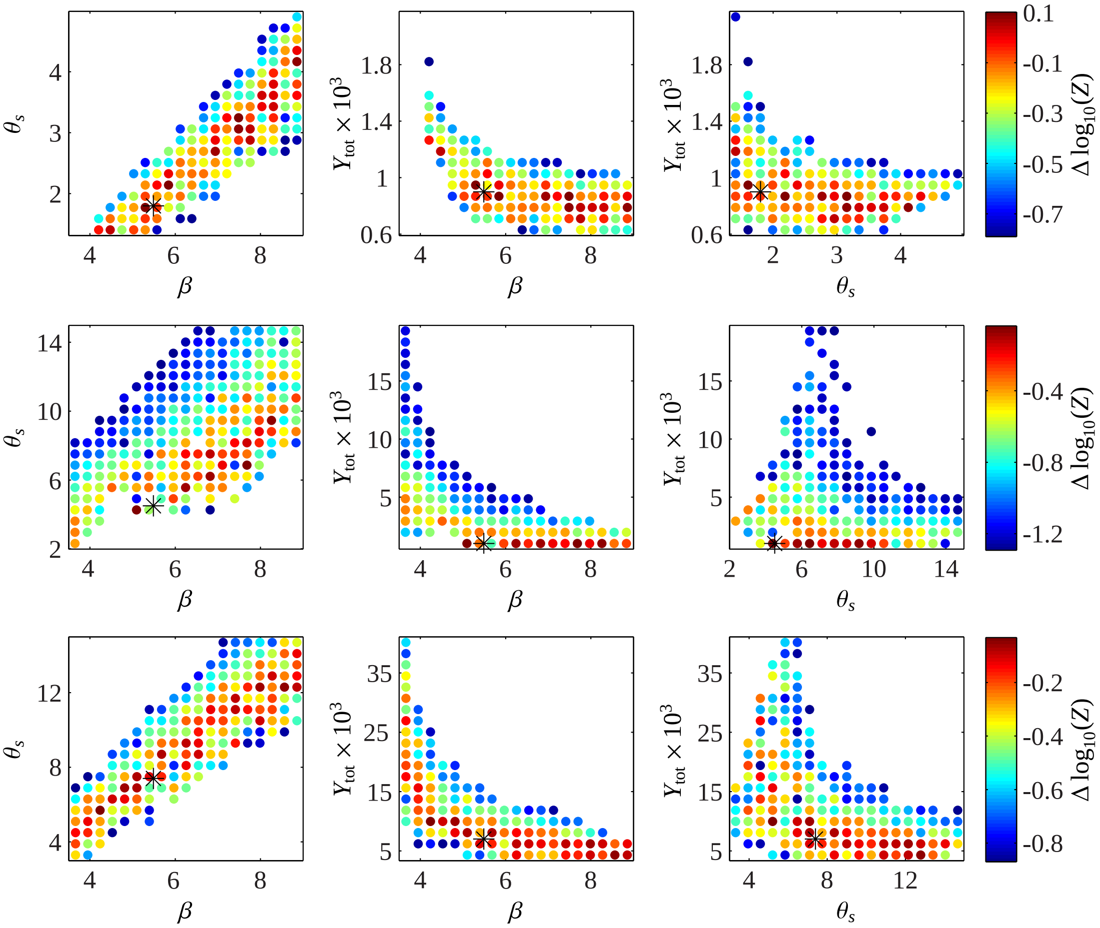

Figure 5.12: The degeneracies between Y_{tot}, θ_s and β for simulated low-noise data, for clusters with $\theta_s = 1.8$ (top), 4.5 (centre) and 7.4 (bottom), with uniform priors on all three parameters. The input values are indicated by a black star.

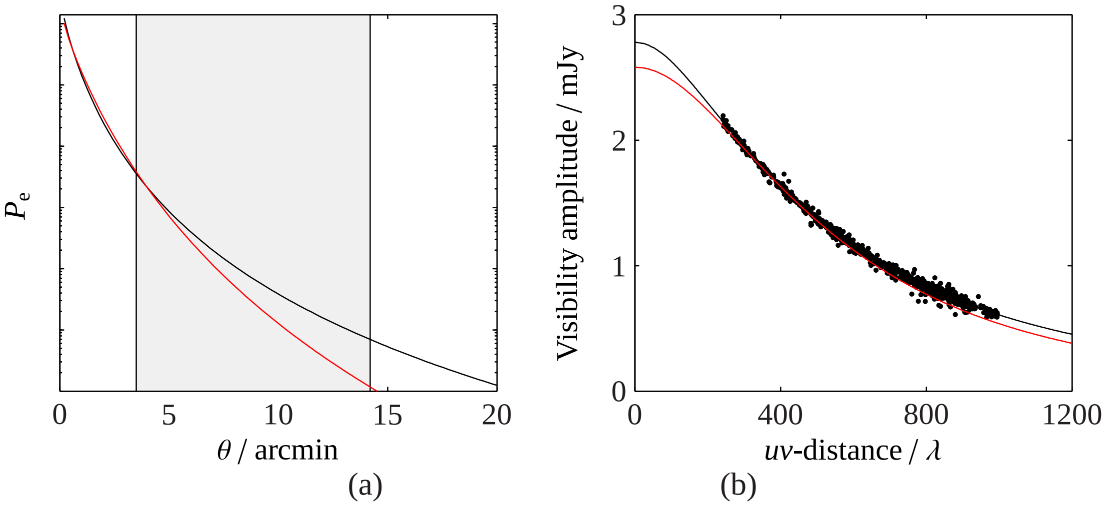

Figure 5.13: A profile generated with $\beta = 5.4905, \theta_s = 1.8$ (black lines) can be mimicked for $\beta = 8.9$ using $\theta_s = 4.1$ and adjusting $Y_{\rm tot}$ downward (red lines). The two profiles are almost identical over the AMI-SA range of baselines. (a) shows the pressure profiles in radial coordinates, with the angular scales corresponding to the AMI-SA baselines indicated by the shaded area (note that the y-axis scale is log), and (b) shows the profiles in uv-space for channel 5, with the input data shown as dots.

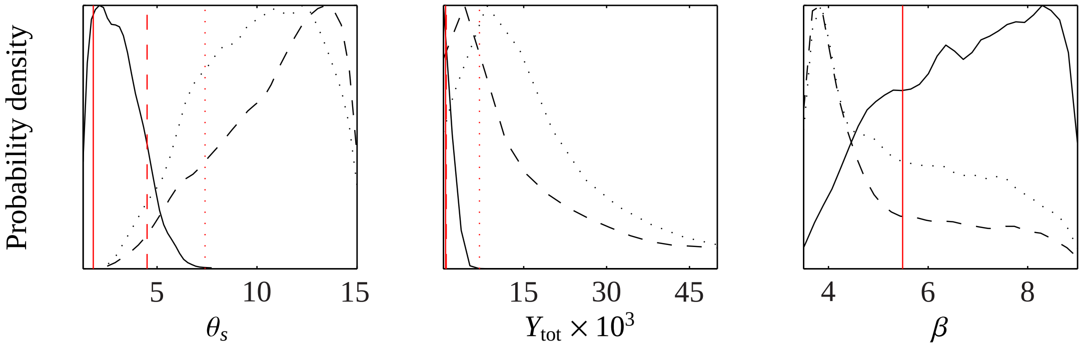

Figure 5.14: The one-dimensional marginal constraints on $Y_{\rm tot}$, θ_s and β for simulated low-noise data, for clusters with $\theta_s = 1.8$ (solid lines), 4.5 (dashed lines) and 7.4 (dotted lines), with uniform priors on all three parameters. Input values are shown as red lines.

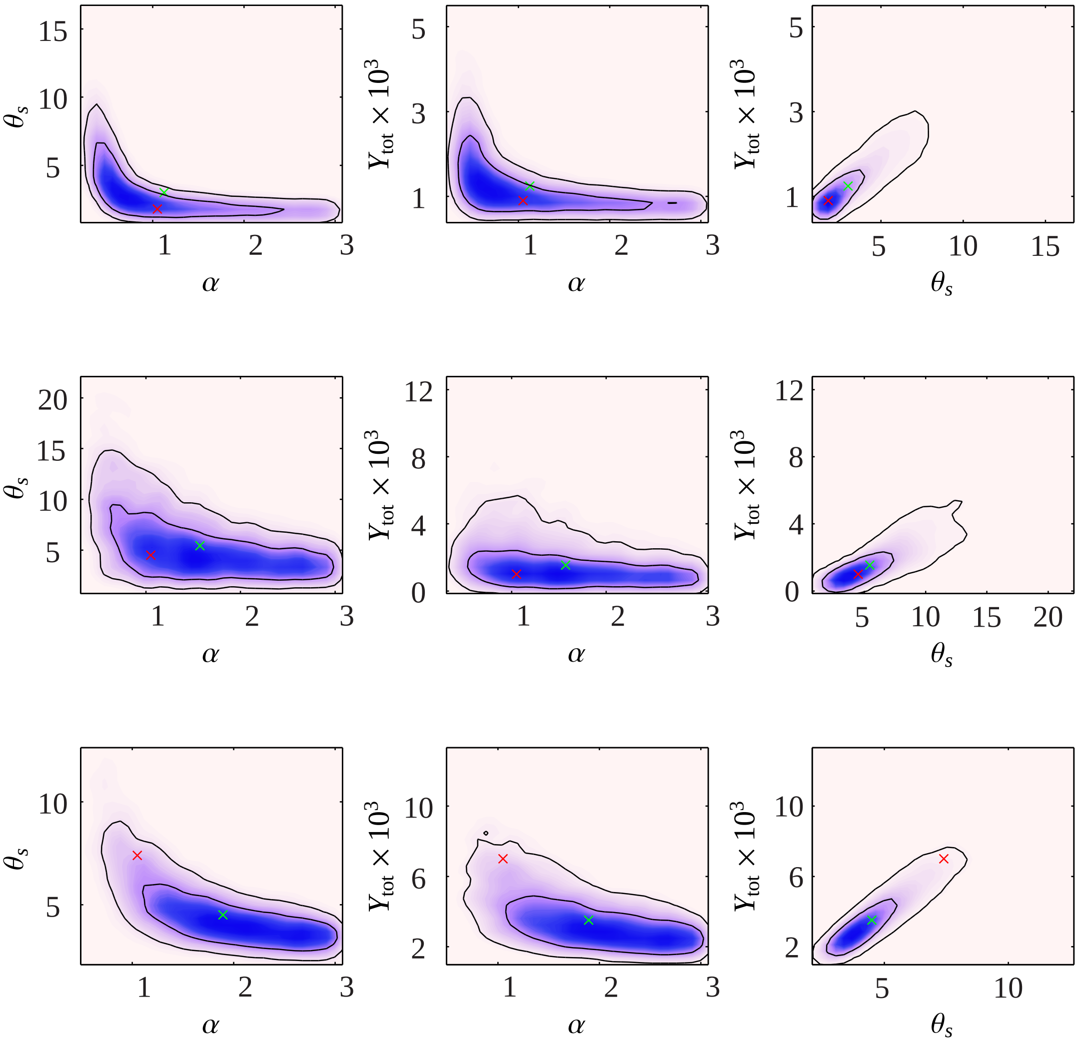

Figure 5.15: The posterior distributions for $Y_{\rm tot}$, θ_s and α for simulated low-noise data, for clusters with $\theta_s = 1.8$ (top), 4.5 (centre) and 7.4 (bottom), with the two-dimensional prior on $Y_{\rm tot}$ and θ_s. The input values are indicated by red lines and crosses, and the posterior means with green lines and crosses. The blue (pink) areas correspond to regions of higher (lower) probability density, and the contours mark the 68% and 95% confidence boundaries. The same convention is used in subsequent figures.

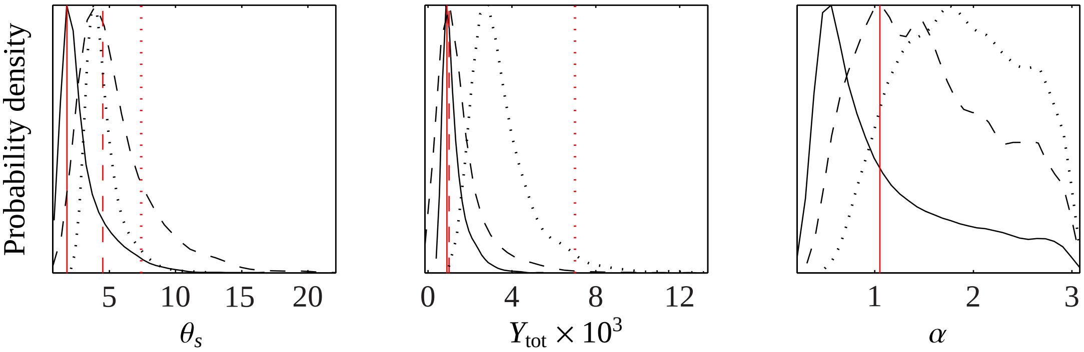

Figure 5.16: The one-dimensional marginal constraints on $Y_{\rm tot}$, θ_s and α for simulated low-noise data, for clusters with $\theta_s = 1.8$ (solid lines), 4.5 (dashed lines) and 7.4 (dotted lines), with the two-dimensional prior on $Y_{\rm tot}$ and θ_s. Input values are shown as red lines.

shape of the β-θ_s degeneracy. The results for the medium-sized cluster are similar, but β is biased more towards higher values. In addition, the parameter values for the largest cluster are not recovered correctly for the same reasons seen when α was varied.

Adding the physically motivated priors is clearly not sufficient to eliminate the biases caused by the limited range of angular scales. A final attempt to control the biases can be made by limiting the ranges of α and β allowed. Ideally, the prior on α would be based on the dispersion in the fit to the stacked profile from the REXCESS sample (assuming the distribution of α does not vary with redshift, and that any biases in the REXCESS sample do not affect the distribution), but since no information on the uncertainties in the fitting parameters is given in the paper and the data used for the fit are not supplied, the best approximation available is to consider the variation in the fitted α values for the individual clusters in the sample. The distribution of α is plotted in Fig. 5.19(a), along with a Gaussian centred on the 'universal' value with width equal to the standard deviation of the sample, 0.47. This is clearly not a satisfactory representation of the distribution of α, which may show a hint of bimodality (there is a clear difference in the profiles of the cool core and morphologically disturbed subsamples; see Fig. 2 of Arnaud et al. 2010, but the sample size is much too small to provide good evidence of bimodality in the distribution) as well as correlation with the fitted γ value (Fig. 5.19(b)), but is also clearly an improvement on the uniform prior.

Figs. 5.20 and 5.21 show the posterior distributions obtained by varying α with this Gaussian prior truncated at $\alpha = 0.3$. For the two smaller angular-size clusters, this

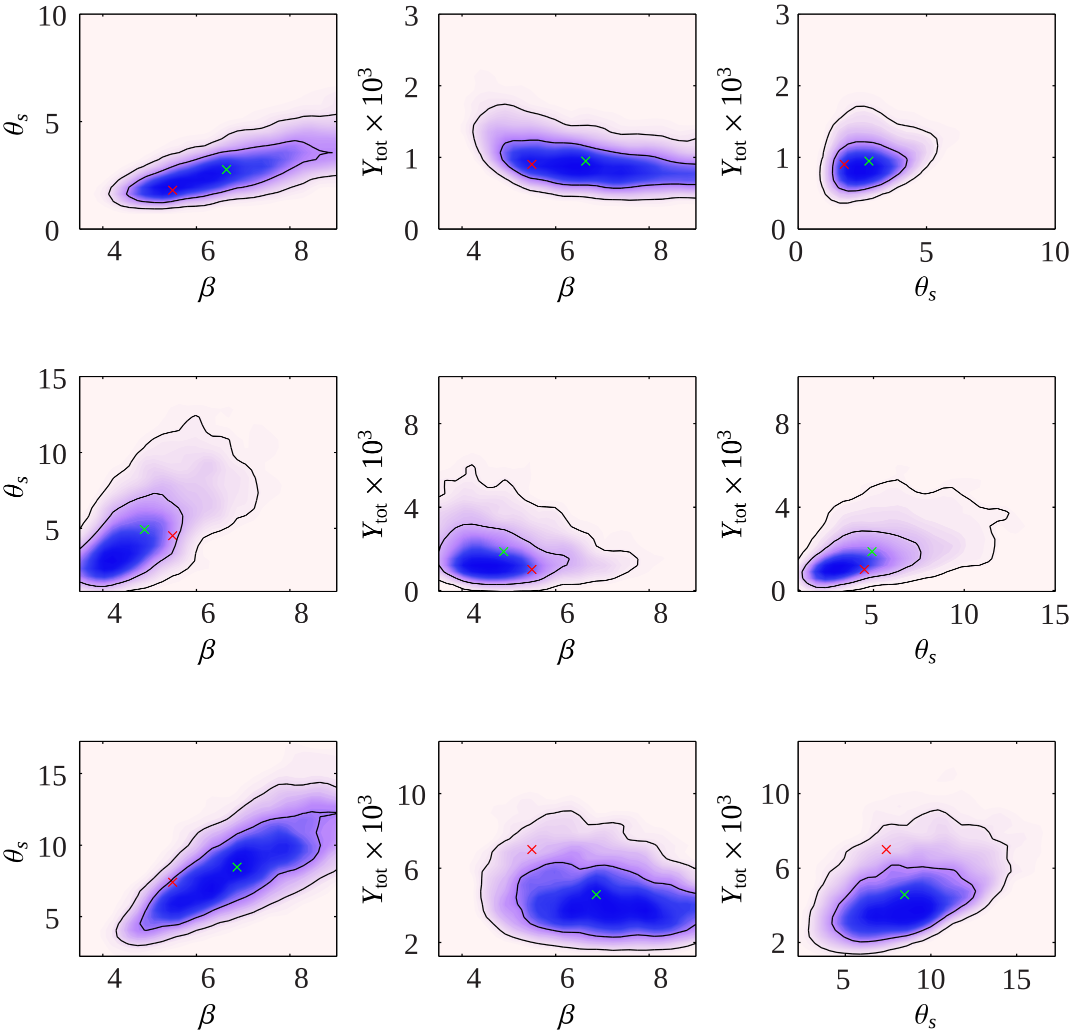

Figure 5.17: The posterior distributions for $Y_{\rm tot}$, θ_s and β for simulated low-noise data, for clusters with $\theta_s = 1.8$ (top), 4.5 (centre) and 7.4 (bottom), with the two-dimensional prior on $Y_{\rm tot}$ and θ_s. The input values are indicated by red lines and crosses, and the posterior means with green lines and crosses.

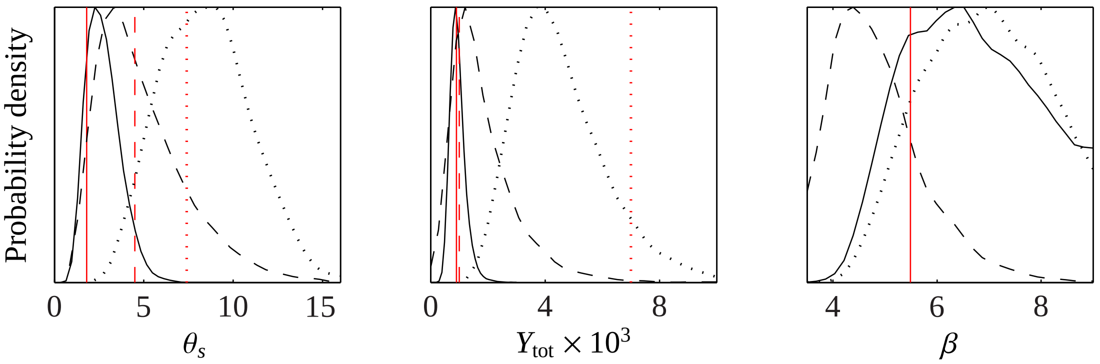

Figure 5.18: The one-dimensional marginal constraints on $Y_{\rm tot}$, θ_s and β for simulated low-noise data, for clusters with $\theta_s = 1.8$ (solid lines), 4.5 (dashed lines) and 7.4 (dotted lines), with the two-dimensional prior on $Y_{\rm tot}$ and θ_s. Input values are shown as red lines.

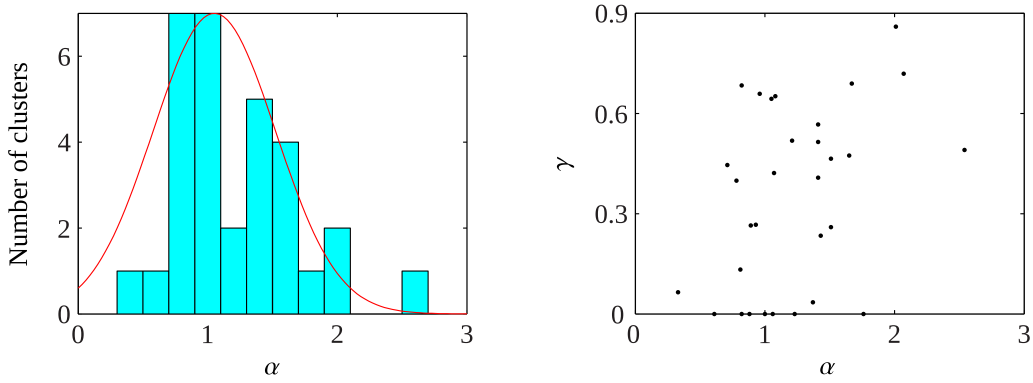

(a)

(b)

Figure 5.19: The distribution of fitted α parameter values for the individual clusters in the REXCESS sample (a), with a Gaussian centred on the 'universal' value with width equal to the standard deviation of the sample, scaled arbitrarily for comparison. (b) shows the correlation between the fitted α and γ values.

combination of priors comes close to eliminating the biases. θ_s and $Y_{\rm tot}$ are recovered correctly. For the smallest cluster, there is still a tendency for lower values of α to be recovered, but the effect is much less pronounced than in the previous analyses with the uniform prior on α. In the case of the largest cluster, the input values are still not recovered well because of the strong effect of the priors, but the suppression of the larger values of α has improved the situation slightly.

In the case of β, since there is little information available on its distribution the only possibility for eliminating or reducing the biases is to restrict the range of allowed values. Figs. 5.22 and 5.23 show the posterior distributions for the three clusters when the range is restricted to $[4.5, 6.5]$. This combination of priors comes reasonably close to eliminating the biases. θ_s is recovered approximately correctly for all three clusters; there is still a tendency for β to push either to high or low values, but it is clear in the two-dimensional posteriors that the 68% confidence level encompasses nearly all of the allowed β range.

Varying α and β simultaneously with these priors results in very similar constraints, i.e. the degeneracy between α and β does not result in any additional biases (Fig. 5.24).

5.4.2 Realistic simulations

Having investigated, understood and minimised as much as possible the biassing that is introduced due to the limited range of spatial scales present in the AMI data, it is necessary to test the effects on more realistic datasets. The three clusters were therefore simulated again with realistic noise levels, as described in Section 5.3.1.

Surprisingly, the parameter constraints obtained using these realistic simulations are virtually identical to those obtained in the previous section with minimal noise added, despite the great increase in scatter in the visibilities (see Fig. 5.25 for a comparison). This indicates that the major factor limiting the information on the cluster shape that can be recovered from AMI data for these well-detected clusters is the limited range of angular scales, rather than the noise levels achievable.

Fig. 5.26 shows the constraints on $Y_{\rm tot}$ and θ_s derived both with α and β varying, and with α and β fixed (dotted lines). For the smallest cluster, the contours are significantly enlarged by varying the profile parameters, indicating that for this size of cluster the goal of marginalising over the uncertainty in α and β has been achieved. For the

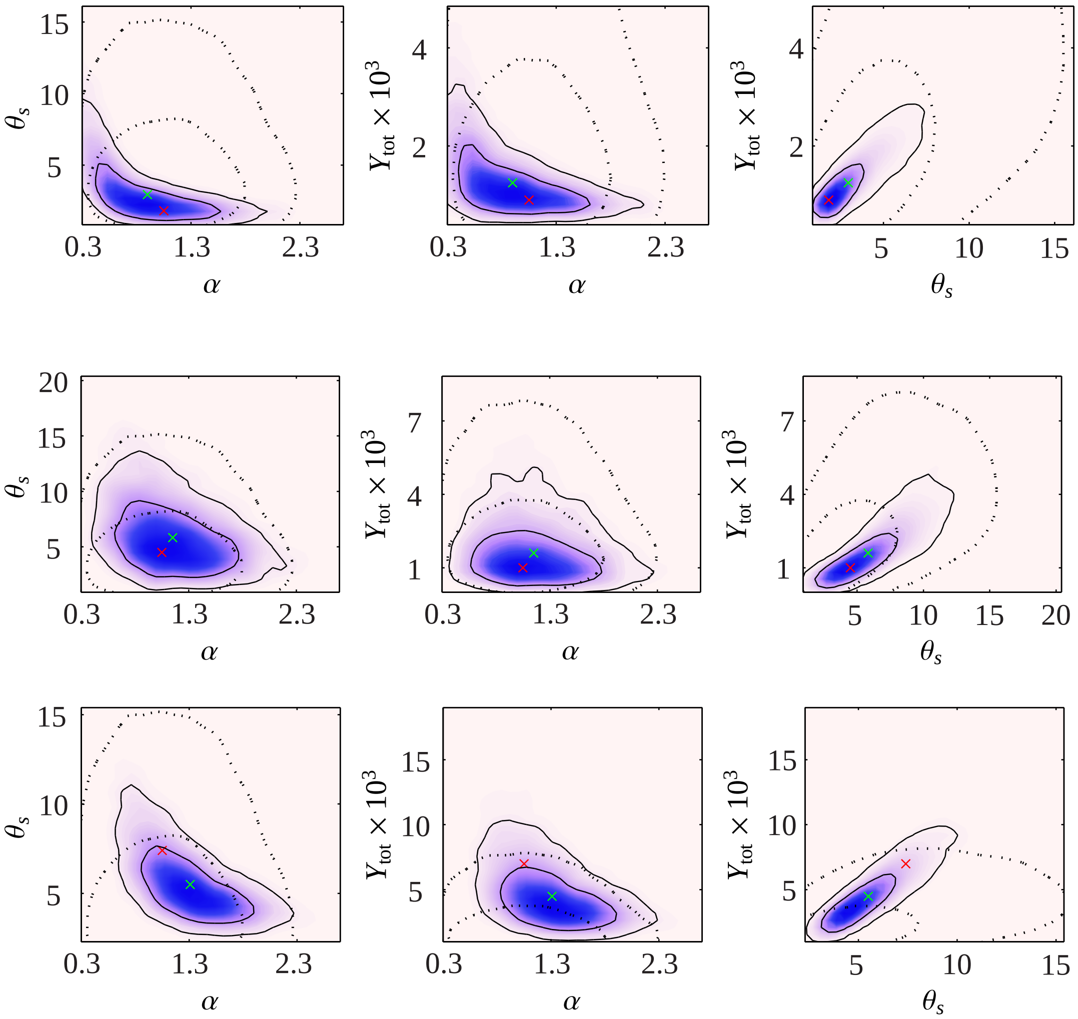

Figure 5.20: The posterior distributions for $Y_{\rm tot}$, θ_s and α for simulated low-noise data, for clusters with $\theta_s = 1.8$ (top), 4.5 (centre) and 7.4 (bottom), using the joint two-dimensional prior on θ_s and $Y_{\rm tot}$ and the truncated Gaussian prior derived from the REXCESS sample on α. The input values are indicated by red lines and crosses, and the posterior means with green lines and crosses. The priors are shown as dotted black lines.

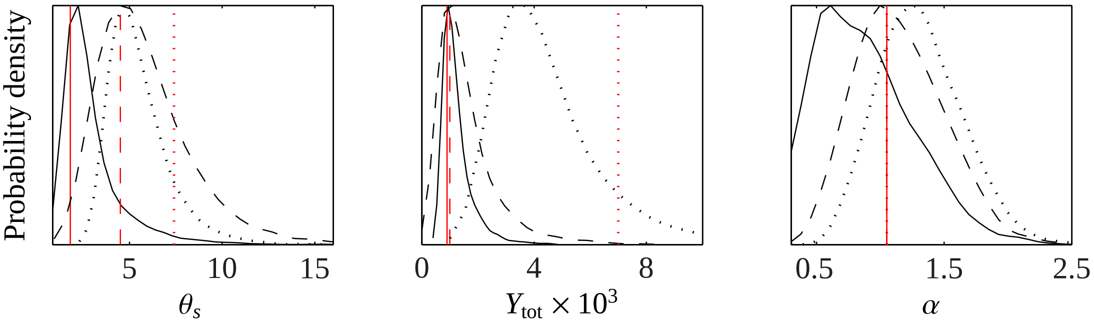

Figure 5.21: The one-dimensional marginal constraints on $Y_{\rm tot}$, θ_s and α for simulated low-noise data, for clusters with $\theta_s = 1.8$ (solid lines), 4.5 (dashed lines) and 7.4 (dotted lines), using the joint two-dimensional prior on θ_s and $Y_{\rm tot}$ and the truncated Gaussian prior derived from the REXCESS sample on α. Input values are shown as red lines.

medium-sized cluster, the contours are approximately the same, probably due to the interaction of the prior on θ_s with the β-θ_s degeneracy, which cuts off the upper end of the β range. For the largest cluster, as noted previously, the input values cannot be recovered, because with more freedom in the model the prior on θ_s and $Y_{\rm tot}$ overcomes the information in the data.

Again, the bank of simulations based on the REXCESS sample were run with these priors; results are shown in Fig. 5.27. For the smallest cluster, the true value of θ_s and $Y_{\rm tot}$ is now always within the 68% confidence limit. By comparison with Fig. 5.5, it is clear that the two-dimensional contours are now more evenly centred around the input value. As expected, α is not constrained for this cluster size, and so the prior on α is mostly recovered, with some tendency for lower values (and therefore higher values of θ_s) to be preferred. This does not seem to bias the recovery of $Y_{\rm tot}$ and θ_s, even in cases where the preferred value of α is quite different to the true value. β tends to be either weakly constrained to the correct value or completely unconstrained. There are no cases where β is constrained to the wrong value.

For the medium-sized cluster, there is now only one case where the true value of θ_s and $Y_{\rm tot}$ is outside the 68% confidence limit, and the contours are marginally better centred on the input value. For this cluster, the best constraint on the shape parameters should be on α, and indeed the one-dimensional constraints show better results than for the small cluster. The information in the data is not enough to pull the posterior

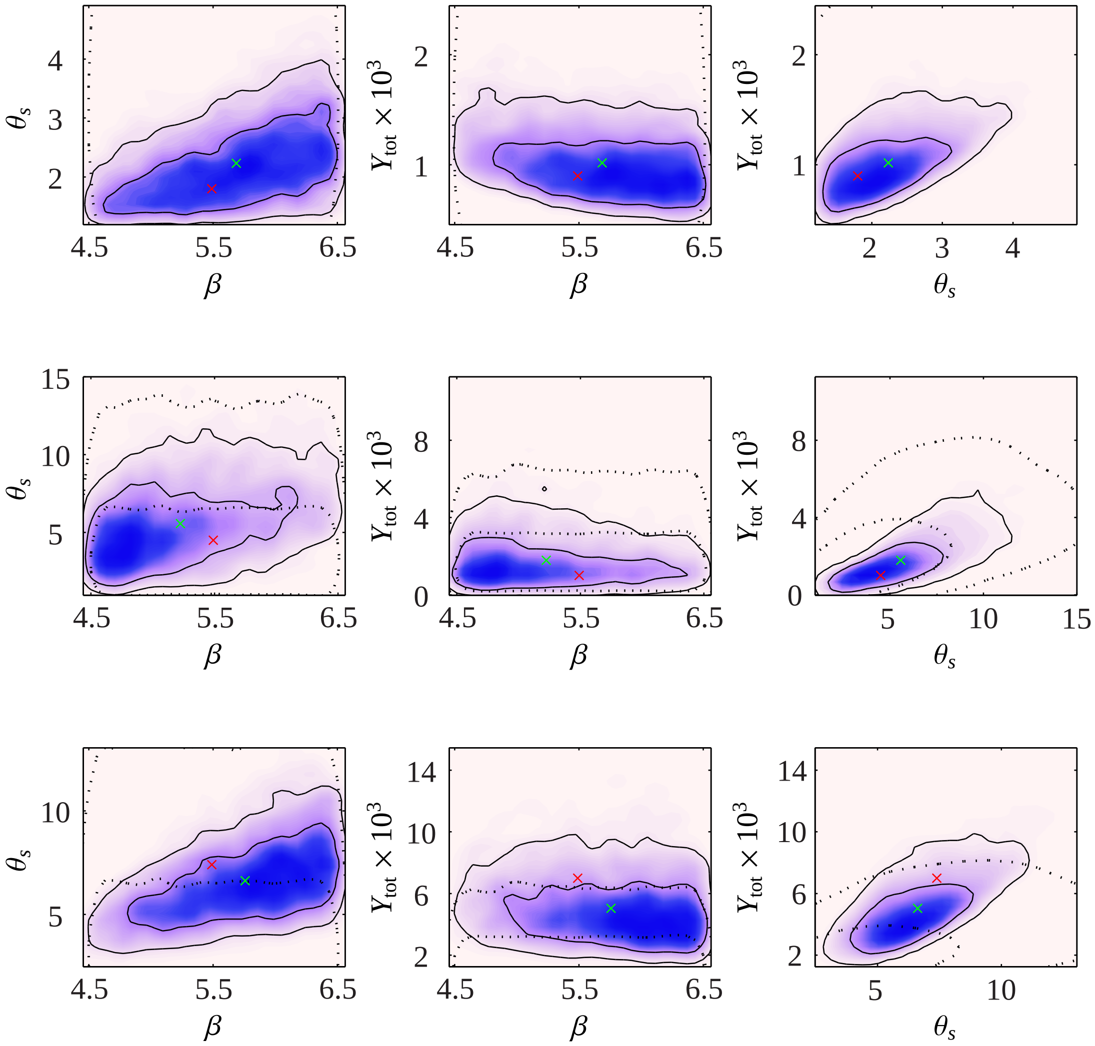

Figure 5.22: The posterior distributions for $Y_{\rm tot}$, θ_s and β for simulated low-noise data, for clusters with $\theta_s = 1.8$ (top), 4.5 (centre) and 7.4 (bottom), with the two-dimensional prior on $Y_{\rm tot}$ and θ_s and the range of β values restricted to $[4.5, 6.5]$. The input values are indicated by red lines and crosses, and the posterior means with green lines and crosses.

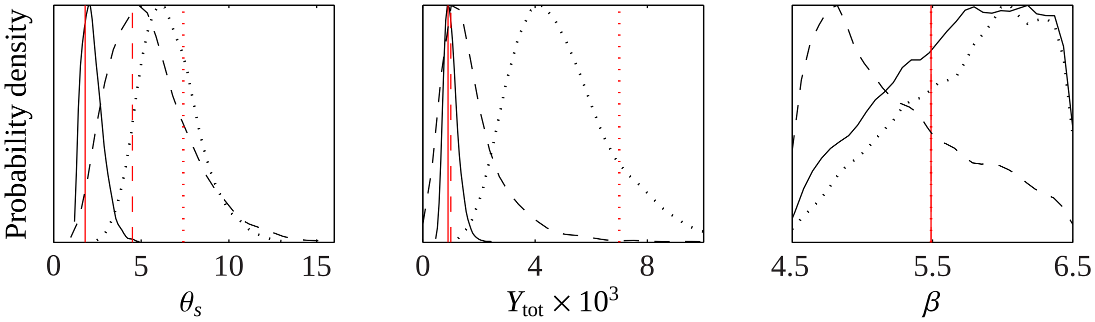

Figure 5.23: The one-dimensional marginal constraints on $Y_{\rm tot}$, θ_s and β for simulated low-noise data, for clusters with $\theta_s = 1.8$ (solid lines), 4.5 (dashed lines) and 7.4 (dotted lines), with the two-dimensional prior on $Y_{\rm tot}$ and θ_s and the range of β values restricted to $[4.5, 6.5]$. Input values are shown as red lines.

very far away from the prior, but it is pulled in the right direction in nearly all cases. β is expected to be unconstrained, and in all cases it is either unconstrained or favours low values of β due to the interaction of the θ_s prior and the θ_s-β degeneracy; the origin of this 'constraint' can be clearly seen by inspecting the two-dimensional posteriors.

The true values of $Y_{\rm tot}$ and θ_s for the largest cluster are, as expected from the previous tests, not recovered. There is not enough information in the data to overcome the prior given the extra freedom to vary β and α. As with the medium-sized cluster, the constraints on α are pushed in the correct direction. Surprisingly, β is often recovered approximately correctly; this can be understood by considering the degeneracies between β and θ_s-$Y_{\rm tot}$ for the largest cluster in Fig. 5.12. Since the degeneracies are approximately orthogonal, the intersection of the two can select the correct value of β. When the prior on θ_s and $Y_{\rm tot}$ suppresses part of the degeneracy, this can lead instead to spurious constraints on β such as in Fig. 5.24.

The final point to consider is whether the variation in γ affects the derived parameter values. Fig. 5.28 shows the fractional difference between the MAP values of θ_s and $Y_{\rm tot}$ as a function of γ. There is some correlation between the fractional difference in θ_s and γ, especially for the two smaller clusters, but mostly any correlation is beneath the level of the noise.

In summary, this combination of priors can be used to marginalise over the uncertainty in the profile shape without biasing the recovery of the true values of θ_s and $Y_{\rm tot}$ for clusters with θ_s up to ≈ 5 arcmin. Caution must be taken in interpreting apparent

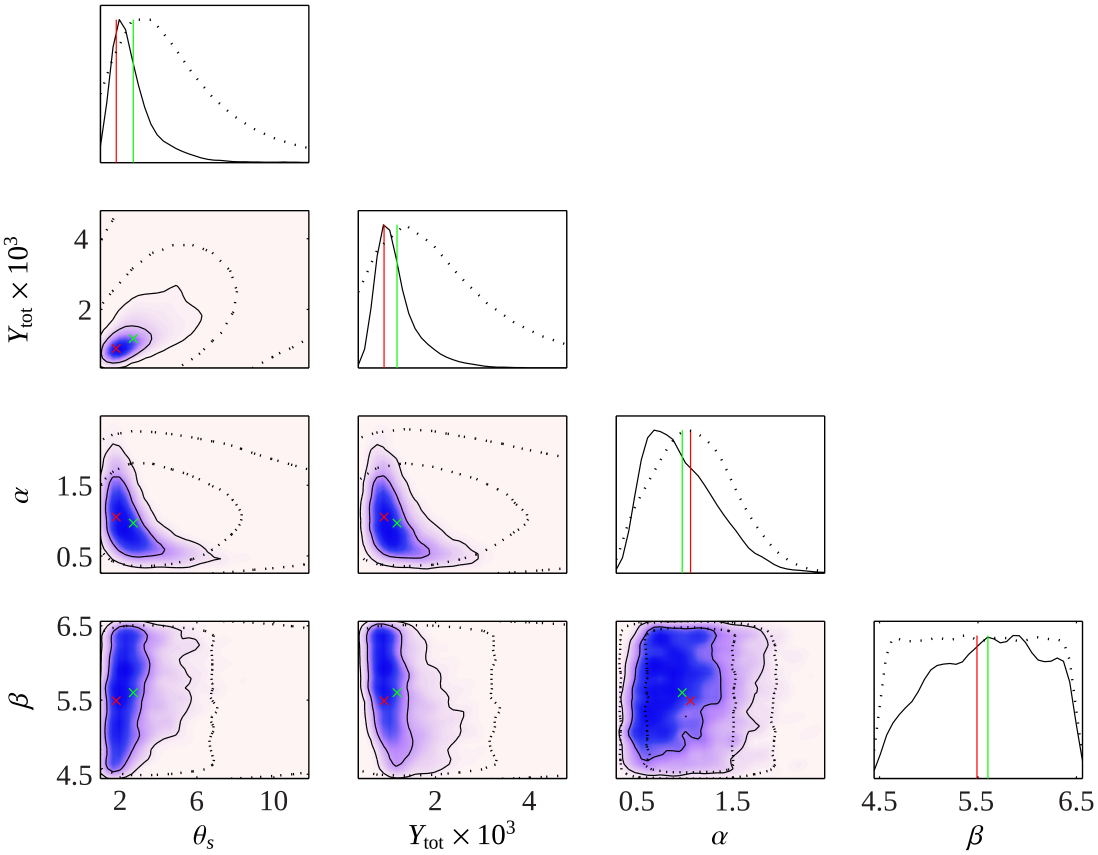

(a)

Figure 5.24: The two- and one-dimensional posterior distributions for simulated low-noise data, for clusters with $\theta_s = 1.8$ (a), 4.5 (b) and 7.4 (c), with the two-dimensional prior on $Y_{\rm tot}$ and θ_s, the prior derived from the REXCESS sample on α, and the restricted uniform prior on β.

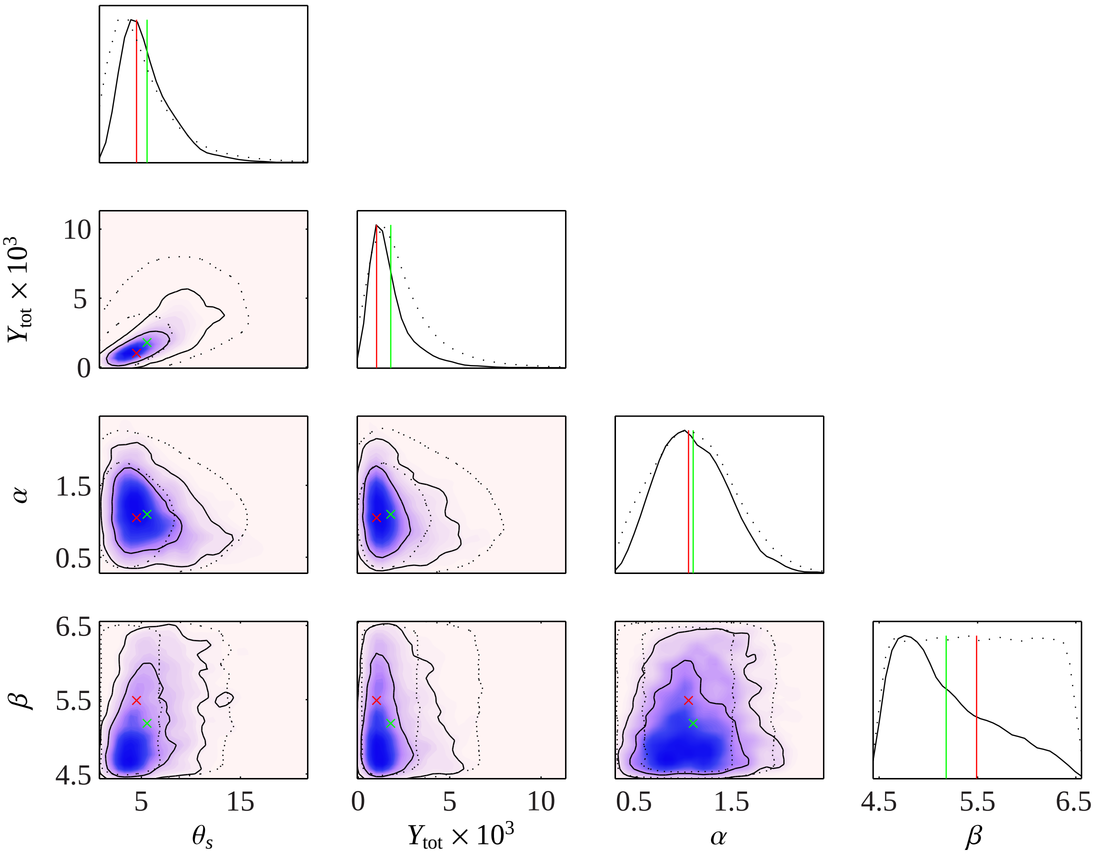

(b)

Figure 5.24: Continued.

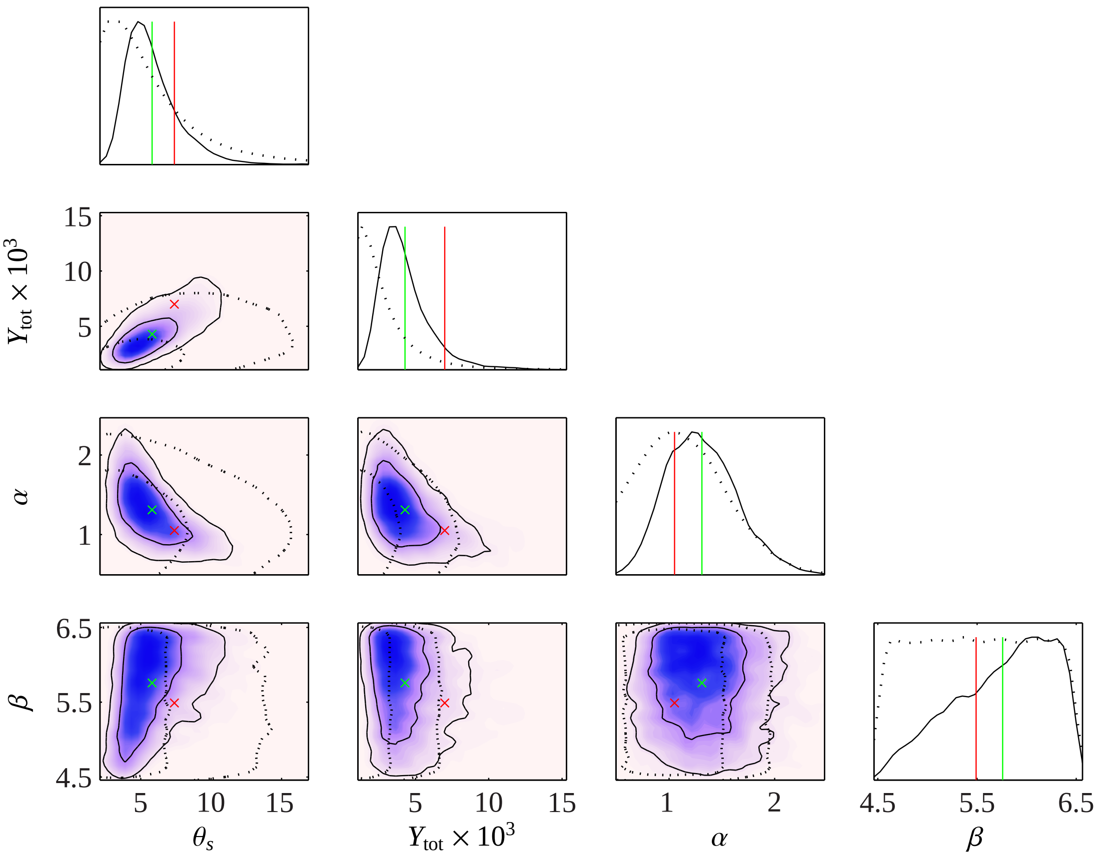

(c)

Figure 5.24: Continued.

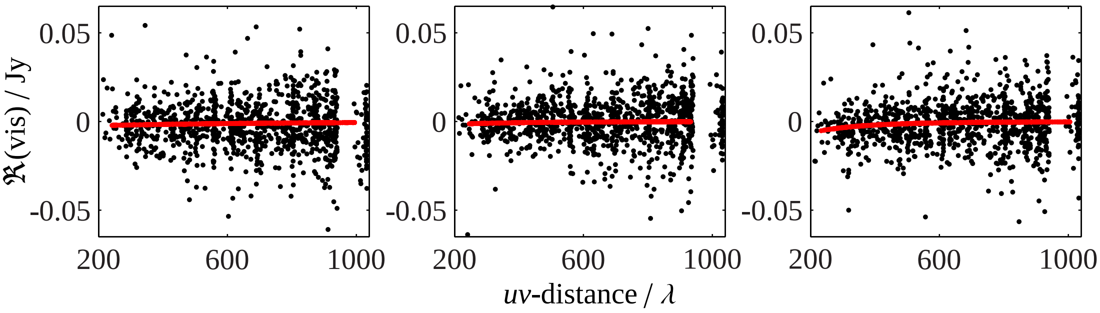

(a) (b) (c)

Figure 5.25: The real parts of the channel 5 visibilities input to McAdam for simulated clusters with $\theta_s = 1.8$ (a), 4.5 (b) and 7.4 (b), with realistic noise levels (black dots) and minimal noise levels (red dots)

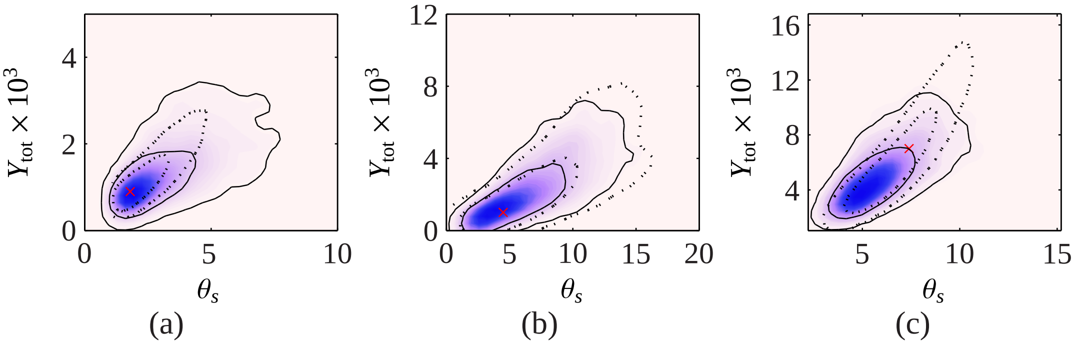

Figure 5.26: The constraints on Y_{tot} and θ_s produced for clusters with $\theta_s = 1.8$ (a), 4.5 (b) and 7.4 (c), with α and β varying (solid lines and colour-scale), and fixed (dotted lines). The true values are plotted with red crosses.

constraints on α and β since these can be due simply to the shape of the degeneracies. For clusters with larger angular sizes, there is simply not enough information available in the angular scales measured by the SA to simultaneously constrain $Y_{\mathrm{tot}}, \theta_s$ and any of the shape parameters, and the values of θ_s and Y_{tot} will be biased downward.

5.4.3 Adding *Planck* information

It seems clear that varying the shape parameters over these wide ranges without some prior knowledge of the angular size of the cluster is dangerous since it can lead to biases in the recovered parameter values, simply due to the limited range of angular scales available in the data. One way to check and, hopefully, improve this problem is to use the constraints on Y_{tot} from *Planck* to effectively constrain the zero-spacing flux of the cluster in the AMI observation.

To test this, I proceeded in a similar manner as in the previous section, using the data simulated with minimal amounts of noise, but fixing Y_{tot} to its true value. First, I varied θ_s, α and β simultaneously, with uniform priors $U[1.3, 15], U[0.1, 3.0]$, and $U[3.5, 9.0]$ respectively. Although results were improved with respect to the case when Y_{tot} was also varied, this approach still led to spurious constraints on α and β when the range of angular scales sampled did not include those affected by one of the parameters (i.e. for α for the smallest cluster).

I then changed the prior on θ_s to be the conditional distribution from the joint prior

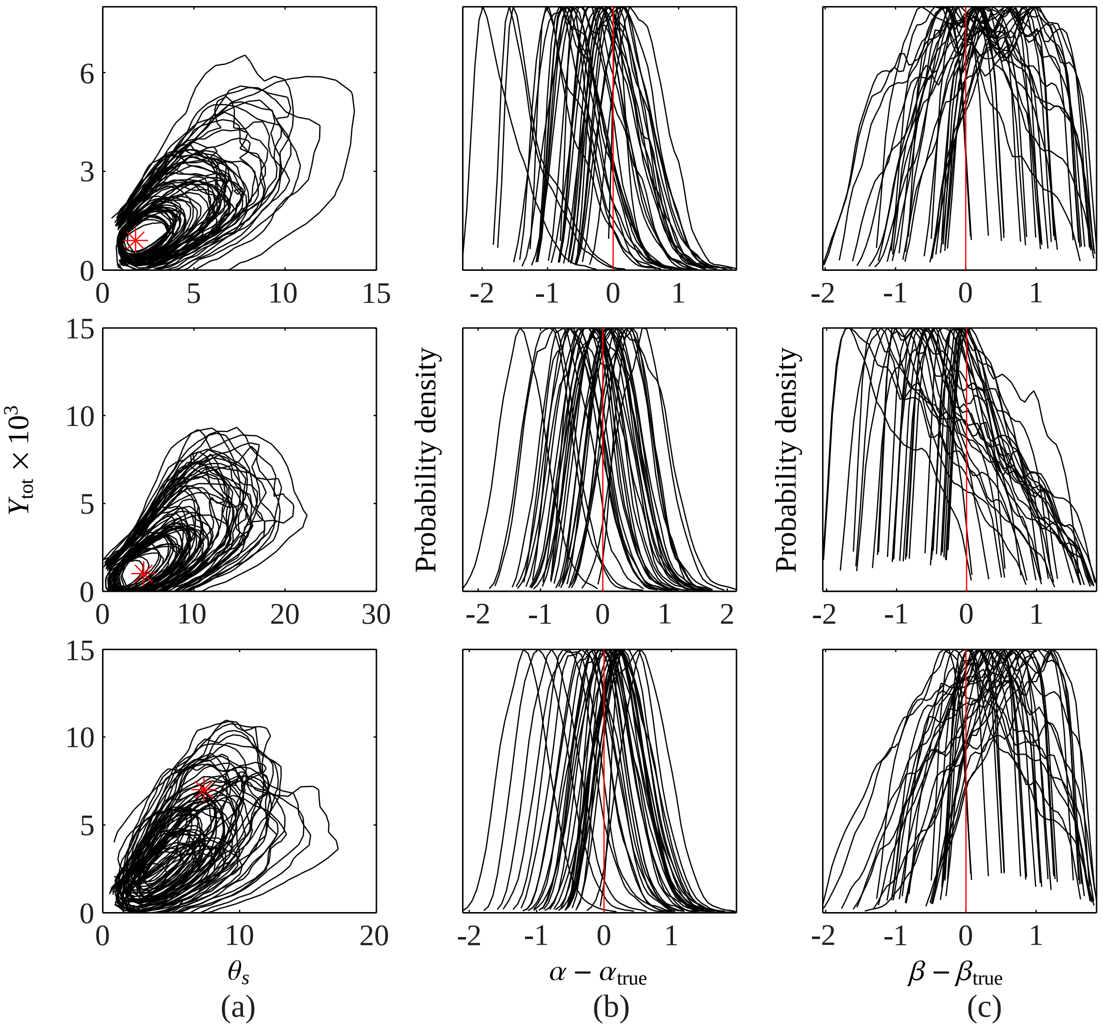

Figure 5.27: The posterior distributions for simulated clusters with realistic noise levels (see text for details), and varying GNFW shape parameter values based on the REXCESS sample. (a) shows the two-dimensional θ_s and Y_{tot} posterior, and (b) and (c) show the one-dimensional posteriors for α and β, shifted to be centred on the appropriate true value. In all cases γ is fixed to the 'universal' value, α has a truncated Gaussian prior based on the REXCESS sample, β is varied uniformly between 4.5 and 6.5, and the joint two-dimensional prior on Y_{tot} and θ_s is used. Results for three different angular sizes are shown (from top to bottom, $\theta_s = 1.8, 4.5$ and 7.4); the input parameter values are marked with red stars and lines.

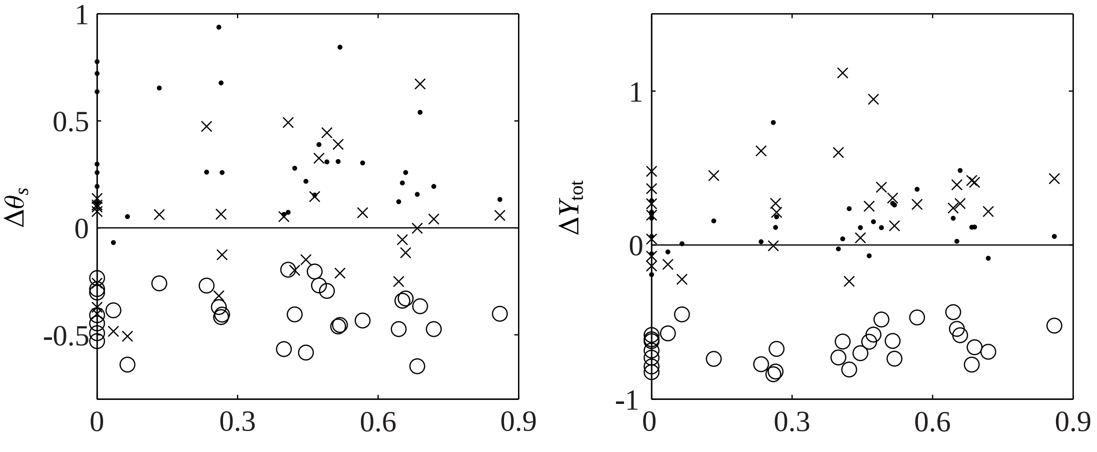

(a) (b)

Figure 5.28: The fractional difference ((MAP value - true value)/(true value)) in θ_s (a) and $Y_{\rm tot}$ (b) as a function of the input value of γ. Clusters with $\theta_s = 1.8$ are plotted as dots, $\theta_s = 4.5$ as crosses and $\theta_s = 7.4$ as open circles.

given the fixed $Y_{\rm tot}$, dP($x|Y$). This resulted in much better constraints, with only a slight bias on the angular size and β value of the medium-sized cluster, due to the interaction of the prior on θ_s and the θ_s-β degeneracy.

For the next step, I therefore place realistic priors on $Y_{\rm tot}$ by fitting Gaussians to the PwS one-dimensional marginalised posteriors for the clusters which the three simulations were based on. For *Planck* data, marginalising over a range of shape parameters has the effect of widening the likelihood for $Y_{\rm tot}$ slightly and decreasing the correlation between $Y_{\rm tot}$ and θ_s (Diana Harrison, private communication), so this is a reasonable approximation to the prior that can be derived from *Planck* data. The priors are centred on the true $Y_{\rm tot}$ values and truncated at zero, and the widths are listed in Table 5.2. In the case of CAJ0303+7755, the prior is actually based on the PwS posterior distribution for another cluster with similar $Y_{\rm tot}$ and θ_s values (CAJ0543+4656) since CAJ0303+7755 is not detected by PwS.

When McAdam is run on the simulations with realistic noise levels, the Gaussian priors on $Y_{\rm tot}$ and conditional priors on θ_s, and the wide uniform priors on α and β, although θ_s and $Y_{\rm tot}$ are recovered correctly, the same biases on α and β are introduced as previously without the Gaussian priors on $Y_{\rm tot}$. This indicates that the constraints that *Planck* data can place on $Y_{\rm tot}$ are not tight enough to overcome the biases introduced

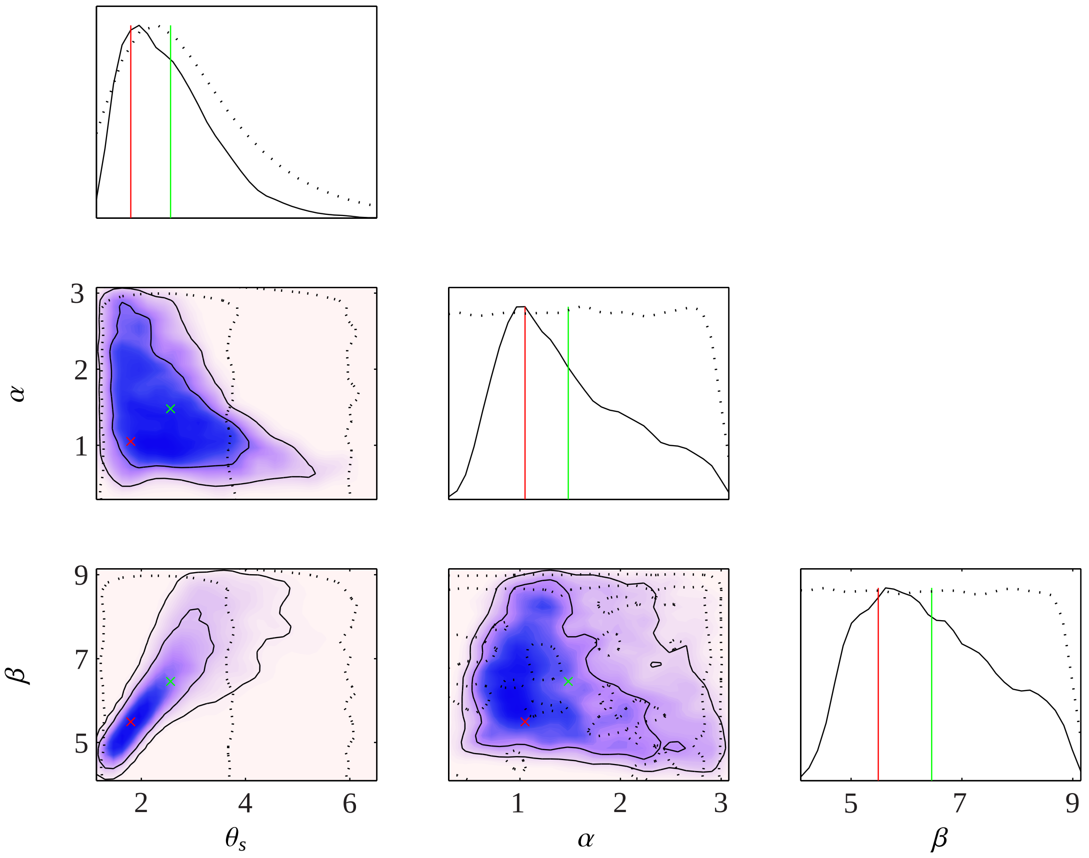

(a)

Figure 5.29: The two- and one-dimensional posterior distributions for simulated low-noise data, for clusters with $\theta_s = 1.8$ (a), 4.5 (b) and 7.4 (c), with $Y_{\rm tot}$ fixed to the true value, and the conditional prior from the two-dimensional prior on θ_s. The priors on α and β are uniform between [0.1, 3] and [3.5, 9.0] respectively. The priors are plotted with dashed black lines.

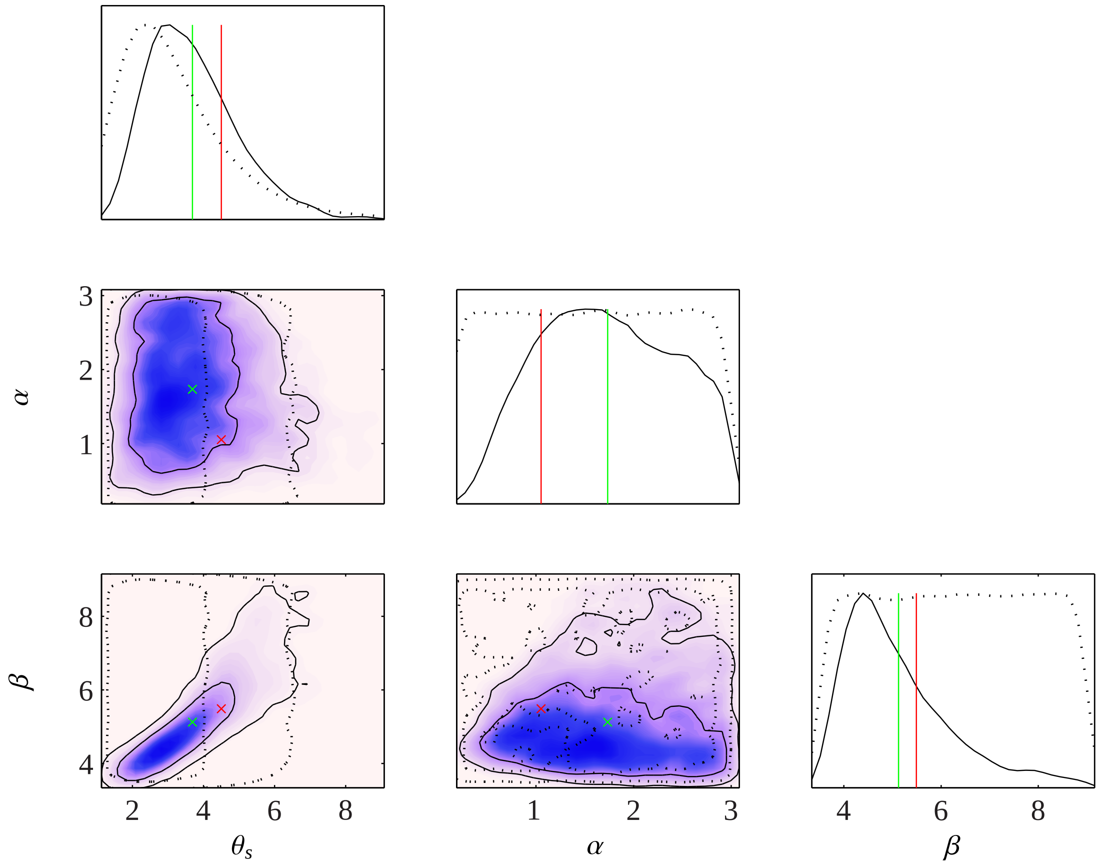

(b)

Figure 5.29: Continued.

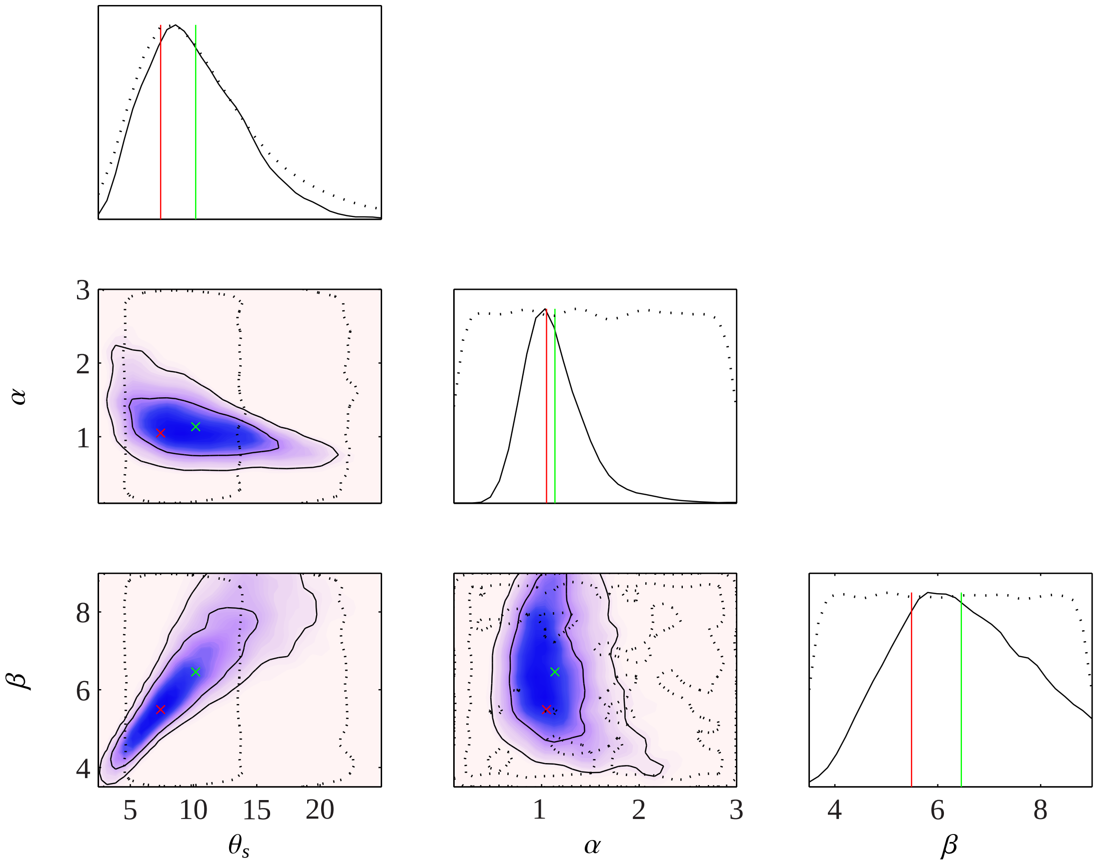

(c)

Figure 5.29: Continued.

Table 5.2: *Planck*-like Gaussian priors used on $Y_{\rm tot}$.

Cluster	μ	σ
CAJ0441+6813	9×10^{-4}	8.55×10^{-4}
CAJ0303+7755 (CAJ0543+4656)	1×10^{-3}	9.77×10^{-4}
A2218	7×10^{-3}	5.61×10^{-4}

by the limited range of angular scales covered by the AMI-SA. The problem is almost solved by introducing the REXCESS-based prior on α and the restricted range on β (Fig. 5.30). The resulting constraints on α and β are very similar to the previous results without the Gaussian priors on $Y_{\rm tot}$, however the bias towards lower values of $Y_{\rm tot}$ and θ_s for the largest cluster has been eliminated.

Fig. 5.31 shows the overall results for the bank of simulations based on the REXCESS sample, using the Gaussian priors on $Y_{\rm tot}$, the conditional priors on θ_s, the REXCESS-based Gaussian prior on α, and the uniform prior on β between 4.5 and 6.5. In comparison with Fig. 5.27, the constraints on θ_s and $Y_{\rm tot}$ are much tighter, and centred on the true values for all three angular-size clusters; the constraints on α and β are approximately the same. The true value of $Y_{\rm tot}$ and θ_s is only outside the 68% confidence limits between once and three times out of 31, and is always within the 95% confidence limits.

5.5 Future work

An important point to consider before attempting this analysis on real data is the effect of point sources lying near the phase centre. An important strength of interferometric data in the analysis of clusters is the difference in the profiles in *uv*-space of (unresolved) point sources and (resolved) clusters; this enables the disentangling of point source flux which would otherwise fill in the decrement. It has been found in the past when modelling clusters with an adaptable shape (e.g. an isothermal β-model) the clear distinction between the two types of profile is lessened, leading to biases in the recovered parameter values. It will be important to test this effect for the GNFW model with variable α and β.

The two-dimensional prior on $Y_{\rm tot}$ and θ_s was derived assuming a scaling relation-

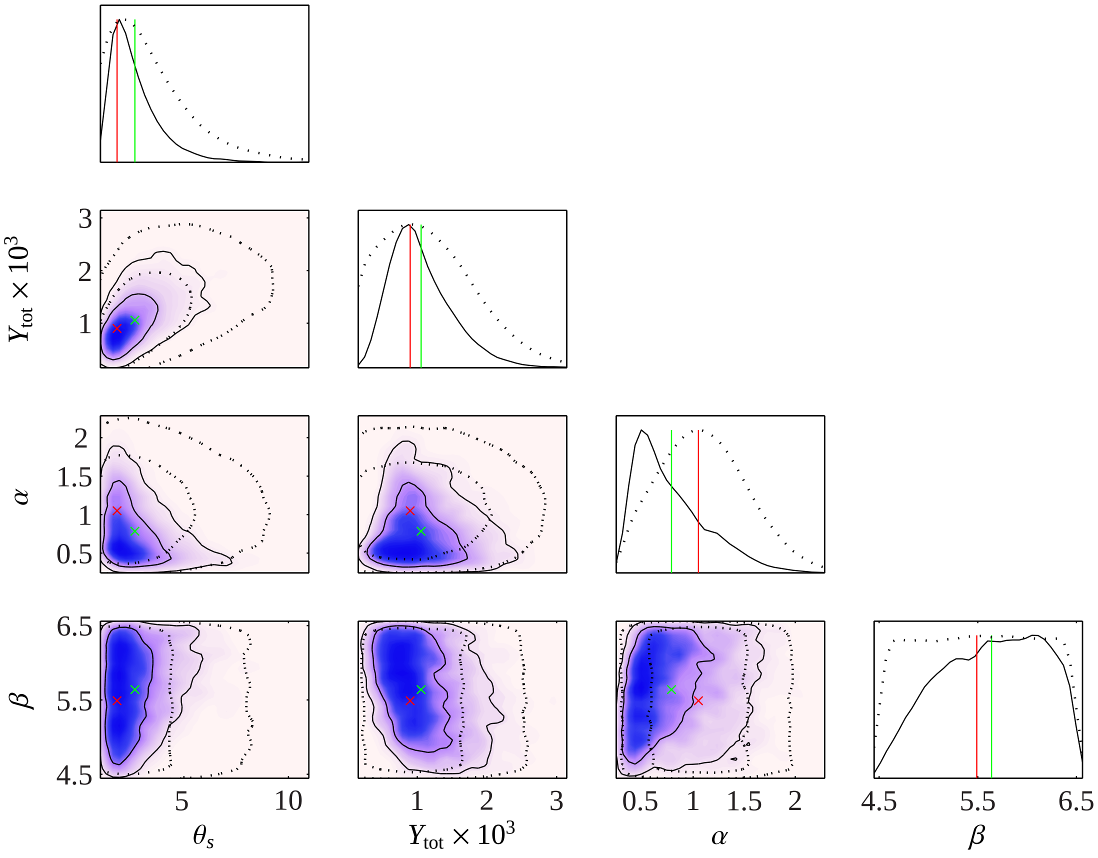

(a)

Figure 5.30: The two- and one-dimensional posterior distributions for data with realistic noise levels, for clusters with $\theta_s = 1.8$ (a), 4.5 (b) and 7.4 (c), with Gaussian priors on $Y_{\rm tot}$ with widths appropriate to *Planck* constraints, and the conditional prior from the two-dimensional prior on θ_s. The priors on α and β are uniform between [0.1, 3] and [3.5, 9.0] respectively. The priors are plotted with dashed black lines.

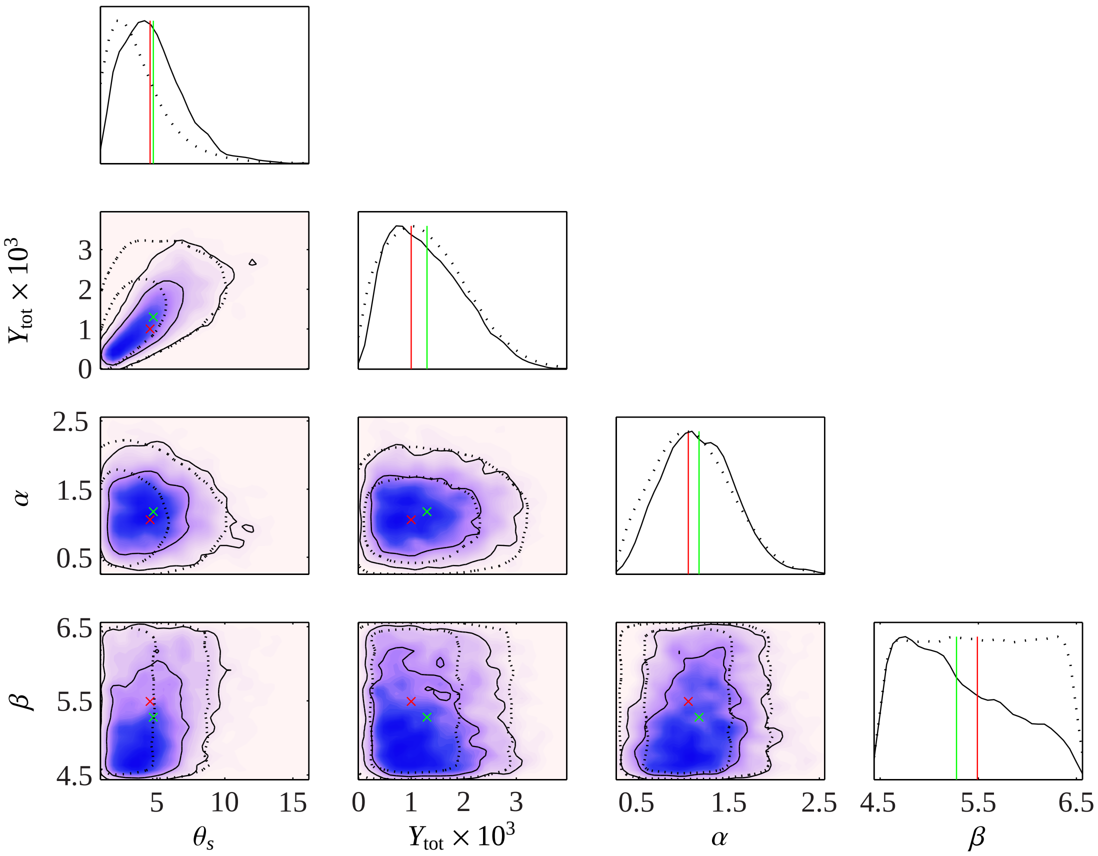

(b)

Figure 5.30: Continued.

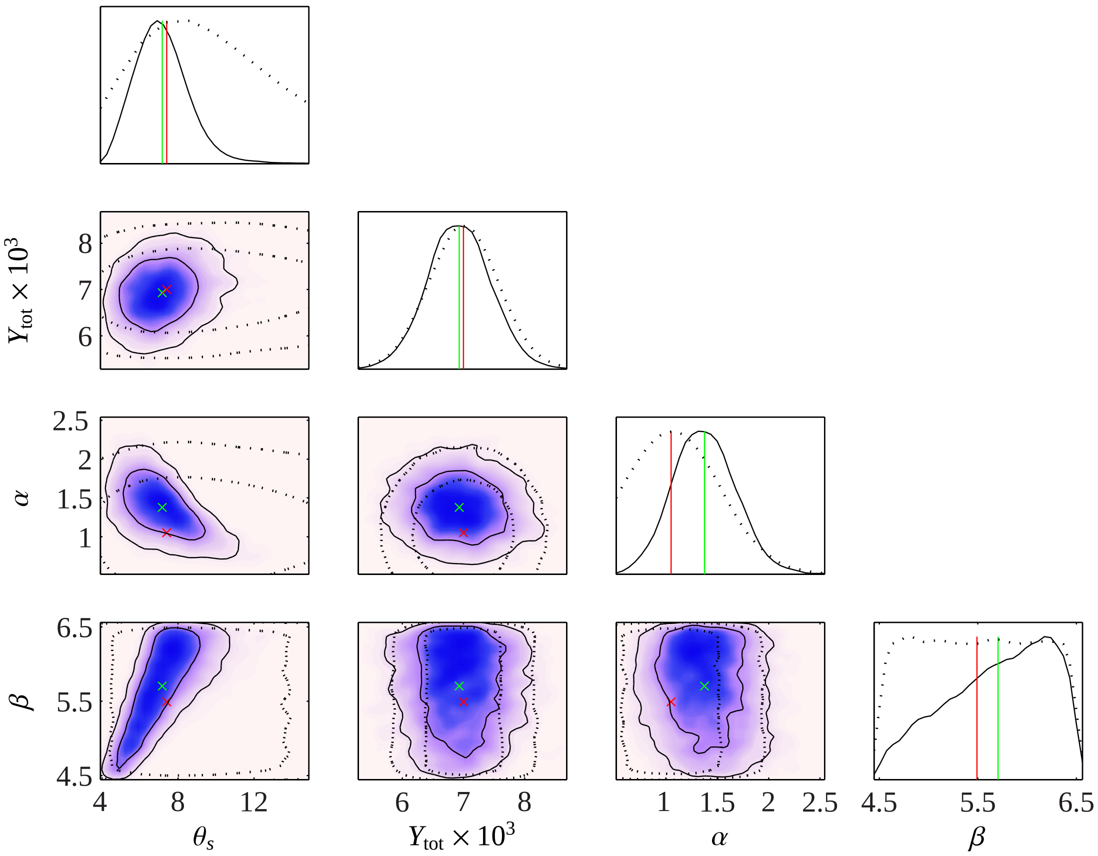

(c)

Figure 5.30: Continued.

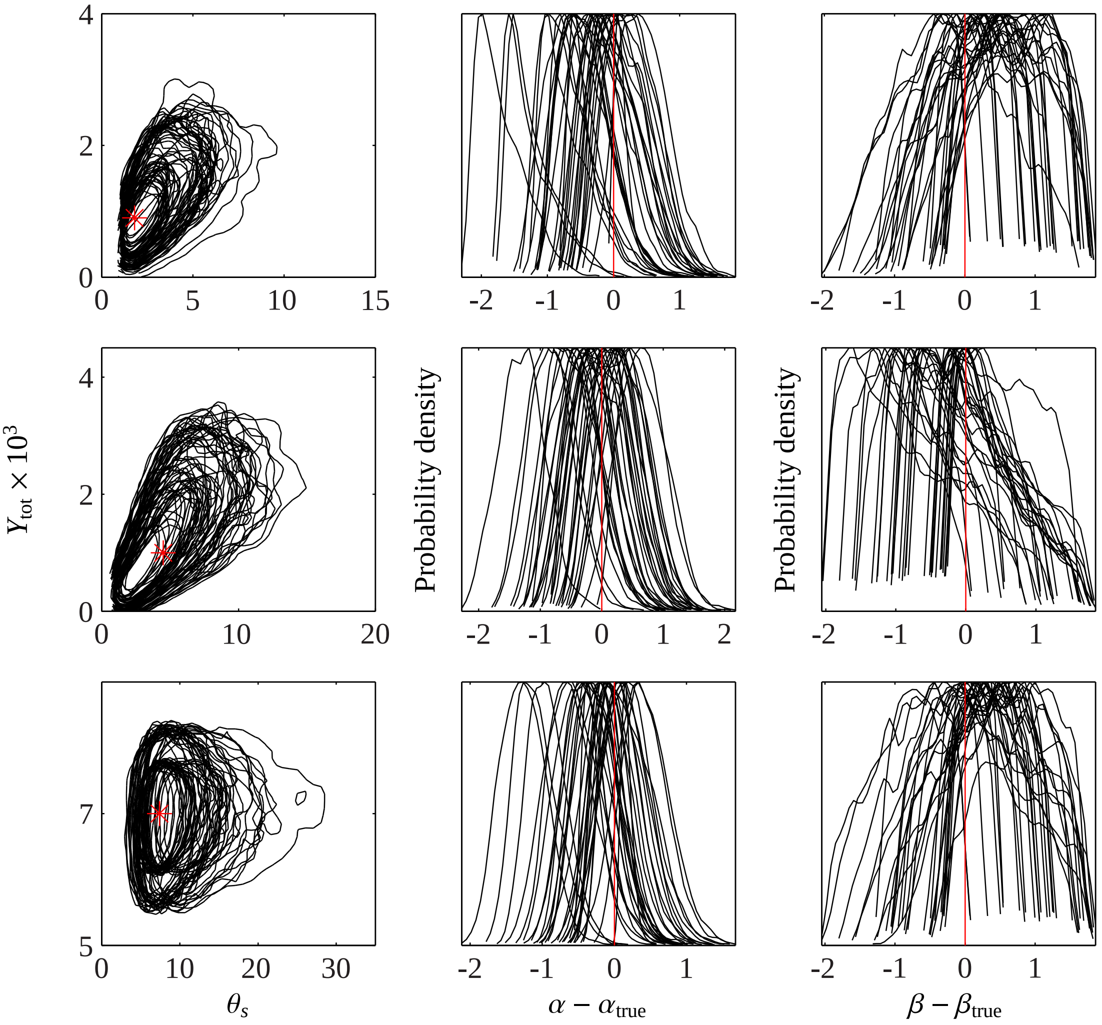

(a) (b) (c)

Figure 5.31: The posterior distributions for simulated clusters with realistic noise levels (see text for details), and varying GNFW shape parameter values based on the REXCESS sample. (a) shows the two-dimensional θ_s and $Y_{\rm tot}$ posterior, and (b) and (c) show the one-dimensional posteriors for α and β, shifted to be centred on the appropriate true value. In all cases γ is fixed to the 'universal' value, α has a truncated Gaussian prior based on the REXCESS sample, β is varied uniformly between 4.5 and 6.5, a *Planck*-like Gaussian prior is used on $Y_{\rm tot}$ and θ_s has the conditional prior drawn from the two-dimensional prior. Results for three different angular sizes are shown (from top to bottom, $\theta_s = 1.8, 4.5$ and 7.4); the input parameter values are marked with red stars and lines.

ship between Y_{500} and $M_{500}^{Y_X}$, an X-ray mass proxy, calibrated using a sample of 71 clusters detected at SNR > 7 by *Planck* with good quality *XMM-Newton* observations available. The Y_{500} values were derived assuming the 'universal' shape and c_{500} values, and so this scaling relationship, and therefore the two-dimensional prior, may be biased if the distributions of α, γ and c_{500} change with redshift and are not the same as those derived from the REXCESS sample and/or if the average value of β across the sample is significantly different from the value derived from numerical simulations. Since a large amount of scatter is added to the relationship, it is likely that any effects are not significant, but this should be investigated further.

A key to constraining the GNFW shape parameters is clearly to maximise the range of angular scales available in the data. There are several ways in which this may be possible:

1. One initial approach would be to include both SA and LA data in the analysis. The LA range of baselines correspond to ≈ 4 to 0.6 arcmin, beginning to probe the α range for the smallest angular-size clusters in the sample, and the γ range for the larger clusters. This would only be useful for the brightest clusters, since the LA (by design) resolves out most of the extended cluster flux. Malak Olamaie is currently modifying McAdam to enable this.

2. Using the *Planck*-like prior on $Y_{\rm tot}$ is a fairly crude way of including *Planck* information in the analysis and does not make the best use of the information available in the *Planck* data on the cluster shape. A full joint analysis of AMI and *Planck* data would fill in the gap in *uv*-coverage between the zero-spacing flux and the shortest AMI-SA baselines, and there would be some overlap with the shortest baselines since the resolution of *Planck* is ≈ 5 arcmin (c.f. Fig. 5.3); this should produce better constraints on the profile shape parameters.

3. The Combined Array for Research in Millimeter-wave Astronomy (CARMA) telescope is another interferometer located in California. Some of its dishes can be used for SZ studies, for which the principle operating frequency is ≈ 30 GHz. It is sensitive to slightly smaller angular scales than the AMI-SA; combining data from the two telescopes should therefore improve the constraints on α. A pipeline for joint analysis of AMI and CARMA data in McAdam already exists

(AMI Consortium: Shimwell et al., 2013a), and since CARMA has also been conducting a *Planck* follow-up programme, there is a large sample of clusters with existing AMI, CARMA and *Planck* data; it should be possible to combine all three datasets.

4. *Chandra* and *XMM-Newton* X-ray data are of higher resolution than SZ data, but the combined problem of sensitivity plus backgrounds mean that observing X-ray emission to large radius in a cluster is problematic. Simulations on analysing X-ray data in a similar, Bayesian manner exist (Olamaie et al., in prep.); it would be interesting to extend this to a joint X-ray-SZ analysis pipeline to aid in constraining α and β.

5.6 Conclusions

In this chapter, I have used simulations to investigate the effects of varying the GNFW shape parameters, commonly fixed to a set of 'universal' values as defined in Arnaud et al. (2010), on the constraints derived from AMI data. I have also investigated the potential of AMI data to constrain some of these parameters. I have found the following.

1. Although AMI data only cover a limited range of angular scales, changing the shape parameter values does have an effect on the part of the cluster profile that is observed with AMI.

2. For small to medium-sized clusters, the true values of Y_{tot} and θ_s are mostly recovered when the cluster is modelled with an (incorrectly) fixed profile, but the shape and size of the resulting constraints can vary wildly.

3. For clusters with large angular sizes, the true values of Y_{tot} and θ_s are often not recovered correctly when an incorrect profile is used as a model.

4. The limited range of angular scales that AMI covers leads to large degeneracies between Y_{tot}, θ_s and all of the shape parameter values, and these can easily lead to biases and spurious constraints in the recovered parameter values if care is not taken when deciding on the priors to be used.

5. For small to medium-sized clusters, the true values of Y_{tot} and θ_s can be recovered correctly while varying the profile parameters α and β, using the joint two-dimensional prior on Y_{tot} and θ_s, a prior based on the REXCESS sample on α, and a uniform prior over a small range of values on β. This method can also place weak constraints on β (α) for small- (medium-) sized clusters, but care must be taken in interpreting these due to remaining biases.

6. For large clusters, some additional information is required to correctly recover Y_{tot} and θ_s; this can be provided by placing a *Planck*-like prior on Y_{tot} and a conditional prior on θ_s. This method can also place weak constraints on α.

7. A *Planck*-like prior on small- to medium-sized clusters acts to tighten the θ_s-Y_{tot} constraints, but does not improve the constraints on the shape parameter values.

Appendix A

For each cluster in the final SZ sample, available information on the cluster (other names, redshift), and *Planck* and AMI detection status is summarised. The *Planck* detection status for the three pipelines is summarised by a 0 (no detection) or 1 (detection), in the order MMF1, MMF3, PwS, i.e. 111 represents detections by all three pipelines. The clusters are ordered by decreasing *Planck* SNR, where the SNR is that reported by PwS if available, and MMF3 otherwise.

AMI source-subtracted maps are shown both with natural weighting and with a Gaussian weighting function of width 600λ at the 30%-power point applied; the symbols × and + show the positions of subtracted sources (as described in Table 4.4), and □ shows the AMI, McAdam-determined position of the cluster. Contours are plotted at $\pm3, \pm4, \ldots\ \pm10\times$ the r.m.s. noise level, and dashed contours are negative. The synthesised beam is shown in the bottom left-hand corner.

Posterior distributions for position offset and cluster model parameters are also shown; in these plots the units are arcsec on the sky for offset from the phase centre in RA (x_0) and δ (y_0), arcmin^2 for $Y_{\rm tot}$ and arcmin for θ_s. The $Y_{\rm tot}$ vs θ_s posterior distribution is shown in black overlaid with that obtained by PwS using *Planck* data for the cluster in red; in the one case where PwS does not detect the cluster, the MMF3 contours are plotted instead, in green. The AMI prior is also plotted as a dashed black line, and the AMI mean value is plotted with a black cross.

CAJ1635+6612 (A2218, RXC J1635.8+6612); z = 0.171

AMI detection category: Y, $\Delta\log_{10}(Z)$ = 33.75

Planck detections 111, SNR = 17.207

AMI-*Planck* distance = 0.62 arcmin = $1.00\sigma_{Planck}$

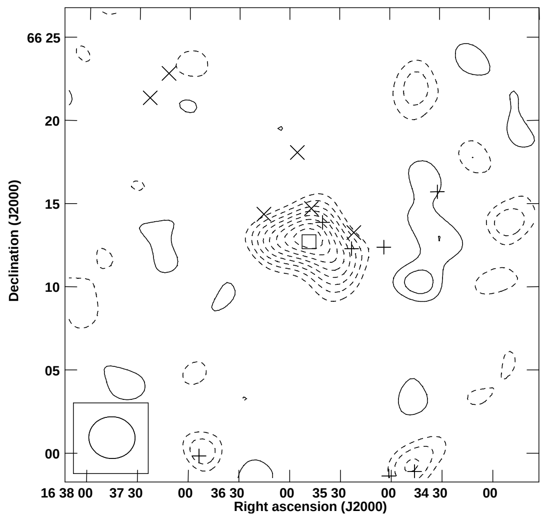

(a) Natural weighting, contours at $\pm(3\text{ to }10)\times 130.8\,\mu\text{Jy beam}^{-1}$

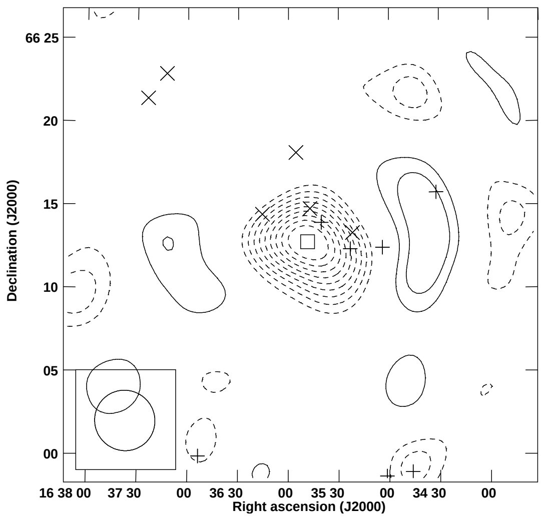

(b) *uv*-taper = 600λ, contours at $\pm(3\text{ to }10)\times 163.1\,\mu\text{Jy beam}^{-1}$

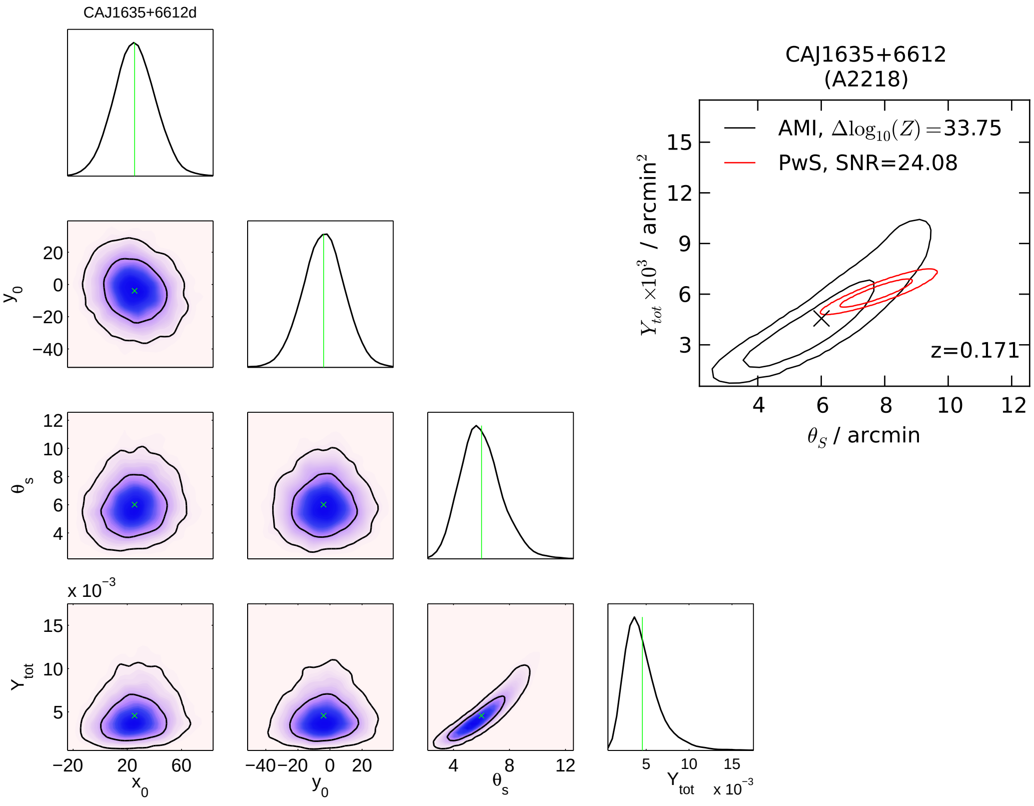

CAJ1938+5409 (CL1938+54, RXC J1938.3+5409); z = 0.26

AMI detection category: Y, $\Delta\log_{10}(Z)$ = 16.01

Planck detections 111, SNR = 14.971

AMI-*Planck* distance = 0.25 arcmin = $0.39\sigma_{Planck}$

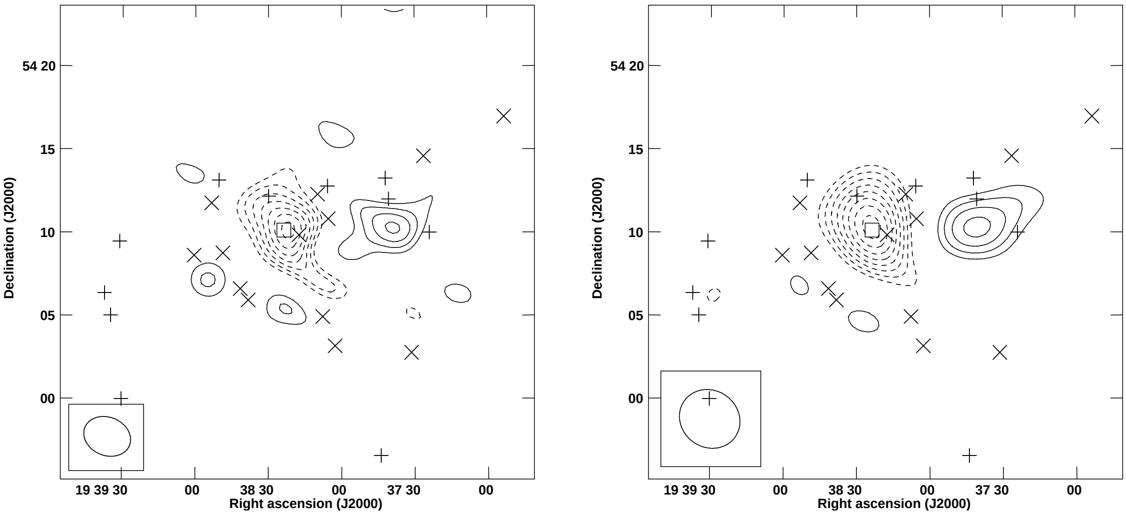

(a) Natural weighting, contours at $\pm(3\text{ to }10)\times 110.4\,\mu$Jy beam^{-1}

(b) *uv*-taper = 600λ, contours at $\pm(3\text{ to }10)\times 153.5\,\mu$Jy beam^{-1}

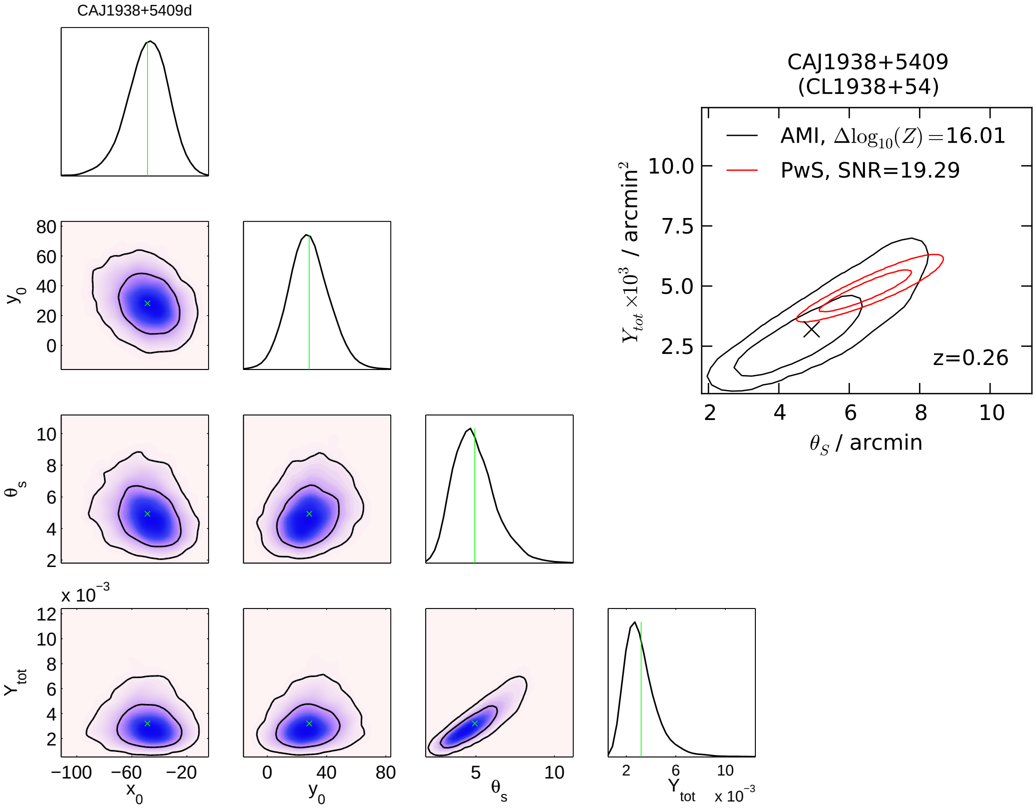

CAJ2122+2311 (ZW8503); z = 0.143
AMI detection category: M, $\Delta\log_{10}(Z) = 1.61$
Planck detections 111, SNR = 13.092
AMI-*Planck* distance = 0.31 arcmin = $0.47\sigma_{Planck}$

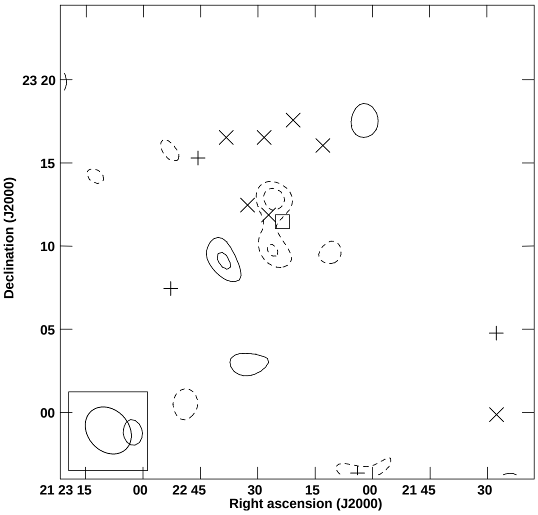

(a) Natural weighting, contours at $\pm(3 \text{ to } 10) \times 89.11\,\mu\text{Jy beam}^{-1}$

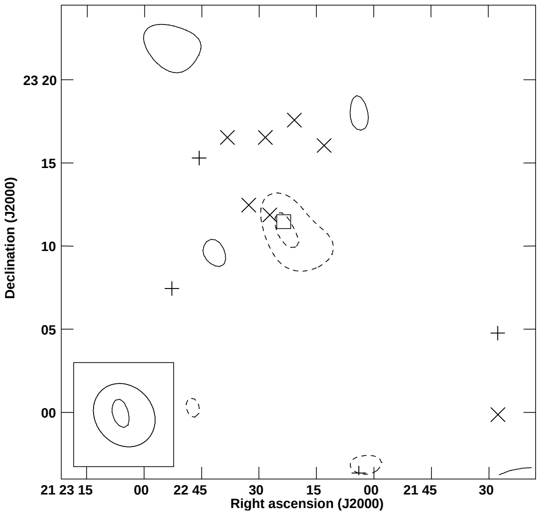

(b) uv-taper = 600λ, contours at $\pm(3 \text{ to } 10) \times 121.5\,\mu\text{Jy beam}^{-1}$

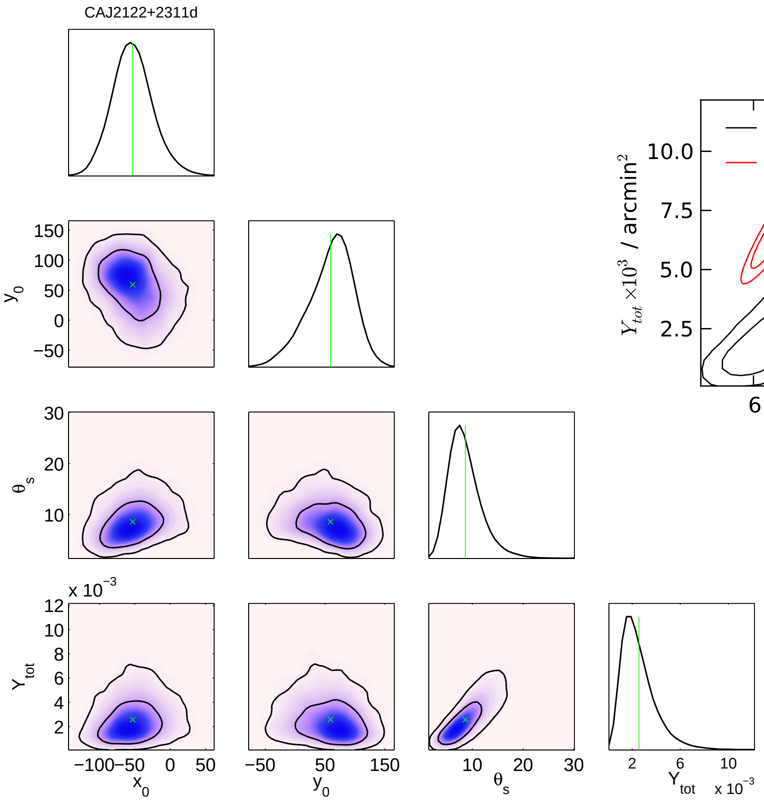

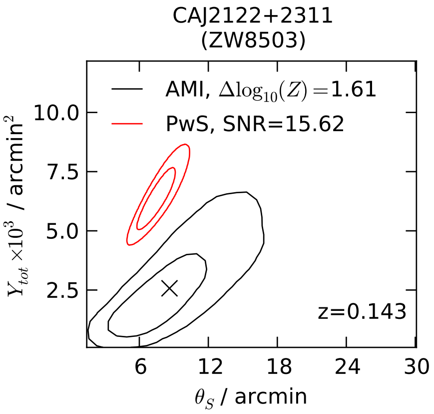

CAJ0830+6551 (A665, RXC J0830.9+6551); z = 0.182
AMI detection category: Y, $\Delta\log_{10}(Z) = 47.39$
Planck detections 111, SNR = 12.974
AMI-*Planck* distance = 0.88 arcmin = $1.40\sigma_{Planck}$

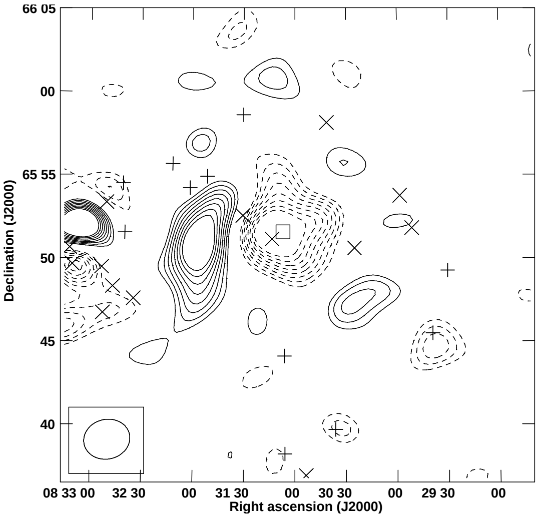

(a) Natural weighting, contours at $\pm(3\text{ to }10) \times 88.19\,\mu\text{Jy beam}^{-1}$

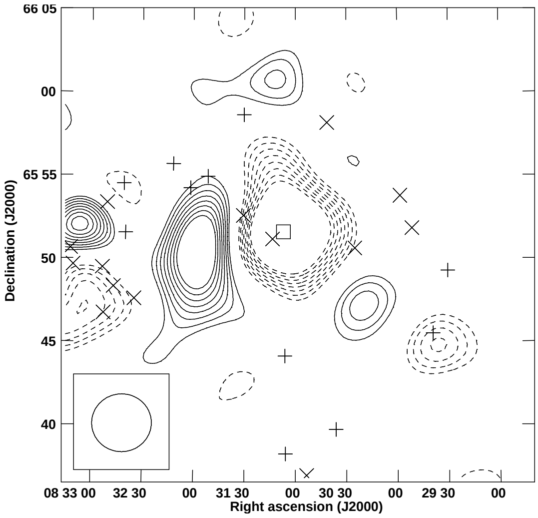

(b) *uv*-taper = 600λ, contours at $\pm(3\text{ to }10) \times 102.2\,\mu\text{Jy beam}^{-1}$

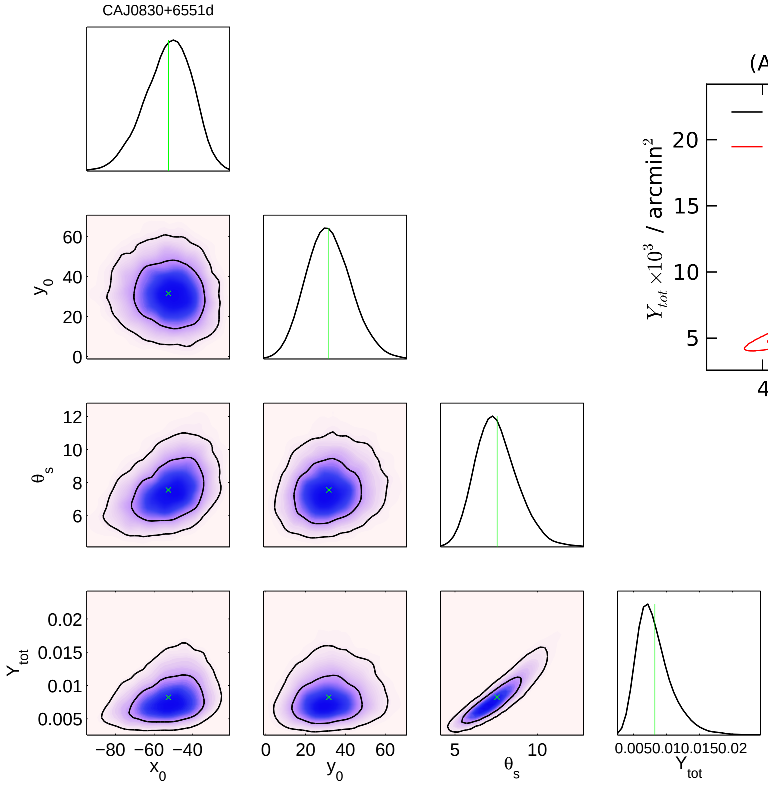

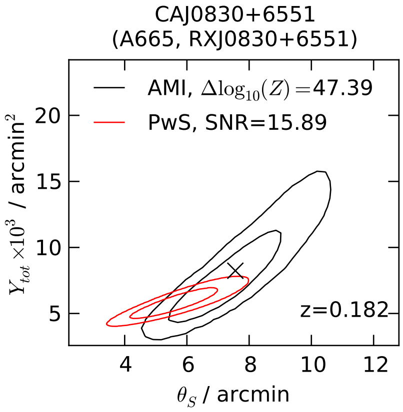

CAJ1425+3750 (A1914, RXC J1426.0+3749); z = 0.171

AMI detection category: Y, $\Delta\log_{10}(Z)$ = 27.71

Planck detections 111, SNR = 11.764

AMI-*Planck* distance = 0.53 arcmin = $0.84\sigma_{Planck}$

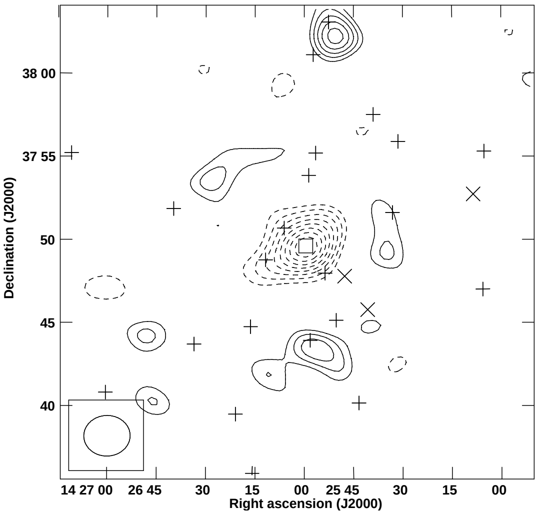

(a) Natural weighting, contours at $\pm(3 \text{ to } 10) \times 118.1\,\mu\text{Jy beam}^{-1}$

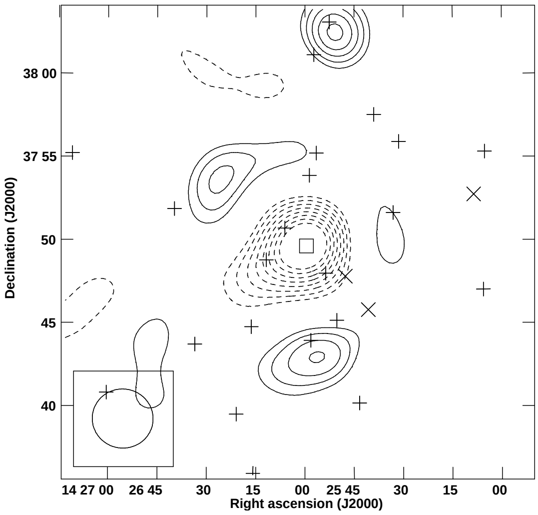

(b) *uv*-taper = 600λ, contours at $\pm(3 \text{ to } 10) \times 145.5\,\mu\text{Jy beam}^{-1}$

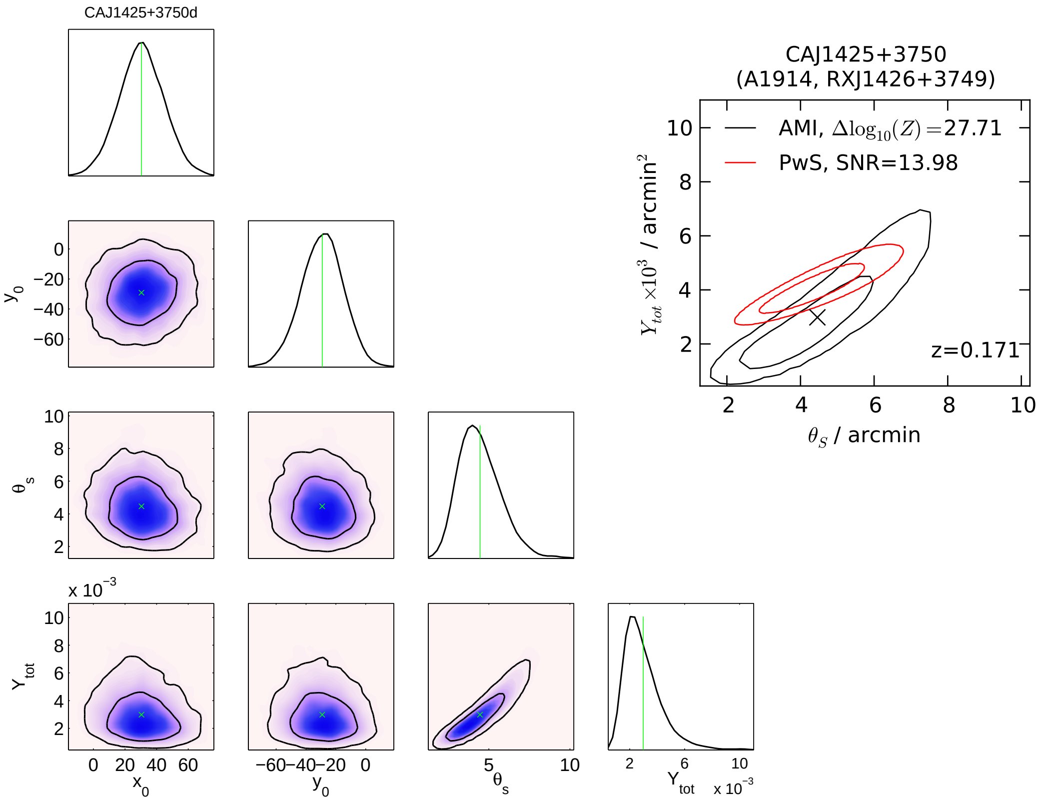

CAJ1510+3329 (A2034, RXC J1510.1+3330); z = 0.113

AMI detection category: Y, $\Delta \log_{10}(Z)$ = 26.59

Planck detections 111, SNR = 10.459

AMI-*Planck* distance = 1.31 arcmin = $1.50\sigma_{Planck}$

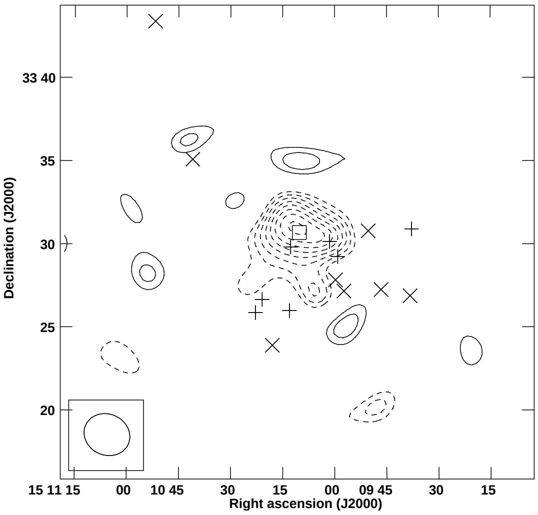

(a) Natural weighting, contours at $\pm$(3 to 10) $\times$ 89.43 μJy beam^{-1}

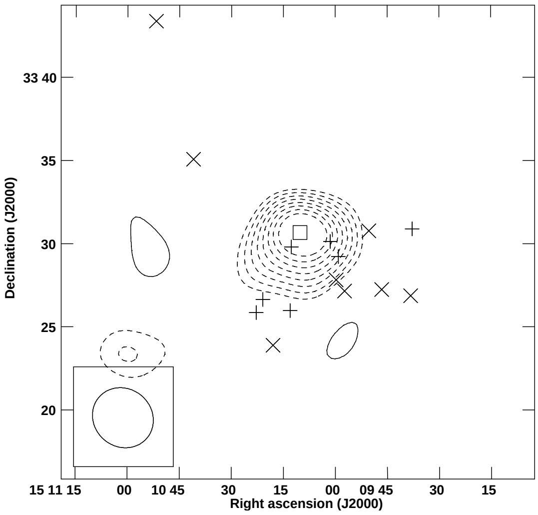

(b) *uv*-taper = 600λ, contours at $\pm$(3 to 10) $\times$ 121.1 μJy beam^{-1}

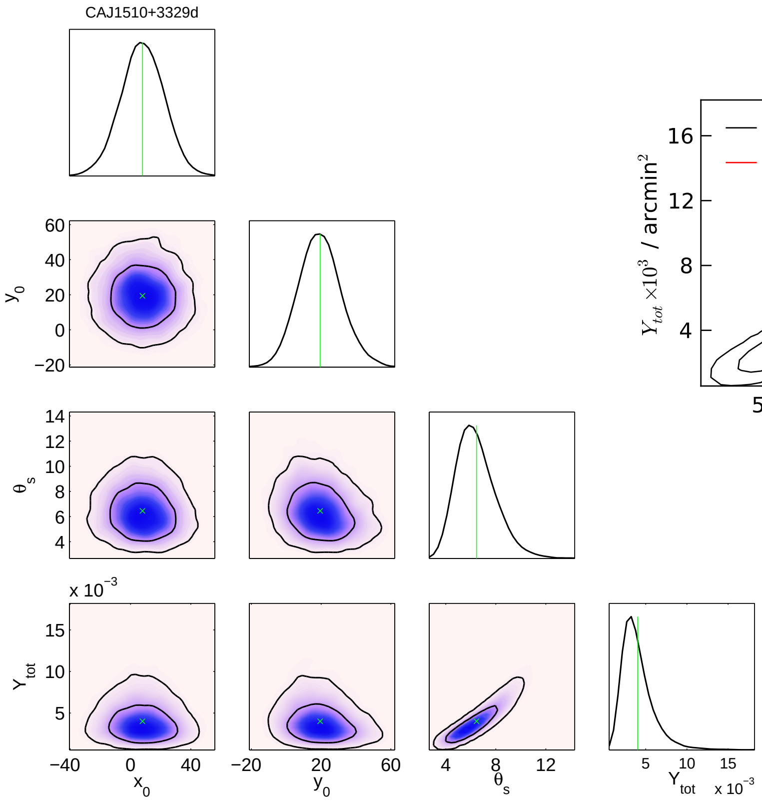

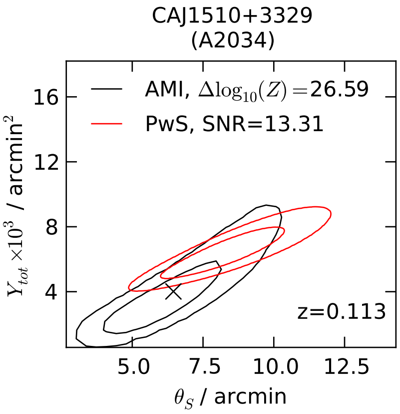

CAJ0107+5407 (RXC J0107.7+5408); z = 0.107

AMI detection category: Y, $\Delta\log_{10}(Z)$ = 18.24

Planck detections 111, SNR = 10.225

AMI-*Planck* distance = 1.91 arcmin = $2.89\sigma_{Planck}$

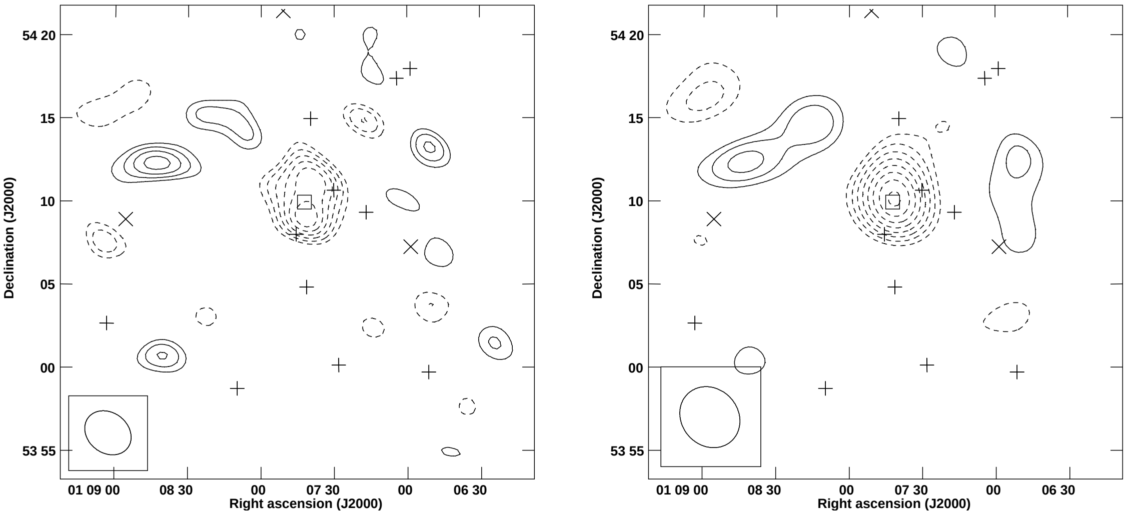

(a) Natural weighting, contours at $\pm(3\text{ to }10) \times 104.4\,\mu$Jy beam^{-1}

(b) *uv*-taper = 600λ, contours at $\pm(3\text{ to }10) \times 141.4\,\mu$Jy beam^{-1}

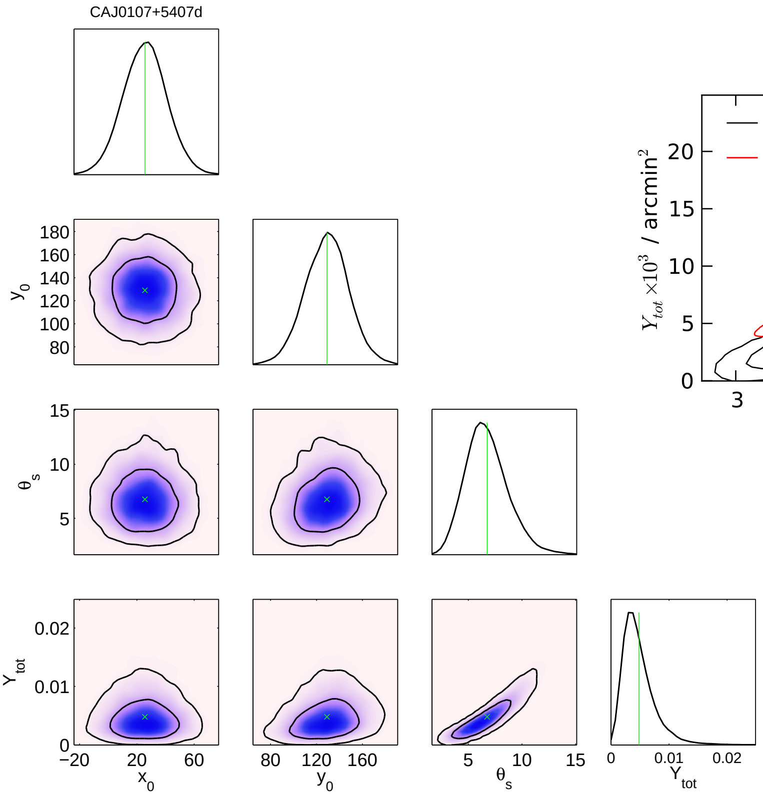

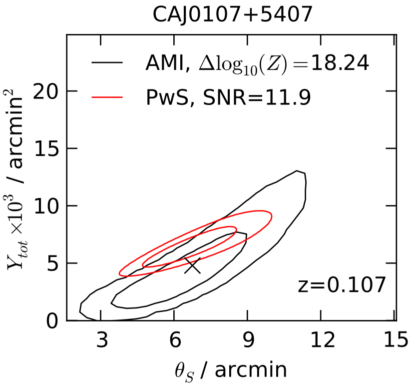

CAJ1720+2637 (RXC J1720.1+2637); z = 0.164

AMI detection category: M, $\Delta \log_{10}(Z) = 1.59$

Planck detections 111, SNR = 9.904

AMI-*Planck* distance = 0.45 arcmin = $0.59\sigma_{Planck}$

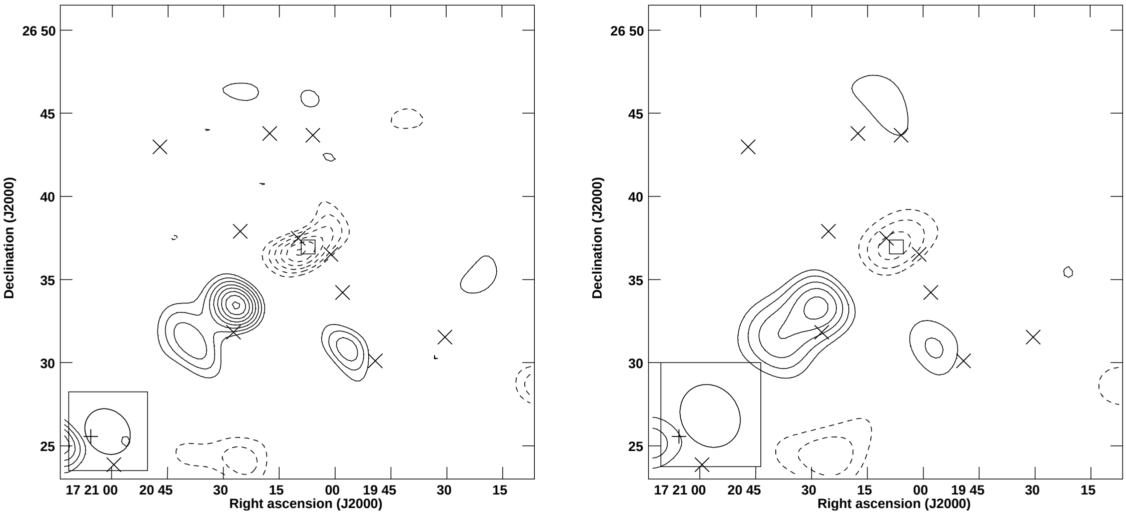

(a) Natural weighting, contours at $\pm(3 \text{ to } 10) \times 83.05\,\mu\text{Jy beam}^{-1}$

(b) *uv*-taper = 600λ, contours at $\pm(3 \text{ to } 10) \times 127.5\,\mu\text{Jy beam}^{-1}$

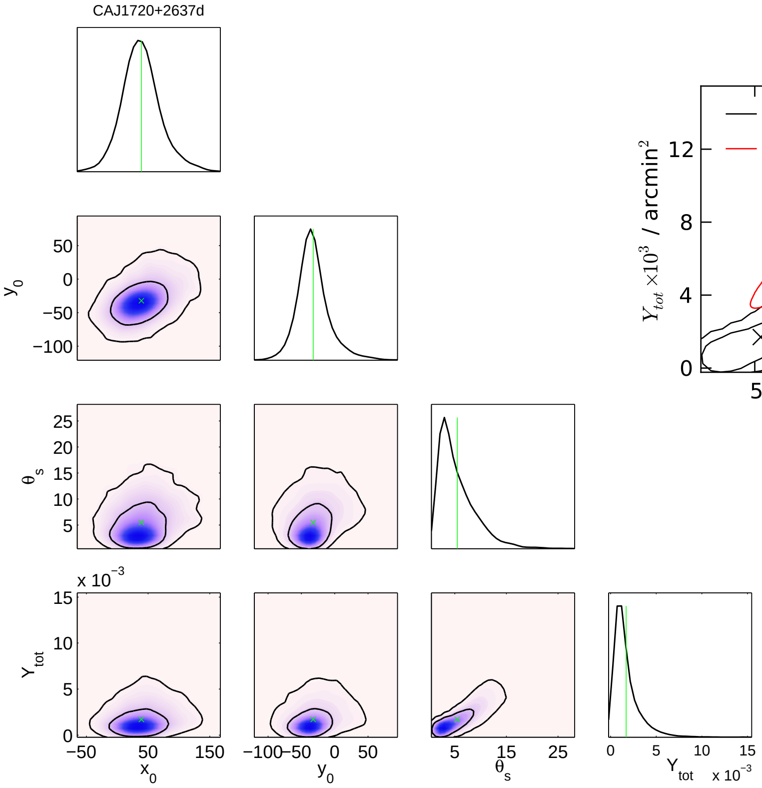

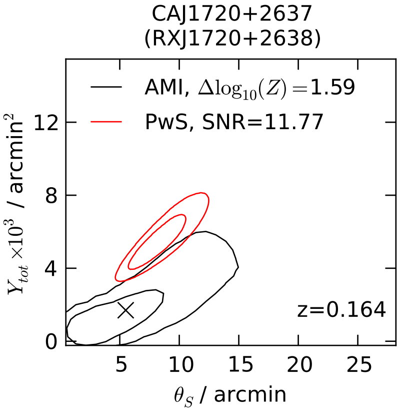

CAJ1155+2324 (A1413, RXC J1155.3+2324); z = 0.143

AMI detection category: Y, $\Delta \log_{10}(Z) = 25.06$

Planck detections 111, SNR = 9.791

AMI-*Planck* distance = 0.43 arcmin = $0.54\sigma_{Planck}$

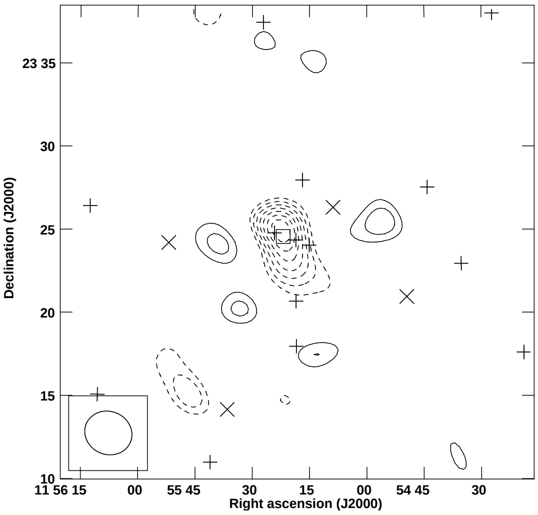

(a) Natural weighting, contours at $\pm(3 \text{ to } 10) \times 108.0\,\mu\text{Jy beam}^{-1}$

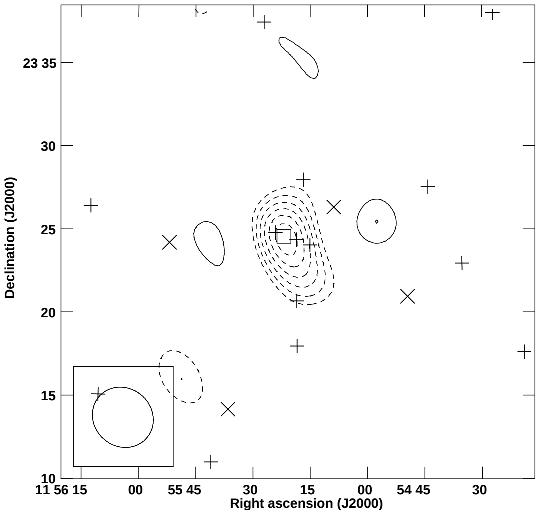

(b) *uv*-taper = 600λ, contours at $\pm(3 \text{ to } 10) \times 154.5\,\mu\text{Jy beam}^{-1}$

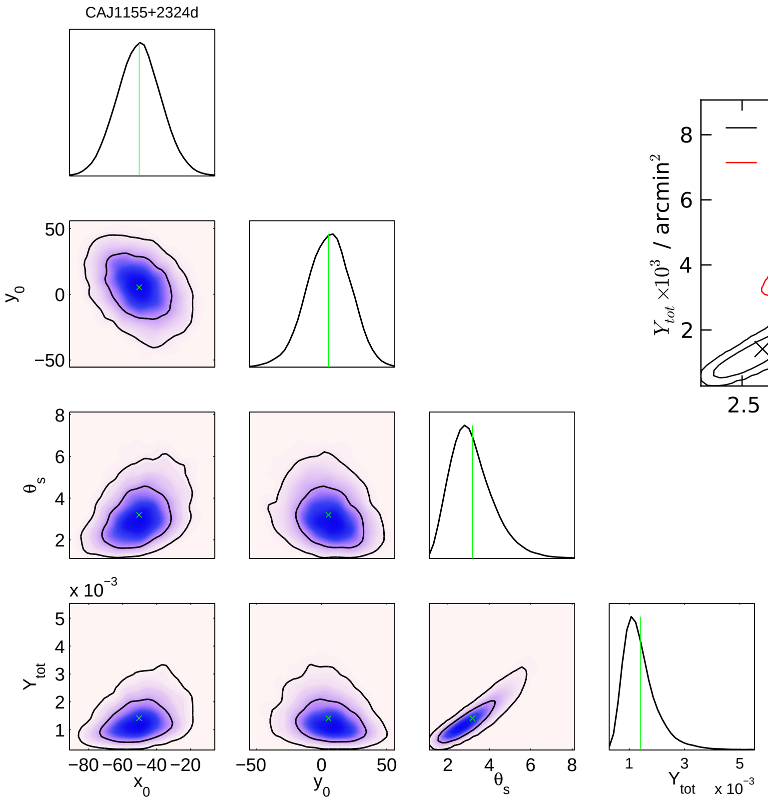

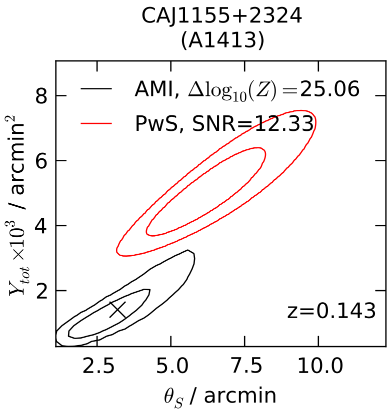

CAJ1948+5114 (RXC J1948.3+5113); z = 0.185
AMI detection category: Y, $\Delta \log_{10}(Z) = 6.62$
Planck detections 111, SNR = 9.544
AMI-*Planck* distance = 1.18 arcmin = $1.58\sigma_{Planck}$

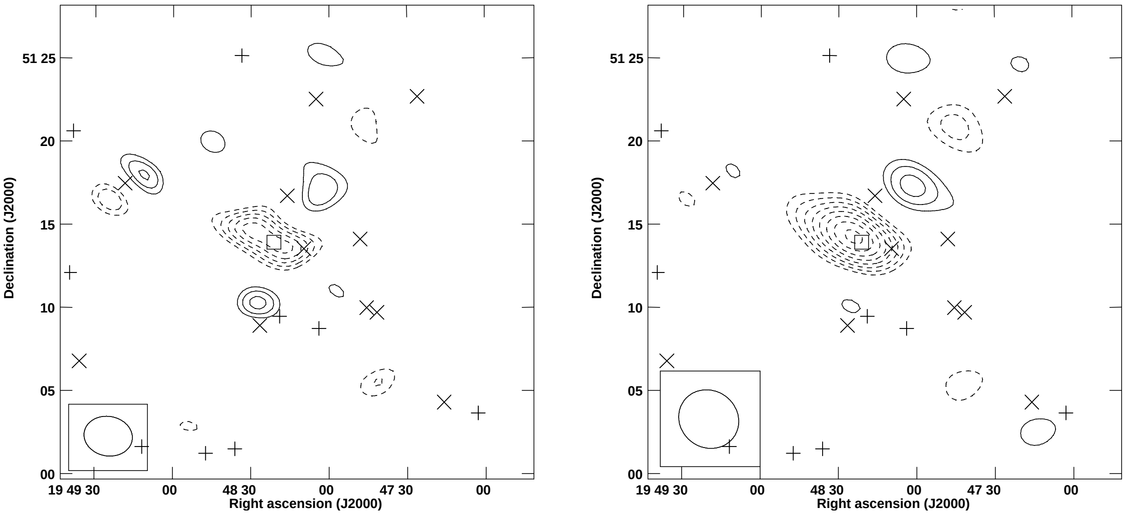

(a) Natural weighting, contours at $\pm(3 \text{ to } 10) \times 103.4\,\mu\text{Jy beam}^{-1}$

(b) *uv*-taper = 600λ, contours at $\pm(3 \text{ to } 10) \times 111.1\,\mu\text{Jy beam}^{-1}$

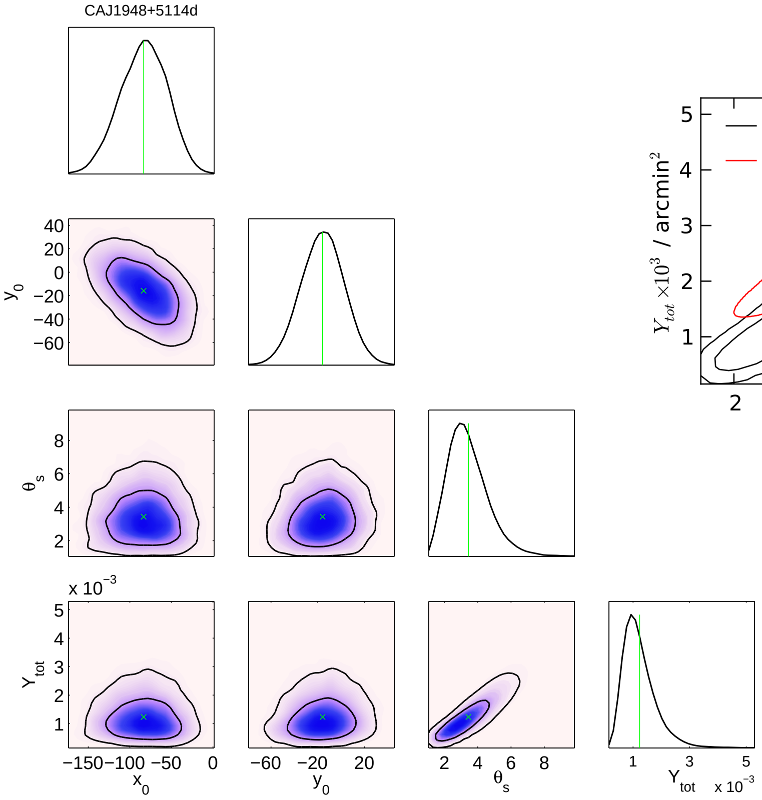

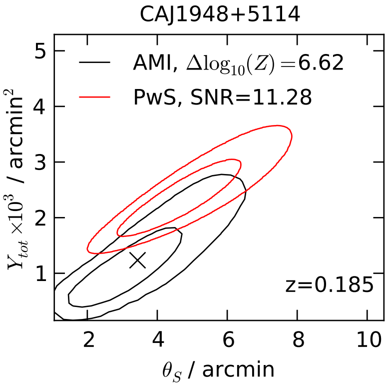

CAJ0917+5143 (A773, RXC J0917.8+5143); z = 0.217

AMI detection category: Y, $\Delta \log_{10}(Z) = 34.23$

Planck detections 111, SNR = 9.527

AMI-*Planck* distance = 1.03 arcmin = $1.08\sigma_{Planck}$

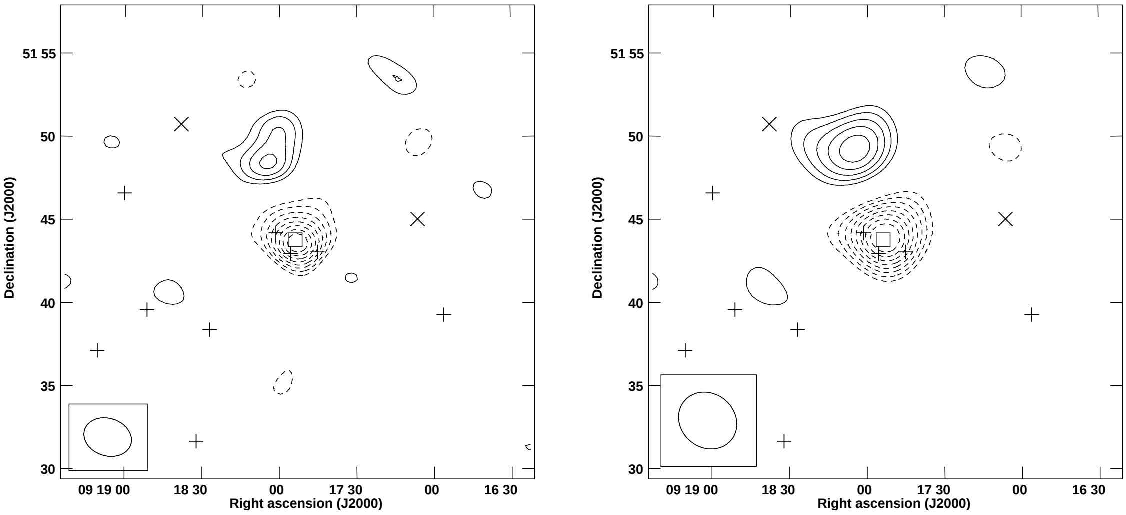

(a) Natural weighting, contours at $\pm(3 \text{ to } 10) \times 103.2\,\mu\text{Jy beam}^{-1}$

(b) *uv*-taper = 600λ, contours at $\pm(3 \text{ to } 10) \times 134.0\,\mu\text{Jy beam}^{-1}$

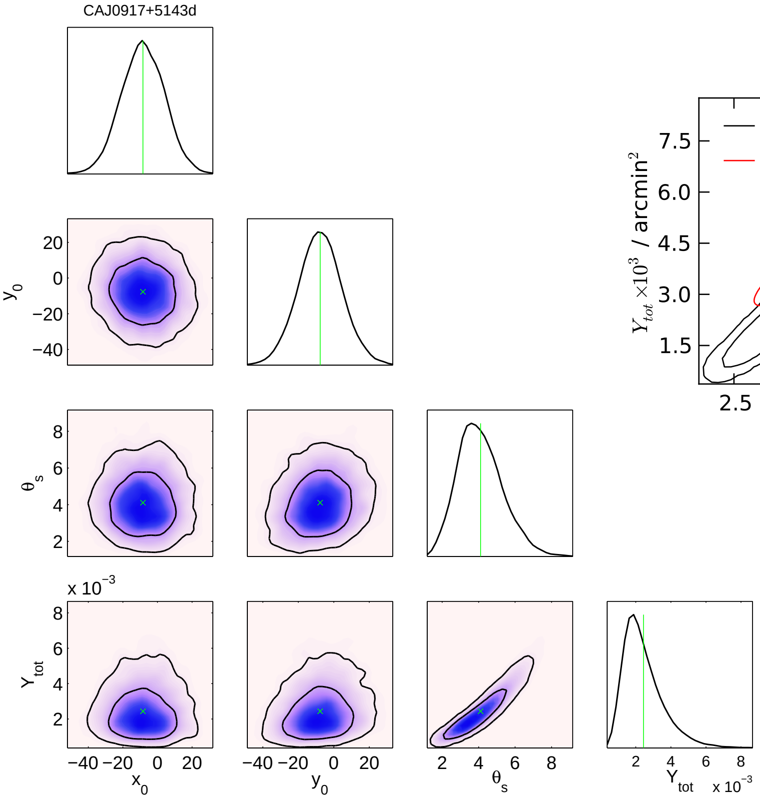

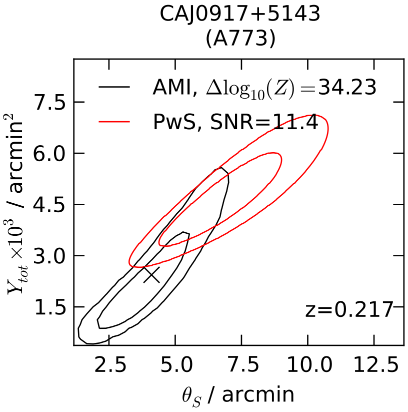

CAJ0638+4748 (ZW1133, RXC J0638.1+4747); z = 0.174

AMI detection category: Y, $\Delta\log_{10}(Z) = 6.51$
Planck detections 111, SNR = 9.425
AMI-*Planck* distance = 0.30 arcmin = $0.27\sigma_{Planck}$

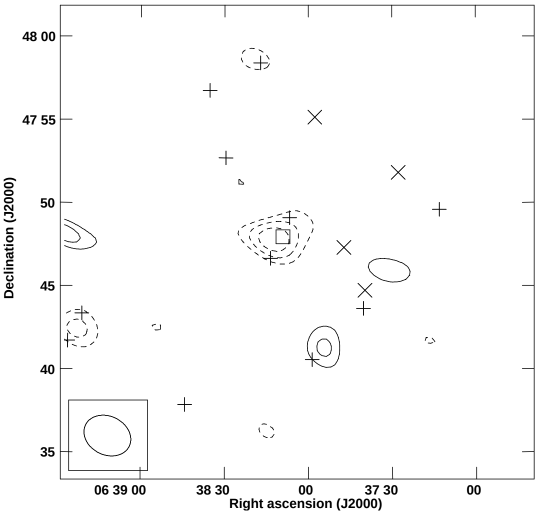

(a) Natural weighting, contours at $\pm(3\text{ to }10)\times 103.1\,\mu\text{Jy beam}^{-1}$

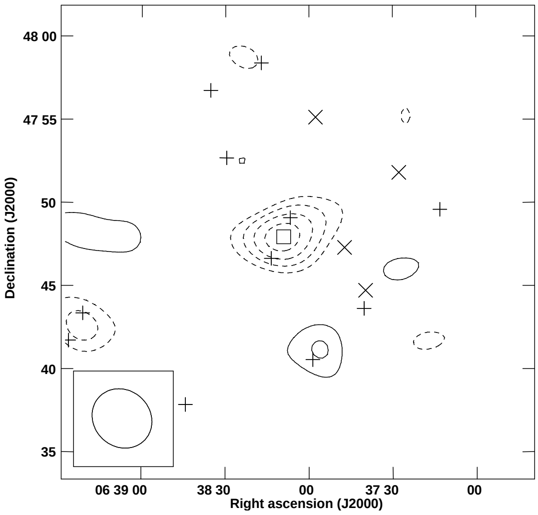

(b) *uv*-taper = 600λ, contours at $\pm(3\text{ to }10)\times 132.0\,\mu\text{Jy beam}^{-1}$

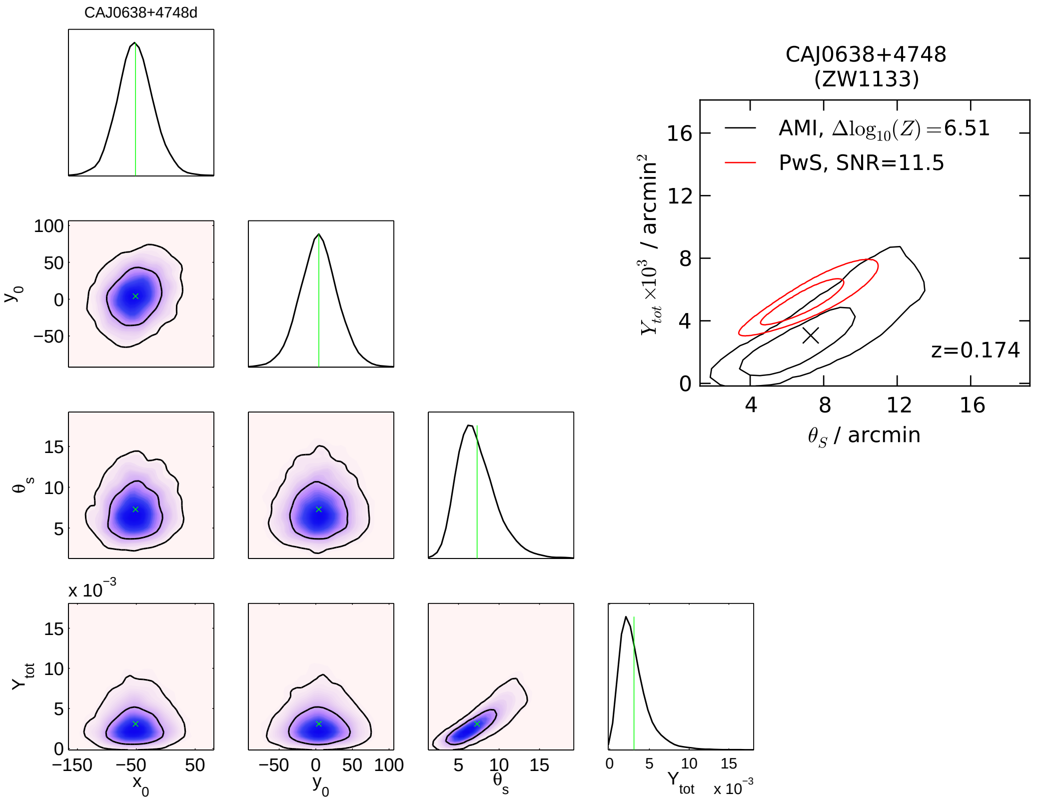

CAJ1414+7116 (A1895, RXC J1414.2+7115); z = 0.225
AMI detection category: Y, $\Delta\log_{10}(Z)$ = 4.53
Planck detections 111, SNR = 8.975
AMI-*Planck* distance = 1.05 arcmin = $1.57\sigma_{Planck}$

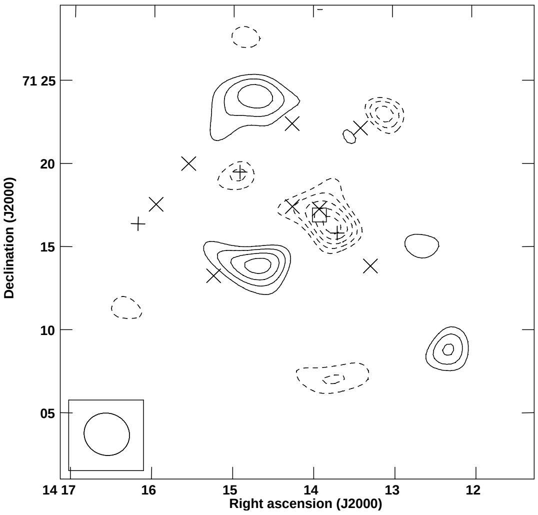

(a) Natural weighting, contours at $\pm(3 \text{ to } 10) \times 106.8\,\mu\text{Jy beam}^{-1}$

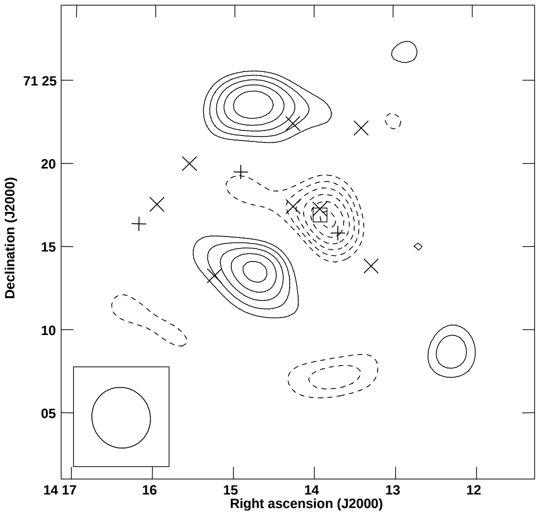

(b) *uv*-taper = 600λ, contours at $\pm(3 \text{ to } 10) \times 125.1\,\mu\text{Jy beam}^{-1}$

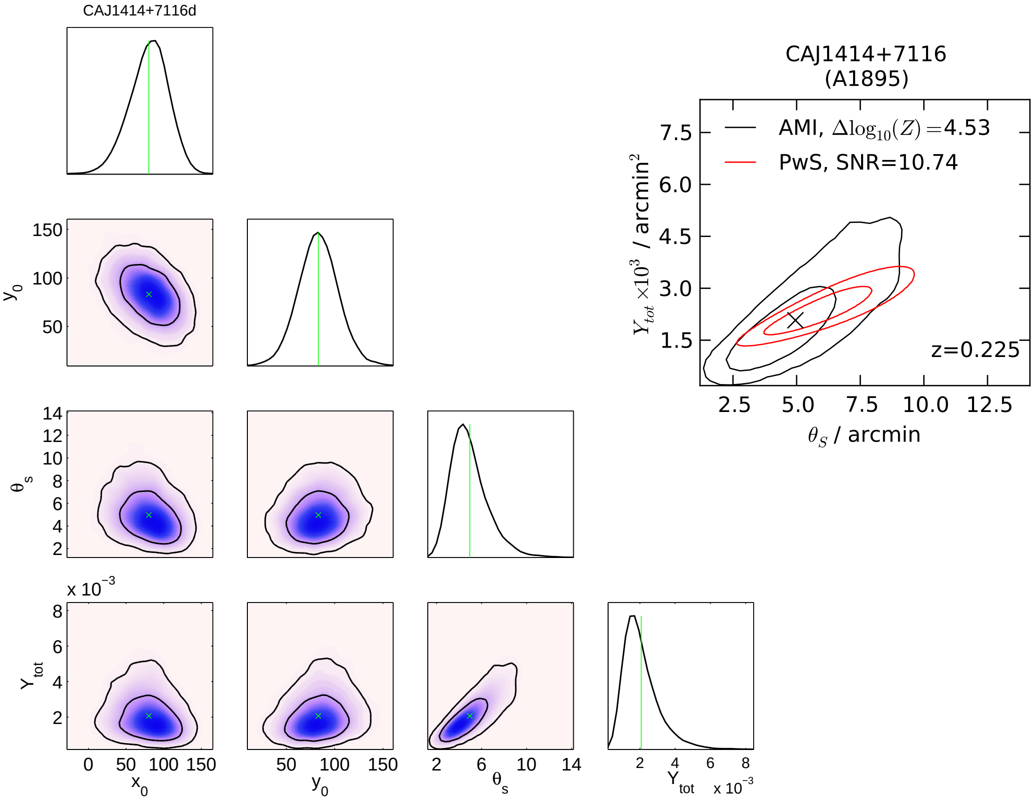

CAJ1524+2954 (A2069, RXC J1524.1+2955); z = 0.115

AMI detection category: M, $\Delta\log_{10}(Z) = 0.91$

Planck detections 111, SNR = 8.964

AMI-*Planck* distance = 0.48 arcmin = $0.50\sigma_{Planck}$

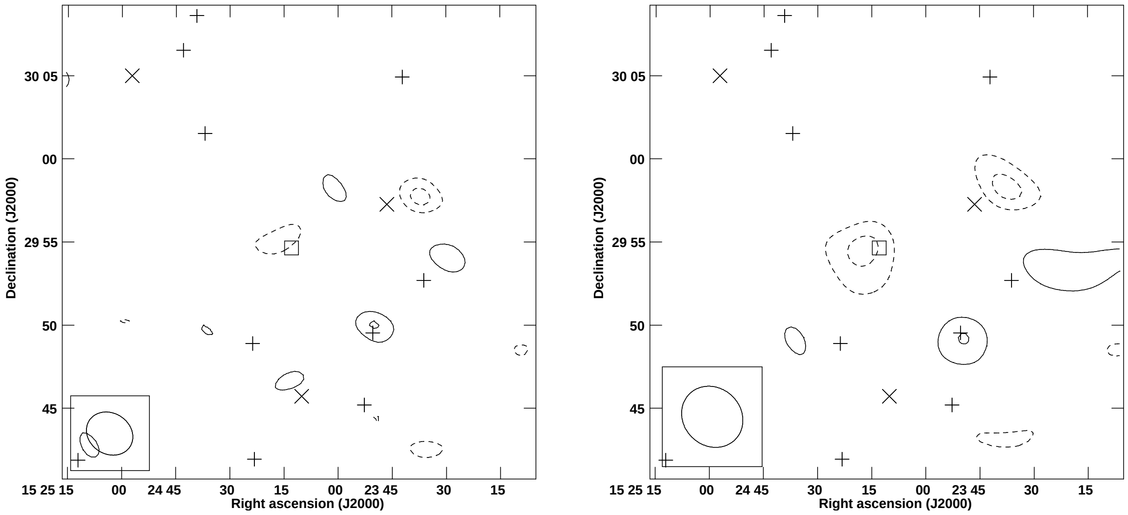

(a) Natural weighting, contours at $\pm(3\text{ to }10) \times 97.24\,\mu\text{Jy beam}^{-1}$

(b) *uv*-taper = 600λ, contours at $\pm(3\text{ to }10) \times 125.4\,\mu\text{Jy beam}^{-1}$

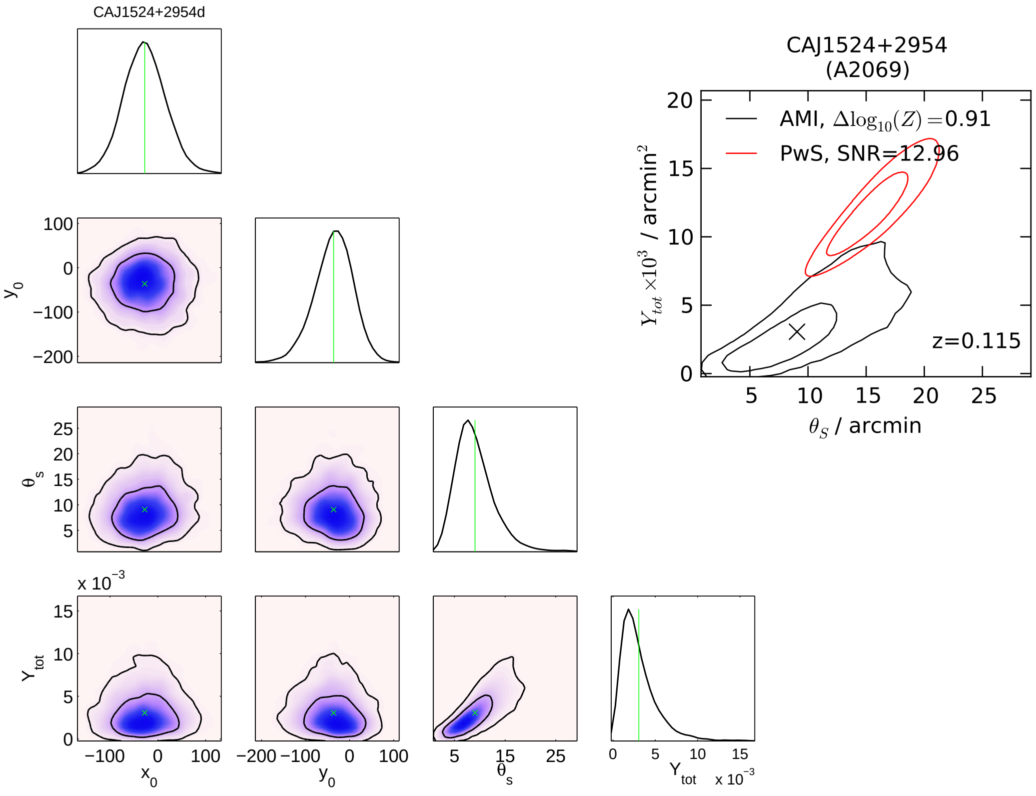

CAJ2200+2058 (A2409, RXC J2200.8+2058); z = 0.147

AMI detection category: Y, $\Delta\log_{10}(Z) = 35.09$

Planck detections 111, SNR = 8.74

AMI-*Planck* distance = 0.46 arcmin = $0.71\sigma_{Planck}$

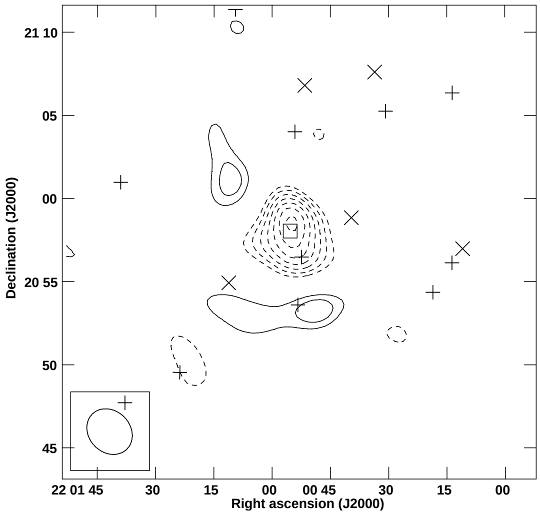

(a) Natural weighting, contours at $\pm(3 \text{ to } 10) \times 125.3\,\mu\text{Jy beam}^{-1}$

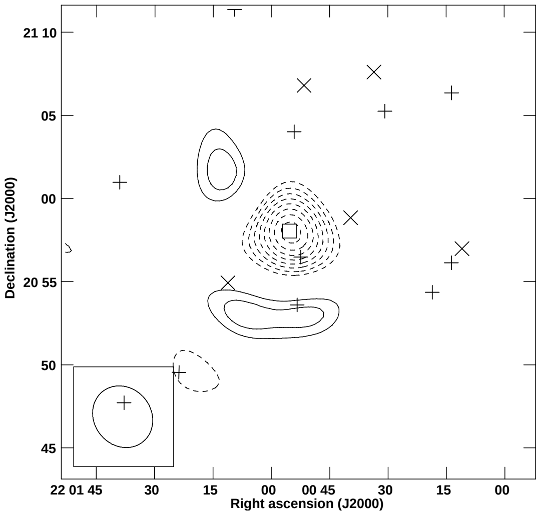

(b) *uv*-taper = 600λ, contours at $\pm(3 \text{ to } 10) \times 162.3\,\mu\text{Jy beam}^{-1}$

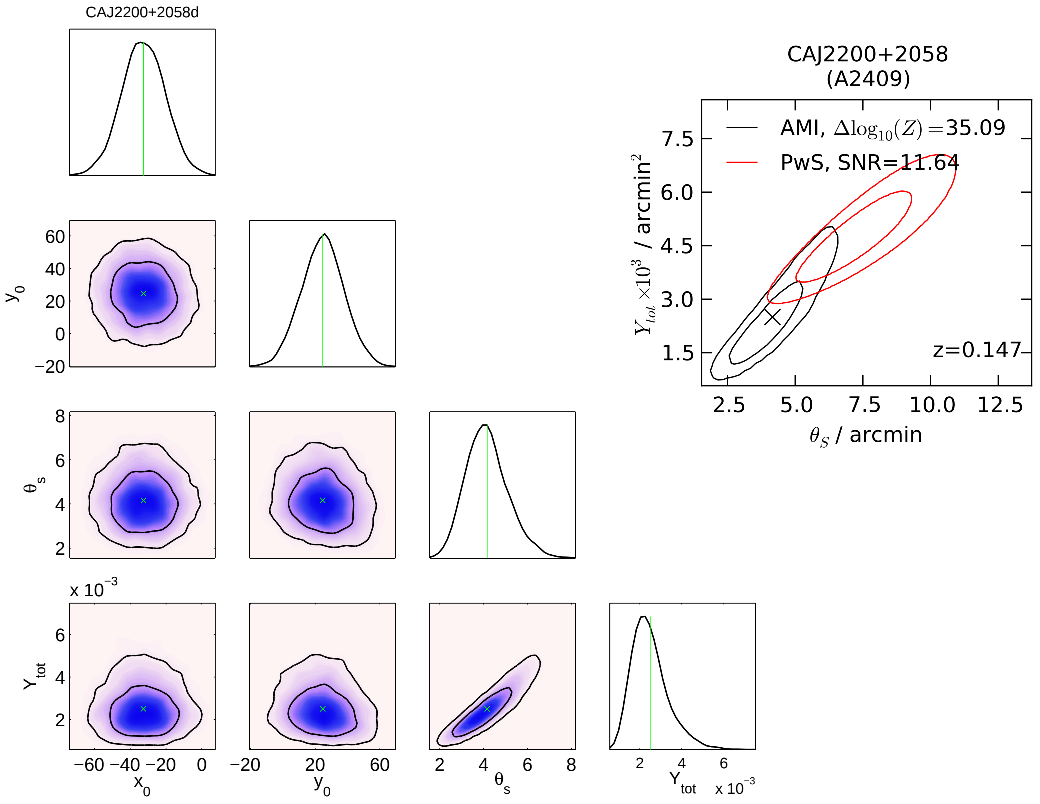

CAJ0622+7442 (PLCKESZ G139.59+24.18); z = 0.267
AMI detection category: Y, $\Delta\log_{10}(Z) = 20.45$
Planck detections 111, SNR = 8.658
AMI-*Planck* distance = 1.05 arcmin = $1.72\sigma_{Planck}$

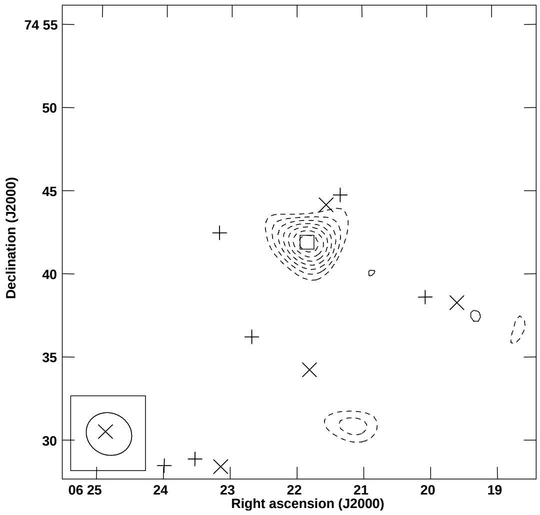

(a) Natural weighting, contours at $\pm(3 \text{ to } 10) \times 88.74\,\mu\text{Jy beam}^{-1}$

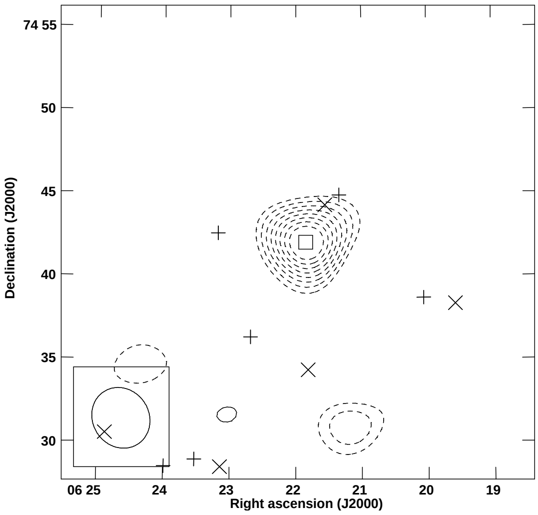

(b) *uv*-taper = 600λ, contours at $\pm(3 \text{ to } 10) \times 96.82\,\mu\text{Jy beam}^{-1}$

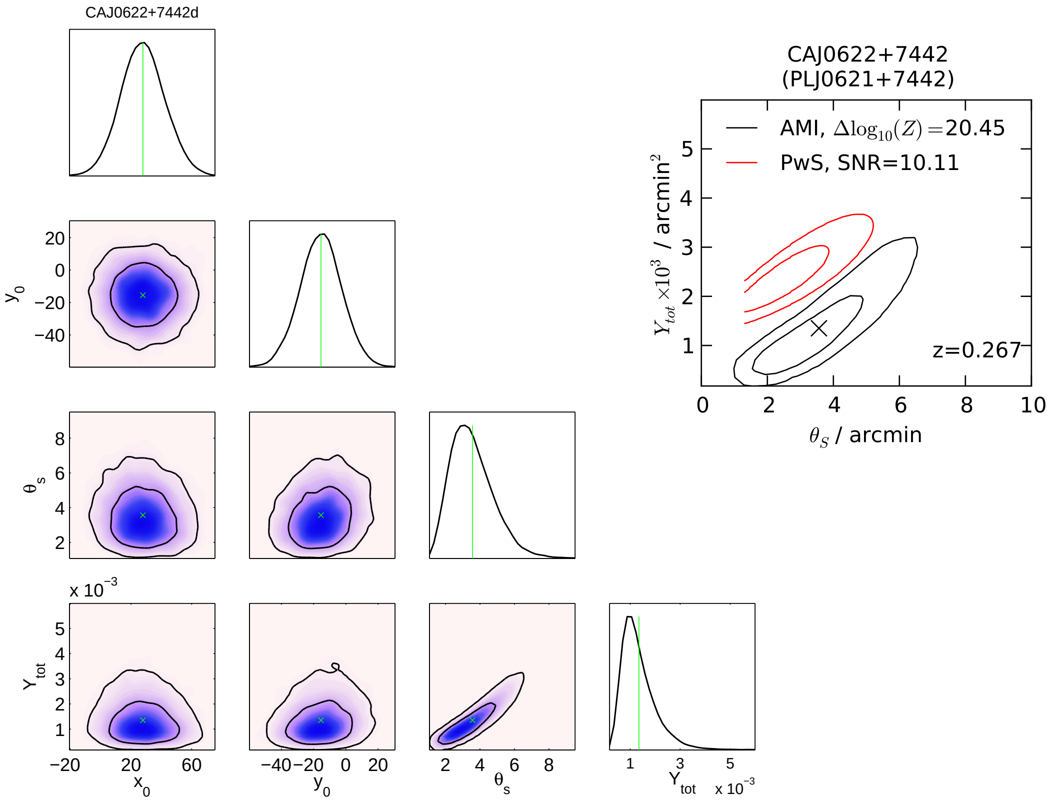

CAJ1724+8553 (A2294, RXC J1723.7+8553); z = 0.178

AMI detection category: Y, $\Delta \log_{10}(Z) = 6.07$

Planck detections 111, SNR = 8.566

AMI-*Planck* distance = 1.13 arcmin = $1.51\sigma_{Planck}$

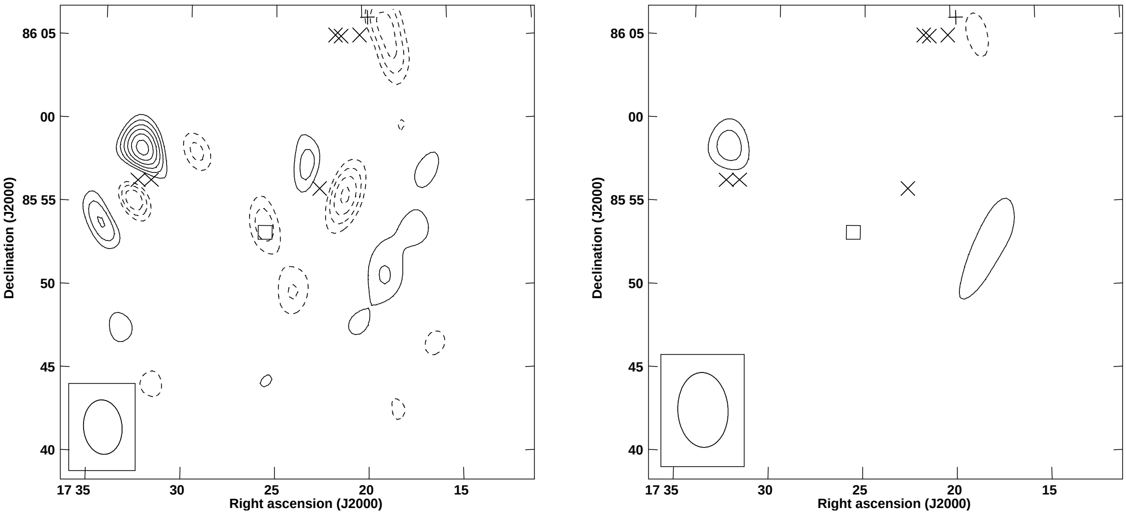

(a) Natural weighting, contours at $\pm(3 \text{ to } 10) \times 130.2\,\mu\text{Jy beam}^{-1}$

(b) *uv*-taper = 600λ, contours at $\pm(3 \text{ to } 10) \times 247.5\,\mu\text{Jy beam}^{-1}$

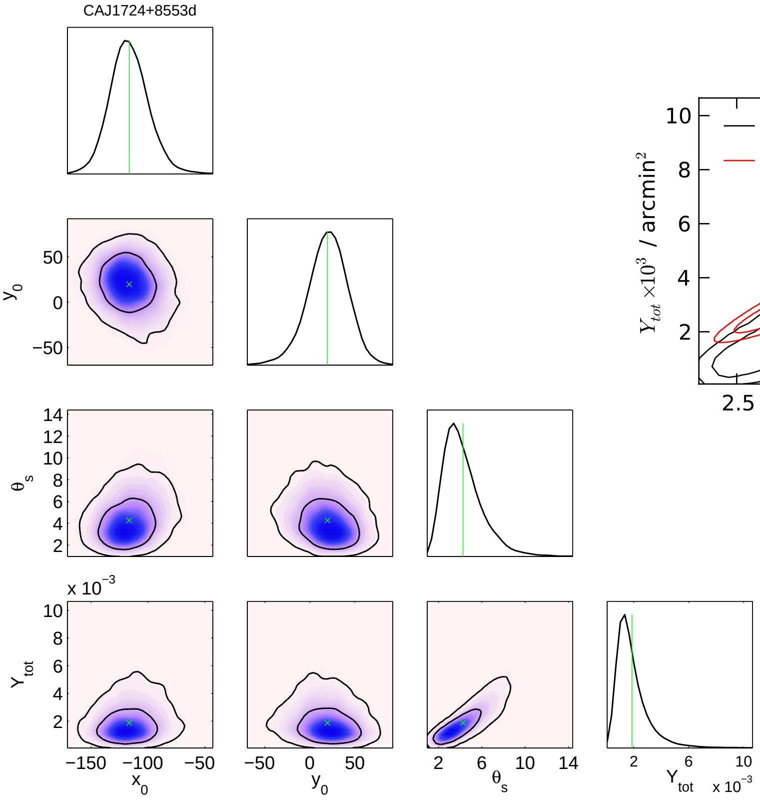

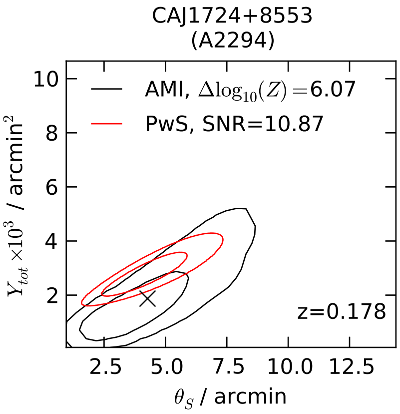

CAJ1752+4440 (MAJ1752+4440, RXC J1752.0+4440); z = 0.366

AMI detection category: Y, $\Delta\log_{10}(Z)$ = 13.38
Planck detections 011, SNR = 8.457
AMI-*Planck* distance = 0.33 arcmin = $0.50\sigma_{Planck}$

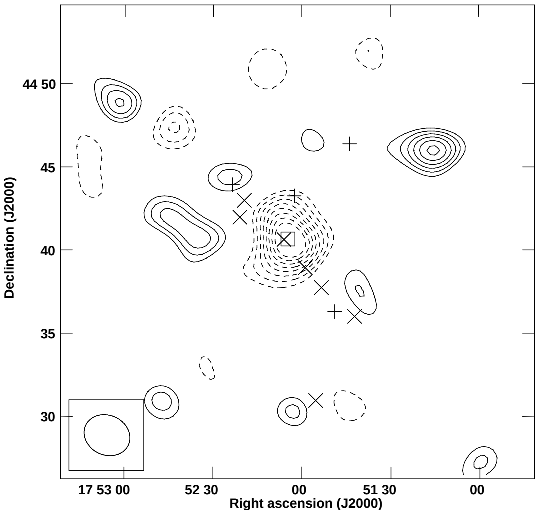

(a) Natural weighting, contours at $\pm(3 \text{ to } 10) \times 72.86\,\mu\text{Jy beam}^{-1}$

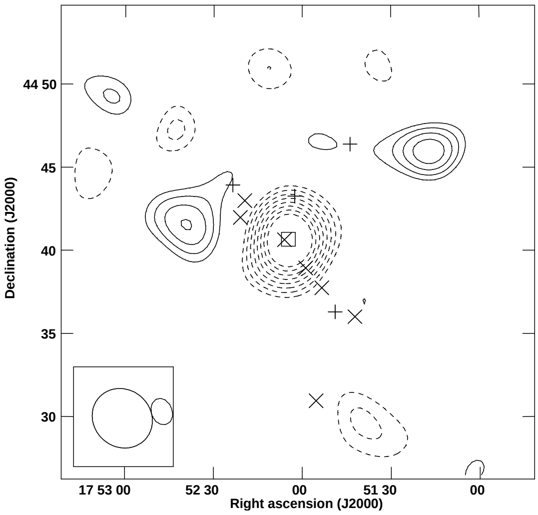

(b) *uv*-taper = 600λ, contours at $\pm(3 \text{ to } 10) \times 97.21\,\mu\text{Jy beam}^{-1}$

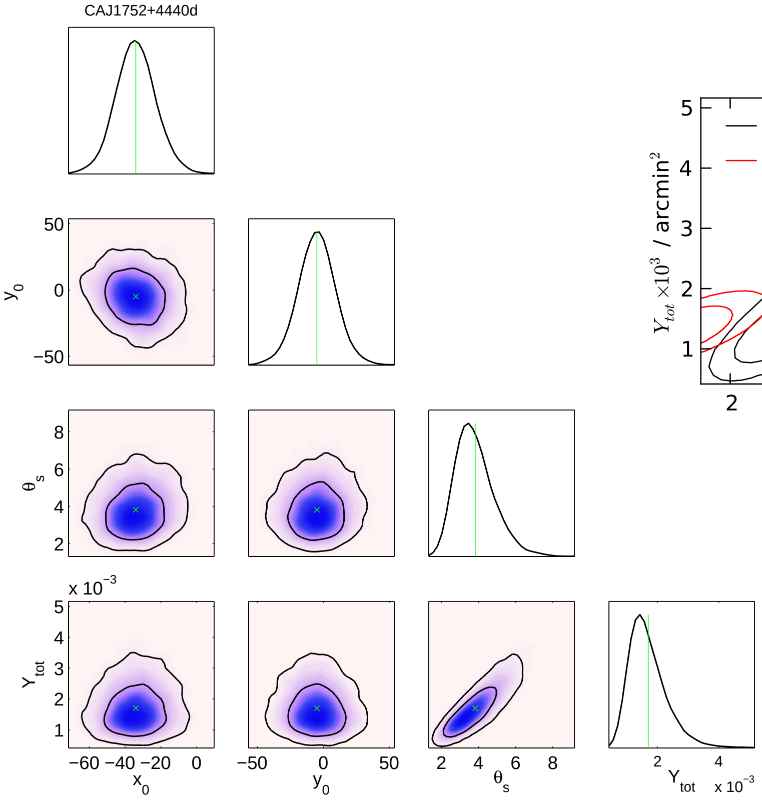

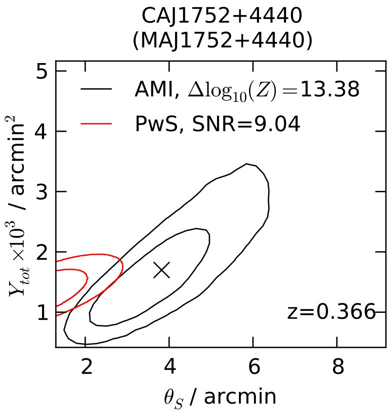

CAJ1023+4907 (A990, RXC J1023.6+4907); z = 0.144
AMI detection category: Y, $\Delta\log_{10}(Z) = 17.43$
Planck detections 111, SNR = 8.444
AMI-*Planck* distance = 0.88 arcmin = $1.16\sigma_{Planck}$

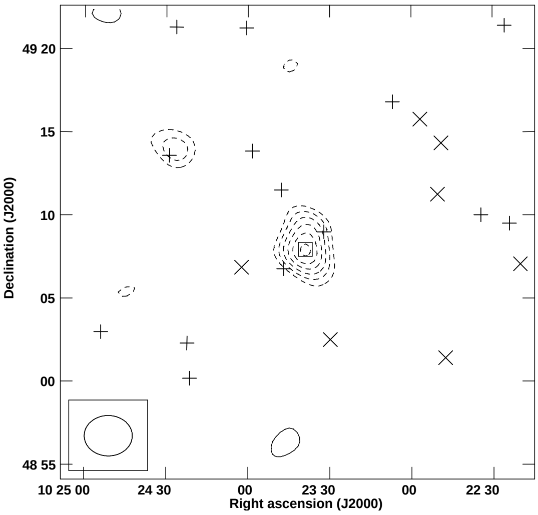

(a) Natural weighting, contours at $\pm(3 \text{ to } 10) \times 147.8\,\mu\text{Jy beam}^{-1}$

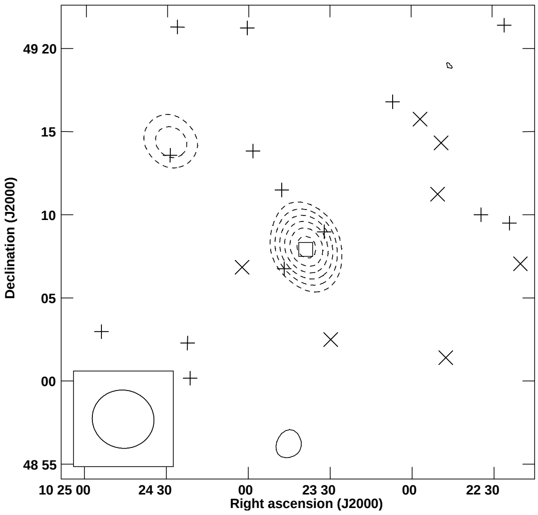

(b) *uv*-taper = 600λ, contours at $\pm(3 \text{ to } 10) \times 182.8\,\mu\text{Jy beam}^{-1}$

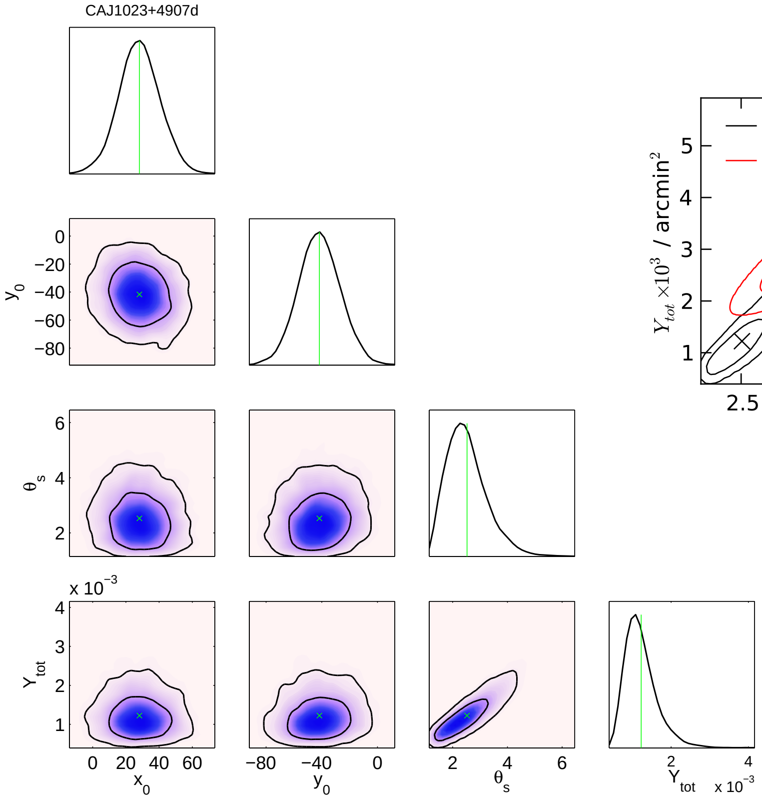

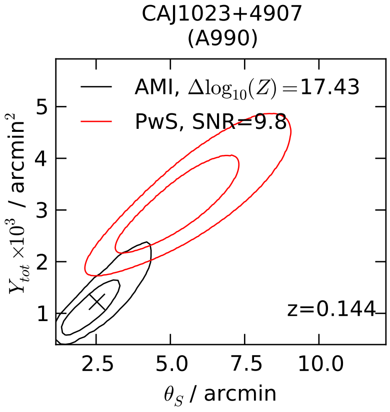

CAJ1157+3336 (A1423, RXC J1157.3+3336); z = 0.214

AMI detection category: Y, $\Delta \log_{10}(Z) = 8.04$
Planck detections 111, SNR = 8.429
AMI-*Planck* distance = 0.25 arcmin = $0.36\sigma_{Planck}$

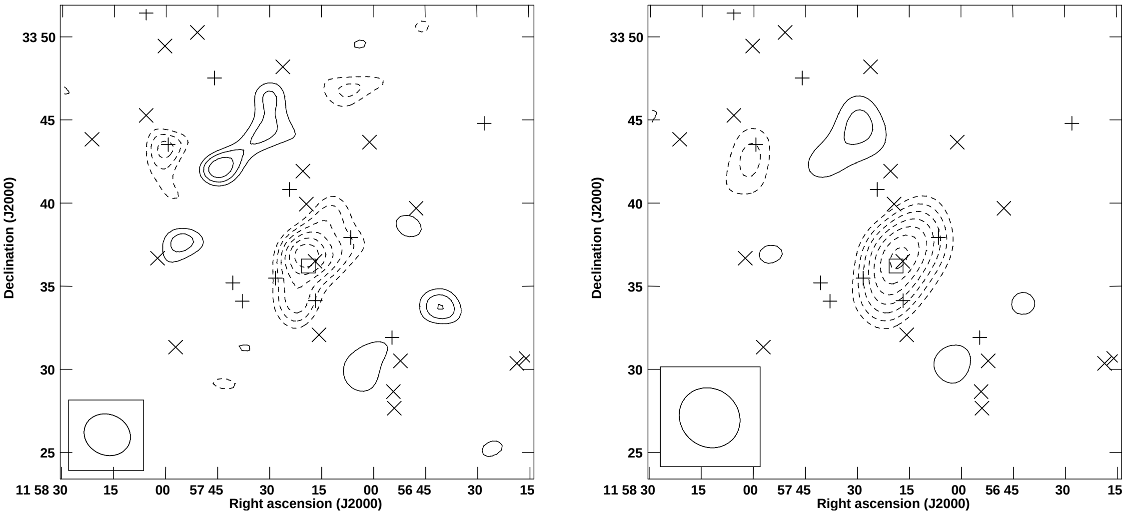

(a) Natural weighting, contours at $\pm(3 \text{ to } 10) \times 66.81\,\mu\text{Jy beam}^{-1}$

(b) *uv*-taper = 600λ, contours at $\pm(3 \text{ to } 10) \times 98.94\,\mu\text{Jy beam}^{-1}$

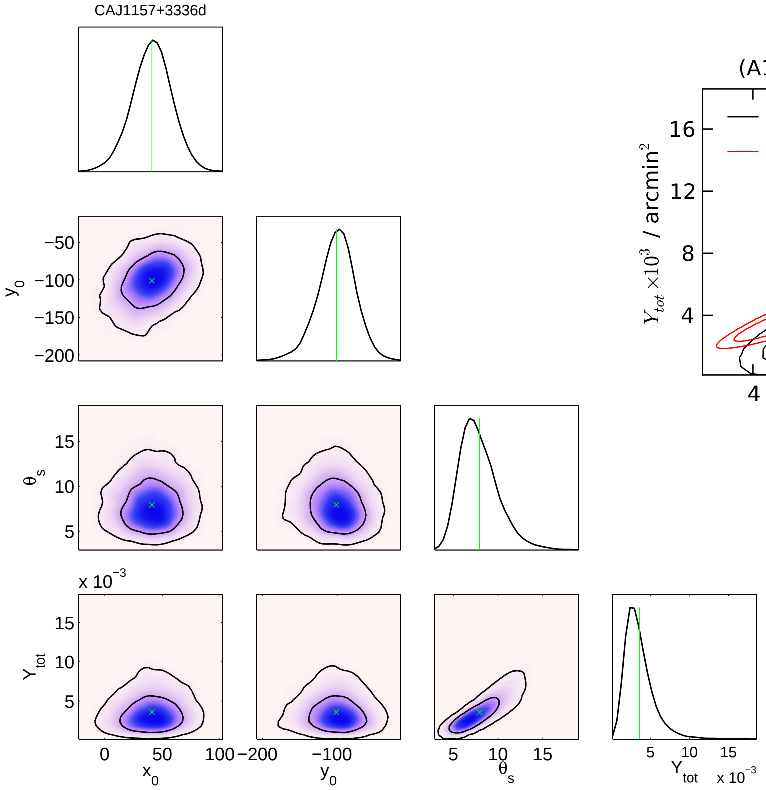

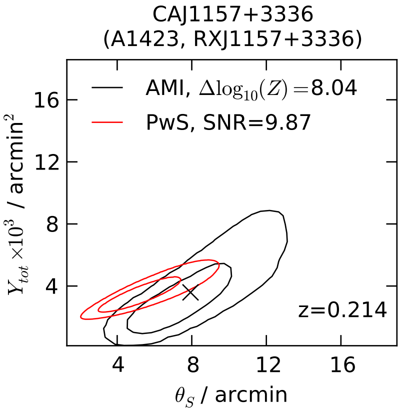

CAJ0308+2645 (MAJ0308+2645, RXC J0308.9+2645); z = 0.356
AMI detection category: Y, $\Delta\log_{10}(Z) = 25.79$
Planck detections 111, SNR = 8.354
AMI-*Planck* distance = 0.52 arcmin = $0.80\sigma_{Planck}$

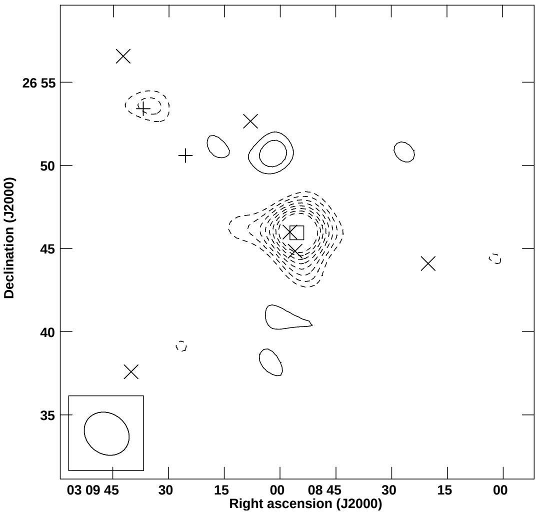

(a) Natural weighting, contours at $\pm(3\text{ to }10) \times 121.3\,\mu\text{Jy beam}^{-1}$

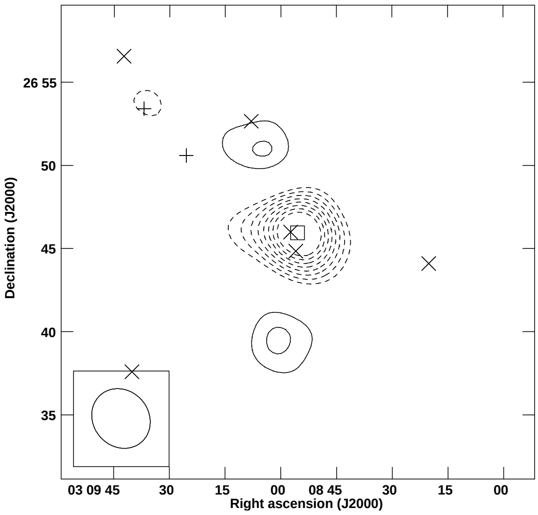

(b) uv-taper = 600λ, contours at $\pm(3\text{ to }10) \times 172.8\,\mu\text{Jy beam}^{-1}$

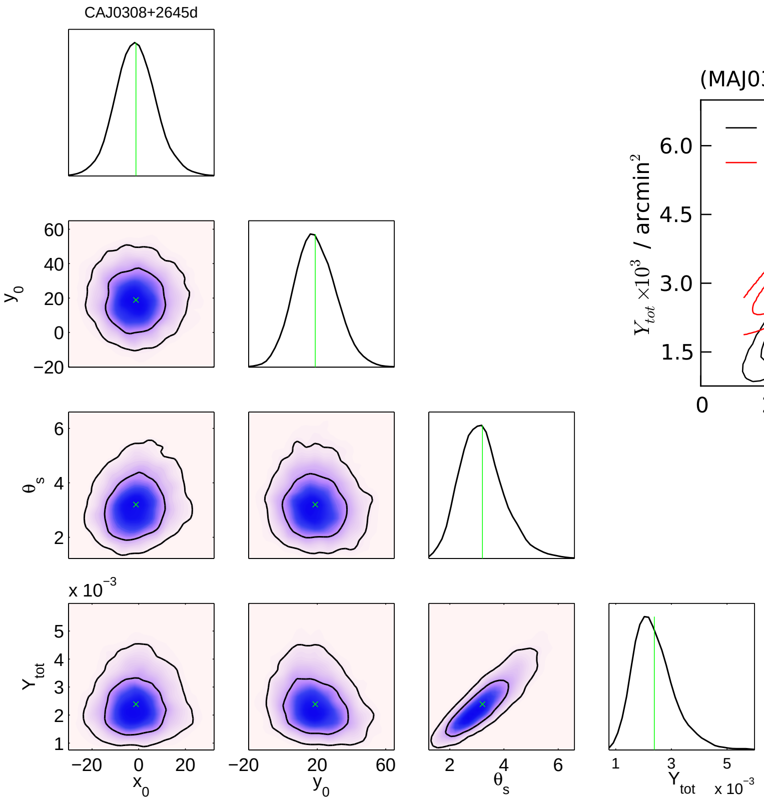

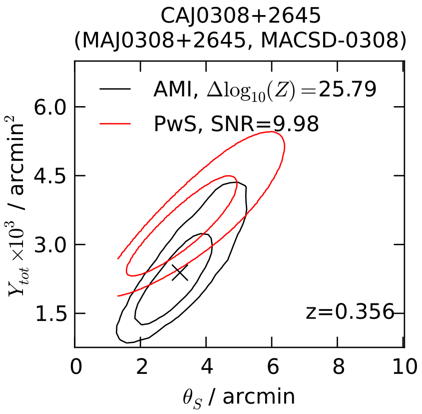

CAJ1022+5006 (A980, RXC J1022.5+5006); z = 0.158

AMI detection category: Y, $\Delta\log_{10}(Z) = 4.76$

Planck detections 111, SNR = 8.261

AMI-*Planck* distance = 0.54 arcmin = $0.69\sigma_{Planck}$

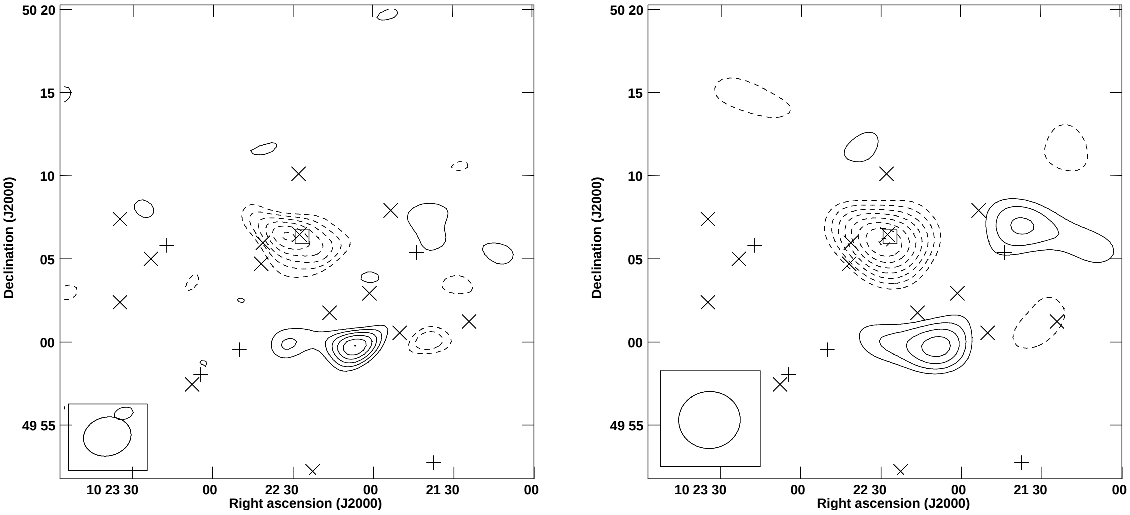

(a) Natural weighting, contours at $\pm(3\text{ to }10) \times 74.17\,\mu\text{Jy beam}^{-1}$

(b) *uv*-taper = 600λ, contours at $\pm(3\text{ to }10) \times 90.54\,\mu\text{Jy beam}^{-1}$

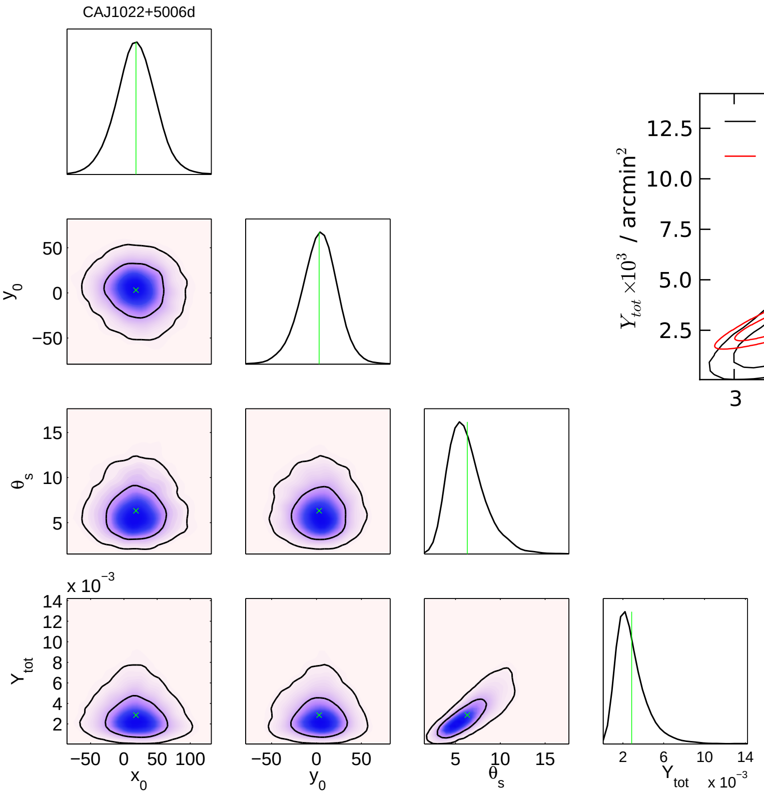

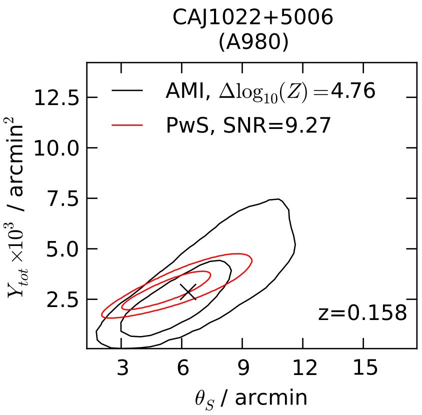

CAJ0748+5941 (RXC J0748.7+5941, [ATZ98] B100)

AMI detection category: Y, $\Delta \log_{10}(Z) = 36.81$

Planck detections 011, SNR = 8.191

AMI-*Planck* distance = 1.10 arcmin = $1.42\sigma_{Planck}$

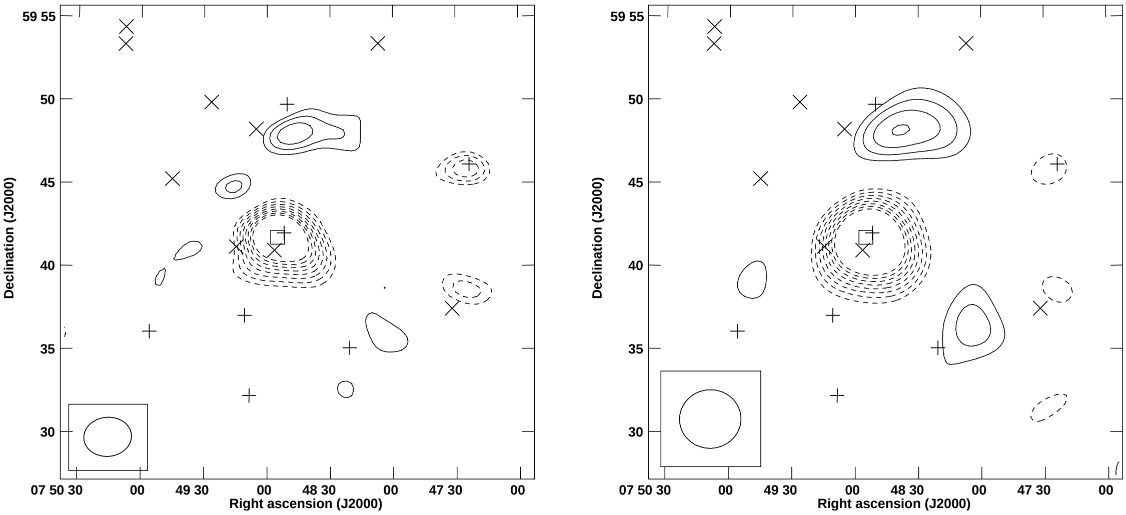

(a) Natural weighting, contours at $\pm(3 \text{ to } 10) \times 67.66\,\mu\text{Jy beam}^{-1}$

(b) *uv*-taper = 600λ, contours at $\pm(3 \text{ to } 10) \times 88.8\,\mu\text{Jy beam}^{-1}$

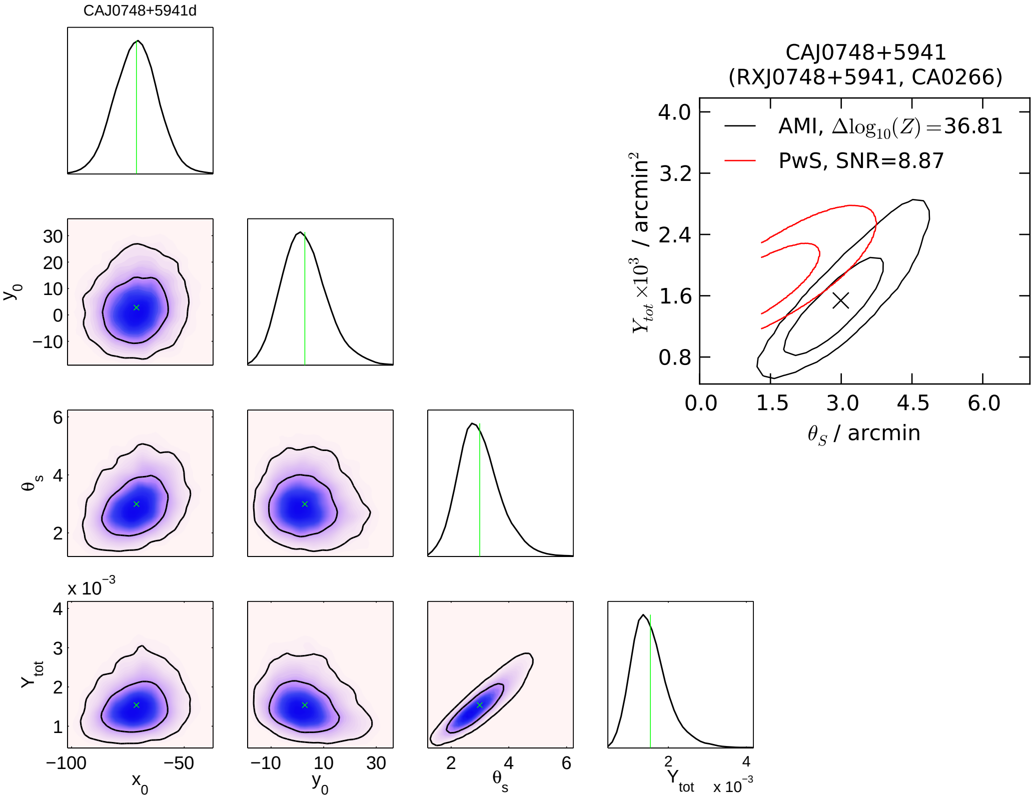

CAJ1159+4946 (RXC J1159.2+4947); z = 0.211

AMI detection category: Y, $\Delta \log_{10}(Z) = 6.25$

Planck detections 111, SNR = 8.186

AMI-*Planck* distance = 1.06 arcmin = $1.39\sigma_{Planck}$

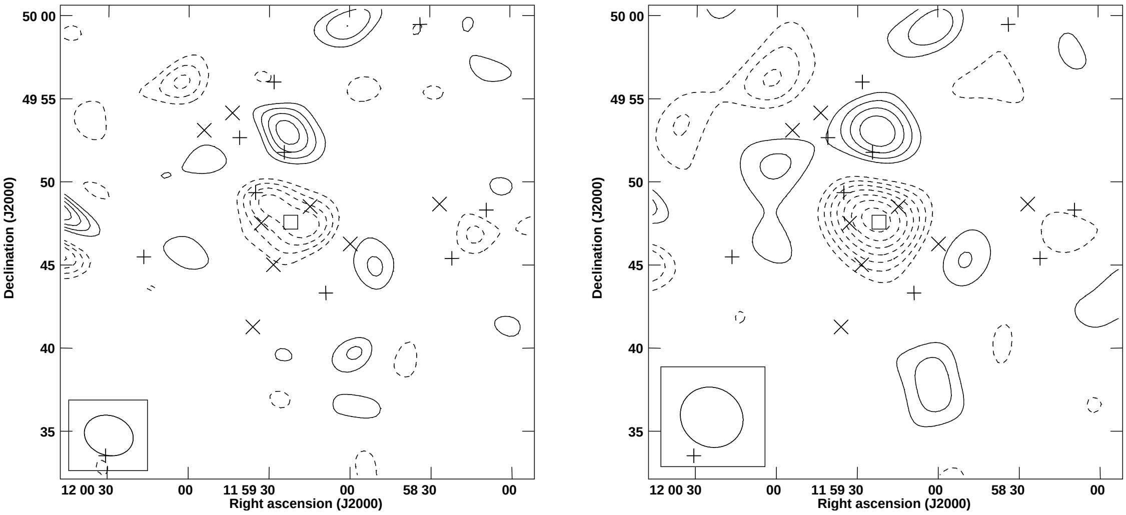

(a) Natural weighting, contours at $\pm(3 \text{ to } 10) \times 97.1\,\mu\text{Jy beam}^{-1}$

(b) *uv*-taper = 600λ, contours at $\pm(3 \text{ to } 10) \times 111.8\,\mu\text{Jy beam}^{-1}$

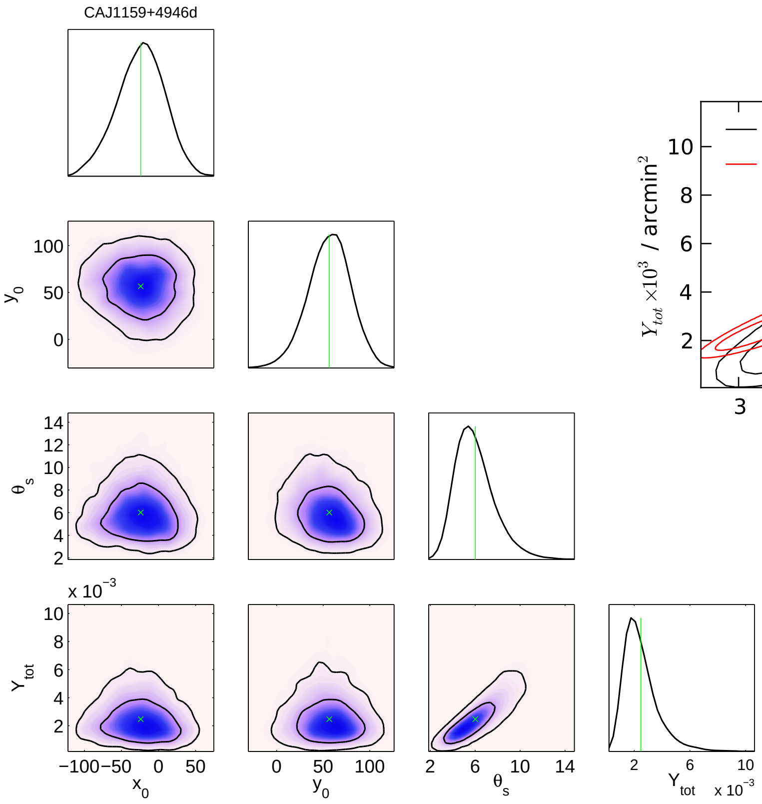

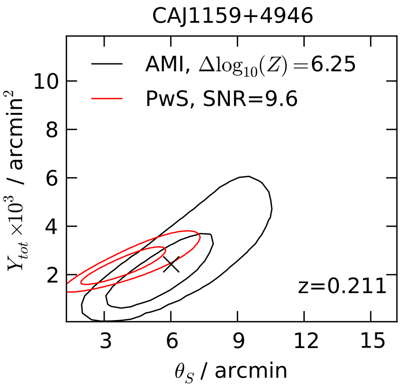

CAJ0142+4438 (RXC J0142.9+4438); z = 0.341
AMI detection category: Y, $\Delta\log_{10}(Z) = 25.15$
Planck detections 111, SNR = 8.087
AMI-*Planck* distance = 0.81 arcmin = $1.18\sigma_{Planck}$

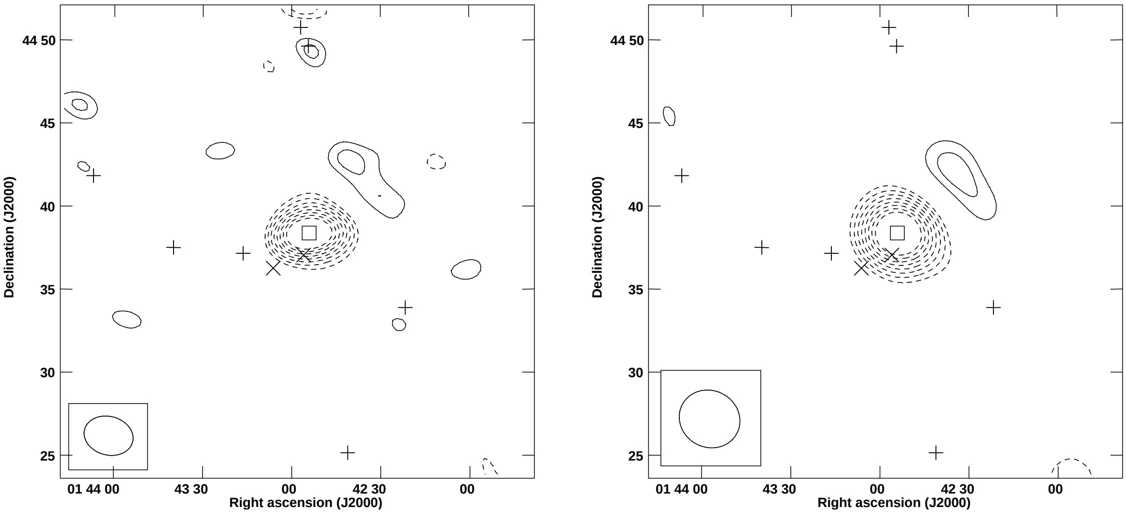

(a) Natural weighting, contours at $\pm(3 \text{ to } 10) \times 95.99\,\mu\text{Jy beam}^{-1}$

(b) uv-taper = 600λ, contours at $\pm(3 \text{ to } 10) \times 127.9\,\mu\text{Jy beam}^{-1}$

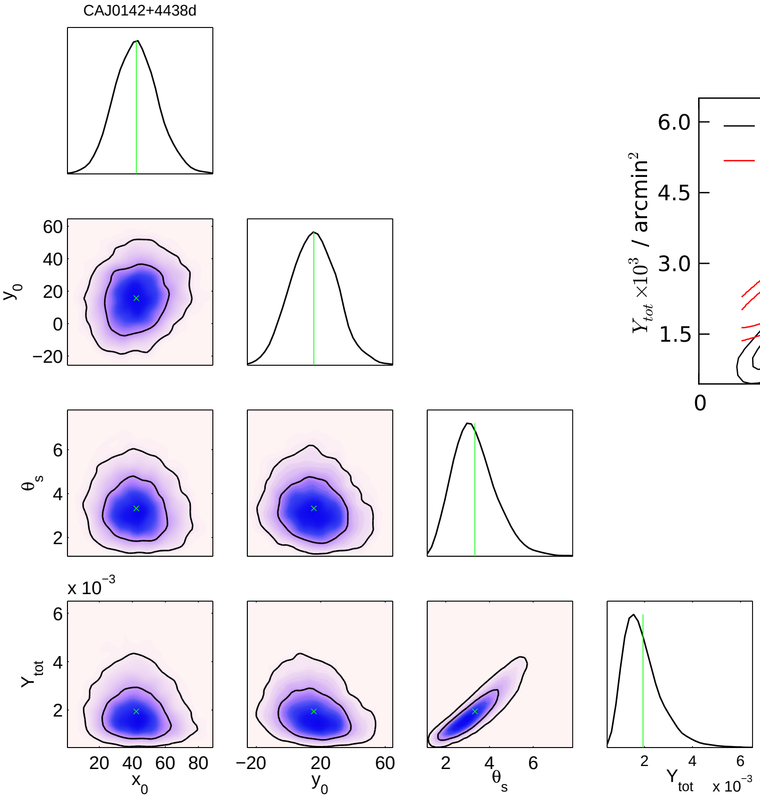

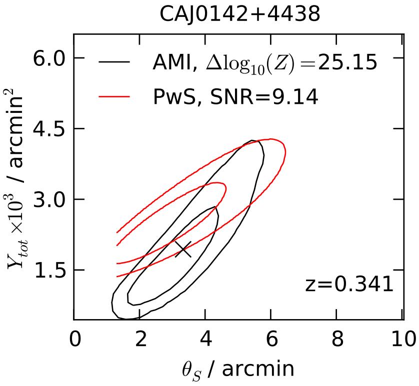

CAJ1115+5320 (XMJ1115+5319, RXC J1115.2+5320); z = 0.47

AMI detection category: Y, $\Delta\log_{10}(Z) = 11.91$

Planck detections 111, SNR = 7.609

AMI-*Planck* distance = 0.77 arcmin = $0.83\sigma_{Planck}$

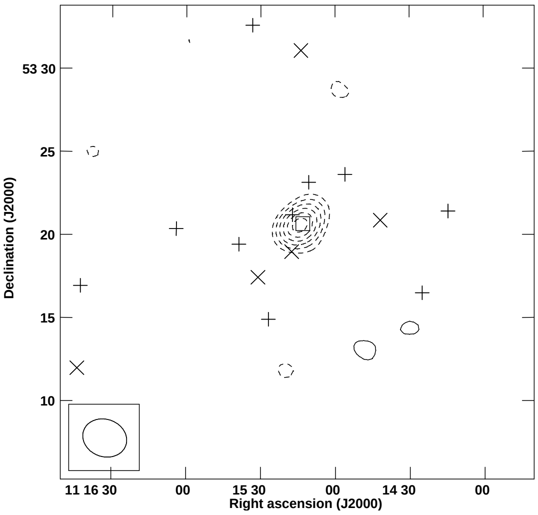

(a) Natural weighting, contours at $\pm(3\text{ to }10) \times 191.4\,\mu\text{Jy beam}^{-1}$

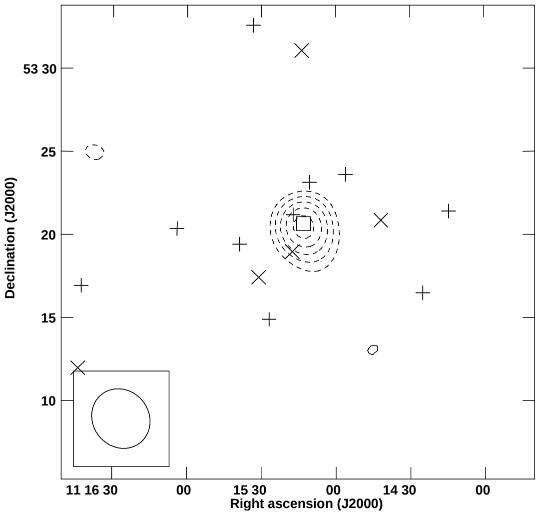

(b) *uv*-taper = 600λ, contours at $\pm(3\text{ to }10) \times 266.0\,\mu\text{Jy beam}^{-1}$

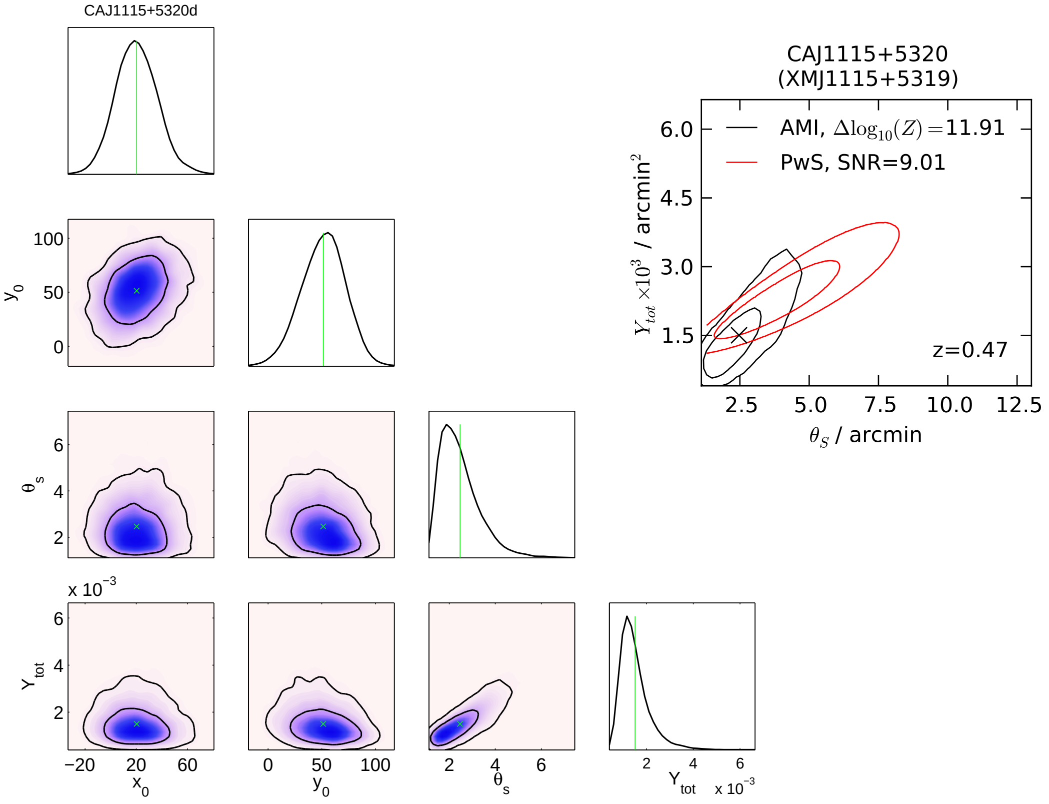

CAJ2228+2037 (RXC J2228.6+2036); z = 0.412
AMI detection category: Y, $\Delta\log_{10}(Z) = 28.47$
Planck detections 111, SNR = 7.261
AMI-*Planck* distance = 0.25 arcmin = $0.27\sigma_{Planck}$

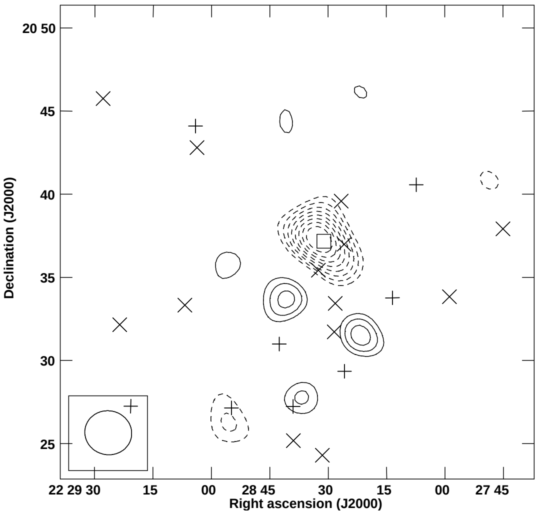

(a) Natural weighting, contours at $\pm(3 \text{ to } 10) \times 117.3\,\mu\text{Jy beam}^{-1}$

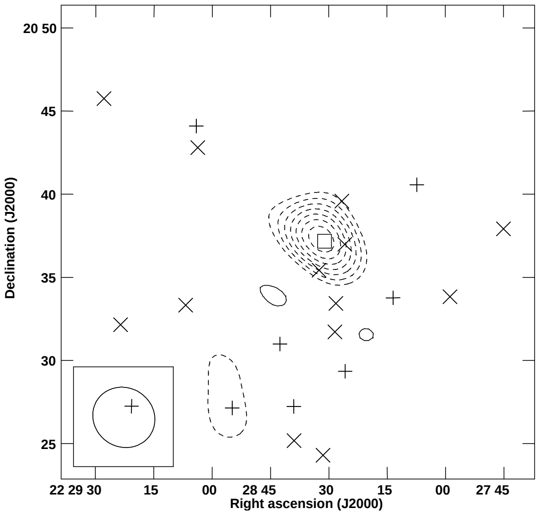

(b) *uv*-taper = 600λ, contours at $\pm(3 \text{ to } 10) \times 178.7\,\mu\text{Jy beam}^{-1}$

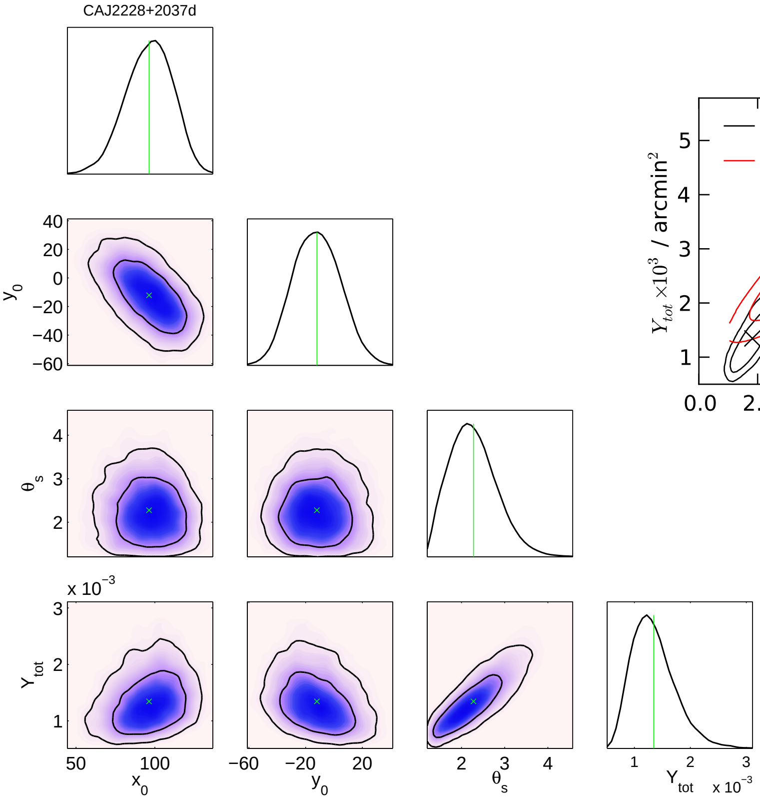

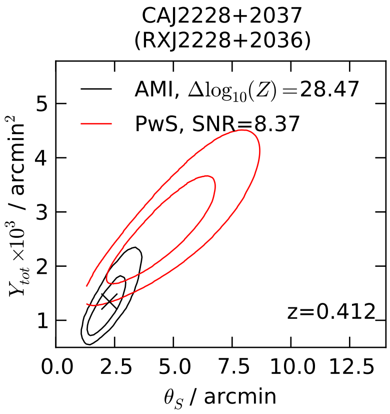

CAJ1858+2916

AMI detection category: Y, $\Delta \log_{10}(Z) = 16.99$

Planck detections 111, SNR = 7.217

AMI-*Planck* distance = 1.46 arcmin = $1.64\sigma_{Planck}$

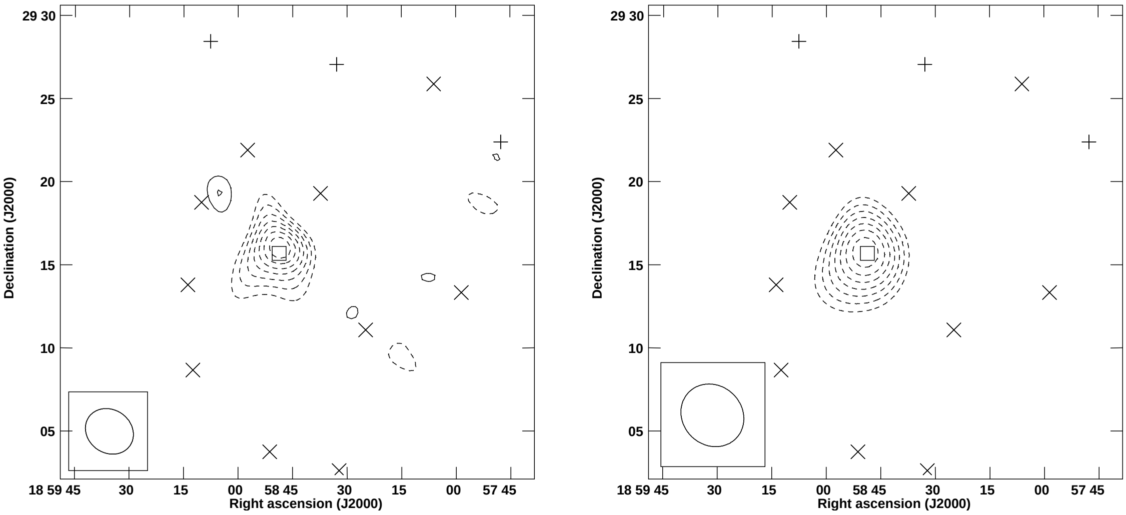

(a) Natural weighting, contours at $\pm(3 \text{ to } 10) \times 98.23\,\mu\text{Jy beam}^{-1}$

(b) *uv*-taper = 600λ, contours at $\pm(3 \text{ to } 10) \times 133.6\,\mu\text{Jy beam}^{-1}$

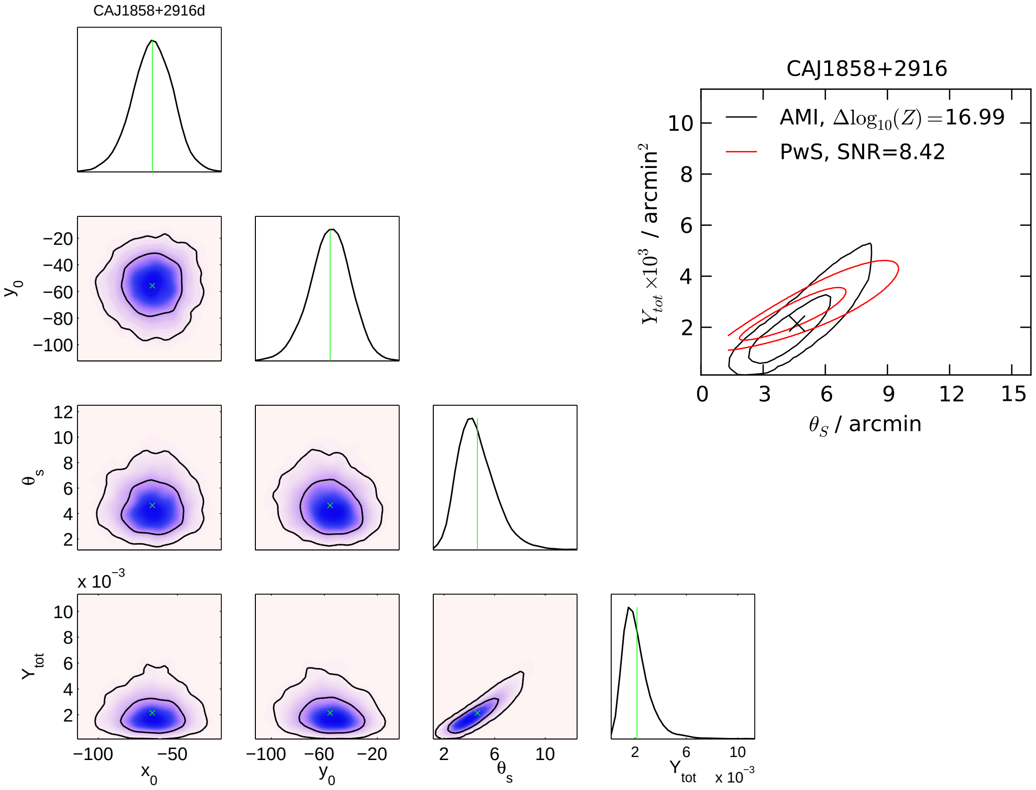

CAJ1212+2732 (RXC J1212.3+2733); z = 0.353

AMI detection category: Y, $\Delta\log_{10}(Z)$ = 13.96

Planck detections 111, SNR = 7.186

AMI-*Planck* distance = 1.44 arcmin = $1.96\sigma_{Planck}$

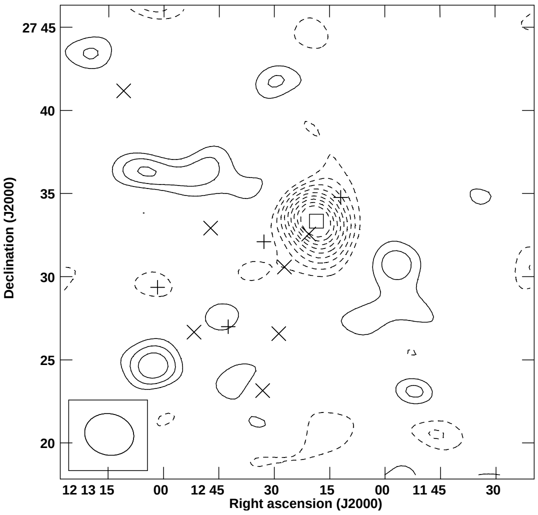

(a) Natural weighting, contours at $\pm(3 \text{ to } 10) \times 118.1\,\mu\text{Jy beam}^{-1}$

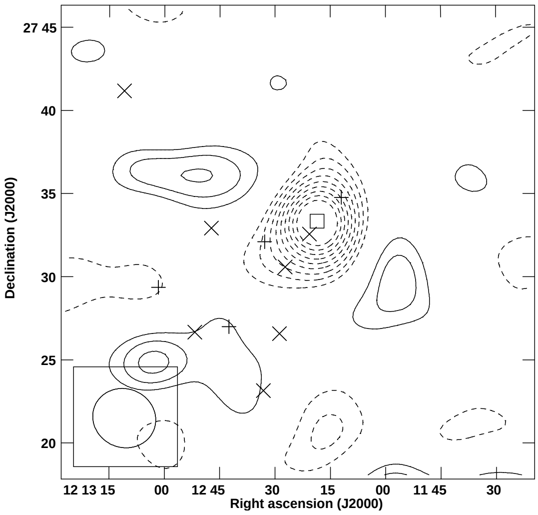

(b) *uv*-taper = 600λ, contours at $\pm(3 \text{ to } 10) \times 163.5\,\mu\text{Jy beam}^{-1}$

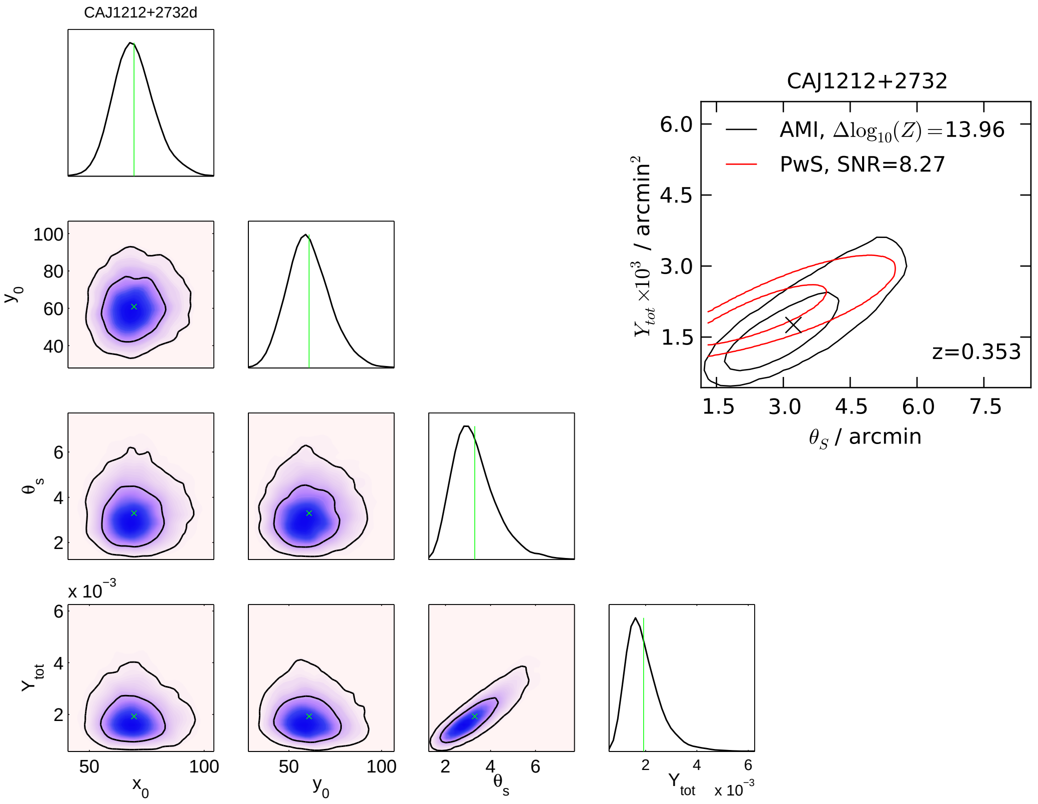

CAJ1819+5711 (RXC J1819.9+5710); z = 0.179

AMI detection category: Y, $\Delta \log_{10}(Z) = 3.34$

Planck detections 111, SNR = 7.129

AMI-*Planck* distance = 3.60 arcmin = $4.28\sigma_{Planck}$

Positional error increased from 0.8 to 3 arcmin

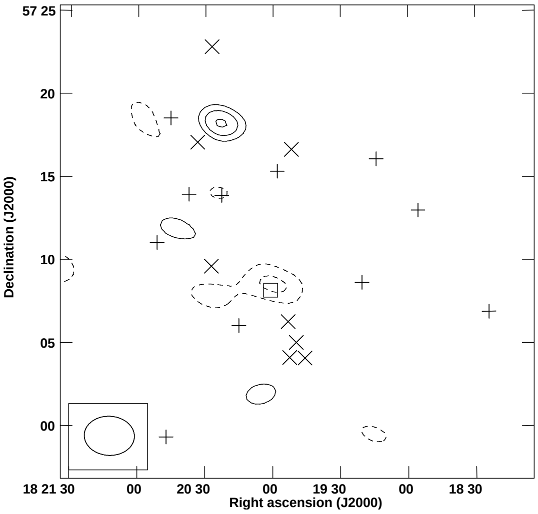

(a) Natural weighting, contours at $\pm$(3 to 10) $\times$ 112.5 μJy beam^{-1}

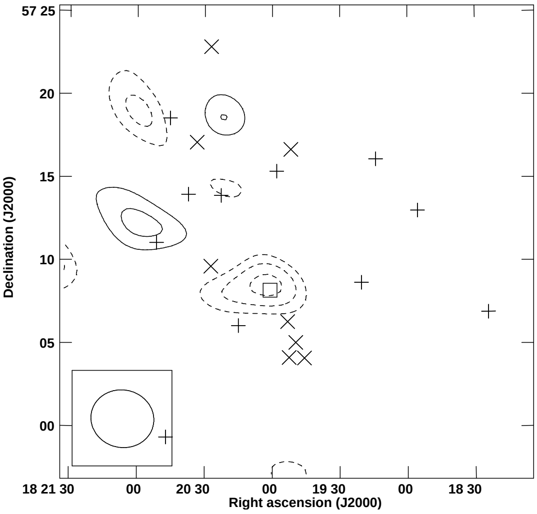

(b) uv-taper = 600λ, contours at $\pm$(3 to 10) $\times$ 137.0 μJy beam^{-1}

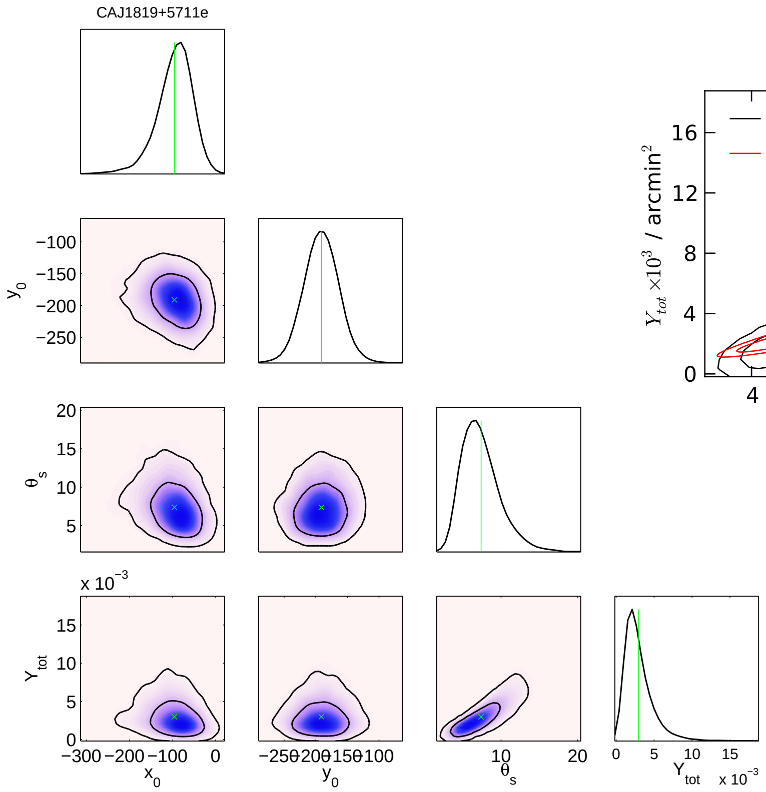

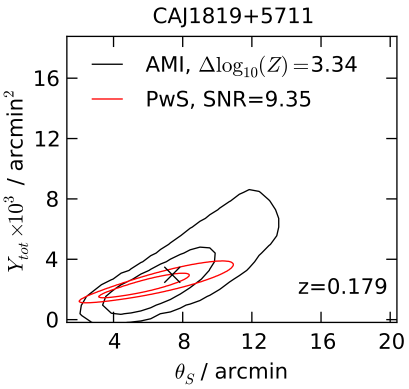

CAJ1149+2223 (MAJ1149+2223, RXC J1149.5+2245); z = 0.545
AMI detection category: Y, $\Delta \log_{10}(Z) = 120.0$
Planck detections 111, SNR = 7.117
AMI-*Planck* distance = 0.60 arcmin = $0.57\sigma_{Planck}$

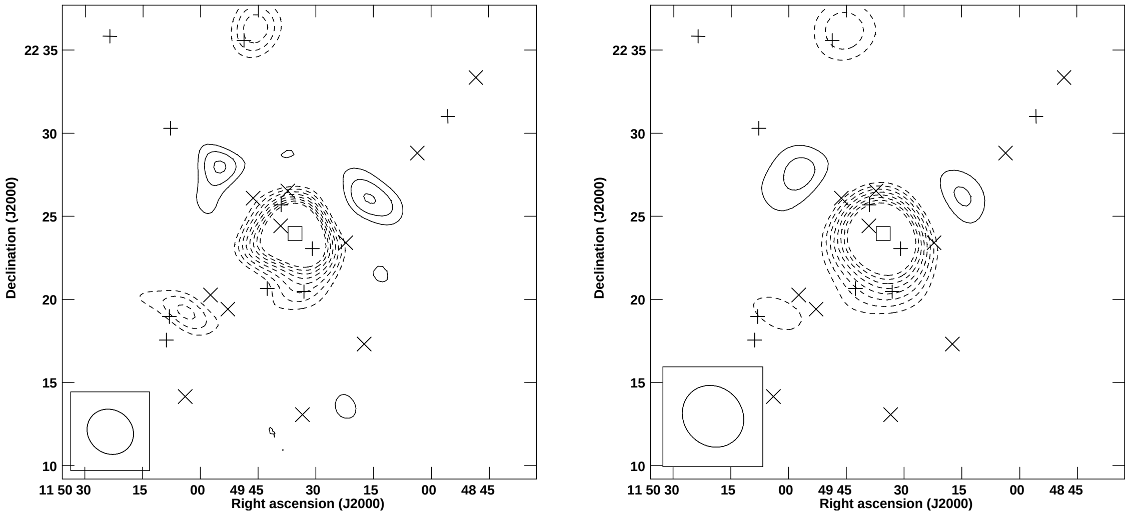

(a) Natural weighting, contours at $\pm(3 \text{ to } 10) \times 93.0\,\mu\text{Jy beam}^{-1}$

(b) *uv*-taper = 600λ, contours at $\pm(3 \text{ to } 10) \times 139.3\,\mu\text{Jy beam}^{-1}$

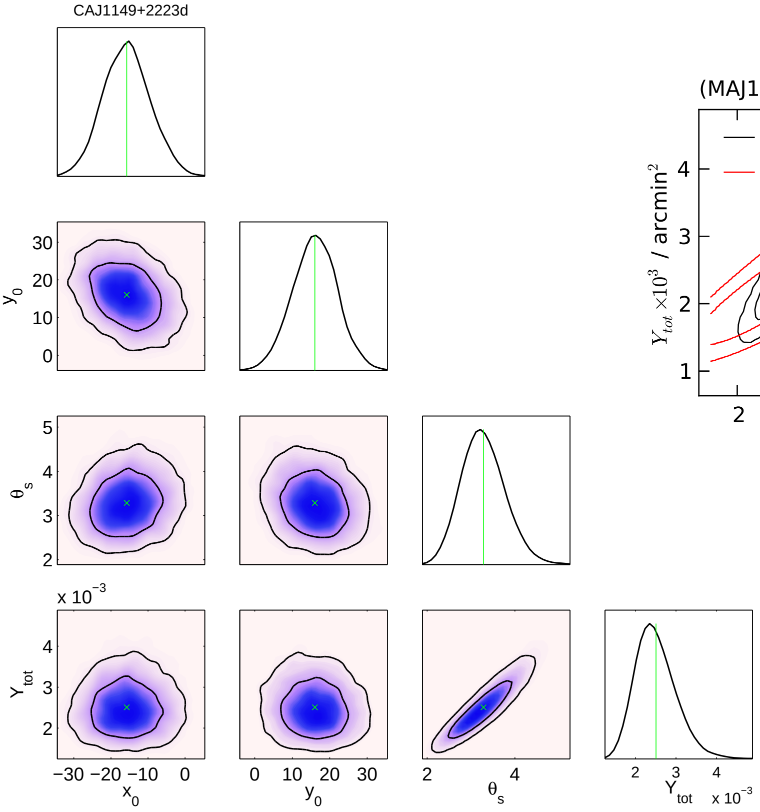

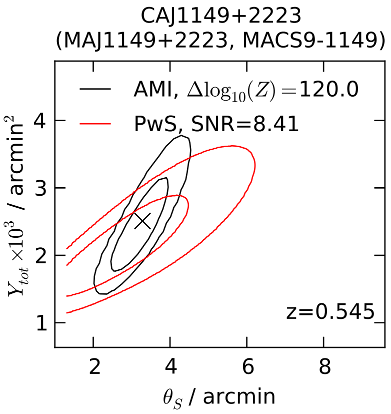

CAJ1428+5651 (A1925, RXC J1428.4+5652); z = 0.105

AMI detection category: N, $\Delta \log_{10}(Z) = -0.29$

Planck detections 111, SNR = 7.056

AMI-*Planck* distance = 0.79 arcmin = $0.61\sigma_{Planck}$

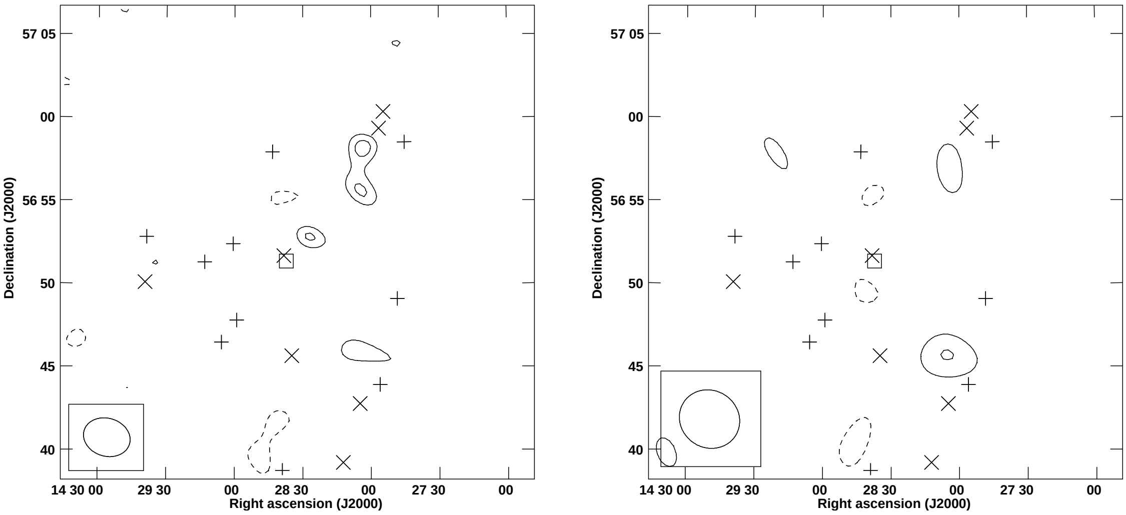

(a) Natural weighting, contours at $\pm(3 \text{ to } 10) \times 106.1\,\mu\text{Jy beam}^{-1}$

(b) uv-taper = 600λ, contours at $\pm(3 \text{ to } 10) \times 129.1\,\mu\text{Jy beam}^{-1}$

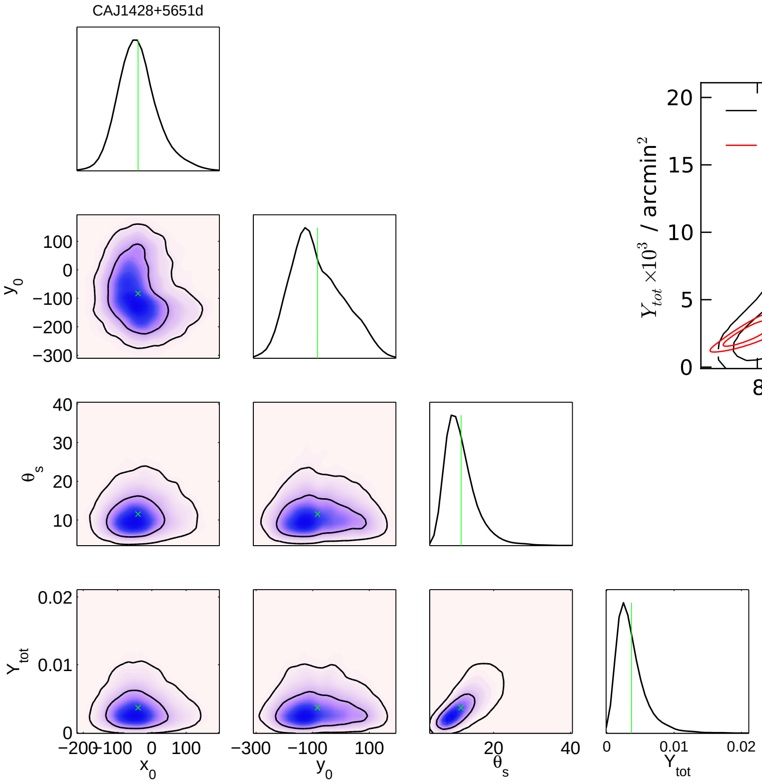

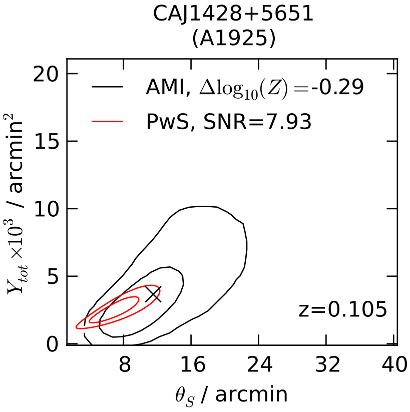

CAJ1747+4512 (ZW8284, RXC J1747.2+4512); z = 0.156

AMI detection category: M, $\Delta \log_{10}(Z) = 2.54$

Planck detections 111, SNR = 7.008

AMI-*Planck* distance = 0.48 arcmin = $0.41\sigma_{Planck}$

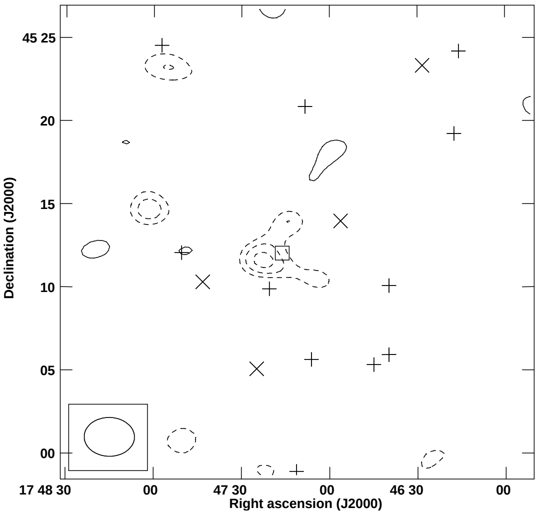

(a) Natural weighting, contours at $\pm(3 \text{ to } 10) \times 114.4\,\mu\text{Jy beam}^{-1}$

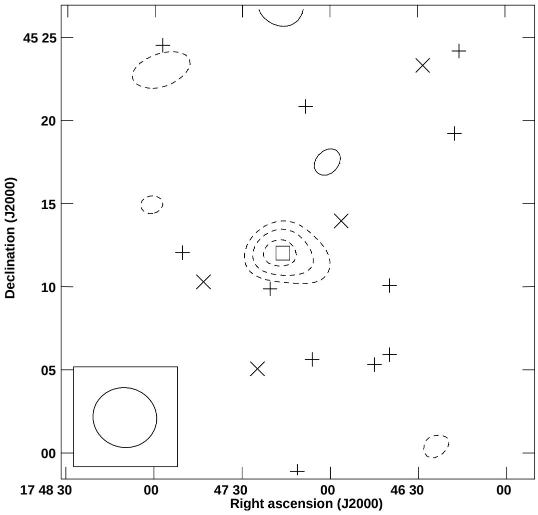

(b) *uv*-taper = 600λ, contours at $\pm(3 \text{ to } 10) \times 143.9\,\mu\text{Jy beam}^{-1}$

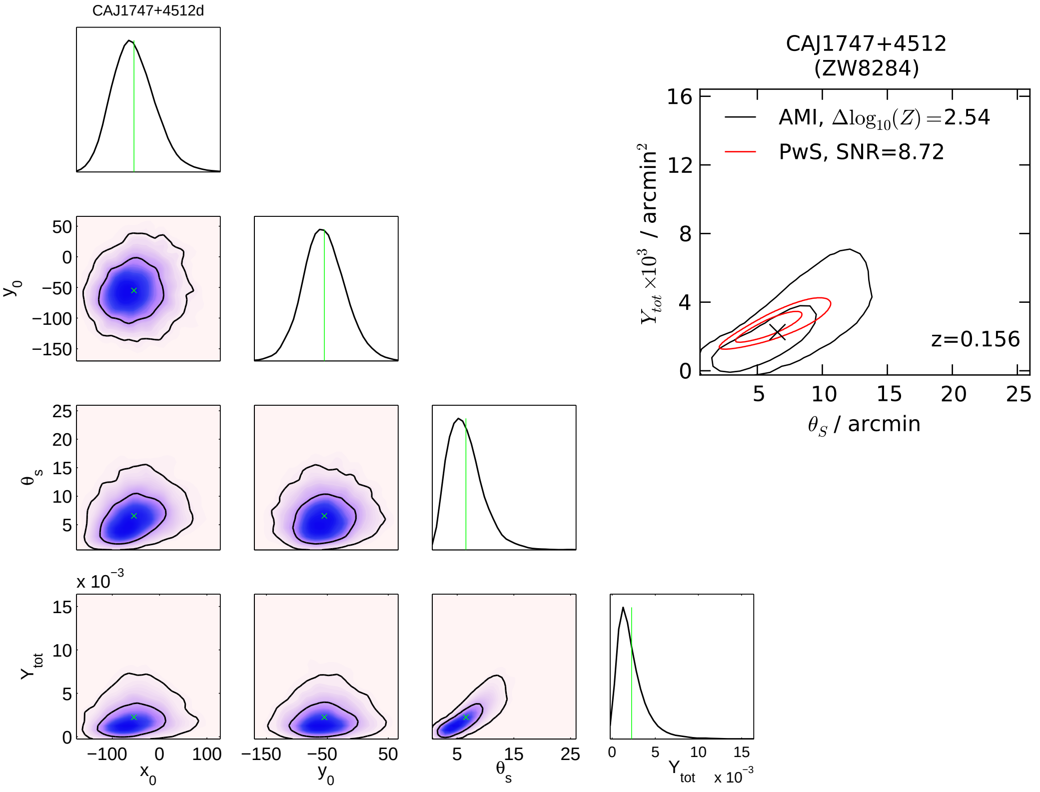

CAJ2226+7818 (PLCKESZ G115.71+17.52)

AMI detection category: Y, $\Delta \log_{10}(Z) = 3.87$
Planck detections 111, SNR = 6.997
AMI-*Planck* distance = 0.67 arcmin = $1.04\sigma_{Planck}$

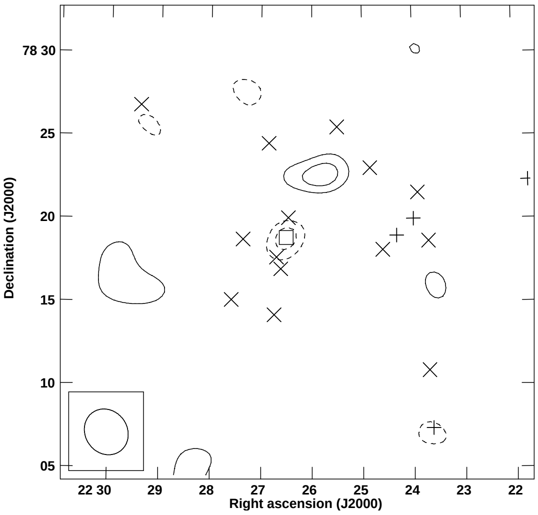

(a) Natural weighting, contours at $\pm(3 \text{ to } 10) \times 118.5\,\mu\text{Jy beam}^{-1}$

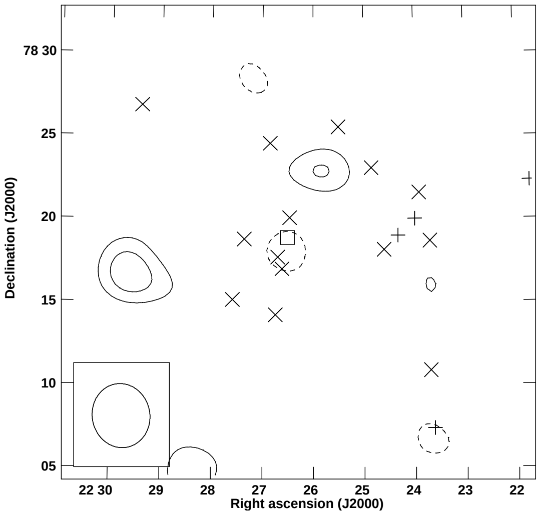

(b) *uv*-taper = 600λ, contours at $\pm(3 \text{ to } 10) \times 181.4\,\mu\text{Jy beam}^{-1}$

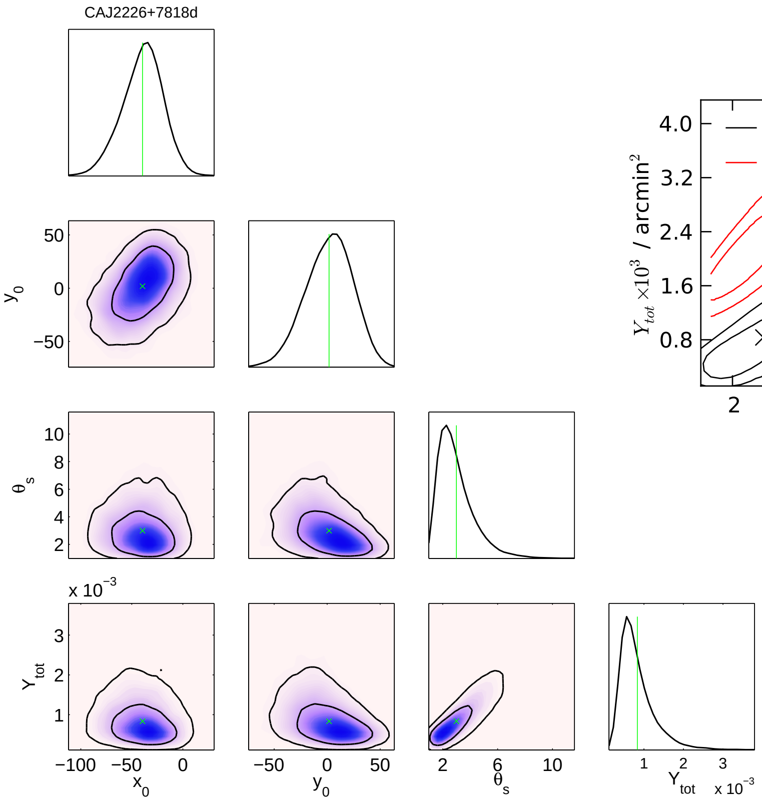

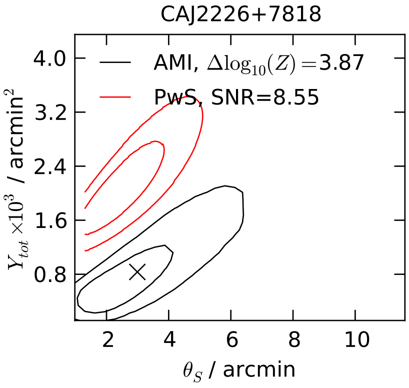

CAJ1229+4737 (RXC J1229.0+4737); z = 0.254

AMI detection category: Y, $\Delta \log_{10}(Z) = 5.25$

Planck detections 111, SNR = 6.969

AMI-*Planck* distance = 1.27 arcmin = $1.26\sigma_{Planck}$

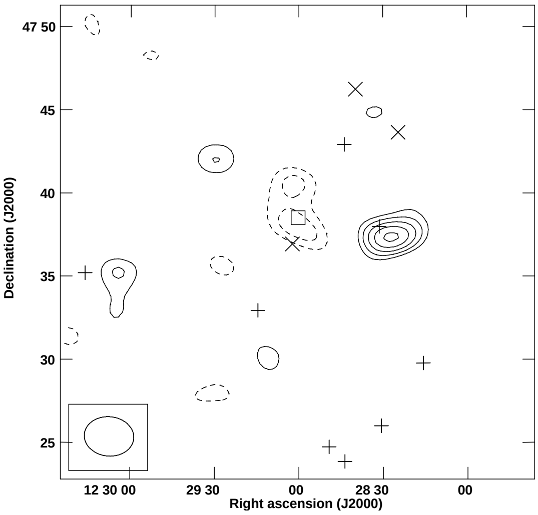

(a) Natural weighting, contours at $\pm(3 \text{ to } 10) \times 97.27\,\mu\text{Jy beam}^{-1}$

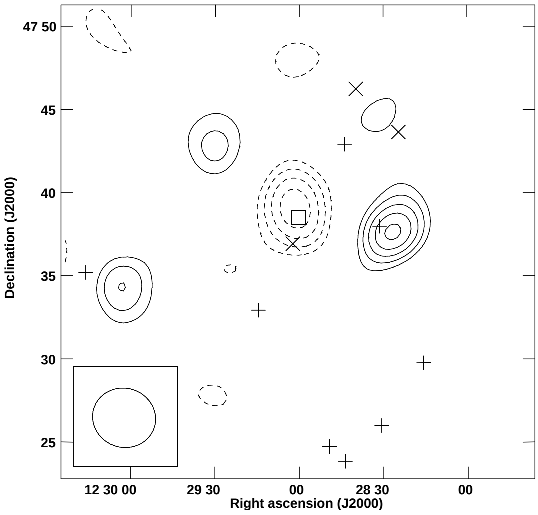

(b) *uv*-taper = 600λ, contours at $\pm(3 \text{ to } 10) \times 113.7\,\mu\text{Jy beam}^{-1}$

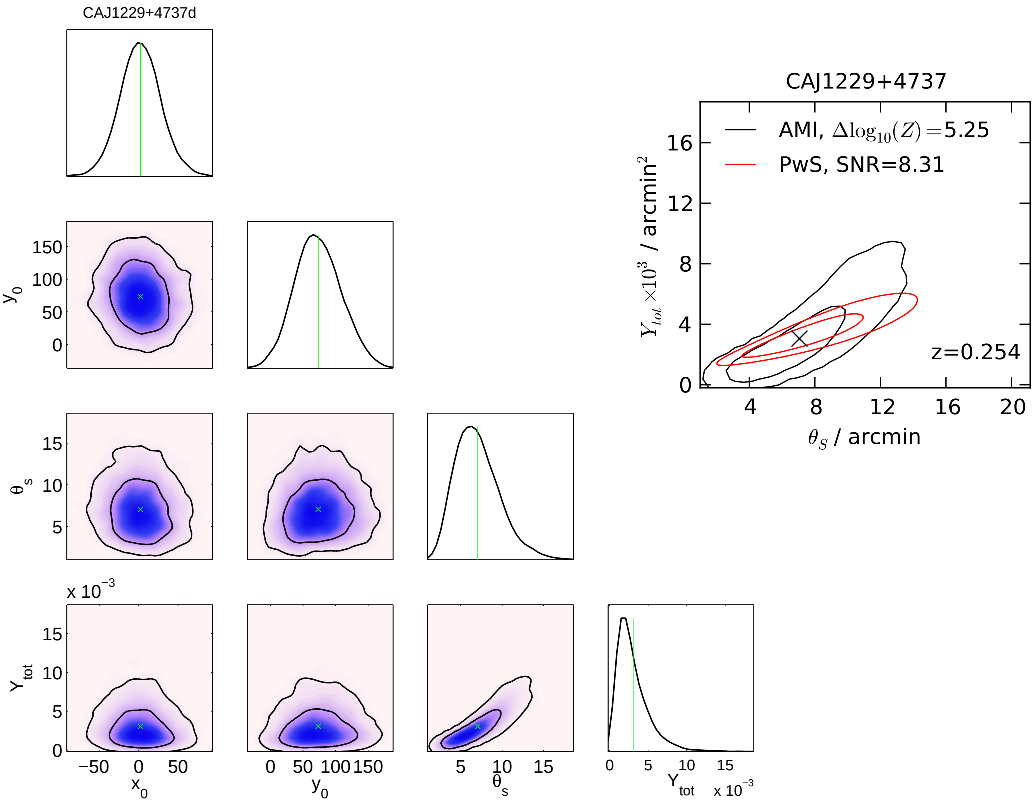

CAJ0742+7414 (ZW1370, RXC J0741.7+7414); z = 0.215
AMI detection category: Y, $\Delta \log_{10}(Z) = 6.3$
Planck detections 111, SNR = 6.942
AMI-*Planck* distance = 0.93 arcmin = $0.94\sigma_{Planck}$

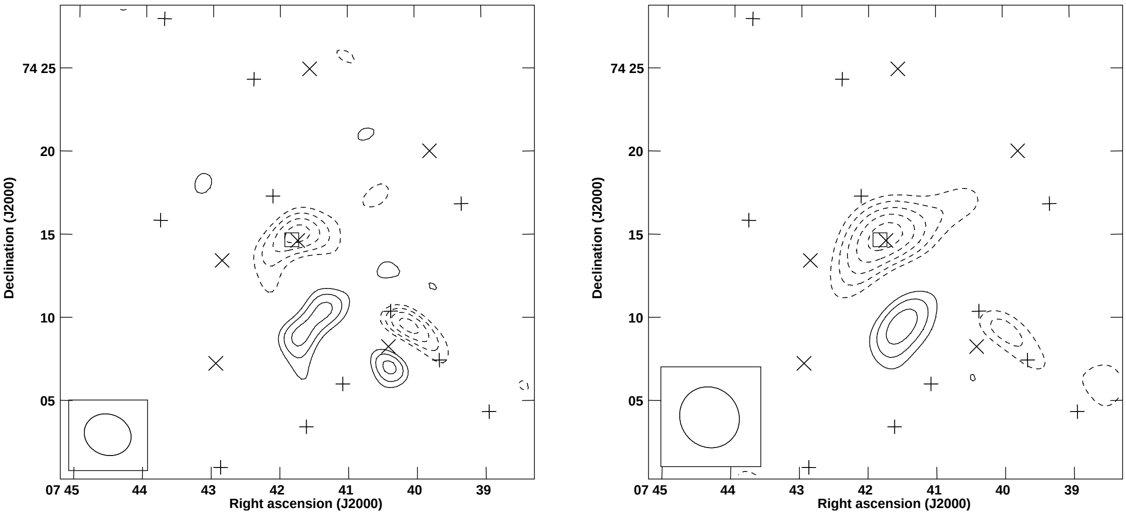

(a) Natural weighting, contours at $\pm(3 \text{ to } 10) \times 114.1\,\mu\text{Jy beam}^{-1}$

(b) *uv*-taper = 600λ, contours at $\pm(3 \text{ to } 10) \times 144.0\,\mu\text{Jy beam}^{-1}$

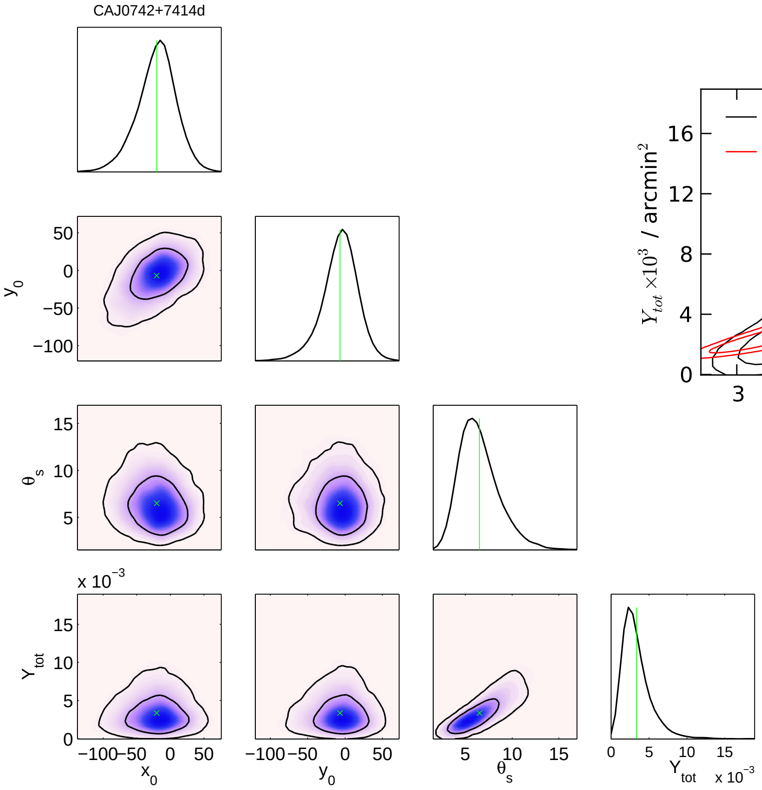

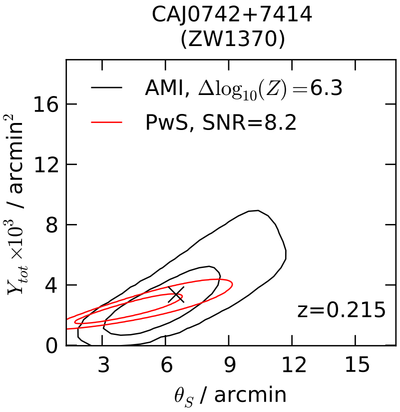

CAJ1856+6622 (ZwCl 1856.8+6616); z = 0.3

AMI detection category: Y, $\Delta \log_{10}(Z) = 3.27$

Planck detections 111, SNR = 6.891

AMI-*Planck* distance = 0.64 arcmin = $0.72\sigma_{Planck}$

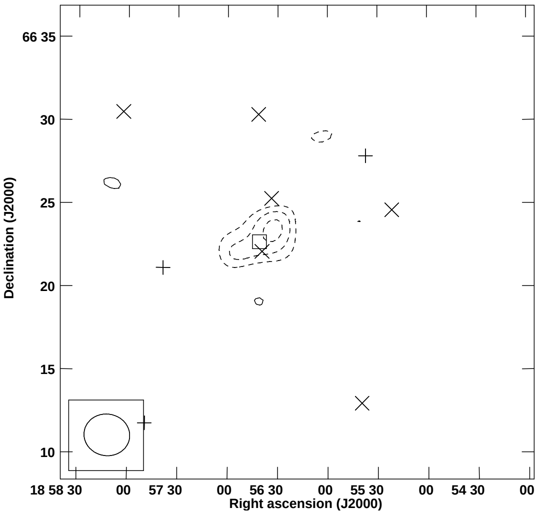

(a) Natural weighting, contours at $\pm(3 \text{ to } 10) \times 108.4\,\mu\text{Jy beam}^{-1}$

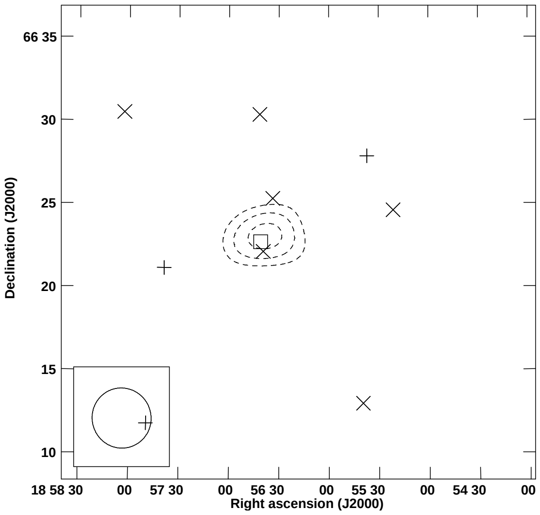

(b) *uv*-taper = 600λ, contours at $\pm(3 \text{ to } 10) \times 168.8\,\mu\text{Jy beam}^{-1}$

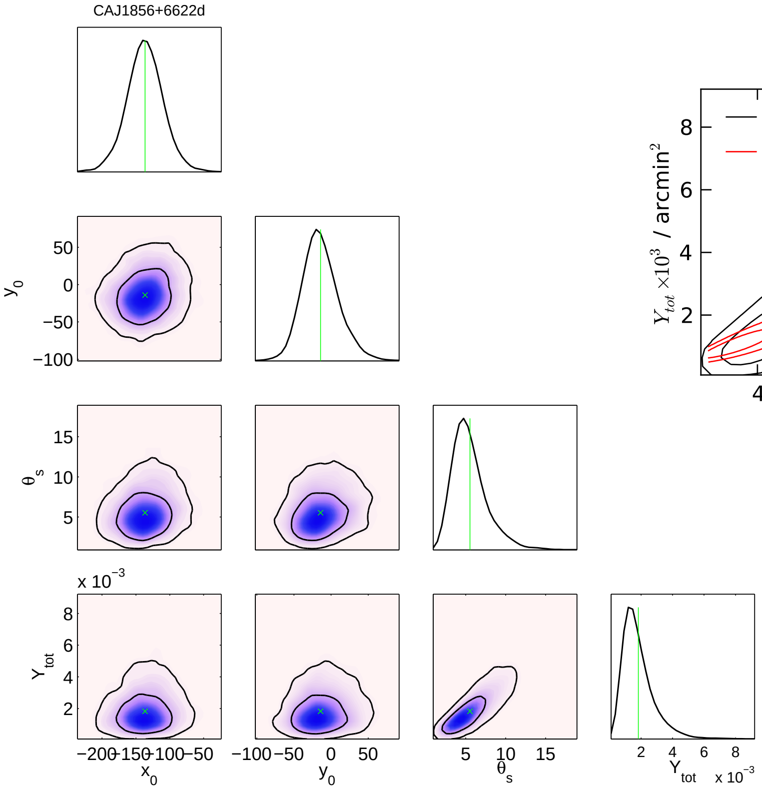

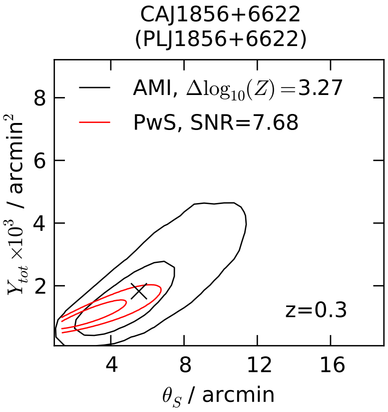

CAJ0227+4904

AMI detection category: Y, $\Delta \log_{10}(Z) = 11.09$

Planck detections 111, SNR = 6.857

AMI-*Planck* distance = 1.08 arcmin = $0.98\sigma_{Planck}$

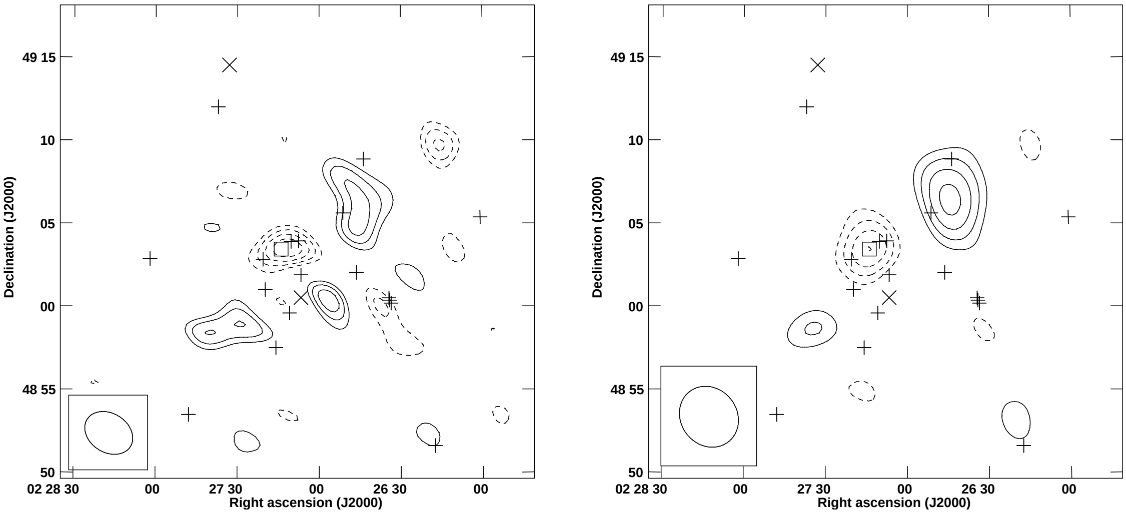

(a) Natural weighting, contours at $\pm(3 \text{ to } 10) \times 92.01\,\mu\text{Jy beam}^{-1}$

(b) *uv*-taper = 600λ, contours at $\pm(3 \text{ to } 10) \times 131.4\,\mu\text{Jy beam}^{-1}$

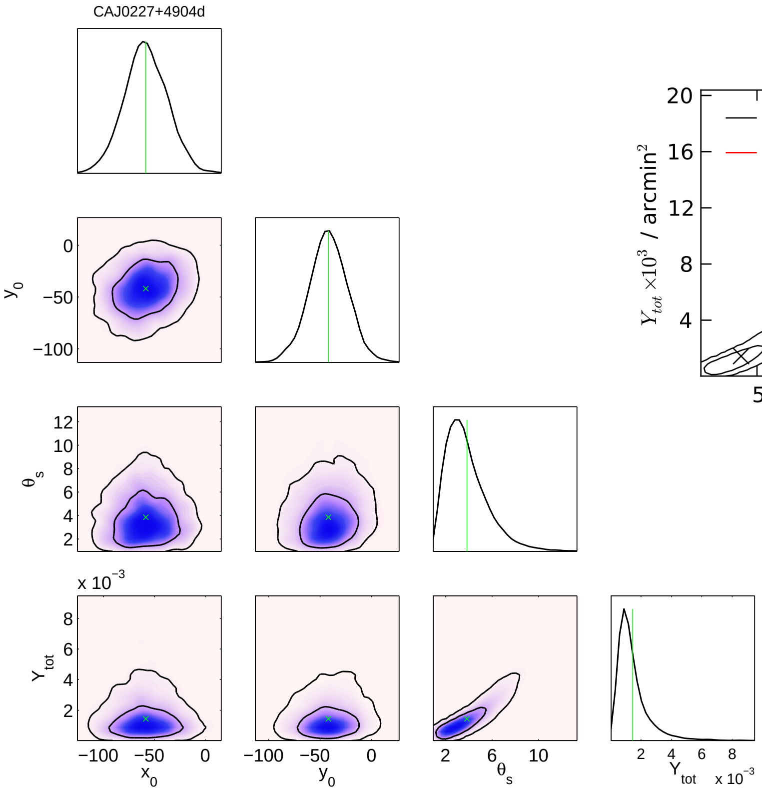

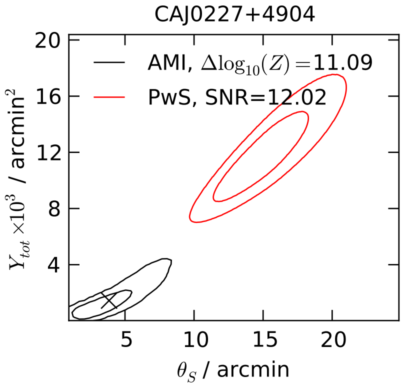

CAJ0842+6234

AMI detection category: N, $\Delta \log_{10}(Z) = -1.88$

Planck detections 010, SNR = 6.848

AMI-*Planck* distance = 0.93 arcmin = $0.12\sigma_{Planck}$

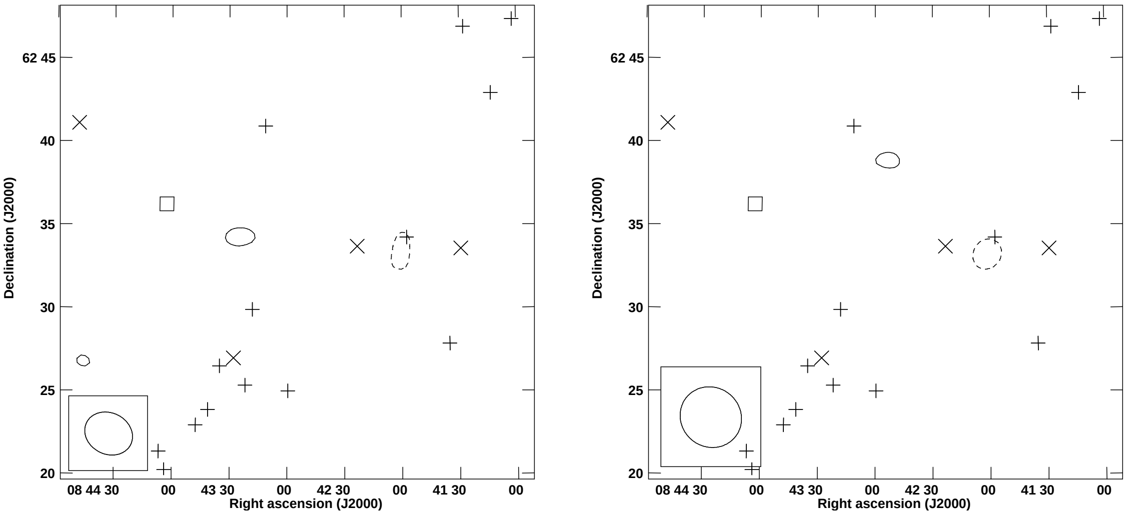

(a) Natural weighting, contours at $\pm(3 \text{ to } 10) \times 118.4\,\mu$Jy beam^{-1}

(b) *uv*-taper = 600λ, contours at $\pm(3 \text{ to } 10) \times 157.7\,\mu$Jy beam^{-1}

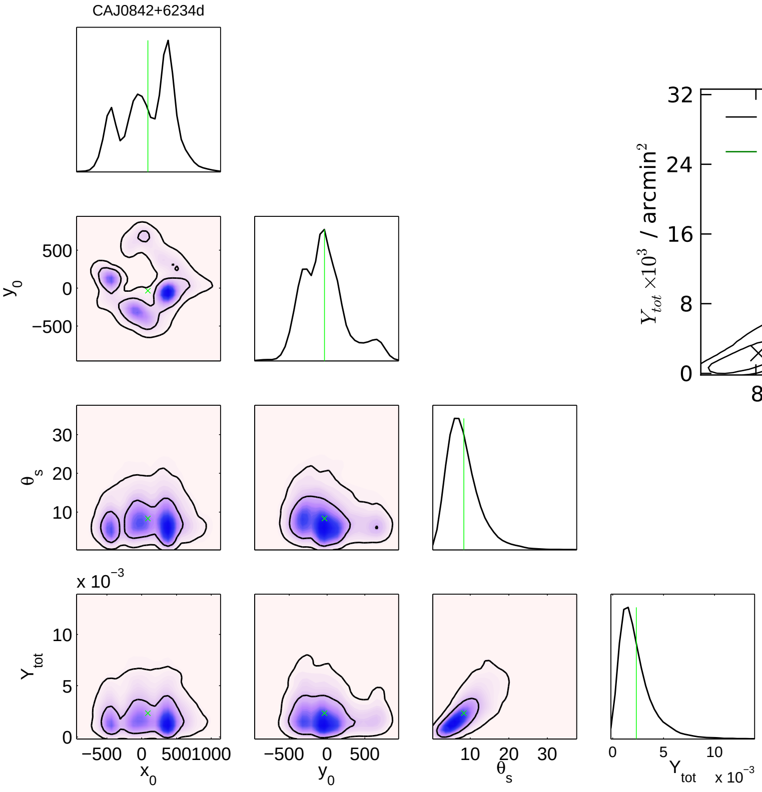

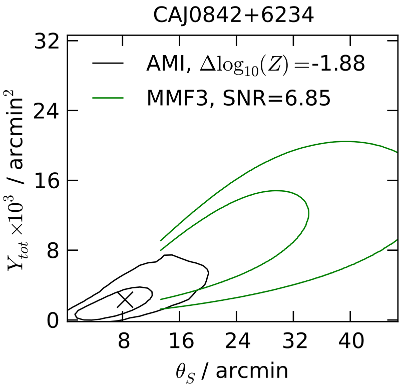

CAJ0637+6654

AMI detection category: Y, $\Delta\log_{10}(Z) = 3.76$

Planck detections 111, SNR = 6.766

AMI-*Planck* distance = 1.94 arcmin = $1.62\sigma_{Planck}$

Large residuals are from real, extended emission resolved out by the LA; doesn't appear to be creating the decrement

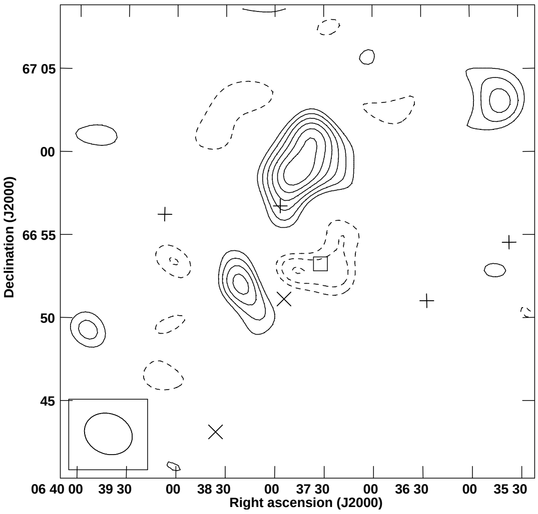

(a) Natural weighting, contours at $\pm(3\text{ to }10) \times 83.76\,\mu\text{Jy beam}^{-1}$

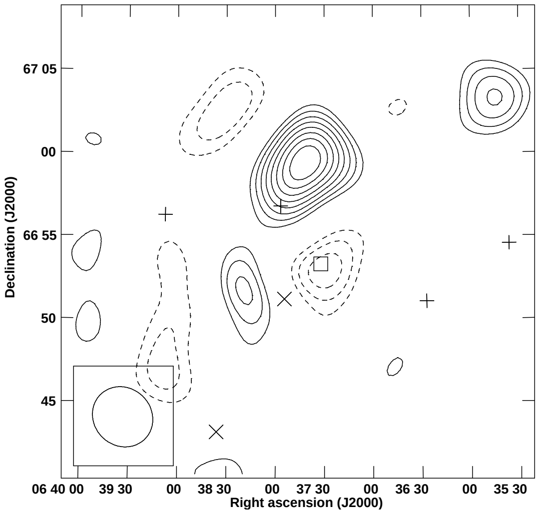

(b) *uv*-taper = 600λ, contours at $\pm(3\text{ to }10) \times 110.2\,\mu\text{Jy beam}^{-1}$

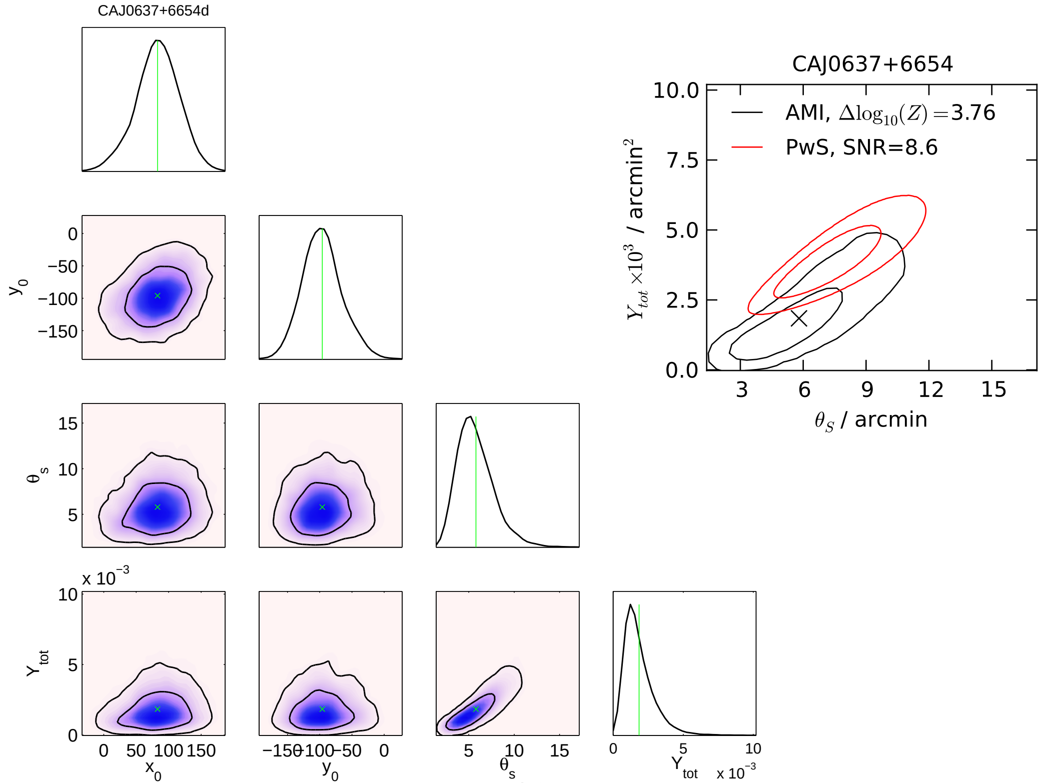

CAJ1259+6004 (PLCKESZ G121.11+57.01); z = 0.344

AMI detection category: Y, $\Delta\log_{10}(Z) = 12.76$

Planck detections 111, SNR = 6.721

AMI-*Planck* distance = 1.47 arcmin = $1.43\sigma_{Planck}$

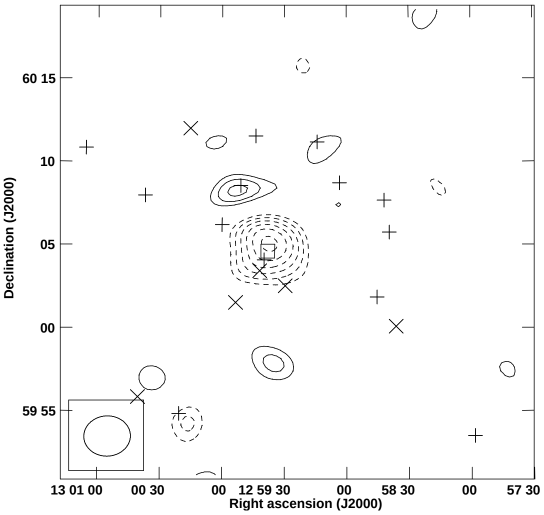

(a) Natural weighting, contours at $\pm(3 \text{ to } 10) \times 76.35\,\mu\text{Jy beam}^{-1}$

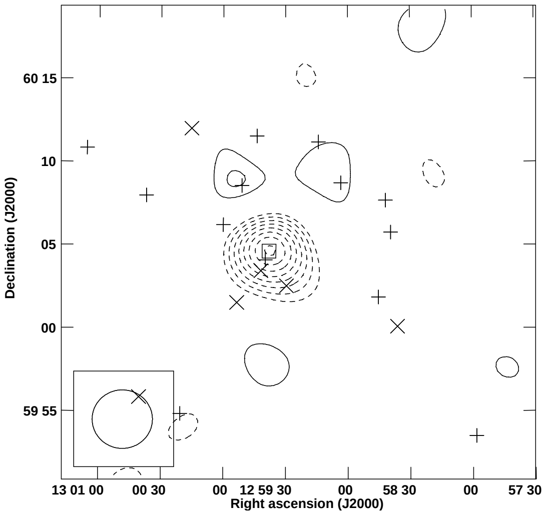

(b) *uv*-taper = 600λ, contours at $\pm(3 \text{ to } 10) \times 95.78\,\mu\text{Jy beam}^{-1}$

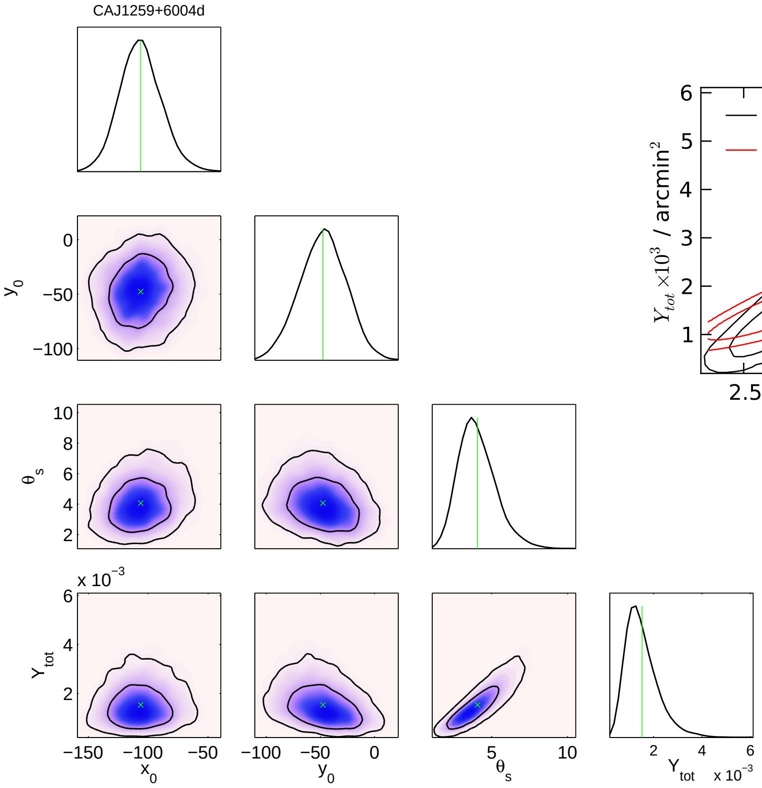

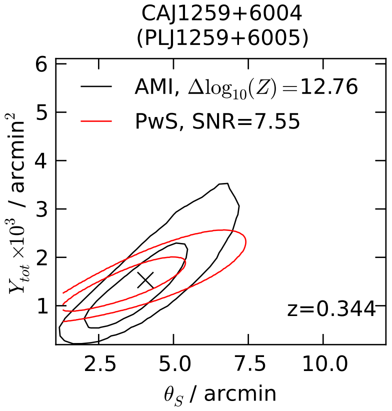

CAJ1354+7714 (RXC J1354.6+7715); z = 0.397

AMI detection category: Y, $\Delta\log_{10}(Z) = 6.63$

Planck detections 111, SNR = 6.669

AMI-*Planck* distance = 1.55 arcmin = $1.54\sigma_{Planck}$

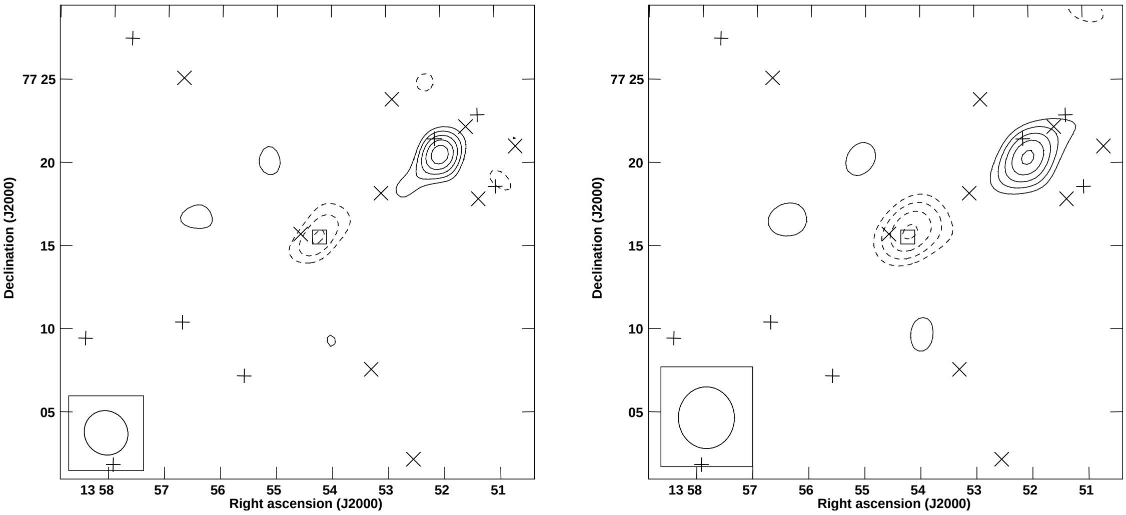

(a) Natural weighting, contours at $\pm(3 \text{ to } 10) \times 122.3\,\mu\text{Jy beam}^{-1}$

(b) *uv*-taper = 600λ, contours at $\pm(3 \text{ to } 10) \times 145.6\,\mu\text{Jy beam}^{-1}$

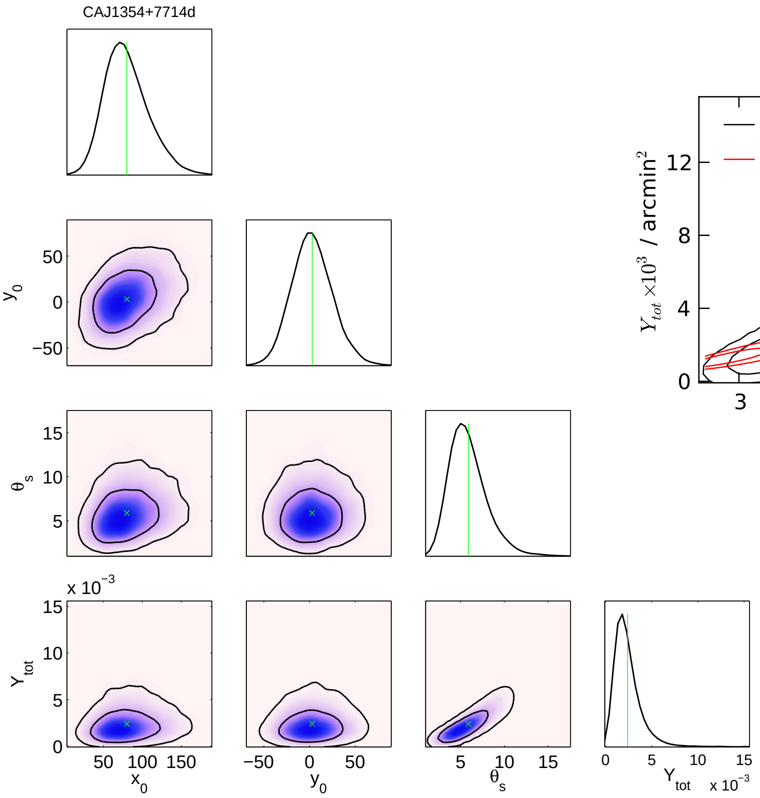

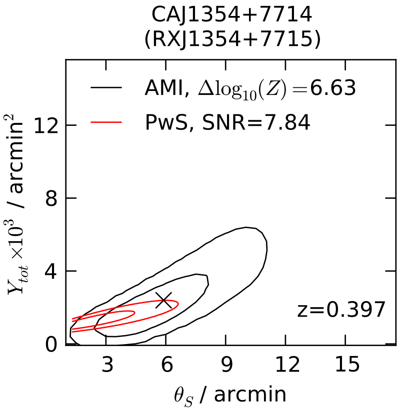

CAJ1832+6449 (RXC J1832.5+6449); z = 0.162

AMI detection category: N, $\Delta \log_{10}(Z) = -1.27$

Planck detections 111, SNR = 6.656

AMI-*Planck* distance = 2.05 arcmin = $1.46\sigma_{Planck}$

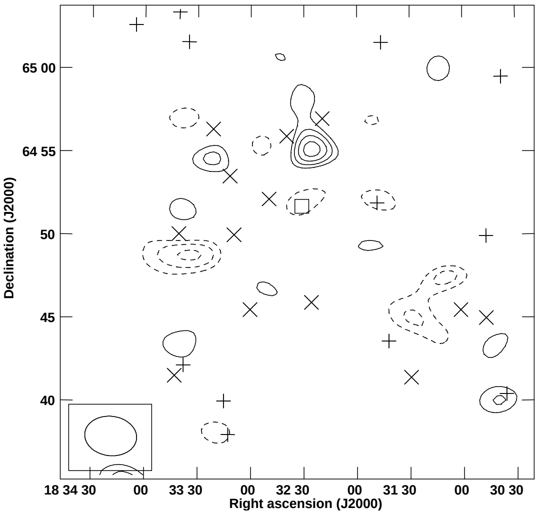

(a) Natural weighting, contours at $\pm(3 \text{ to } 10) \times 95.74\,\mu\text{Jy beam}^{-1}$

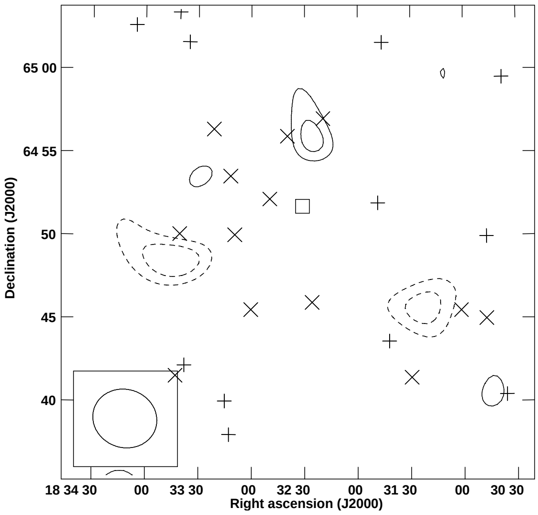

(b) uv-taper = 600λ, contours at $\pm(3 \text{ to } 10) \times 131.9\,\mu\text{Jy beam}^{-1}$

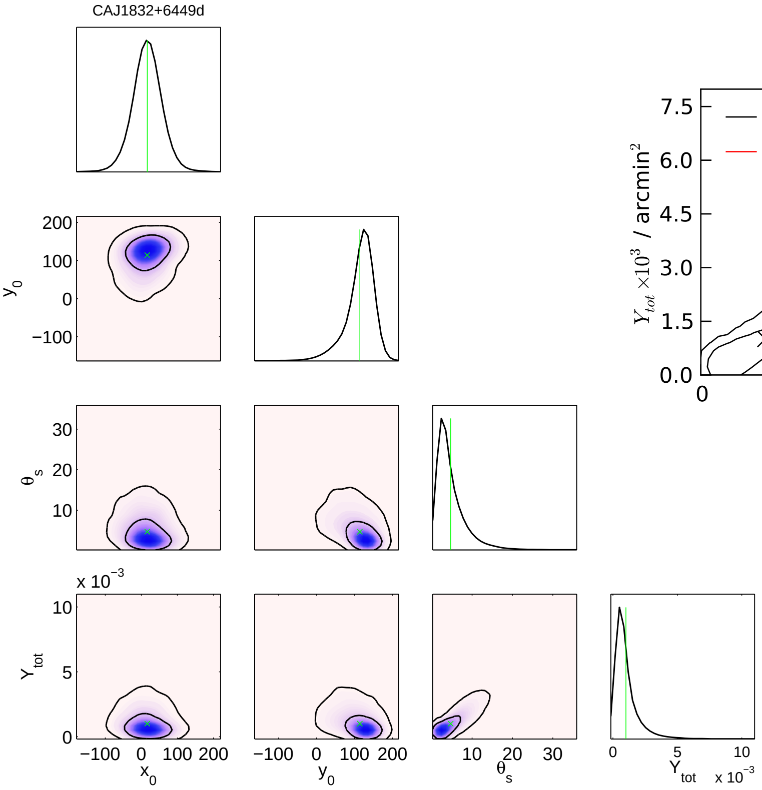

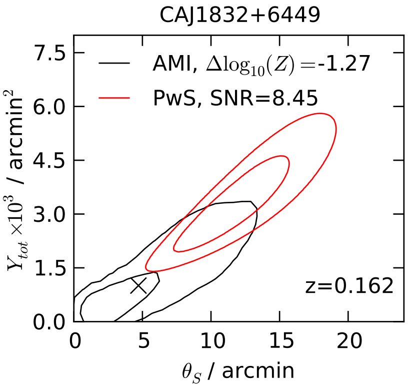

CAJ2137+3531

AMI detection category: Y, $\Delta \log_{10}(Z) = 25.76$
Planck detections 011, SNR = 6.585
AMI-*Planck* distance = 2.65 arcmin = $1.54\sigma_{Planck}$
Large residuals are from real, extended emission resolved out by the LA; doesn’t appear to be creating the decrement

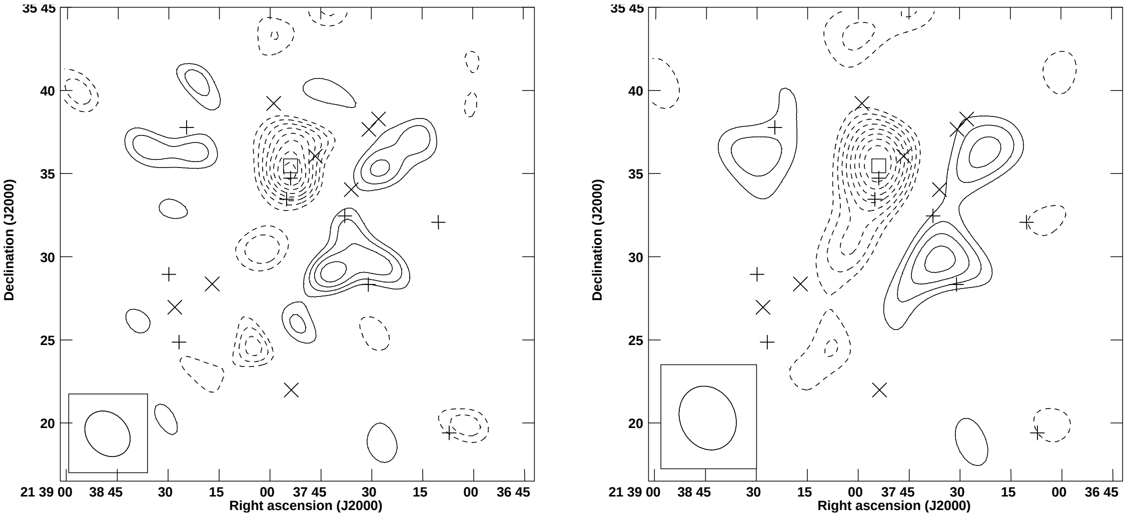

(a) Natural weighting, contours at $\pm(3 \text{ to } 10) \times 93.19\,\mu\text{Jy beam}^{-1}$

(b) *uv*-taper = 600λ, contours at $\pm(3 \text{ to } 10) \times 130.6\,\mu\text{Jy beam}^{-1}$

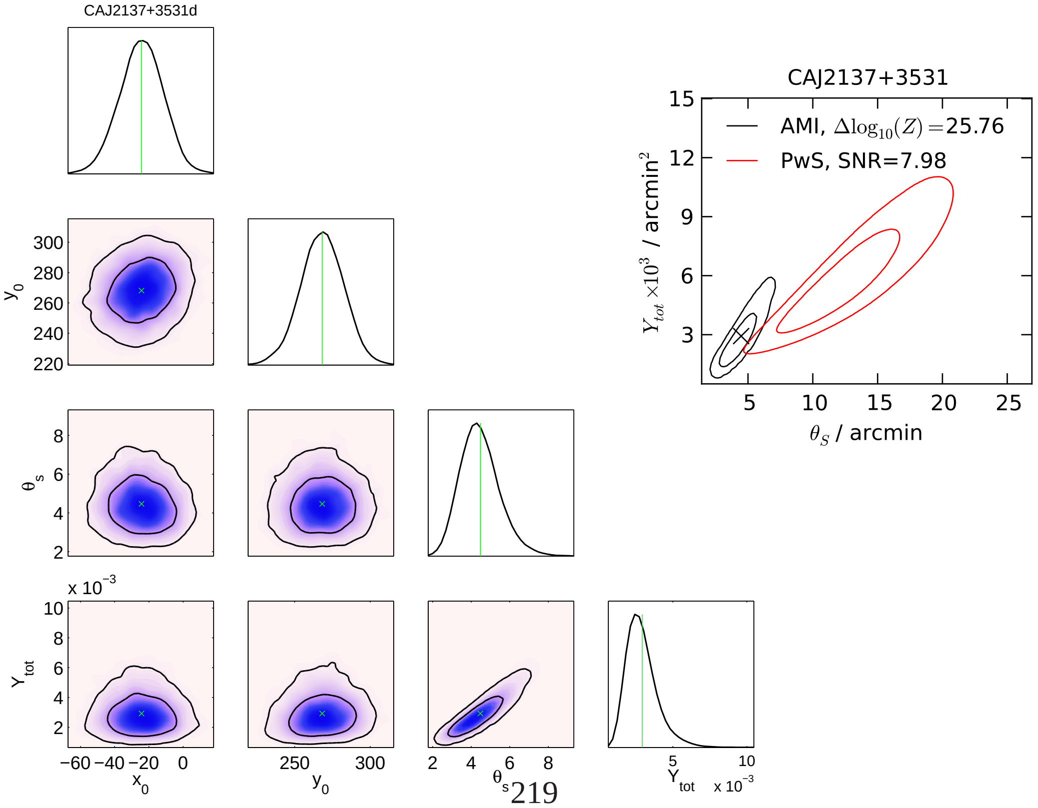

CAJ2234+5243

AMI detection category: Y, $\Delta\log_{10}(Z) = 6.77$

Planck detections 011, SNR = 6.562

AMI-*Planck* distance = 1.74 arcmin = $2.70\sigma_{Planck}$

Large residuals are from real, extended emission resolved out by the LA; doesn't appear to be creating the decrement

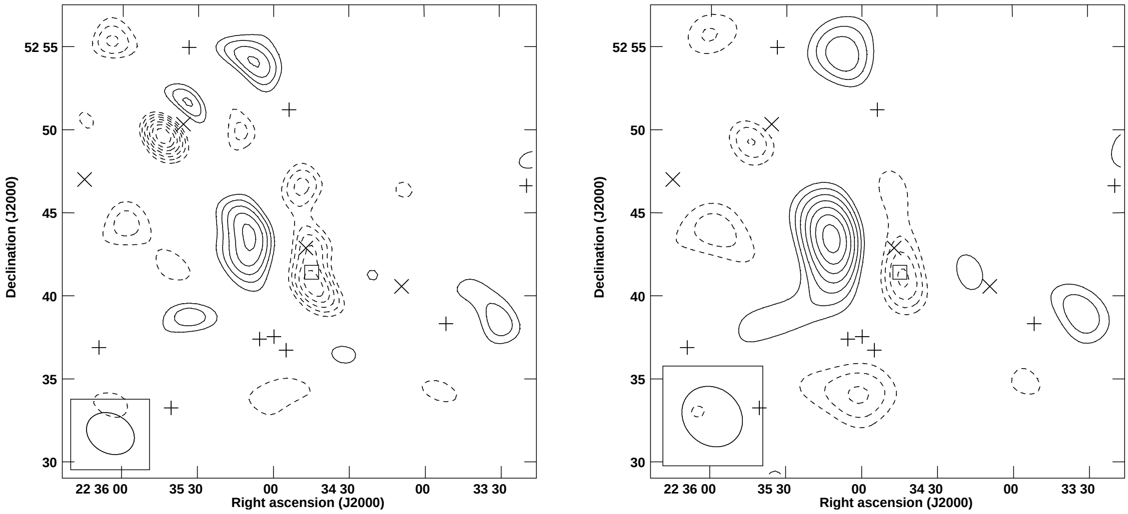

(a) Natural weighting, contours at $\pm$(3 to 10) $\times$ 88.11 μJy beam^{-1}

(b) *uv*-taper = 600λ, contours at $\pm$(3 to 10) $\times$ 112.4 μJy beam^{-1}

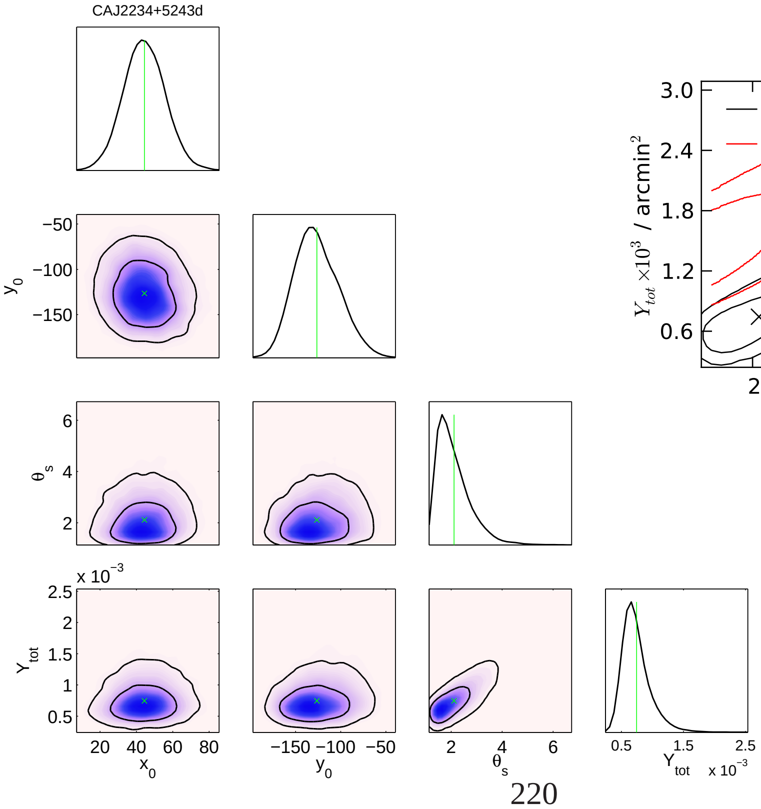

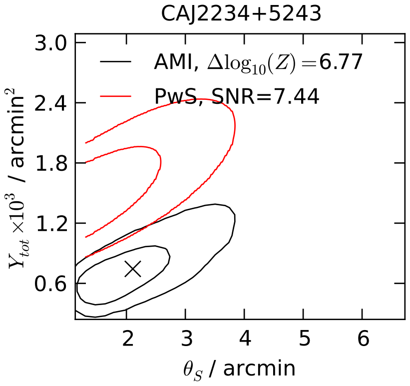

CAJ1905+3233

AMI detection category: M, $\Delta\log_{10}(Z) = 2.07$

Planck detections 111, SNR = 6.526

AMI-*Planck* distance = 0.80 arcmin = $1.16\sigma_{Planck}$

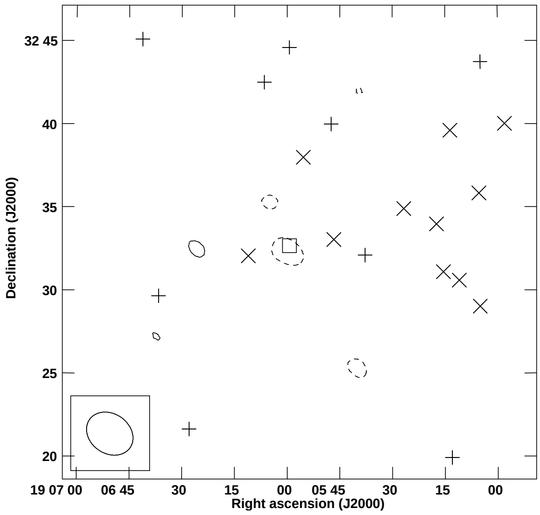

(a) Natural weighting, contours at $\pm(3 \text{ to } 10) \times 113.0\,\mu\text{Jy beam}^{-1}$

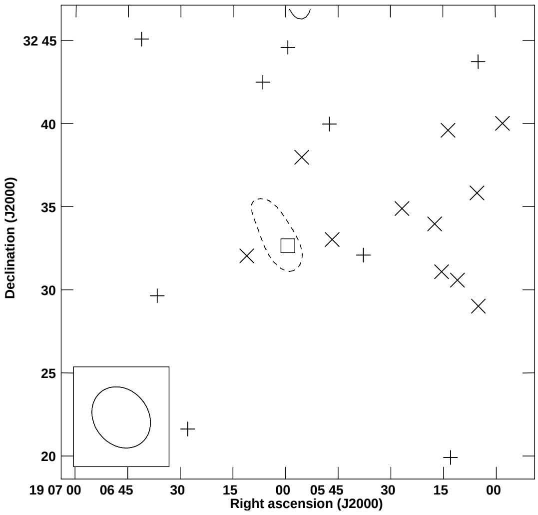

(b) *uv*-taper = 600λ, contours at $\pm(3 \text{ to } 10) \times 146.2\,\mu\text{Jy beam}^{-1}$

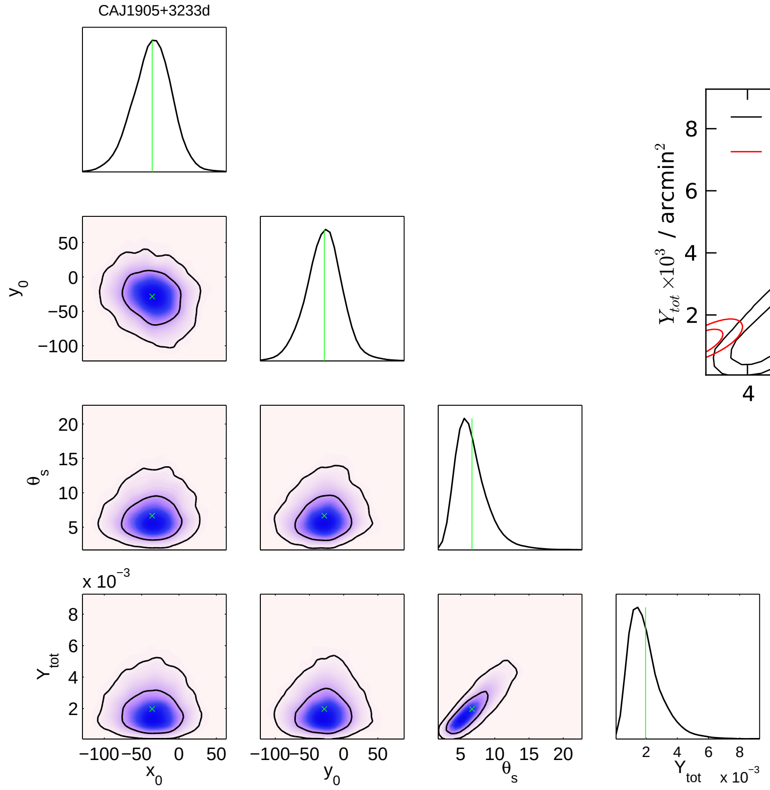

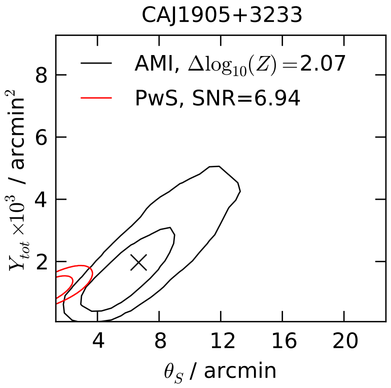

CAJ2322+4845

AMI detection category: Y, $\Delta \log_{10}(Z)$ = 18.47

Planck detections 111, SNR = 6.493

AMI-*Planck* distance = 0.57 arcmin = $0.47\sigma_{Planck}$

Large residuals are from real, extended emission resolved out by the LA; doesn't appear to be creating the decrement

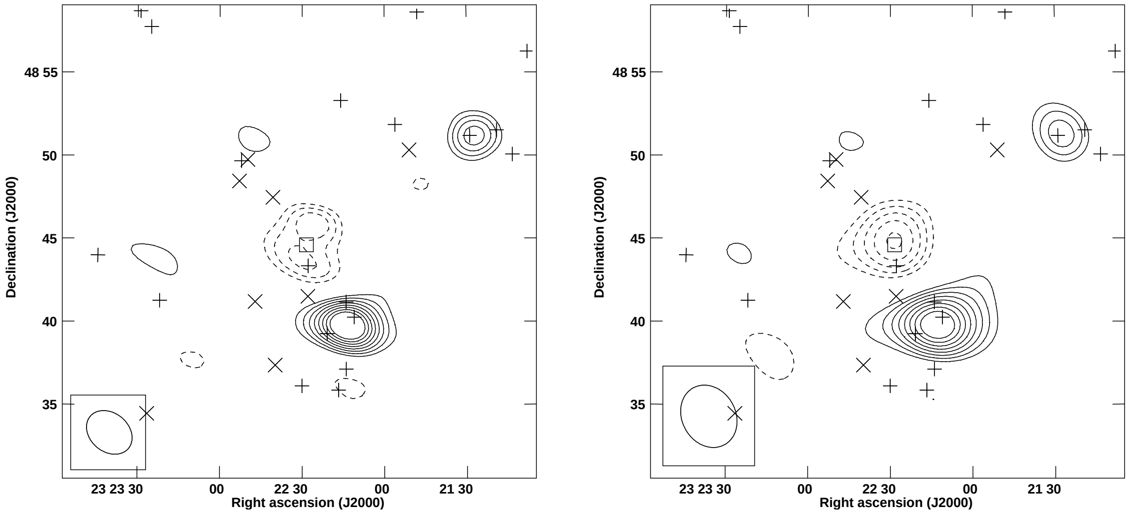

(a) Natural weighting, contours at $\pm(3 \text{ to } 10) \times 104.2\,\mu\text{Jy beam}^{-1}$

(b) uv-taper = 600λ, contours at $\pm(3 \text{ to } 10) \times 139.7\,\mu\text{Jy beam}^{-1}$

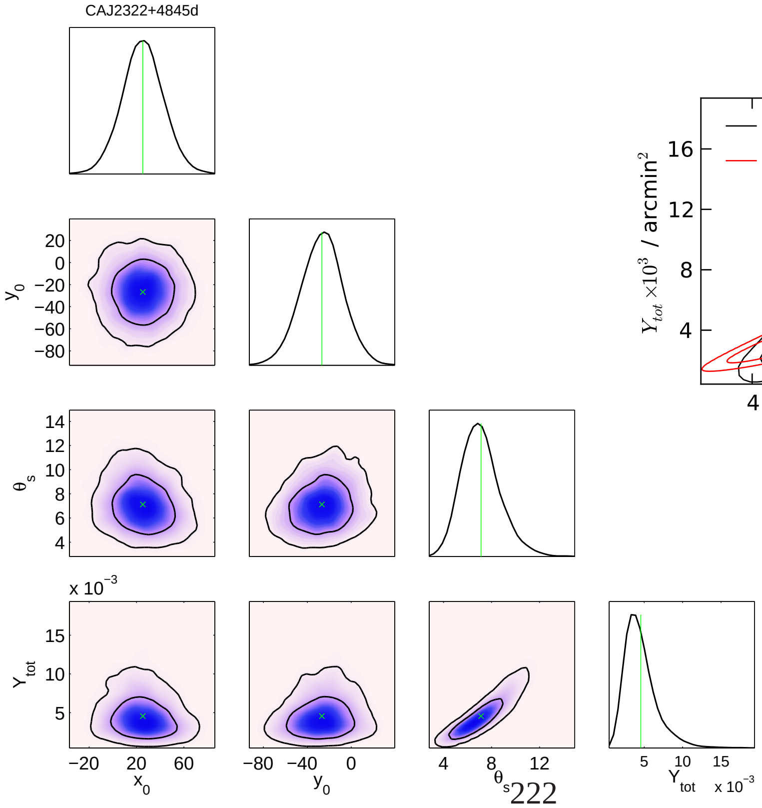

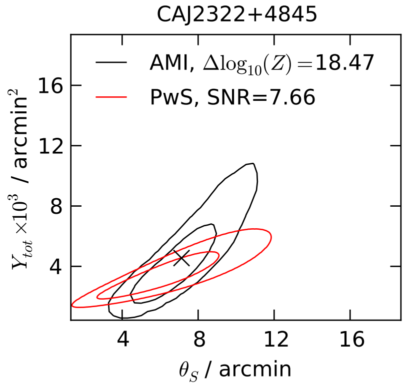

CAJ1756+4007 (WHL J269.219+40.1353); z = 0.57

AMI detection category: Y, $\Delta \log_{10}(Z)$ = 16.0

Planck detections 111, SNR = 6.476

AMI-*Planck* distance = 1.27 arcmin = $1.27\sigma_{Planck}$

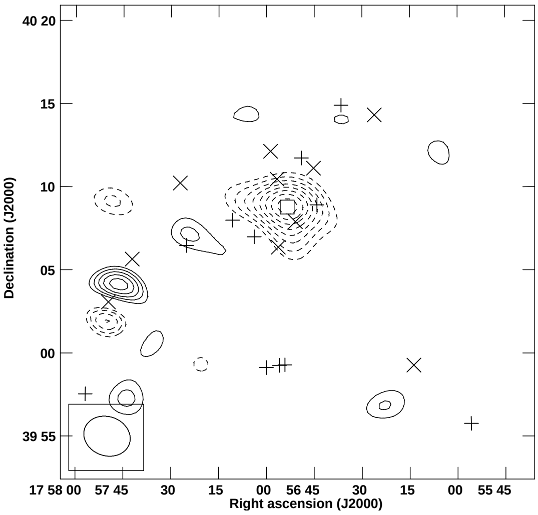

(a) Natural weighting, contours at $\pm(3 \text{ to } 10) \times 119.3\,\mu\text{Jy beam}^{-1}$

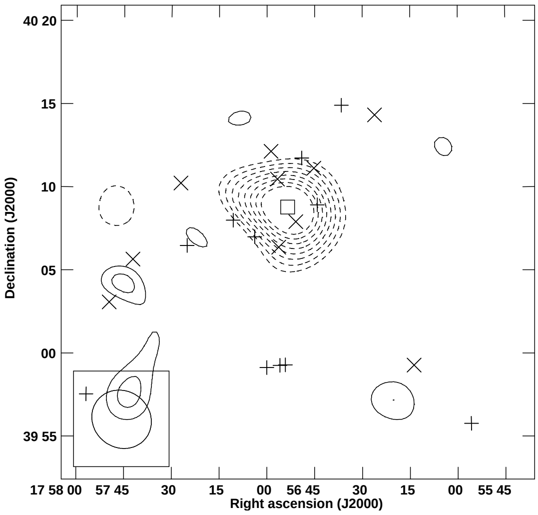

(b) *uv*-taper = 600λ, contours at $\pm(3 \text{ to } 10) \times 141.9\,\mu\text{Jy beam}^{-1}$

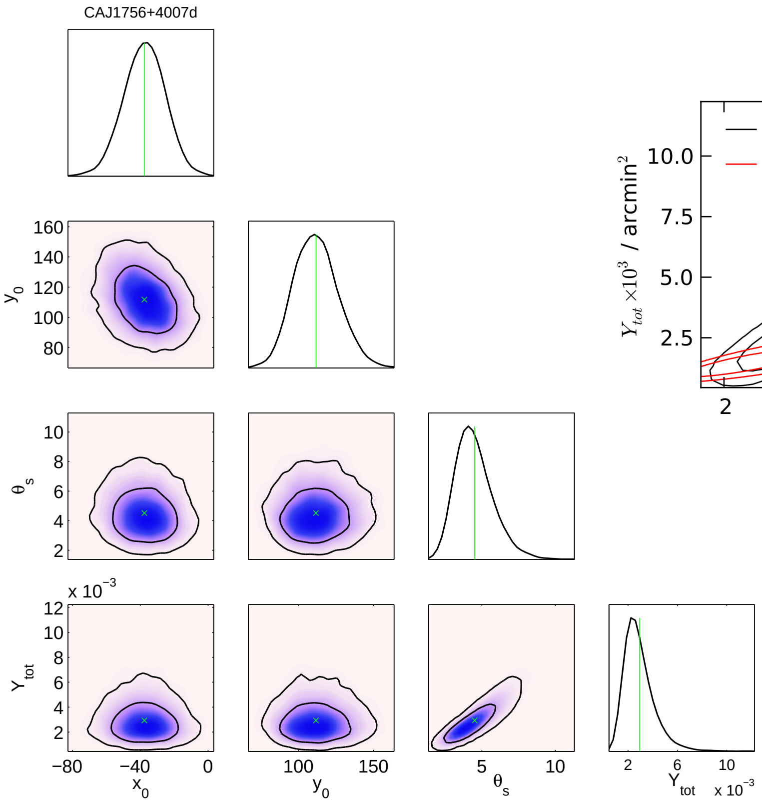

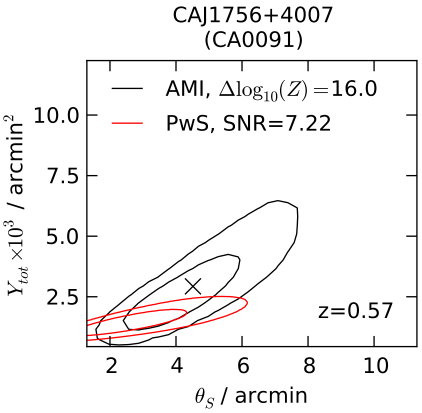

CAJ0909+5133 (RXC J0909.3+5133); z = 0.232

AMI detection category: Y, $\Delta\log_{10}(Z)$ = 4.24

Planck detections 111, SNR = 6.376

AMI-*Planck* distance = 1.31 arcmin = $1.19\sigma_{Planck}$

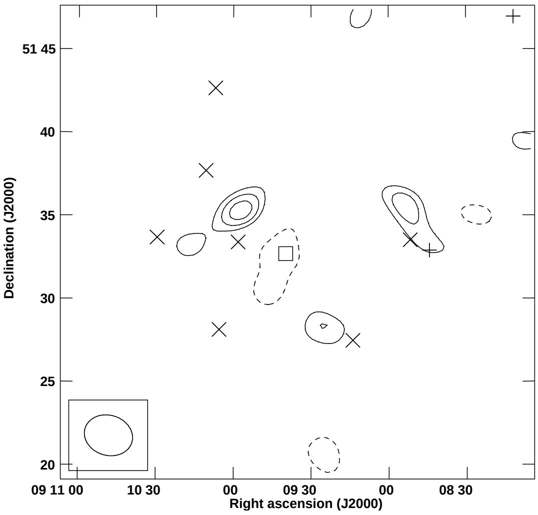

(a) Natural weighting, contours at ±(3 to 10) × 94.56 μJy beam^{-1}

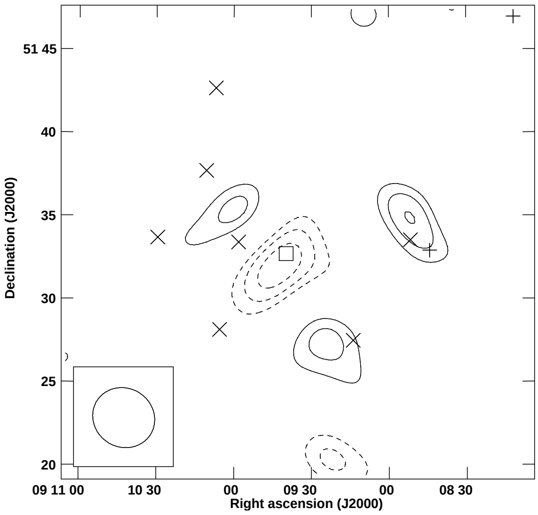

(b) *uv*-taper = 600λ, contours at ±(3 to 10) × 112.1 μJy beam^{-1}

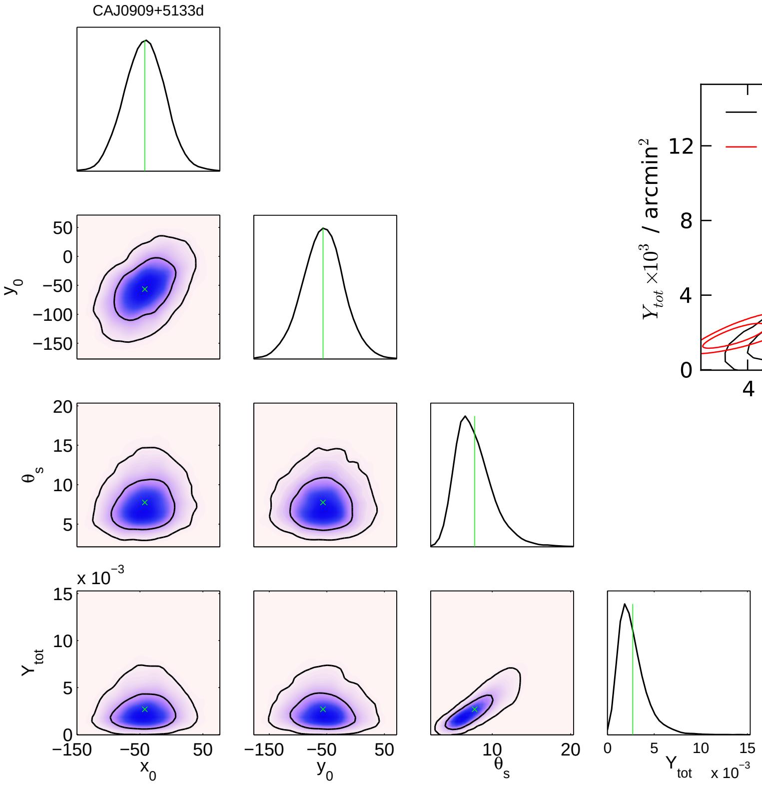

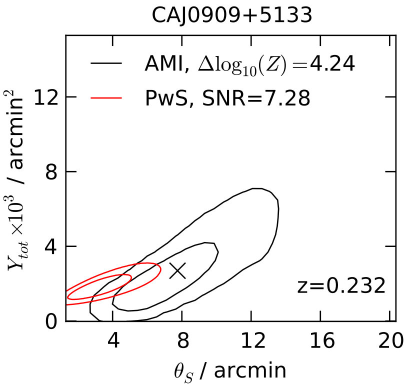

CAJ1414+5447 (WHL J213.697+54.7844); z = 0.631

AMI detection category: Y, $\Delta \log_{10}(Z)$ = 34.62

Planck detections 111, SNR = 6.351

AMI-*Planck* distance = 0.48 arcmin = $0.39\sigma_{Planck}$

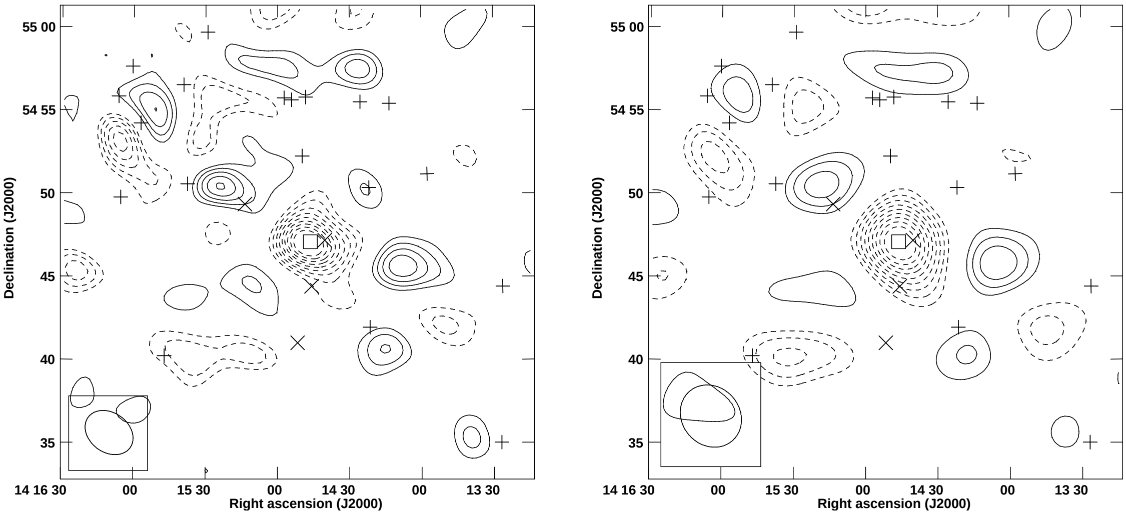

(a) Natural weighting, contours at $\pm$(3 to 10) $\times$ 103.0 μJy beam^{-1}

(b) *uv*-taper = 600λ, contours at $\pm$(3 to 10) $\times$ 130.3 μJy beam^{-1}

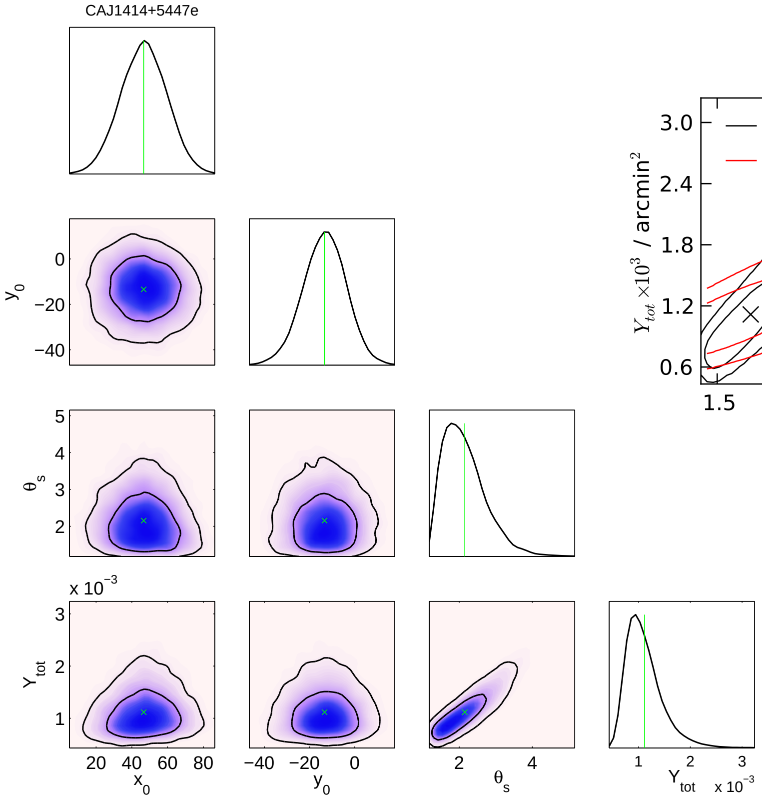

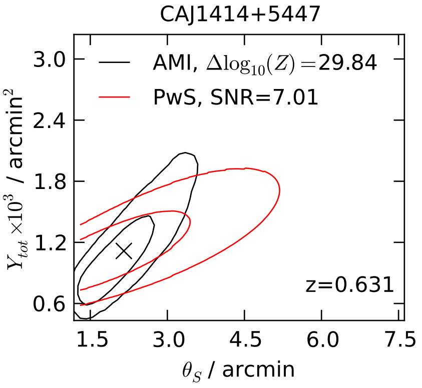

CAJ1539+3426 (A2111, RXC J1539.7+3424); z = 0.229

AMI detection category: Y, $\Delta \log_{10}(Z) = 17.02$

Planck detections 111, SNR = 6.314

AMI-*Planck* distance = 0.65 arcmin = $0.52\sigma_{Planck}$

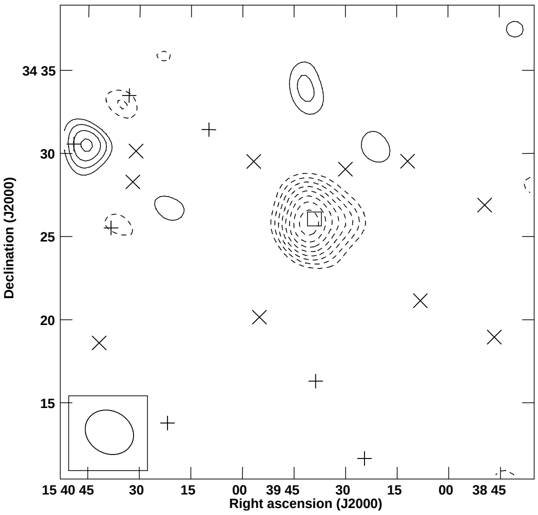

(a) Natural weighting, contours at $\pm(3 \text{ to } 10) \times 81.76\,\mu\text{Jy beam}^{-1}$

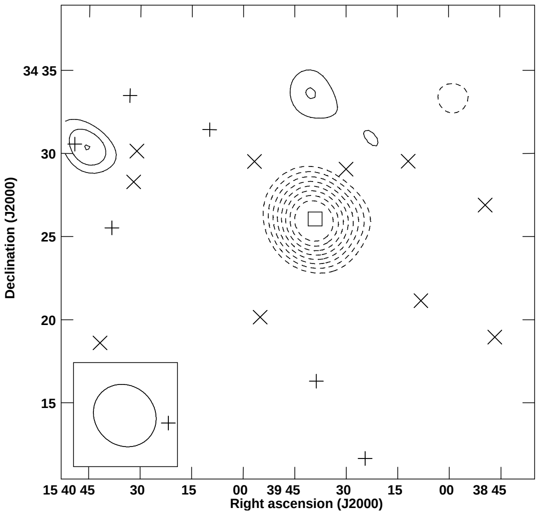

(b) uv-taper = 600λ, contours at $\pm(3 \text{ to } 10) \times 108.1\,\mu\text{Jy beam}^{-1}$

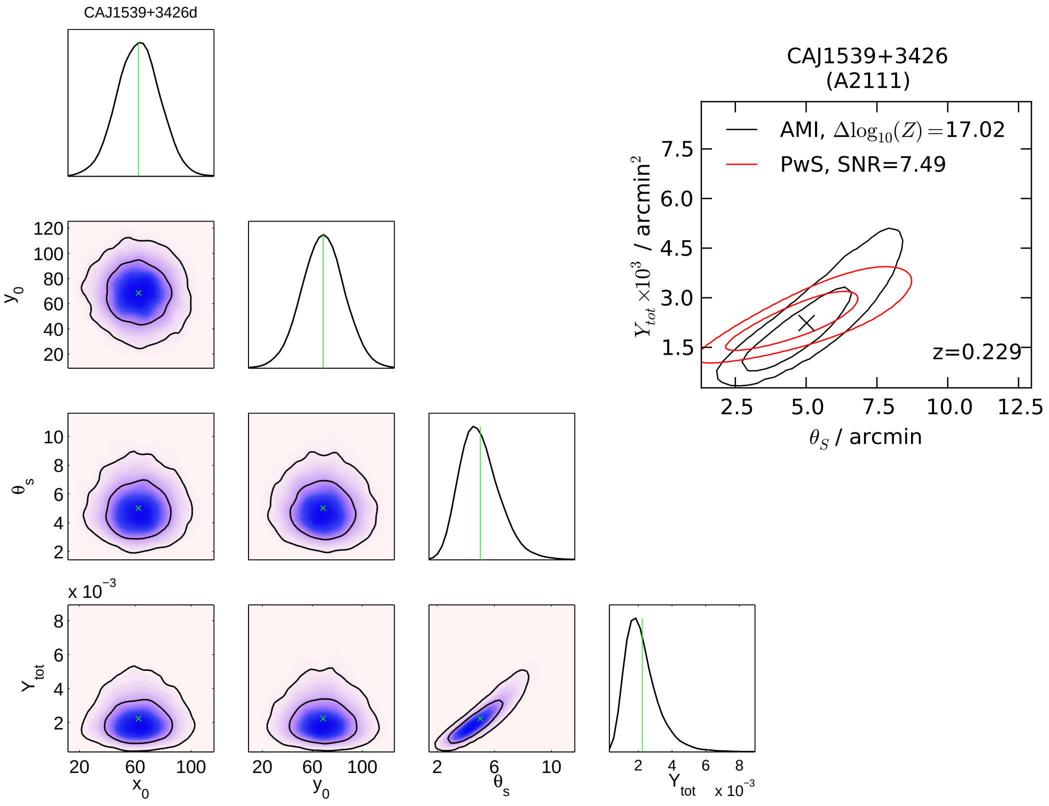

CAJ1314+6433 (A1704, RXC J1314.4+6434); z = 0.22

AMI detection category: Y, $\Delta \log_{10}(Z) = 26.98$

Planck detections 111, SNR = 6.249

AMI-*Planck* distance = 4.21 arcmin = $3.82\sigma_{Planck}$

Large residuals are from real, extended emission resolved out by the LA; doesn't appear to be creating the decrement

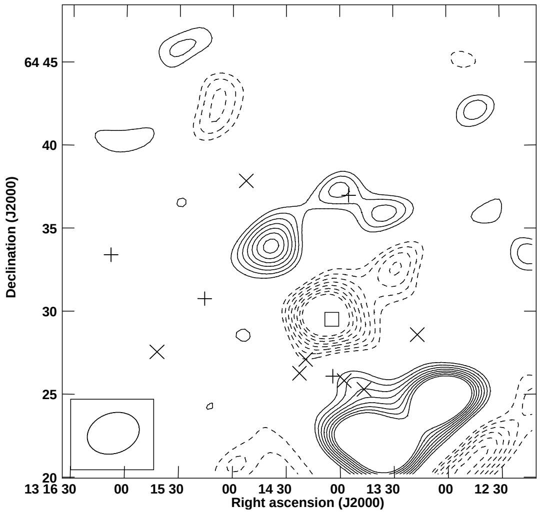

(a) Natural weighting, contours at $\pm(3 \text{ to } 10) \times 71.18\,\mu\text{Jy beam}^{-1}$

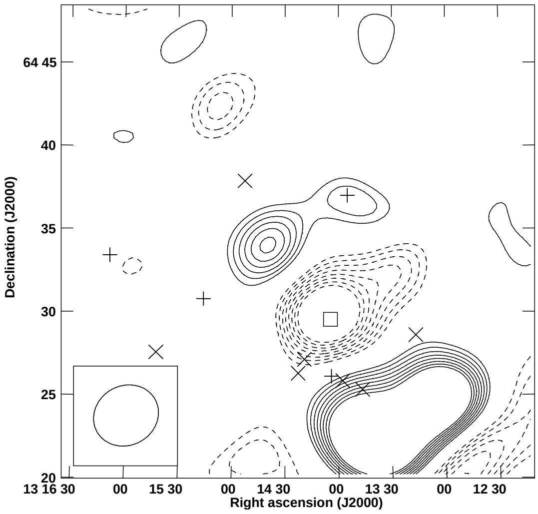

(b) *uv*-taper = 600λ, contours at $\pm(3 \text{ to } 10) \times 86.97\,\mu\text{Jy beam}^{-1}$

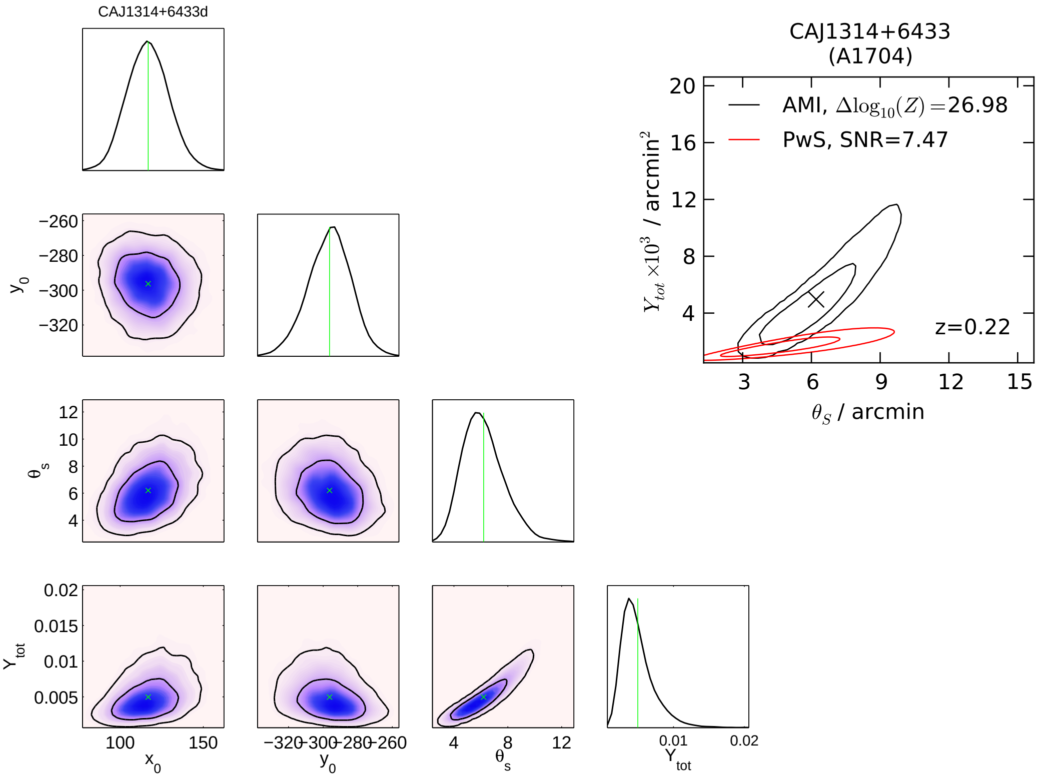

CAJ0850+3604 (ZW1953, RXC J0850.2+3603); z = 0.378

AMI detection category: Y, $\Delta \log_{10}(Z) = 4.65$

Planck detections 111, SNR = 6.225

AMI-*Planck* distance = 0.85 arcmin = $0.82\sigma_{Planck}$

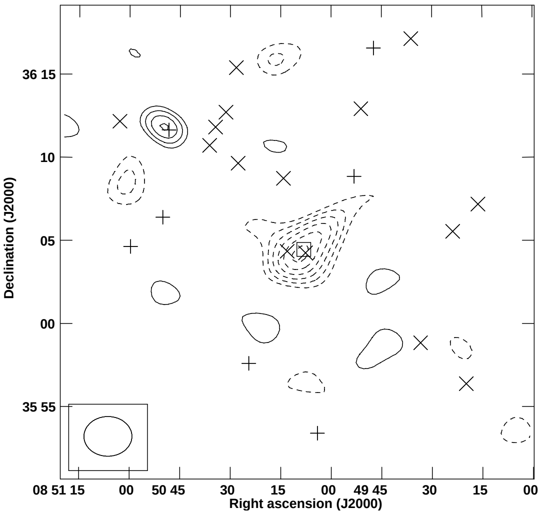

(a) Natural weighting, contours at $\pm(3 \text{ to } 10) \times 83.68\,\mu\text{Jy beam}^{-1}$

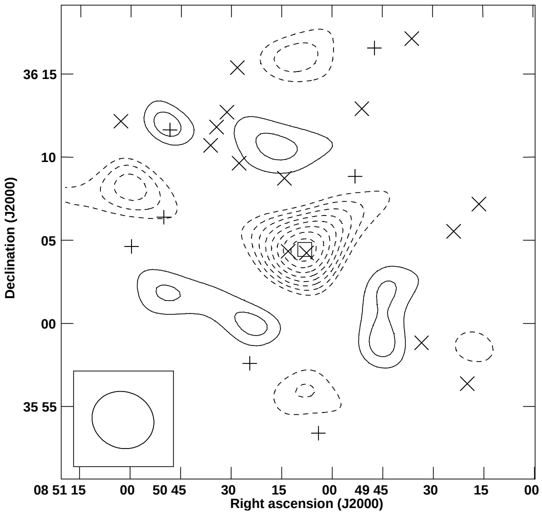

(b) *uv*-taper = 600λ, contours at $\pm(3 \text{ to } 10) \times 97.93\,\mu\text{Jy beam}^{-1}$

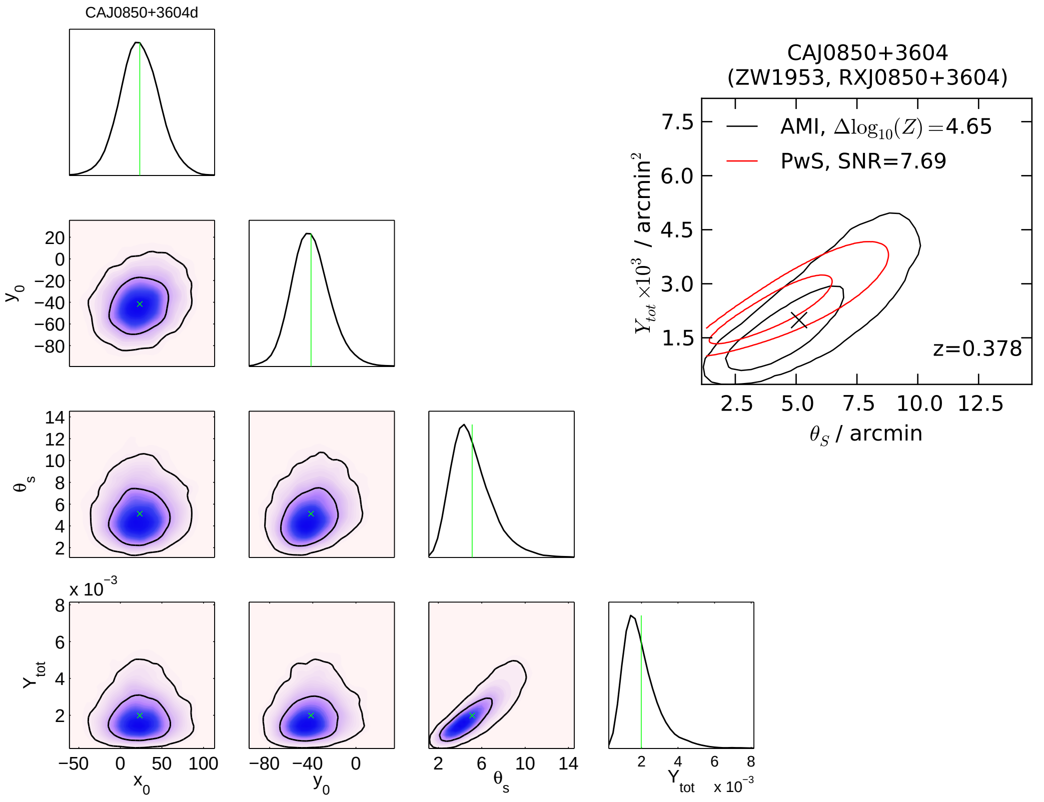

CAJ1016+3339 (A961, RXC J1016.3+3338); z = 0.124

AMI detection category: M, $\Delta \log_{10}(Z) = 0.04$
Planck detections 111, SNR = 6.142
AMI-*Planck* distance = 0.44 arcmin = $0.41\sigma_{Planck}$

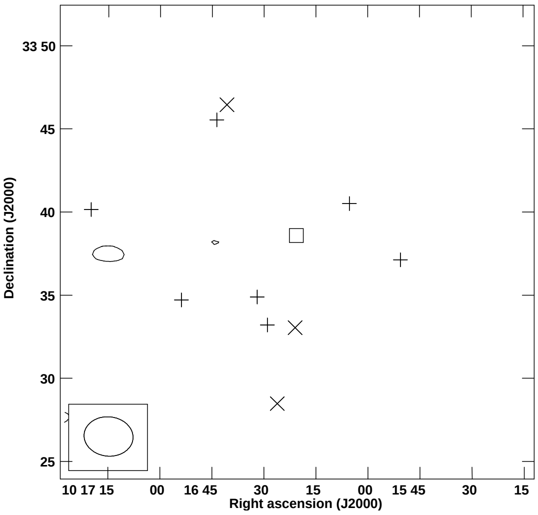

(a) Natural weighting, contours at $\pm(3 \text{ to } 10) \times 104.8\,\mu\text{Jy beam}^{-1}$

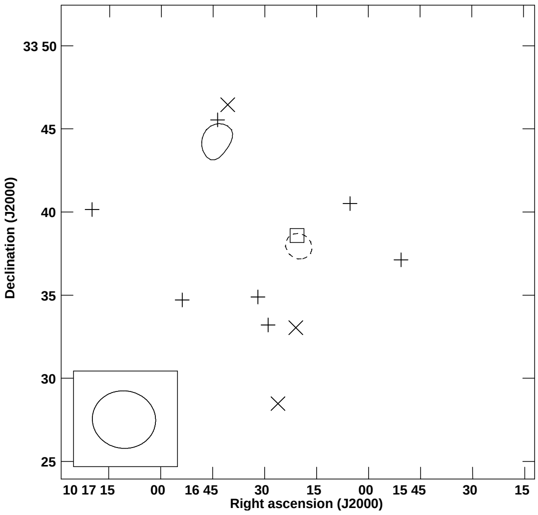

(b) *uv*-taper = 600λ, contours at $\pm(3 \text{ to } 10) \times 142.9\,\mu\text{Jy beam}^{-1}$

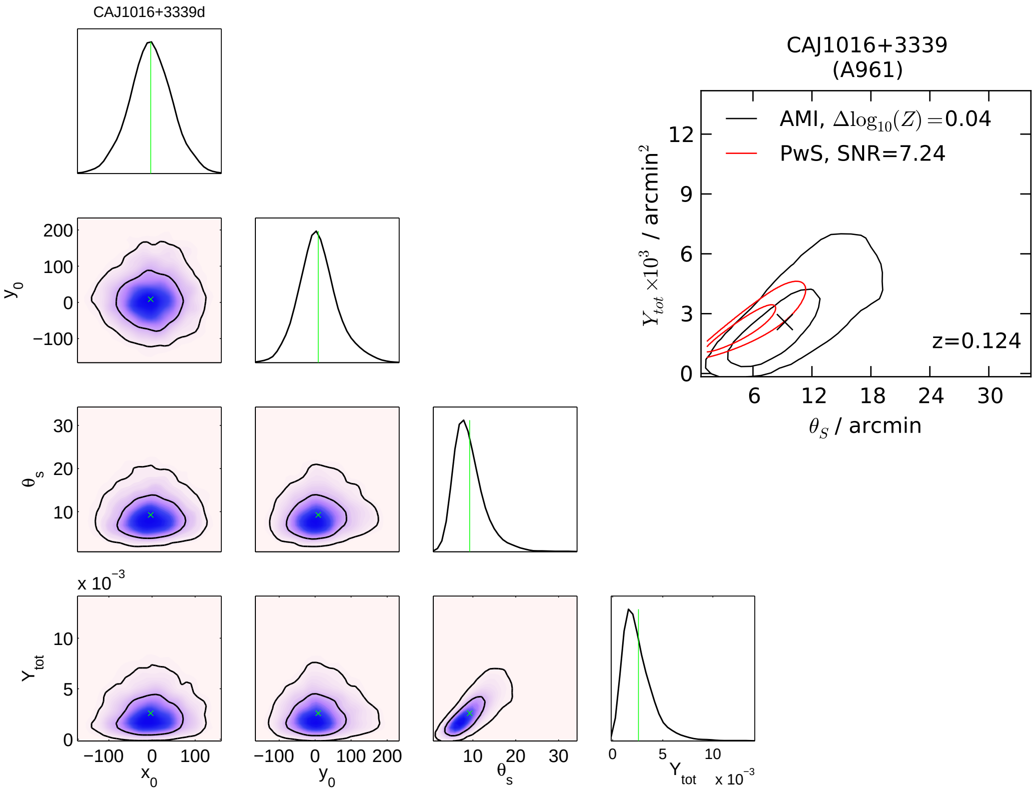

CAJ0947+7622 (MAJ0947+7623, RXC J0947.2+7623); z = 0.345

AMI detection category: Y, $\Delta\log_{10}(Z) = 7.86$

Planck detections 111, SNR = 6.123

AMI-*Planck* distance = 0.48 arcmin = $0.65\sigma_{Planck}$

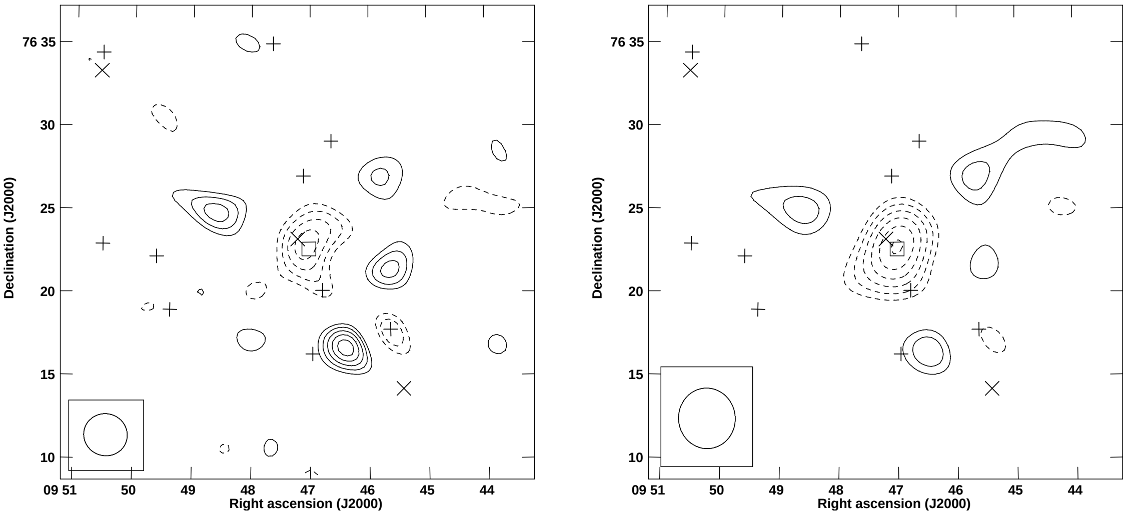

(a) Natural weighting, contours at $\pm(3 \text{ to } 10) \times 78.57\,\mu\text{Jy beam}^{-1}$

(b) uv-taper = 600λ, contours at $\pm(3 \text{ to } 10) \times 113.4\,\mu\text{Jy beam}^{-1}$

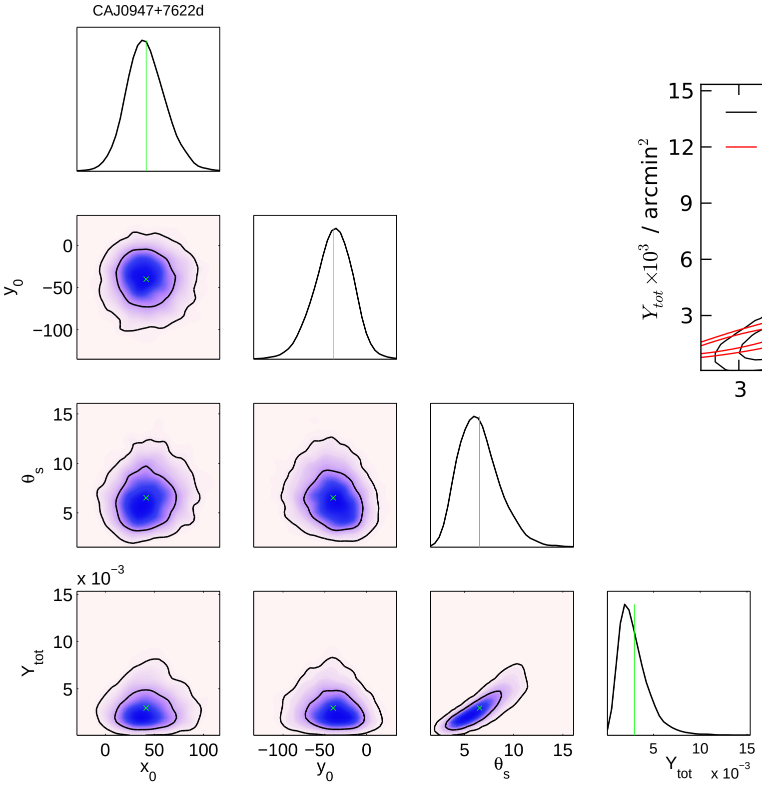

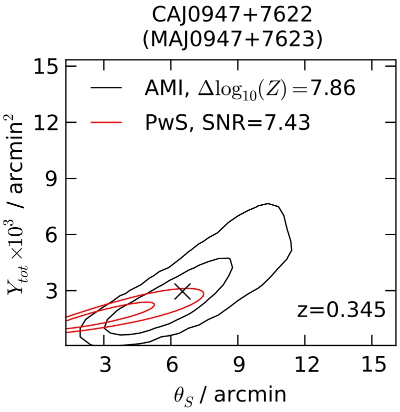

CAJ2146+2029 (ZwCl 2143.5+201); z = 0.25

AMI detection category: N, $\Delta\log_{10}(Z) = -1.03$

Planck detections 111, SNR = 6.096

AMI-*Planck* distance = 2.68 arcmin = $1.96\sigma_{Planck}$

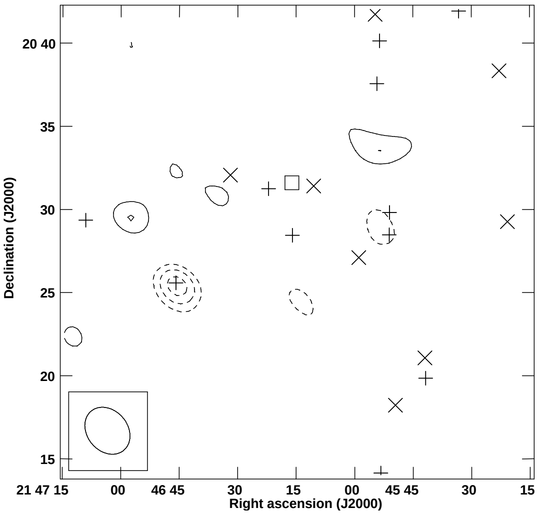

(a) Natural weighting, contours at $\pm(3 \text{ to } 10) \times 123.6\,\mu\text{Jy beam}^{-1}$

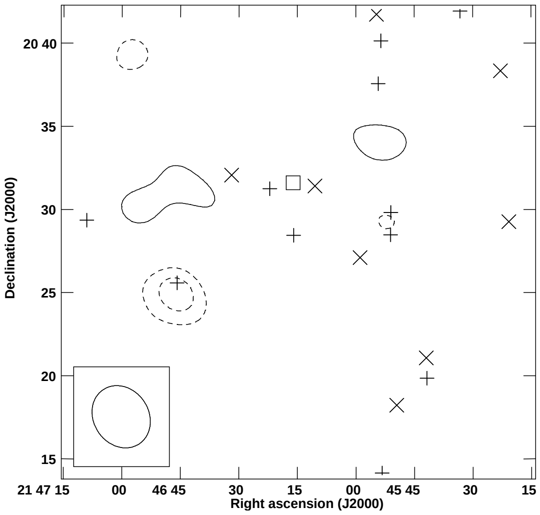

(b) *uv*-taper = 600λ, contours at $\pm(3 \text{ to } 10) \times 179.3\,\mu\text{Jy beam}^{-1}$

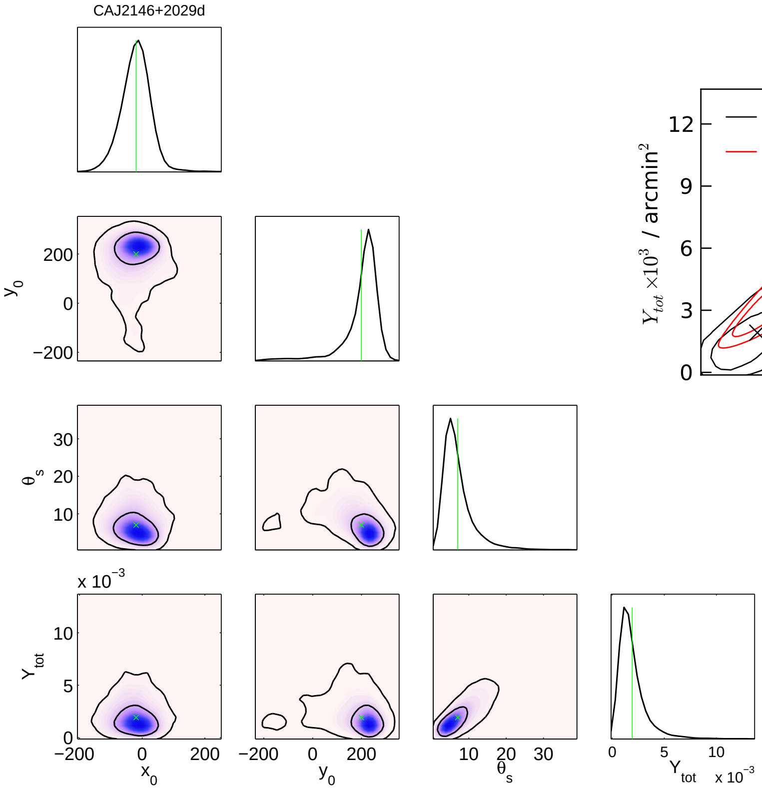

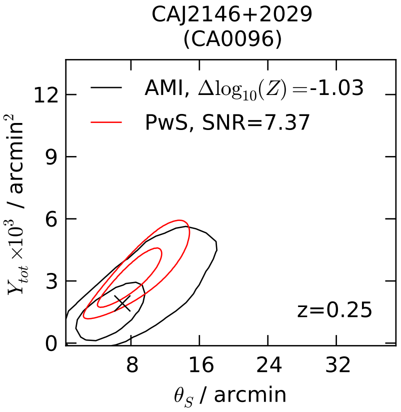

CAJ1123+2128 (A1246, RXC J1123.9+2129); z = 0.19

AMI detection category: M, $\Delta \log_{10}(Z) = 0.29$

Planck detections 111, SNR = 6.085

AMI-*Planck* distance = 0.93 arcmin = $0.79\sigma_{Planck}$

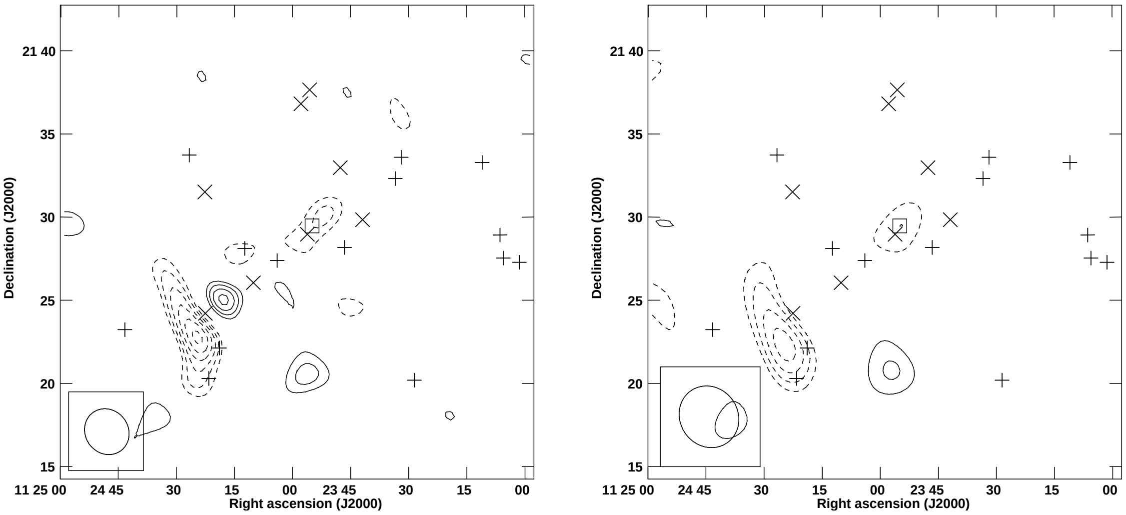

(a) Natural weighting, contours at $\pm(3 \text{ to } 10) \times 105.1\,\mu\text{Jy beam}^{-1}$

(b) *uv*-taper = 600λ, contours at $\pm(3 \text{ to } 10) \times 142.0\,\mu\text{Jy beam}^{-1}$

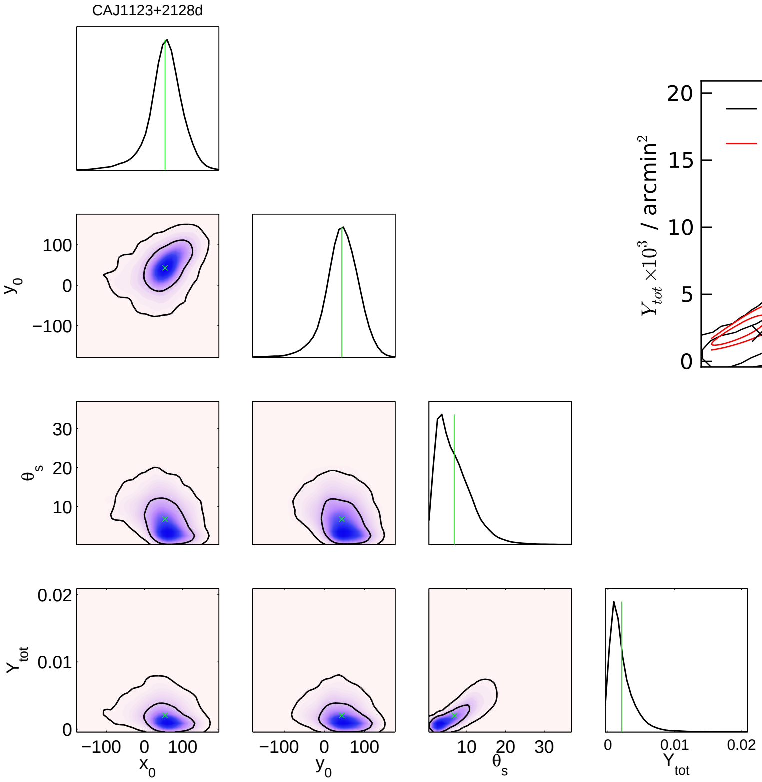

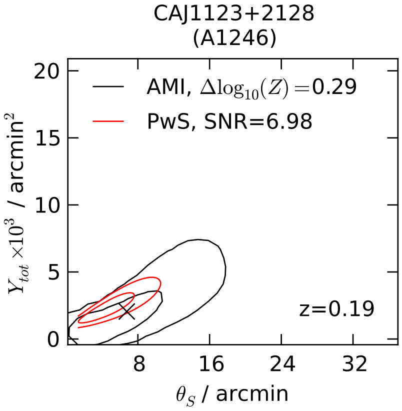

CAJ0801+3605 (A611, RXC J0800.9+3602); z = 0.288

AMI detection category: Y, $\Delta\log_{10}(Z) = 21.91$

Planck detections 101, SNR = 6.065

AMI-*Planck* distance = 2.00 arcmin = $1.40\sigma_{Planck}$

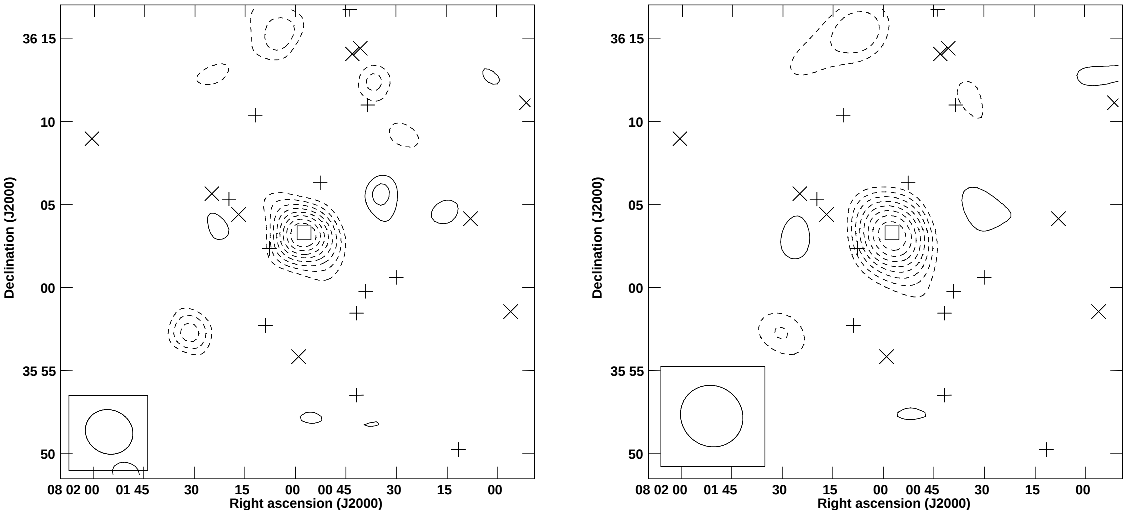

(a) Natural weighting, contours at $\pm(3 \text{ to } 10) \times 82.68\,\mu\text{Jy beam}^{-1}$

(b) *uv*-taper = 600λ, contours at $\pm(3 \text{ to } 10) \times 110.3\,\mu\text{Jy beam}^{-1}$

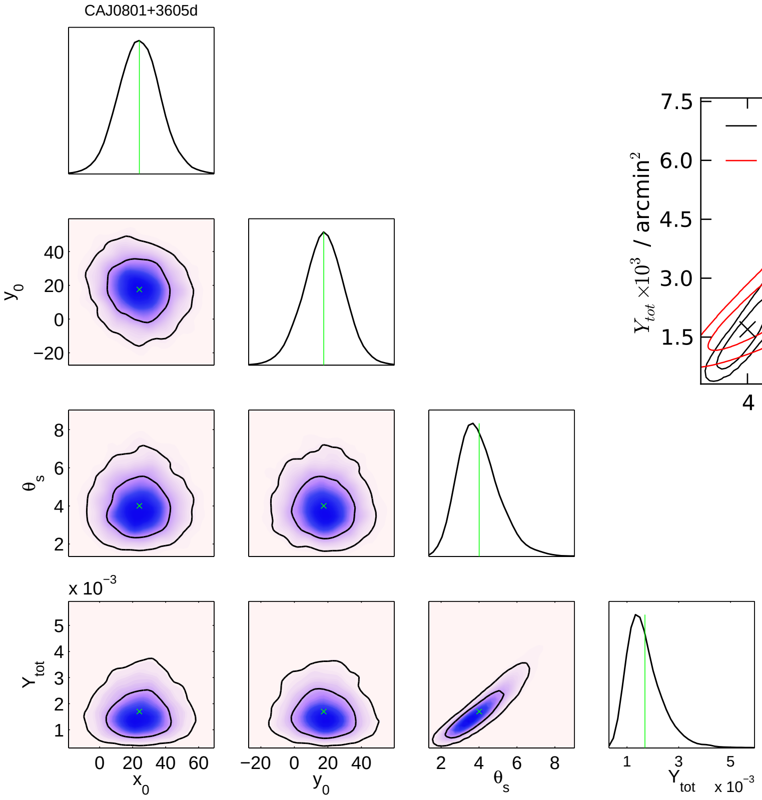

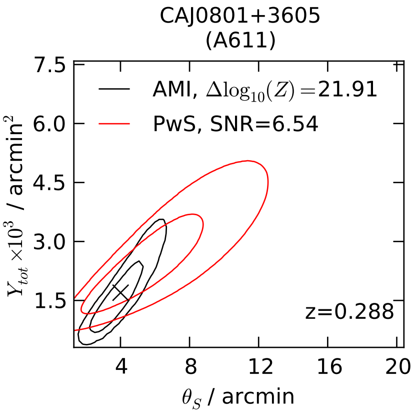

CAJ0851+4829 ; z = 0.513
AMI detection category: Y, $\Delta \log_{10}(Z) = 23.26$
Planck detections 111, SNR = 6.009
AMI-*Planck* distance = 0.66 arcmin = $0.76\sigma_{Planck}$

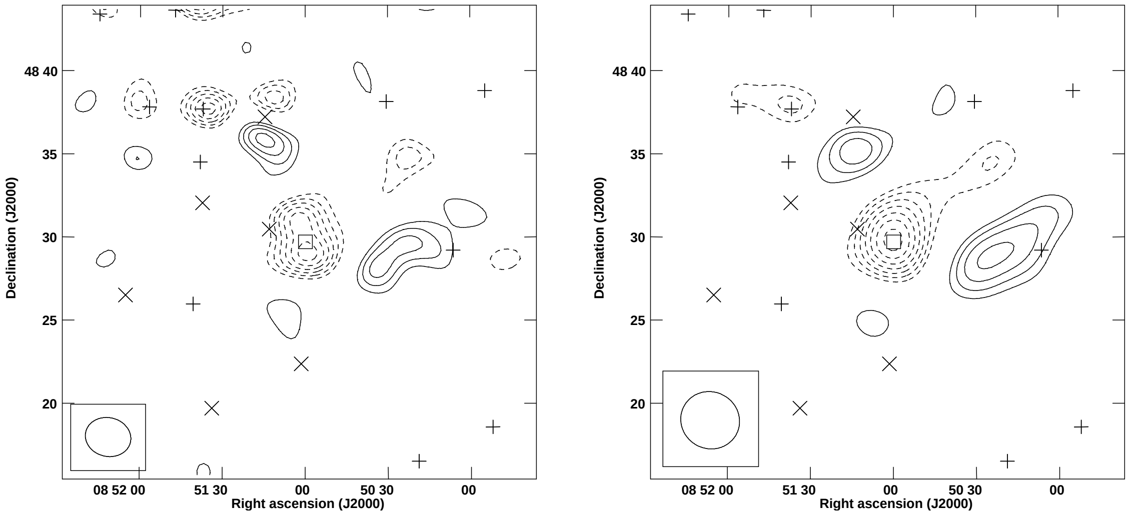

(a) Natural weighting, contours at $\pm(3 \text{ to } 10) \times 92.89\,\mu\text{Jy beam}^{-1}$

(b) *uv*-taper = 600λ, contours at $\pm(3 \text{ to } 10) \times 134.6\,\mu\text{Jy beam}^{-1}$

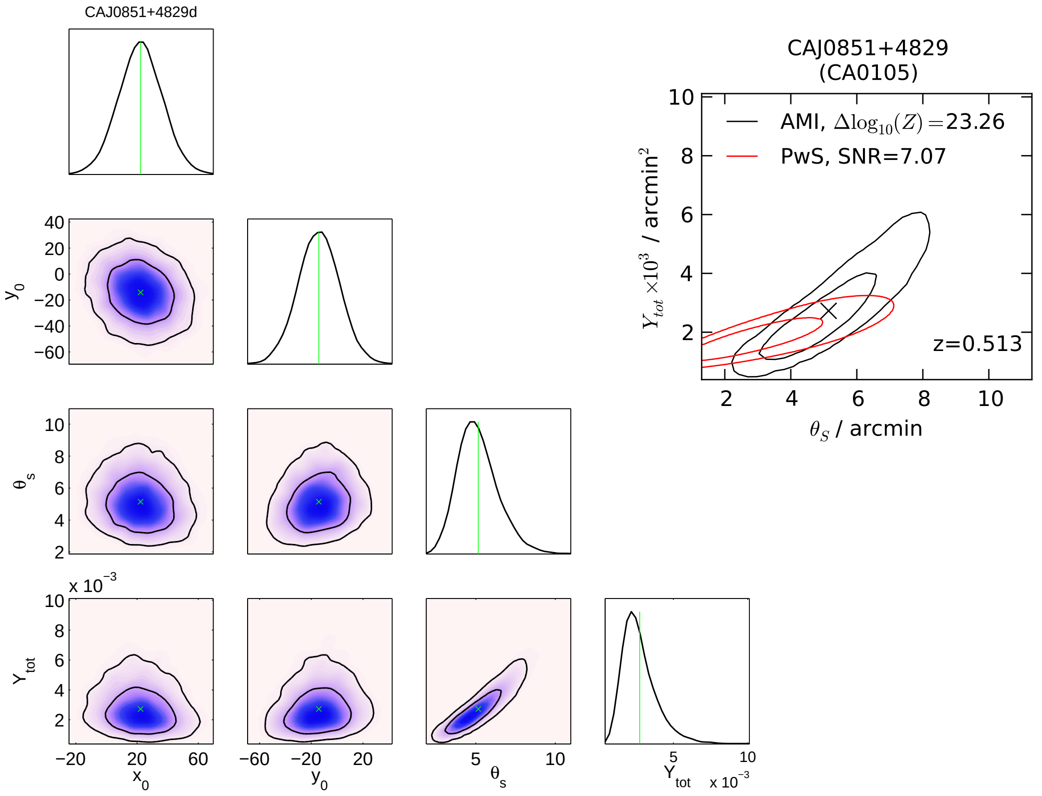

References

G. O. Abell. The Distribution of Rich Clusters of Galaxies. ApJS, 3:211, May 1958. 116

R. L. Adgie, H. P. Palmer, and M. V. Penston. A new variable radio source in Cygnus. MNRAS, 170:31P–34P, February 1975. 62

S. W. Allen, A. C. Edge, A. C. Fabian, H. Bohringer, C. S. Crawford, H. Ebeling et al. Optical spectroscopy of the ROSAT X-ray brightest clusters. MNRAS, 259:67–81, November 1992. 116

W. J. Altenhoff, D. Downes, T. Pauls, and J. Schraml. Survey of the galactic plane at 4.875 GHz. A&AS, 35:23–54, January 1979. 37

AMI Consortium: R. Barker, P. Biddulph, D. Bly, R. Boysen, A. Brown, C. Clementson et al. High-significance Sunyaev-Zel'dovich measurement: Abell 1914 seen with the Arcminute Microkelvin Imager. MNRAS, 369:L1–L4, June 2006. 112

AMI Consortium: M. L. Davies, T. M. O. Franzen, E. M. Waldram, K. J. B. Grainge, M. P. Hobson, N. Hurley-Walker et al. 10C survey of radio sources at 15.7 GHz - II. First results. MNRAS, 415:2708–2722, August 2011. 44, 55, 103

AMI Consortium: T. M. O. Franzen, M. L. Davies, R. D. Davies, R. J. Davis, F. Feroz, R. Génova-Santos et al. Follow-up observations at 16 and 33GHz of extragalactic sources from WMAP 3-yr data: II - Flux density variability. MNRAS, 400:995–1005, December 2009. 43, 44

AMI Consortium: T. M. O. Franzen, M. L. Davies, E. M. Waldram, K. J. B. Grainge, M. P. Hobson, N. Hurley-Walker et al. 10C survey of radio sources at 15.7 GHz

- I. Observing, mapping and source extraction. MNRAS, 415:2699–2707, August 2011. 29

AMI Consortium: N. Hurley-Walker, M. L. Davies, T. M. O. Franzen, K. Grainge, D. A. Green, M. P. Hobson et al. G64.5+0.9: a new shell supernova remnant with unusual central emission. MNRAS, 398:249–254, September 2009a. 10

AMI Consortium: N. Hurley-Walker, A. M. M. Scaife, D. A. Green, M. L. Davies, K. Grainge, M. P. Hobson et al. AMI observations of northern supernova remnants at 14-18GHz. MNRAS, 396:365–376, June 2009b. 10

AMI Consortium: N. Hurley-Walker, M. L. Brown, M. L. Davies, F. Feroz, T. M. O. Franzen, K. Grainge et al. Further Sunyaev-Zel'dovich observations of two Planck ERCSC clusters with the Arcminute Microkelvin Imager. MNRAS, 414:L75–L79, June 2011. 112

AMI Consortium: N. Hurley-Walker, S. Bridle, E. S. Cypriano, M. L. Davies, T. Erben, F. Feroz et al. Bayesian analysis of weak gravitational lensing and Sunyaev-Zel'dovich data for six galaxy clusters. MNRAS, 419:2921–2942, February 2012. 112

AMI Consortium: Y. C. Perrott, A. M. M. Scaife, D. A. Green, M. L. Davies, T. M. O. Franzen, K. J. B. Grainge et al. AMI Galactic Plane Survey at 16 GHz - I. Observing, mapping and source extraction. MNRAS, 429:3330–3340, March 2013a. 36, 98

AMI Consortium: C. Rodríguez-Gonzálvez, T. W. Shimwell, M. L. Davies, F. Feroz, T. M. O. Franzen, K. J. B. Grainge et al. Detailed Sunyaev-Zel'dovich study with AMI of 19 LoCuSS galaxy clusters: masses and temperatures out to the virial radius. MNRAS, 425:162–203, September 2012. 112, 116

AMI Consortium: A. M. M. Scaife, N. Hurley-Walker, M. L. Davies, P. J. Duffett-Smith, F. Feroz, K. J. B. Grainge et al. AMI limits on 15-GHz excess emission in northern HII regions. MNRAS, 385:809–822, April 2008. 9

AMI Consortium: A. M. M. Scaife, N. Hurley-Walker, D. A. Green, M. L. Davies, T. M. O. Franzen, K. J. B. Grainge et al. AMI observations of Lynds dark nebulae: further evidence for anomalous cm-wave emission. MNRAS, 400:1394–1412, December 2009a. 10

AMI Consortium: A. M. M. Scaife, N. Hurley-Walker, D. A. Green, M. L. Davies, K. J. B. Grainge, M. P. Hobson et al. An excess of emission in the dark cloud LDN1111 with the Arcminute Microkelvin Imager. MNRAS, 394:L46–L50, March 2009b. 10, 35

AMI Consortium: A. M. M. Scaife, D. A. Green, G. G. Pooley, M. L. Davies, T. M. O. Franzen, K. J. B. Grainge et al. High-resolution AMI Large Array imaging of spinning dust sources: spatially correlated 8μm emission and evidence of a stellar wind in L675. MNRAS, 403:L46–L50, March 2010a. 10, 35

AMI Consortium: A. M. M. Scaife, B. Nikolic, D. A. Green, R. Beck, M. L. Davies, T. M. O. Franzen et al. Microwave observations of spinning dust emission in NGC6946. MNRAS, 406:L45–L49, July 2010b. 10

AMI Consortium: A. M. M. Scaife, E. I. Curtis, M. Davies, T. M. O. Franzen, K. J. B. Grainge, M. P. Hobson et al. AMI Large Array radio continuum observations of Spitzer c2d small clouds and cores. MNRAS, 410:2662–2678, February 2011a. 11

AMI Consortium: A. M. M. Scaife, J. Hatchell, M. Davies, T. M. O. Franzen, K. J. B. Grainge, M. P. Hobson et al. AMI-LA radio continuum observations of Spitzer c2d small clouds and cores: Perseus region. MNRAS, 415:893–910, July 2011b. 11

AMI Consortium: T. W. Shimwell, R. W. Barker, P. Biddulph, D. Bly, R. C. Boysen, A. R. Brown et al. A blind detection of a large, complex, Sunyaev-Zel'dovich structure. MNRAS, 423:1463–1473, June 2012. 7

AMI Consortium: T. W. Shimwell, J. M. Carpenter, F. Feroz, K. J. B. Grainge, M. P. Hobson, N. Hurley-Walker et al. A joint analysis of AMI and CARMA observations of the recently discovered SZ galaxy cluster system AMI-CL J0300+2613. MNRAS, 433:2036–2046, August 2013a. 173

AMI Consortium: T. W. Shimwell, C. Rodríguez-Gonzálvez, F. Feroz, T. M. O. Franzen, K. J. B. Grainge, M. P. Hobson et al. Sunyaev-Zel'dovich observations with AMI of the hottest galaxy clusters detected in the XMM-Newton Cluster Survey. MNRAS, 433:2920–2937, August 2013b. 112

AMI Consortium: J. T. L. Zwart, R. W. Barker, P. Biddulph, D. Bly, R. C. Boysen, A. R. Brown et al. The Arcminute Microkelvin Imager. MNRAS, 391:1545–1558, December 2008. 1, 3, 6

AMI Consortium: J. T. L. Zwart, F. Feroz, M. L. Davies, T. M. O. Franzen, K. J. B. Grainge, M. P. Hobson et al. Sunyaev-Zel'dovich observations of galaxy clusters out to the virial radius with the Arcminute Microkelvin Imager. MNRAS, 418: 2754–2772, December 2011. 112

L. Angelini, S. Park, N. E. White, and P. Giommi. An update to the WGACAT ROSAT PSPC source catalog. In *American Astronomical Society Meeting Abstracts #196*, volume 32 of *Bulletin of the American Astronomical Society*, page 760, May 2000. 80

G. Anglada. Centimeter Continuum Emission from Outflow Sources. In S. Lizano and J. M. Torrelles, editors, *Circumstellar Disks, Outflows and Star Formation*, volume 1 of *Revista Mexicana de Astronomia y Astrofisica Conference Series*, page 67, April 1995. 35

M. Arnaud, G. W. Pratt, R. Piffaretti, H. Böhringer, J. H. Croston, and E. Pointecouteau. The universal galaxy cluster pressure profile from a representative sample of nearby systems (REXCESS) and the Y_{SZ} - M_{500} relation. A&A, 517:A92, July 2010. 106, 132, 150, 173

I. Bains, M. Cohen, J. M. Chapman, R. M. Deacon, and M. P. Redman. Revealing the transition from post-AGB stars to planetary nebulae: non-thermal and thermal radio continuum observations. MNRAS, 397:1386–1401, August 2009. 35

A. J. Beasley, D. Gordon, A. B. Peck, L. Petrov, D. S. MacMillan, E. B. Fomalont et al. The VLBA Calibrator Survey-VCS1. ApJS, 141:13–21, July 2002. 36, 39

R. H. Becker, R. L. White, D. J. Helfand, and S. Zoonematkermani. A 5 GHz VLA survey of the galactic plane. ApJS, 91:347–387, March 1994. 37

R. H. Becker, D. J. Helfand, R. L. White, and D. D. Proctor. Variable Radio Sources in the Galactic Plane. AJ, 140:157–166, July 2010. 45

M. Birkinshaw. The Sunyaev-Zel'dovich effect. Phys. Rep., 310:97–195, March 1999. 3

H. Böhringer, W. Voges, J. P. Huchra, B. McLean, R. Giacconi, P. Rosati et al. The Northern ROSAT All-Sky (NORAS) Galaxy Cluster Survey. I. X-Ray Properties of Clusters Detected as Extended X-Ray Sources. ApJS, 129:435–474, August 2000. 116

H. Böhringer, P. Schuecker, L. Guzzo, C. A. Collins, W. Voges, R. G. Cruddace et al. The ROSAT-ESO Flux Limited X-ray (REFLEX) Galaxy cluster survey. V. The cluster catalogue. A&A, 425:367–383, October 2004. 8

W. Brinkmann, J. Siebert, E. D. Feigelson, R. I. Kollgaard, S. A. Laurent-Muehleisen, W. Reich et al. Radio-loud active galaxies in the northern ROSAT All-Sky Survey. II. Multi-frequency properties of unidentified sources. A&A, 323:739–748, July 1997. 80

J. E. Carlstrom, G. P. Holder, and E. D. Reese. Cosmology with the Sunyaev-Zel'dovich Effect. ARA&A, 40:643–680, 2002. 4

P. Carvalho, G. Rocha, and M. P. Hobson. A fast Bayesian approach to discrete object detection in astronomical data sets - PowellSnakes I. MNRAS, 393:681–702, March 2009. 101

P. Carvalho, G. Rocha, M. P. Hobson, and A. Lasenby. PowellSnakes II: a fast Bayesian approach to discrete object detection in multi-frequency astronomical data sets. MNRAS, 427:1384–1400, December 2012. 101, 106

S. Casassus, G. F. Cabrera, F. Förster, T. J. Pearson, A. C. S. Readhead, and C. Dickinson. Morphological Analysis of the Centimeter-Wave Continuum in the Dark Cloud LDN 1622. ApJ, 639:951–964, March 2006. 35

A. Challinor, A. Lasenby, S. Somaroo, C. Doran, and S. Gull. Tunnelling times of electrons. *Physics Letters A*, 227:143–152, February 1997. 4

J. A. Combi, J. F. Albacete-Colombo, and J. Martí. A new search strategy for microquasar candidates using NVSS/2MASS and XMM-Newton data. A&A, 477: 125–132, January 2008. 80

J. A. Combi, J. F. Albacete Colombo, L. Pellizza, J. López-Santiago, G. E. Romero, J. Martí et al. A systematic cross-search for radio/infrared counterparts of XMM-Newton sources. Ap&SS, 331:53–61, January 2011. 80

J. J. Condon, W. D. Cotton, E. W. Greisen, Q. F. Yin, R. A. Perley, G. B. Taylor et al. The NRAO VLA Sky Survey. ApJ, 115:1693–1716, May 1998. 39, 71

M. Davies. *Investigating the high-frequency-radio source population using the Acrminute Microkelvin Imager*. PhD thesis, University of Cambridge, Cavendish Astrophysics & Peterhouse, 2010. 13

G. de Zotti, M. Massardi, M. Negrello, and J. Wall. Radio and millimeter continuum surveys and their astrophysical implications. A&A Rev., 18:1–65, February 2010. 55

V. D'Elia, M. Perri, S. Puccetti, M. Capalbi, P. Giommi, D. N. Burrows et al. The seven year Swift-XRT point source catalog (1SWXRT). A&A, 551:A142, March 2013. 80

B. T. Draine and A. Lazarian. Diffuse Galactic Emission from Spinning Dust Grains. ApJ, 494:L19, February 1998a. 9, 35

B. T. Draine and A. Lazarian. Electric Dipole Radiation from Spinning Dust Grains. ApJ, 508:157–179, November 1998b. 9, 35

S. A. Dzib, C. B. Rodríguez-Garza, L. F. Rodríguez, S. E. Kurtz, L. Loinard, L. A. Zapata et al. The Compact, Time-variable Radio Source Projected Inside W3(OH): Evidence for a Photoevaporated Disk? ApJ, 772:151, August 2013. 74

M. P. Egan, S. D. Price, K. E. Kraemer, D. R. Mizuno, S. J. Carey, C. O. Wright et al. The Midcourse Space Experiment Point Source Catalogue Version 2.3 Explanatory Guide. `http://irsa.ipac.caltech.edu/data/MSX/docs/msxpsc2.3_explguide.pdf`, 2003. [Online; accessed 31-July-2013]. 83

F. Feroz, M. P. Hobson, J. T. L. Zwart, R. D. E. Saunders, and K. J. B. Grainge. Bayesian modelling of clusters of galaxies from multifrequency-pointed Sunyaev-Zel'dovich observations. MNRAS, 398:2049–2060, October 2009. 103

E. Flesch. An All-Sky Atlas of Radio/X-ray Associations. PASA, 27:283–289, June 2010. 80

J. Forbrich and S. J. Wolk. On the radio-X-ray connection in young stellar objects in the Orion nebula cluster. A&A, 551:A56, March 2013. 81

J. Franco, G. Tenorio-Tagle, and P. Bodenheimer. On the formation and expansion of H II regions. ApJ, 349:126–140, January 1990. 61

E. Fürst, W. Reich, P. Reich, and K. Reif. A Radio Continuum Survey of the Galactic Plane at 11-CENTIMETER Wavelength - Part Four - a List of 6483 Small Diameter Sources. A&AS, 85:805, October 1990. 71, 76

R. A. Gaume, W. M. Goss, H. R. Dickel, T. L. Wilson, and K. J. Johnston. The NGC 7538 IRS 1 region of star formation: Observations of the H66 alpha recombination line with a spatial resolution of 300 AU. ApJ, 438:776–783, January 1995. 58

U. Giveon, R. H. Becker, D. J. Helfand, and R. L. White. A New Catalog of Radio Compact H II Regions in the Milky Way. II. The 1.4 GHz Data. AJ, 130:156–164, July 2005. 76

I. S. Gradshteyn, I. M. Ryzhik, A. Jeffrey, and D. Zwillinger. *Table of Integrals, Series, and Products*. Elsevier Academic Press, 2007. 132

K. Grainge, M. E. Jones, G. Pooley, R. Saunders, A. Edge, W. F. Grainger et al. Measuring the Hubble constant from Ryle Telescope and X-ray observations, with application to Abell 1413. MNRAS, 333:318–326, June 2002. 25

D. A. Green. A revised Galactic supernova remnant catalogue. *Bulletin of the Astronomical Society of India*, 37:45–61, March 2009. 49

P. C. Gregory and A. R. Taylor. Radio patrol of the northern Milky Way - A catalog of sources. II. AJ, 92:371–411, August 1986. 71, 79

P. C. Gregory, W. K. Scott, K. Douglas, and J. J. Condon. The GB6 Catalog of Radio Sources. ApJS, 103:427, April 1996. 71

S. F. Gull and K. J. E. Northover. Detection of hot gas in clusters of galaxies by observation of the microwave background radiation. Nature, 263:572, October 1976. 116

V. V. Gvaramadze and K. M. Menten. Discovery of a parsec-scale bipolar nebula around MWC 349A. A&A, 541:A7, May 2012. 76

T. Handa, Y. Sofue, N. Nakai, H. Hirabayashi, and M. Inoue. A radio continuum survey of the Galactic plane at 10 GHz. PASJ, 39:709–753, 1987. 36, 37

S. Harris and P. F. Scott. Observations of five thermal sources at 15 GHz with the 5-km telescope. MNRAS, 175:371–379, May 1976. 74

M. Hasselfield, M. Hilton, T. A. Marriage, G. E. Addison, L. F. Barrientos, N. Battaglia et al. The Atacama Cosmology Telescope: Sunyaev-Zel'dovich selected galaxy clusters at 148 GHz from three seasons of data. J. Cosmology Astropart. Phys., 7:008, July 2013. 7

D. J. Helfand, R. H. Becker, R. L. White, A. Fallon, and S. Tuttle. MAGPIS: A Multi-Array Galactic Plane Imaging Survey. AJ, 131:2525–2537, May 2006. 37

G. Helou and D. W. Walker, editors. *Infrared astronomical satellite (IRAS) catalogs and atlases. Volume 7: The small scale structure catalog*, volume 7, 1988. 82

T. Hirota, T. Bushimata, Y. K. Choi, M. Honma, H. Imai, K. Iwadate et al. Distance to Orion KL Measured with VERA. PASJ, 59:897–903, October 2007. 58

L. Hirsch, J. D. Adams, T. L. Herter, J. L. Hora, J. M. De Buizer, S. T. Megeath et al. SOFIA/FORCAST and Spitzer/IRAC Imaging of the Ultracompact H II Region W3(OH) and Associated Protostars in W3. ApJ, 757:113, October 2012. 74

M. P. Hobson and J. E. Baldwin. Markov-Chain Monte Carlo Approach to the Design of Multilayer Thin-Film Optical Coatings. Appl. Opt., 43:2651–2660, May 2004. 66

N. Hurley-Walker. *Targeted Science Observations with the Arcminute Microkelvin Imager (AMI)*. PhD thesis, University of Cambridge, Cavendish Astrophysics & Corpus Christi College, 2010. 14, 20

R. Ignace and E. Churchwell. Free-Free Spectral Energy Distributions of Hierarchically Clumped H II Regions. ApJ, 610:351–360, July 2004. 61

K. Immer, A. Brunthaler, M. J. Reid, A. Bartkiewicz, Y. K. Choi, K. M. Menten et al. The VLBA Calibrator Search for the BeSSeL Survey. ApJS, 194:25, June 2011. 71, 79

N. Itoh, Y. Kohyama, and S. Nozawa. Relativistic Corrections to the Sunyaev-Zeldovich Effect for Clusters of Galaxies. ApJ, 502:7, July 1998. 4

M. Jones, R. Saunders, P. Alexander, M. Birkinshaw, N. Dilon, K. Grainge et al. An image of the Sunyaev-Zel'dovich effect. Nature, 365:320–323, September 1993. 116

T. Kaneko. Toward the arrival of SZ cluster surveys: the Arcminute Microkelvin Imager Small Array. In *Society of Photo-Optical Instrumentation Engineers (SPIE) Conference Series*, volume 6267 of *Society of Photo-Optical Instrumentation Engineers (SPIE) Conference Series*, July 2006. 6

C. R. Kerton and C. M. Brunt. The association of IRAS sources and ^{12}CO emission in the outer Galaxy. A&A, 399:1083–1099, March 2003. 82

E. Komatsu, K. M. Smith, J. Dunkley, C. L. Bennett, B. Gold, G. Hinshaw et al. Seven-year Wilkinson Microwave Anisotropy Probe (WMAP) Observations: Cosmological Interpretation. ApJS, 192:18, February 2011. 137

G. Langston, A. Minter, L. D'Addario, K. Eberhardt, K. Koski, and J. Zuber. The First Galactic Plane Survey at 8.35 and 14.35 GHz. AJ, 119:2801–2827, June 2000. 35, 37

S. A. Laurent-Muehleisen, R. I. Kollgaard, P. J. Ryan, E. D. Feigelson, W. Brinkmann, and J. Siebert. Radio-loud active galaxies in the northern ROSAT All-Sky Survey. I. Radio identifications. A&AS, 122:235–247, April 1997. 80

E. M. Leitch, A. C. S. Readhead, T. J. Pearson, and S. T. Myers. An Anomalous Component of Galactic Emission. ApJ, 486:L23, September 1997. 9, 35

S. Lizano. Hypercompact HII Regions. In H. Beuther, H. Linz, and T. Henning, editors, *Massive Star Formation: Observations Confront Theory*, volume 387 of *Astronomical Society of the Pacific Conference Series*, page 232, May 2008. 84

M. Longair. Radio Astronomy and Cosmology: Lessons from the Past -3C,4C. In M. N. Bremer, N. Jackson, and I. Perez-Fournon, editors, *Observational Cosmology with the New Radio Surveys*, volume 226 of *Astrophysics and Space Science Library*, page 3, 1998. 34

P. W. Lucas, M. G. Hoare, A. Longmore, A. C. Schröder, C. J. Davis, A. Adamson et al. The UKIDSS Galactic Plane Survey. MNRAS, 391:136–163, November 2008. 83

P. G. Mezger and A. P. Henderson. Galactic H II Regions. I. Observations of Their Continuum Radiation at the Frequency 5 GHz. ApJ, 147:471, February 1967. 35

P. G. Mezger, W. Altenhoff, J. Schraml, B. F. Burke, E. C. Reifenstein, III, and T. L. Wilson. A New Class of Compact H II Regions Associated with OH Emission Sources. ApJ, 150:L157, December 1967. 74

T. Murphy, M. Cohen, R. D. Ekers, A. J. Green, R. M. Wark, and V. Moss. Ultra- and hyper-compact HII regions at 20 GHz. MNRAS, 405:1560–1572, July 2010a. 58, 60

T. Murphy, E. M. Sadler, R. D. Ekers, M. Massardi, P. J. Hancock, E. Mahony et al. The Australia Telescope 20 GHz Survey: the source catalogue. MNRAS, 402:2403–2423, March 2010b. 35, 37

D. Nagai, A. V. Kravtsov, and A. Vikhlinin. Effects of Galaxy Formation on Thermodynamics of the Intracluster Medium. ApJ, 668:1–14, October 2007. 130

J. F. Navarro, C. S. Frenk, and S. D. M. White. The Structure of Cold Dark Matter Halos. ApJ, 462:563, May 1996. 130

J. F. Navarro, C. S. Frenk, and S. D. M. White. A Universal Density Profile from Hierarchical Clustering. ApJ, 490:493, December 1997. 130

M. Olamaie, F. Feroz, K. J. B. Grainge, M. P. Hobson, J. S. Sanders, and R. D. E. Saunders. Bayes-X: a Bayesian inference tool for the analysis of X-ray observations of galaxy clusters. MNRAS, in prep. 173

B. M. Pazderska, M. P. Gawroński, R. Feiler, M. Birkinshaw, I. W. A. Browne, R. Davis et al. Survey of planetary nebulae at 30 GHz with OCRA-p. A&A, 498: 463–470, May 2009. 78

R. A. Perley and B. J. Butler. An Accurate Flux Density Scale from 1 to 50 GHz. ApJS, 204:19, February 2013. 14, 43

Y. C. Perrott, A. M. M. Scaife, N. Hurley-Walker, and K. J. B. Grainge. Investigating the Source of Planck-Detected AME: High-Resolution Observations at 15 GHz. *Advances in Astronomy*, 2013:354259, 2013b. 9

R. Piffaretti, M. Arnaud, G. W. Pratt, E. Pointecouteau, and J.-B. Melin. The MCXC: a meta-catalogue of x-ray detected clusters of galaxies. A&A, 534:A109, October 2011. 8

A. Piters, C. de Jager, and H. Nieuwenhuijzen. The atmospheric structure, stellar wind and binary characteristics of the hypergiant HR 8752 (G0-5Ia+). A&A, 196: 115–127, May 1988. 77

Planck Collaboration, P. A. R. Ade, N. Aghanim, M. Arnaud, M. Ashdown, J. Aumont et al. Planck early results. I. The Planck mission. A&A, 536:A1, December 2011a. 100

Planck Collaboration, P. A. R. Ade, N. Aghanim, M. Arnaud, M. Ashdown, J. Aumont et al. Planck early results. XX. New light on anomalous microwave emission from spinning dust grains. A&A, 536:A20, December 2011b. 97

Planck Collaboration, P. A. R. Ade, N. Aghanim, C. Armitage-Caplan, M. Arnaud, M. Ashdown et al. Planck 2013 results. XXIX. Planck catalogue of Sunyaev-Zeldovich sources. *ArXiv e-prints*, March 2013a. 7, 8, 100, 106

Planck Collaboration, P. A. R. Ade, N. Aghanim, C. Armitage-Caplan, M. Arnaud, M. Ashdown et al. Planck 2013 results. VII. HFI time response and beams. *ArXiv e-prints*, March 2013b. 101

Planck Collaboration, P. A. R. Ade, N. Aghanim, C. Armitage-Caplan, M. Arnaud, M. Ashdown et al. Planck 2013 results. XX. Cosmology from Sunyaev-Zeldovich cluster counts. *ArXiv e-prints*, March 2013c. 146

Planck Collaboration, P. A. R. Ade, N. Aghanim, M. Arnaud, M. Ashdown, F. Atrio-Barandela et al. Planck intermediate results. V. Pressure profiles of galaxy clusters from the Sunyaev-Zeldovich effect. A&A, 550:A131, February 2013d. 134, 136

Planck Collaboration, N. Aghanim, C. Armitage-Caplan, M. Arnaud, M. Ashdown, F. Atrio-Barandela et al. Planck 2013 results. IV. Low Frequency Instrument beams and window functions. *ArXiv e-prints*, March 2013e. 101

Planck Collaboration, AMI Collaboration, P. A. R. Ade, N. Aghanim, M. Arnaud, M. Ashdown et al. Planck intermediate results. II. Comparison of Sunyaev-Zeldovich measurements from Planck and from the Arcminute Microkelvin Imager for 11 galaxy clusters. A&A, 550:A128, February 2013f. 101, 112

S. D. Price, M. P. Egan, S. J. Carey, D. R. Mizuno, and T. A. Kuchar. Midcourse Space Experiment Survey of the Galactic Plane. AJ, 121:2819–2842, May 2001. 82

C. R. Purcell, M. G. Hoare, and P. Diamond. The CORNISH Survey of the Galactic Plane. In H. Beuther, H. Linz, and T. Henning, editors, *Massive Star Formation: Observations Confront Theory*, volume 387 of *Astronomical Society of the Pacific Conference Series*, page 389, May 2008. 37

P. Reich, W. Reich, and E. Fürst. The Effelsberg 21 cm radio continuum survey of the Galactic plane between L = 95.5 deg and L = 240 deg. A&AS, 126:413–435, December 1997. 37

W. Reich, E. Fürst, C. G. T. Haslam, P. Steffen, and K. Reif. A radio continuum survey of the Galactic Plane at 11 cm wavelength. I - The area L = 357.4 to 76 deg, B = -1.5 to +1.5 deg. A&AS, 58:197–199, November 1984. 37

W. Reich, E. Fürst, P. Reich, and K. Reif. A radio continuum survey of the Galactic Plane at 11 cm wavelength. II - The area L = 358-76 deg, B = -5 to 5 deg. III. A&AS, 85:633–690, October 1990a. 37

W. Reich, P. Reich, and E. Fürst. The Effelsberg 21 cm radio continuum survey of the Galactic plane between L = 357 deg and L = 95.5 deg. A&AS, 83:539–568, June 1990b. 37

C. L. Reichardt, B. Stalder, L. E. Bleem, T. E. Montroy, K. A. Aird, K. Andersson et al. Galaxy Clusters Discovered via the Sunyaev-Zel'dovich Effect in the First 720 Square Degrees of the South Pole Telescope Survey. ApJ, 763:127, February 2013. 7

K. Reif, W. Reich, P. Steffen, P. Müller, and H. Weiland. The Stockert 2.72 GHz Radio-continuum Survey of the Galactic Plane - Part I. *Mitteilungen der Astronomischen Gesellschaft Hamburg*, 70:419, 1987. 37

ROSAT Consortium. Second ROSAT PSPC Catalog (ROSAT, 2000). *VizieR Online Data Catalog*, 9030:0, July 2000. 80

D. J. Rudy, D. O. Muhleman, G. L. Berge, B. M. Jakosky, and P. R. Christensen. Mars - VLA observations of the northern hemisphere and the north polar region at wavelengths of 2 and 6 cm. Icarus, 71:159–177, July 1987. 14

R. Sahai, M. R. Morris, and G. G. Villar. Young Planetary Nebulae: Hubble Space Telescope Imaging and a New Morphological Classification System. AJ, 141:134, April 2011. 78, 81

S. Sharpless. A Catalogue of H II Regions. ApJS, 4:257, December 1959. 49

N. Siódmiak and R. Tylenda. An analysis of the observed radio emission from planetary nebulae. A&A, 373:1032–1042, July 2001. 77

M. F. Skrutskie, R. M. Cutri, R. Stiening, M. D. Weinberg, S. Schneider, J. M. Carpenter et al. The Two Micron All Sky Survey (2MASS). AJ, 131:1163–1183, February 2006. 83

J. M. Stil, A. R. Taylor, J. M. Dickey, D. W. Kavars, P. G. Martin, T. A. Rothwell et al. The VLA Galactic Plane Survey. AJ, 132:1158–1176, September 2006. 37

R. A. Sunyaev and Y. B. Zeldovich. The Spectrum of Primordial Radiation, its Distortions and their Significance. *Comments on Astrophysics and Space Physics*, 2:66, March 1970. 3

R. A. Sunyaev and Y. B. Zeldovich. The Observations of Relic Radiation as a Test of the Nature of X-Ray Radiation from the Clusters of Galaxies. *Comments on Astrophysics and Space Physics*, 4:173, November 1972. 3

M. Tavani, A. Bulgarelli, G. Piano, S. Sabatini, E. Striani, Y. Evangelista et al. Extreme particle acceleration in the microquasar CygnusX-3. *Nature*, 462:620–623, December 2009. 11

A. R. Taylor, S. J. Gibson, M. Peracaula, P. G. Martin, T. L. Landecker, C. M. Brunt et al. The Canadian Galactic Plane Survey. AJ, 125:3145–3164, June 2003. 36, 37

M. A. Thompson, J. Hatchell, A. J. Walsh, G. H. MacDonald, and T. J. Millar. A SCUBA imaging survey of ultracompact HII regions. The environments of massive star formation. A&A, 453:1003–1026, July 2006. 96

C. T. Tibbs, N. Flagey, R. Paladini, M. Compiègne, S. Shenoy, S. Carey et al. Spitzer characterization of dust in an anomalous emission region: the Perseus cloud. MNRAS, 418:1889–1900, December 2011. 35

J. Tinker, A. V. Kravtsov, A. Klypin, K. Abazajian, M. Warren, G. Yepes et al. Toward a Halo Mass Function for Precision Cosmology: The Limits of Universality. ApJ, 688:709–728, December 2008. 106

M. Todorović, R. D. Davies, C. Dickinson, R. J. Davis, K. A. Cleary, R. Génova-Santos et al. A 33-GHz Very Small Array survey of the Galactic plane from l = 27 deg to 46 deg. MNRAS, 406:1629–1643, August 2010. 37

S. A. Trushkin. The RATAN Galactic Plane Survey. In B. J. McLean, D. A. Golombek, J. J. E. Hayes, and H. E. Payne, editors, *New Horizons from Multi-Wavelength Sky Surveys*, volume 179 of *IAU Symposium*, page 103, 1998. 37

J. S. Urquhart, A. L. Busfield, M. G. Hoare, S. L. Lumsden, R. D. Oudmaijer, T. J. T. Moore et al. The RMS survey. ^{13}CO observations of candidate massive YSOs in the northern Galactic plane. A&A, 487:253–264, August 2008. 74

J. S. Urquhart, M. G. Hoare, C. R. Purcell, S. L. Lumsden, R. D. Oudmaijer, T. J. T. Moore et al. The RMS survey. 6 cm continuum VLA observations towards candidate massive YSOs in the northern hemisphere. A&A, 501:539–551, July 2009. 74

S. J. Vessey and D. A. Green. The 7C(G) survey of radio sources at 151 MHz - The Galactic plane at L between 80 and 104 deg and L between 126 and 180 deg, for /b/ less than or equal to 5.5 deg. MNRAS, 294:607, March 1998. 37

K. Viironen, R. Greimel, R. L. M. Corradi, A. Mampaso, M. Rodríguez, L. Sabin et al. Candidate planetary nebulae in the IPHAS photometric catalogue. A&A, 504: 291–301, September 2009. 77

E. M. Waldram, G. G. Pooley, K. J. B. Grainge, M. E. Jones, R. D. E. Saunders, P. F. Scott et al. 9C: a survey of radio sources at 15 GHz with the Ryle Telescope. MNRAS, 342:915–925, July 2003. 35

E. M. Waldram, G. G. Pooley, M. L. Davies, K. J. B. Grainge, and P. F. Scott. 9C continued: results from a deeper radio-source survey at 15 GHz. MNRAS, 404: 1005–1017, May 2010. 57

M. G. Watson, A. C. Schröder, D. Fyfe, C. G. Page, G. Lamer, S. Mateos et al. The XMM-Newton serendipitous survey. V. The Second XMM-Newton serendipitous source catalogue. A&A, 493:339–373, January 2009. 80

R. A. Watson, R. Rebolo, J. A. Rubiño-Martín, S. Hildebrandt, C. M. Gutiérrez, S. Fernández-Cerezo et al. Detection of Anomalous Microwave Emission in the Perseus Molecular Cloud with the COSMOSOMAS Experiment. ApJ, 624:L89–L92, May 2005. 35

H. J. Wendker. Radio continuum emission from stars: a catalogue update. A&AS, 109:177–179, January 1995. 71, 76, 77, 78

I. H. Whittam, J. M. Riley, D. A. Green, M. J. Jarvis, I. Prandoni, G. Guglielmino et al. The faint source population at 15.7 GHz - I. The radio properties. MNRAS, 429: 2080–2097, March 2013. 64

D. O. S. Wood and E. Churchwell. The morphologies and physical properties of ultracompact H II regions. ApJS, 69:831–895, April 1989. 58

E. L. Wright, P. R. M. Eisenhardt, A. K. Mainzer, M. E. Ressler, R. M. Cutri, T. Jarrett et al. The Wide-field Infrared Survey Explorer (WISE): Mission Description and Initial On-orbit Performance. AJ, 140:1868, December 2010. 83

Y. Xu, M. J. Reid, X. W. Zheng, and K. M. Menten. The Distance to the Perseus Spiral Arm in the Milky Way. *Science*, 311:54–57, January 2006. 58

N. Zacharias, D. G. Monet, S. E. Levine, S. E. Urban, R. Gaume, and G. L. Wycoff. The Naval Observatory Merged Astrometric Dataset (NOMAD). In *American Astronomical Society Meeting Abstracts*, volume 36 of *Bulletin of the American Astronomical Society*, page 1418, December 2004. 83

A. A. Zdziarski, G. G. Pooley, and G. K. Skinner. The doubling of the superorbital period of Cyg X-1. MNRAS, 412:1985–1992, April 2011. 11

A. A. Zijlstra, P. A. M. van Hoof, and R. A. Perley. The Evolution of NGC 7027 at Radio Frequencies: A New Determination of the Distance and Core Mass. ApJ, 681:1296–1309, July 2008. 43

S. Zoonematkermani, D. J. Helfand, R. H. Becker, R. L. White, and R. A. Perley. A catalog of small-diameter radio sources in the Galactic plane. ApJS, 74:181–224, September 1990. 37

J. Zwart. *Preparing for Blind Surveys with the Arcminute Microkelvin Imager*. PhD thesis, University of Cambridge, Cavendish Astrophysics & Jesus College, 2007. 5